

## University of Southampton Research Repository ePrints Soton

Copyright © and Moral Rights for this thesis are retained by the author and/or other copyright owners. A copy can be downloaded for personal non-commercial research or study, without prior permission or charge. This thesis cannot be reproduced or quoted extensively from without first obtaining permission in writing from the copyright holder/s. The content must not be changed in any way or sold commercially in any format or medium without the formal permission of the copyright holders.

When referring to this work, full bibliographic details including the author, title, awarding institution and date of the thesis must be given e.g.

AUTHOR (year of submission) "Full thesis title", University of Southampton, name of the University School or Department, PhD Thesis, pagination

**UNIVERSITY OF SOUTHAMPTON**

**FACULTY OF ENGINEERING AND THE ENVIRONMENT**  
national Centre for Advanced Tribology at Southampton

&

**FACULTY OF PHYSICAL AND APPLIED SCIENCE**

School of Electronics and Computer Science  
Nano Research Group

**Development of a Quasi-Concertina MEMS Sensor  
for the  
Characterisation of Biopolymers**

by

**David Grech**

Thesis for the degree of Doctor of Philosophy

November 2014

Supervisors: Dr. Harold M.H. Chong

Prof. Robert J. K. Wood

Dr. Jurgita Zekonyte



UNIVERSITY OF SOUTHAMPTON

## **ABSTRACT**

FACULTY OF ENGINEERING AND THE ENVIRONMENT  
NATIONAL CENTRE FOR ADVANCED TRIBOLOGY (nCATS)

&

FACULTY OF PHYSICAL AND APPLIED SCIENCE  
ELECTRONICS AND COMPUTER SCIENCE

A thesis submitted in partial fulfilment for the degree of Doctor of Philosophy

### **DEVELOPMENT OF A QUASI-CONCERTINA MEMS SENSOR FOR THE CHARACTERISATION OF BIOPOLYMERS**

By David Grech

The main objective of this project was to develop a Force-Displacement microelectromechanical systems (MEMS) sensor with a broad measurement range for the mechanical characterisation of soft biopolymers and adaptable for in-vivo measurement applications. The device was designed to take advantage of the relatively small size, high resolution, and batch fabrication capabilities of MEMS technology.

The sensor is based on a novel Quasi-Concertina (QC) spring which is a design that exhibits high out-of-plane compliance, linearity, and deflection and low in-plane compliance. These are features which are essential when high accuracy over large deflections is required. In this work QC springs with a spring constant of 4.5 N/m and 0.28 N/m have been developed and shown to exhibit a F-D linearity as little as 0.48% at a deflection of 100  $\mu\text{m}$  and a total deflection before fracture of as much as 8000  $\mu\text{m}$  with a F-D linearity of 27.6%.

To enable F-D detection, piezoresistive transduction with a full Wheatstone bridge configuration was integrated into the QC spring. This method of transduction enables the sensor to function without external lasers, magnetic fields, or optical microscopes and requires minimum experiment setup expertise, no sample preparation, and does not subject the samples to laser heating. Furthermore the sensors were optimised for a high force resolution and low power dissipation for quasi-static measurements (1-10 Hz).

The fabricated sensors have a measured F-D resolution of 5.4 nN and 1.2 nm with polysilicon piezoresistors and a theoretical F-D resolution of 19 pN and 9 pm with crystalline silicon piezoresistors.

The polysilicon p-type piezoresistors used in the fabricated sensors were deposited using Hot-Wire Chemical Vapour Deposition (HWCVD). A gauge factor of as much as 44 was measured for these piezoresistors for which no data has been previously published.

The large surface area and the low spring constant of the sensors proved incompatible with conventional methods of microfabrication. Initial attempts resulted in damaged, over etched devices or devices damaged by stiction. To circumvent these issues, a novel stiction free process was developed. In this process the suspended structure is semi-released, before front side fabrication, using a wet etch and completely released, following front side fabrication, using a dry etch.

For proof of concept, the QC sensor was used to measure the stiffness of agarose hydrogels at different levels of concentration. Agarose was purposely used for these measurements as it is a biopolymer which mimics the mechanical stiffness of soft biological tissue such as cartilage. These measurements showed that the sensor can accurately differentiate between different concentrations of agarose. Moreover, the measured values of the Young's modulus of the hydrogels were in close agreement with published data, thus confirming the potential of the QC sensor for the F-D measurements of biopolymers.

The research work disclosed in this publication is partially funded by the Strategic Educational Pathways Scholarship Scheme (Malta). The scholarship is part-financed by the European Union European Social Fund



# Contents

<b>Chapter 1 Introduction</b> .....	<b>1</b>
1.1 Motivation of the thesis.....	1
1.2 Objectives.....	2
1.3 Organisation of the thesis.....	3
<b>Chapter 2 Literature Review</b> .....	<b>5</b>
2.1 F-D techniques.....	5
2.1 MEMS flexures.....	9
2.1.1 Linear and Non-linear Deflections.....	9
2.2 Sensor Transduction Mechanisms.....	15
2.2.1 A review of piezoresistive transduction.....	17
2.1 Conclusions.....	29
<b>Chapter 3 Design, Simulation and Optimisation</b> .....	<b>37</b>
3.1 Mechanical Design.....	37
3.1.1 Design Rationale.....	38
3.1.2 Out-of-plane Spring Constant.....	41
3.1.3 First-mode resonant frequency.....	42
3.1.4 Linearity.....	44
3.2 Electrical Design.....	45
3.3 Optimisation.....	47
3.3.1 Optimisation Algorithm.....	48
3.3.2 Piezoresistor Positioning.....	56
3.4 Simulation.....	58
3.4.1 Mechanical properties.....	58
3.4.2 Sensor readout error versus angle of actuation.....	60
3.5 Macroscale Prototype.....	61
3.6 Conclusions.....	64

<b>Chapter 4 Fabrication</b> .....	<b>69</b>
4.1 Initial Trials.....	69
4.1.1 Device release trial 1 – ICP Si etch.....	69
4.1.2 Device release trial 2 – Hydrofluoric vapour etch.....	72
4.2 QC Fabrication Process.....	73
4.2.1 Wafer Preparation.....	74
4.2.2 Backside Semi-Release.....	74
4.2.3 Defining the Suspended Structure.....	76
4.2.4 Defining the Piezoresistors.....	76
4.2.5 Defining the Electrical Contact Terminals.....	77
4.2.6 Sensor Release.....	77
4.2.7 Fabricated Devices.....	80
4.3 Conclusions.....	83
<b>Chapter 5 Characterisation</b> .....	<b>85</b>
5.1 Mechanical characterisation.....	85
5.1.1 Spring Constant, Linearity and Maximum Deflection Measurements.....	86
5.1.2 Resonant frequencies .....	93
5.2 Electrical Characterisation.....	94
5.2.1 Contact resistance and doping concentration .....	94
5.2.2 Electrical Test Circuit.....	97
5.2.3 Electrical Noise Characterisation.....	101
5.2.4 Determining the Sensitivity.....	103
5.2.5 Minimum Force and Displacement Resolution.....	108
5.3 Characterisation of the HWCVD Polysilicon Piezoresistors.....	110
5.3.1 Raman Spectroscopy.....	110

5.3.2	AFM.....	112
5.3.3	Determining the Gauge Factor.....	113
5.3.4	Determining the Hooke Factor.....	115
5.4	Conclusions.....	116
<b>Chapter 6 Towards Biosensing Applications.....</b>		<b>121</b>
6.1	Materials and methods.....	124
6.1.1	Indentation.....	126
6.1.2	Determining Young's Modulus.....	126
6.2	Results and discussion.....	128
6.3	Conclusions.....	131
<b>Chapter 7 Conclusions, Future work and Possible Applications.....</b>		<b>135</b>
7.1	Conclusions.....	135
7.2	Future work.....	137
<b>Appendix 1.....</b>		<b>143</b>
	QC first resonant frequency Solver – MATLAB Code.....	143
	Non-Linear Deflection Calculator – MATLAB Code.....	147
	Optimisation Program – MATLAB Code.....	149
<b>Appendix 2.....</b>		<b>159</b>
	Fabrication Recipes.....	159
	Photolithography Masks.....	162
	Images of Additional Fabricated Suspended Structures.....	166

**Appendix 3** .....167  
Modified Cantilever on Cantilever Derivation .....167

# List of figures

<b>Figure 2-1:</b> Force application or active techniques for biomechanical measurements. ...	6
<b>Figure 2-2:</b> Force sensing or passive techniques for biomechanical traction measurements.....	6
<b>Figure 2-3:</b> Range relevant to representative biological structures and processes.....	7
<b>Figure 2-4:</b> Graphical representation of the piezoresistive cantilever developed by Park et al.....	8
<b>Figure 2-5:</b> (a) SEM image of the F-D sensor developed by Rajagopalan et al., (b) magnified view of the probe and reference beam. ....	9
<b>Figure 2-6:</b> Deflected cantilever beam showing the radius of curvature ( $r$ ) and the angle of deflection ( $\theta$ ). ....	10
<b>Figure 2-7:</b> Typical beam configurations (a) cantilever, (b) guided cantilever and (c) fixed-fixed beam. ....	11
<b>Figure 2-8:</b> Comparison between linear beam theory and non-linear theory shows that they are approximately equal for only small deflections .....	14
<b>Figure 2-9:</b> Common MEMS transduction mechanisms.....	15
<b>Figure 2 10:</b> Force resolution versus maximum force for capacitive, piezoelectric and piezoresistive transduction mechanisms .....	17
<b>Figure 2-11:</b> Typical Wheatstone bridge configurations (a) quarter bridge, (b) half bridge, and (c) full bridge.....	19
<b>Figure 2-12:</b> Two polysilicon structures: (a) random crystal or, (b) column structure..	24
<b>Figure 2-13:</b> Examples of two polysilicon films deposited at (a) 560°C and (b) 601°C. In both cases, the grain size was approximately 60 nm. The image shows that the deposition at 560°C has less crystalline Si grains, thus there is a greater distance between the crystals. This allows the crystals to grow further when annealed.....	25
<b>Figure 2-14:</b> Grain size as a function of deposition temperature. After LPCVD deposition, samples were implanted with boron and annealed at 1000°C for 30 min. ....	25
<b>Figure 2-15:</b> Simple electrical model for polysilicon.....	26

<b>Figure 2-16:</b> Resistivity versus doping concentration for crystalline Si, polysilicon deposited at 560°C and polysilicon deposited at 610°C.....	27
<b>Figure 2-17:</b> Gauge Factor as a function of deposition temperature. All films were annealed at 1000 °C after implantation.....	27
<b>Figure 2-18:</b> Graph of gauge factor as a function of doping concentration for both boron and phosphorus doped material. All films were deposited at 560°C.....	28
<b>Figure 2-19:</b> Layers which make up a polycrystalline piezoresistive device.....	28
<b>Figure 3-1:</b> MEMS spring types (a) Cantilever, (b) Double Clamped Beams, (c) Meander, (d) Hammock, (e) Crab-leg , (f) Folded, (g) Lateral Suspension, and (h) Spring-Supported Diaphragm. ....	38
<b>Figure 3-2:</b> Geometric parameters of a cantilever.....	38
<b>Figure 3-3:</b> A model of the Quasi-Concertina (QC) Spring developed in this work. ....	40
<b>Figure 3-4:</b> (a) Top view of a QC spring with an in-plane force ( $F_x$ ) applied to the suspended platform, (b) the spring is simplified by taking only one set of beams into consideration, and (c) the deflection of the suspended platform is restrained by beams that bend (B) which have high compliance, and beams that go into tension (T) and compression (C) which have a low compliance.....	40
<b>Figure 3-5:</b> (a) QC spring with a force, $F_z$ , applied to the platform, (b) the spring is simplified by ignoring the beam sets on three of the four sides leaving the set shown and an applied load of, $F_z/4$ and (c) the beam is simplified further by focusing on just one beam.....	41
<b>Figure 3-6:</b> A simplified representation of the QC spring with the mass of the springs ignored and only the mass of the suspended platform taken into consideration. This facilitates the analytical calculation of the first-mode resonant frequency of the spring. ....	42
<b>Figure 3-7:</b> (a) A simplified representation of a QC spring with 6 beam sets. Each beam set is replaced by massless spring and a discrete mass, and (b) a FBD showing the resultant forces acting on the suspended platform.....	44
<b>Figure 3-8:</b> To investigate the linearity of the spring versus the deflection further simplification is necessary. (a) Simplified beam, (b) through symmetry the right hand	

side of the device is ignored leaving a cantilever with a load of  $F/8$  and a moment  $M_{beam}$ , (c) additional simplification is possible by considering only half the remaining beam which leaves a cantilever of length  $l/4$  and a load of  $F/8$ . ..... 45

**Figure 3-9:** The double clamped beam can be simplified to two beams in series of length  $l/4$ , in parallel with two identical cantilevers in series ..... 45

**Figure 3-10:** (a) Quarter, (b) half, and (c) full Wheatstone bridge configurations. .... 46

**Figure 3-11:** Areas in compression and in tension of a double clamped beam with a central load. .... 46

**Figure 3-12:** Top view of a QC sensor with piezoresistors for self-sensing. The beams are in compression and in tension in the areas indicated only when a load is applied directly into the page. The piezoresistors are positioned in areas that are in compression and in tension to fulfil the requirements of a full Wheatstone bridge. The piezoresistors in each leg are divided into two equal parts and positioned over two beams orthogonal to one another. This feature allows any photolithographic misalignment to effect each piezoresistors leg equally, thus the bridge remains balanced. .... 47

**Figure 3-13:** Flow chart showing the process used to optimise the QC MEMS sensor. 50

**Figure 3-14:** GA output graphs for QC 5 (a) Power vs.  $F_{min}$ , (b)  $V_{Bridge}$ , vs.  $F_{min}$  (c) Number of beam sets vs.  $F_{min}$ , and (d)  $w$  vs.  $F_{min}$ . Each data point represents a possible design solution. The data point in red represents the solution selected. .... 53

**Figure 3-15:** GA output graphs for QC 5 (a)  $t_{pr}$  vs.  $F_{min}$ , (b)  $l_{pr}/l$ , vs.  $F_{min}$  (c)  $w_{sep}$  sets vs.  $F_{min}$ , and (d)  $l_{sp}$  vs.  $F_{min}$ . The data point in red represents the solution selected. .... 54

**Figure 3-16:** QC sensor top view and cross-sectional view showing the piezoresistor offset direction. Using a parametric numerical analysis the piezoresistor is incrementally offset along the beam. The percentage change in resistance is calculated at each offset. .... 57

**Figure 3-17:** Piezoresistive percentage change in resistance versus the piezoresistor offset from the centre of the beam (from compression to tension). To ensure a linear relationship between ***VOutput*** and the displacement, the percentage change in resistance needs to be equal and opposite between the piezoresistors in tension and in compression. The graph can be used to determine the position of the piezoresistors. For

example if the piezoresistors in compression is positioned at  $0 \mu\text{m}$ , i.e. has a change in resistance of  $-4.5 \times 10^{-5} \%$ , the piezoresistor in tension would need to be positioned at  $600 \mu\text{m}$  where the change in resistance is equal and opposite that of the piezoresistor in compression (i.e. at  $+4.5 \times 10^{-5} \%$ )..... 57

**Figure 3-18:** Numerical analysis of a QC 2 spring with a load applied to the platform. The simulation shows that deflections as large as  $8300 \mu\text{m}$  are possible with a QC spring..... 59

**Figure 3-19:** Direction of actuation of the suspended platform for the QC MEMS sensor readout versus the angle of actuation analysis. .... 60

**Figure 3-20:** Graphs for  $V_{\text{Output}}/V_{\text{Bridge}}$  versus an applied force with an  $0-45^\circ$  angle of incidence and  $V_{\text{Output}}/V_{\text{Bridge}}$  versus the out-of-plane component of an applied force with  $0-45^\circ$  angle of incidence for (a-b) QC 1, (c-d) QC 2, and (e-f) QC 3 respectively. .... 61

**Figure 3-21:** The macroscale prototype was fabricated using Stereolithography (SLA) rapid prototyping. Strain gauges were bonded to the beams to mimic the piezoresistors. .... 62

**Figure 3-22:** Circuit used to test the macroscale prototype..... 62

**Figure 3-23:** A translation stage with Vernier head was used to actuate the macroscale prototype during characterisation..... 63

**Figure 3-24:** Force-displacement characteristics of the macroscale model using measurements from the prototype, analytical calculations and numerical analysis. .... 64

**Figure 4-1:** Cross-section of the DRIE release ..... 70

**Figure 4-2:** Scanning Electron Microscope image of the top view of a partially released QC sensor fabricated using an ICP Si etch to remove the WHB. The outline of the un-etched Si along the perimeter of the structure can be seen through the beams. In the centre the BOX layer has been breached and the top layer of the structure shows evidence of being etched. If this etch was continued, the suspended structure would have been damaged. .... 71

**Figure 4-3:** Scanning Electron Microscope image of the bottom view of the device shown in Figure 4.2. The un-etched Si can be seen along the perimeter. The image also

shows that the BOX etch-stop, the photoresist and SiO <sub>2</sub> hard mask have been completely etched away. ....	71
<b>Figure 4-4:</b> Cross-section schematic of the Dicing Free process - post trench DRIE pre HF vapour release. ....	72
<b>Figure 4-5:</b> Cross-section schematic of the Dicing Free process - post vapour HF release, pre WHB removal, and pre wafer grid separation. ....	72
<b>Figure 4-6:</b> Cross-section schematic of the Dicing Free process - post WHB removal and post separation from grid.....	73
<b>Figure 4-7:</b> Scanning Electron Microscope image of the top view of a device fabricated using the Dicing Free process. The image shows the WHB post removal from the sensor with the suspended structure still attached to it through stiction. ....	73
<b>Figure 4-8:</b> The fabrication process begins with a(a) SOI wafer clean, (b) PECVD deposition of SiO <sub>2</sub> on the f/s and (c), HWCVD deposition of doped polysilicon on the f/s.....	74
<b>Figure 4-9:</b> The semi-release process involves (a) PECVD deposition of Si <sub>3</sub> N <sub>4</sub> on f/s and b/s, (b) protective coating of photoresist on the f/s, (c) photoresist and release photo-lithography on the b/s, (d) RIE of the Si <sub>3</sub> N <sub>4</sub> layer on the b/s and a (e) KOH wet etch. ....	75
<b>Figure 4-10:</b> To define the suspended structure the (a) Si <sub>3</sub> N <sub>4</sub> on the f/s is removed using RIE, (b) photoresist and the structure photo-lithography is applied to the f/s and (c) the polysilicon/SiO <sub>2</sub> /Si is etched using ICP.....	76
<b>Figure 4-11:</b> The piezoresistors are defined by (a) applying photoresist and piezoresistor photo-lithography on the f/s and a (b) polysilicon ICP etch.....	77
<b>Figure 4-12:</b> : The terminals are defined by (a) Al deposition on the f/s, (b) applying photoresist and terminal photo-lithography and a (c) Al wet etch.....	77
<b>Figure 4-13:</b> The sensor is released by (a) dicing, (b) ICP Si etch to the BOX layer on b/s, (c) RIE SiO <sub>2</sub> etch to the suspended structure and a (d) RIE SiO <sub>2</sub> etch on the f/s. ...	78
<b>Figure 4-14:</b> Cross-section schematic of the novel process developed for the fabrication of the QC sensor.....	78

<b>Figure 4-15:</b> SEM images of QC springs (a) QC 1, (b) QC 2 and (c) QC 3 microfabricated using the process outlined in this chapter. ....	81
<b>Figure 4-16:</b> SEM image of (a) an isometric view (b) bottom view and (c) close up of beams with integrated piezoresistors and terminals of an QC MEMS sensor (QC 1s). ..	82
<b>Figure 5-1:</b> The schematic shows the set-up of the cantilever-on-cantilever method as it was adapted to measure the spring constant of the QC spring.....	86
<b>Figure 5-2:</b> Representative graph for the DUT spring constant measurement. Measurements were made with the AFM microscope in the F-D mode and using the modified cantilever-on-cantilever method. ....	87
<b>Figure 5-3:</b> Schematic of the F–D jig used for the mechanical out-of-plane characterisation of the QC spring. The DUT is mounted on a precision balance directly beneath a Vernier micrometre head using a cyanoacrylate adhesive. The suspended structure of the DUT (shown deflected and not to scale) is connected to the Vernier micrometre head with flexible piano wire fixed at both ends using a cyanoacrylate adhesive.....	88
<b>Figure 5-4:</b> The images show the QC 2 DUT mounted onto the precision balance. The suspended platform is bonded to a short piece of piano wire which is attached to the Vernier micrometre head (not shown). Using the Vernier the suspended platform is pulled away from the device. The force required for each incremental deflection is calculated from the change in mass displayed on the balance. ....	89
<b>Figure 5-5:</b> Force-displacement graphs for (a) QC 1s, (b) QC 2, and (c) QC 3 based on analytical, numerical (MATLAB and ANSYS), extrapolated AFM measurement, and F-D jig measurement results. (d) The graph shows the linearity % versus displacement for QC 1, QC 2, and QC 3. ....	90
<b>Figure 5-6:</b> SEM image of a deflected QC 2. The device was mounted on a soft vinyl block using cyanoacrylate adhesive. A metal pin inserted into the vinyl was used to deflect the suspended platform away from the device and the vinyl block as shown. The shape of the deflected beams is analogous to those seen in the numerical analysis simulations and of the double clamped beams in series used in the analytical model. ..	91
<b>Figure 5-7:</b> An SEM image of (a) QC 1s, (b) QC 2, and (c) QC 3 spring deflected by 575 $\mu\text{m}$ . These images show that the beams bend as shown in the numerical analysis	

simulations. This also confirms that the beams can be considered to be double-clamped beams in series as was used in the analytical calculations. ....	92
<b>Figure 5-8:</b> (a) Typical I-V characteristics and (b) resistance versus the gap spacing showing a linear ohmic relationship of the metallised aluminium on polysilicon contacts. ....	95
<b>Figure 5-9:</b> Resistivity as a function of the doping concentration for crystalline silicon, LPCVD polysilicon from published literature, and HWCVD polysilicon from this work. ....	96
<b>Figure 5-10:</b> Signal amplification schematic. Resistors R1 to R4 represent the piezoresistive Wheatstone bridge. R5 is the gain adjustment resistor, R6 and R7 are the adjustable potential divider for the bridge bias voltage, and R8 and R9 are course and fine potentiometers for the amplifier reference voltage used to null the bridge. U1, U2A/B, and U3 are a voltage regulator, operational amplifiers (used here as buffers), and a precision instrumentation amplifier respectively, and C1 to C9 are decoupling capacitors. ....	97
<b>Figure 5-11:</b> (a) QC 1s mounted onto a connector using Crystalbond and connected electrically using wire bonding, (b) pin side of the DUT connector. (c) SEM images of QC 1s (d) and TC 1s mounted and wire bonded to the DUT connector. ....	98
<b>Figure 5-12:</b> Bottom view of the PCB with the DUT inserted in the socket. ....	99
<b>Figure 5-13:</b> Breakout box for connecting the PCB with the DUT to a battery and a SA or DMM. ....	99
<b>Figure 5-14:</b> AFM adapter fabricated to interface the DUT and PCB to the AFM microscope. ....	100
<b>Figure 5-15:</b> The DUT and PCB assembled on to the AFM adapter using four spring loaded screws. This allowed for course adjustment of the position of the DUT relative to the sample stage. ....	100
<b>Figure 5-16:</b> The complete DUT, PCB, AFM adapter and coarse and fine reference voltage adjustment potentiometers assembled on to an AFM microscope. ....	100
<b>Figure 5-17:</b> Noise spectra of (a) QC 1s and (b) TC 1s. ....	102

<b>Figure 5-18:</b> A metal disc with piano wire $\varnothing$ 100 $\mu\text{m}$ x 2 mm length of piano wire bonded using cyanoacrylate adhesive. This was mounted on the AFM microscope's sample stage and used to deflect the suspended platform.....	103
<b>Figure 5-19:</b> Representative calibration sensitivity curves for QC 1s and TC 1s measured using an AFM microscope in F-D measurement mode. The curves have been smoothed using Savitzky-Golay digital filters. The curve for QC 1s shows hysteresis which may be due to the piezoelectric stack approaching its end of travel or deflections in the piano wire used to actuate it. The curve for TC 1s displays a poor signal to noise ratio. ....	105
<b>Figure 5-20:</b> Representative calibration sensitivity curves for QC 1s for deflections as large as 600 $\mu\text{m}$ . Measurements were made using the DUT/PCB/AFM adapter assembly with the suspended platform connected to a Vernier micrometre via a short piece of piano wire in a setup similar to the F-D jig.....	106
<b>Figure 5-21:</b> Displacement and force sensitivity versus the bridge voltage for (a) QC 1s, (b) TC 1s. The data for the graphs was extracted from the micro and macro (QC 1s only) calibration sensitivity measurements.....	107
<b>Figure 5-22:</b> Representative integrated noise and minimal displacement resolution versus the frequency for measurements made with a bridge voltage of 0.39 V for (a) QC 1s and (b) TC 1s.....	109
<b>Figure 5-23:</b> A representative Raman spectroscopy and deconvolution of the Raman spectrum of the HWCVD polysilicon piezoresistors.....	111
<b>Figure 5-24:</b> (a) AFM surface imaging and (b) AFM 3D surface topography of the HWCVD polysilicon piezoresistors taken at a resolution of 2944 x 2944 pixels in contact mode using a sharp AFM tip with a nominal tip radius of 10 nm.....	112
<b>Figure 5-25:</b> HWCVD polysilicon grains as determined by the Watershed algorithm. ....	112
<b>Figure 5-26:</b> Polysilicon grain size versus deposition temperature .....	113
<b>Figure 5-27:</b> Doping concentraion versus gauge factor for various polysilicon deposition technecques. ....	114

<b>Figure 5-28:</b> The range of the Hooke factor measured in this work for HWCVD polysilicon and as reported in published work for LPCVD polysilicon and crystalline Si. ....	115
<b>Figure 6-1:</b> Experimental techniques including sensors developed in this work versus the force range and biological events.....	123
<b>Figure 6-2:</b> Experimental techniques including sensors developed in this work versus the displacement range and dimensions of biological structures.....	123
<b>Figure 6-3:</b> Young’s modulus of several biomaterials.....	124
<b>Figure 6-4:</b> QC MEMS F-D sensor with probe attached. ....	125
<b>Figure 6-5:</b> A schematic showing the surface profile before and after the application of the load. The various variables used in the calculations are also included.....	126
<b>Figure 6-6:</b> A schematic representation of the load versus displacement for a single loading and unloading of the indenter. The graphical representation of the various variables used in the calculations is also included.....	127
<b>Figure 6-7:</b> Representative indents in 1% to 6% agarose hydrogels made using the QC F-D MEMS sensor modified to include probe with a ~200 $\mu\text{m}$ diameter parabolic bead tip. ....	129
<b>Figure 6-8:</b> Average Young’s modulus versus various levels of agarose concentrations measured using the QC MEMS F-D sensor. The graph shows an increase in the Young’s modulus for each incremental increase in agarose concentration. The error bars represent the range of values measured. ....	130
<b>Figure 6-9:</b> Young’s Modulus versus various levels of agarose concentrations from published data and measurements made using the QC MEMS F-D sensor. The graph indicates that the data is distributed into two main groups.....	130
<b>Figure 6-10:</b> Young’s Modulus versus various levels of agarose concentrations from published data and measurements made using the QC MEMS F-D sensor. This is the same data as shown in Figure 6-9; however, the agarose concentration was limited to 6% to magnify the distribution of the measurements at lower concentrations. This graph indicates that the measurements made using the QC MEMS F-D sensor falls between the extremes of the published data.....	131

**Figure 7-1:** QC sensor with circular beams. This may decrease the stress concentrations thus increase the deflection limit further..... 138

**Figure 7-2:** (a) An exploded view and (b) an assembled view with stabilisation diaphragm inflated of a diagnostic tool for the early detection of osteoarthritis. .... 139

**Figure 7-3:** A view of the diagnostic tool for the early detection of osteoarthritis inserted into the knee. .... 139

**Figure 7-4:** A QC sensor adapted as a high accuracy, linearity and large range flow metre..... 140

# List of tables

<b>Table 2-1:</b> Displacement equations for typical beam configuration derived using linear beam theory .....	11
<b>Table 2-2:</b> SEM Images and characteristics of typical flexures used in MEMS.....	13
<b>Table 2-3:</b> Critique of sensing systems proposed to measure sensor deflection.....	16
<b>Table 3-1:</b> Values for the coefficient D.....	43
<b>Table 3-2:</b> Design correlation matrix for a self-sensing cantilever. The matrix shows the effect of an increase in a parameter, relative to the other parameters, on the performance of the sensor with (↑), (↓) and (–) indicating an increase, decrease and no substantial effect respectively .....	49
<b>Table 3-3:</b> Upper and lower values of the parameter set variables used during the GA process used to optimise the graphs in Figure 3-14 and 3-15.....	52
<b>Table 4-1:</b> The details of the process used to fabricate the QC sensor.....	79
<b>Table 5-1:</b> Spring constant, linear range, total deflection before fracture, for QC 1s, 2 and 3, and TC 1s using analytical analysis, numerical analysis, AFM, and F-D jig. ....	91
<b>Table 5-2:</b> First-mode resonant frequencies for QC 1s, 2, and 3 using analytical, numerical and laser Doppler vibrometer measurements.....	94
<b>Table 5-3:</b> Deposition temperatures and annealing details for the HWCVD polysilicon characterised in this work and silicon/polysilicon from published data .....	96
<b>Table 5-4:</b> Anneal details for the data presented in Figure 5-28.....	114



# DECLARATION OF AUTHORSHIP

I, David Grech, declare that this thesis and the work presented in it are my own and has been generated by me as the result of my own original research.

## **“Development of a Quasi-Concertina MEMS Sensor for the Characterisation of Biopolymers”**

I confirm that:

1. This work was done wholly or mainly while in candidature for a research degree at this University;
2. Where any part of this thesis has previously been submitted for a degree or any other qualification at this University or any other institution, this has been clearly stated;
3. Where I have consulted the published work of others, this is always clearly attributed;
4. Where I have quoted from the work of others, the source is always given. With the exception of such quotations, this thesis is entirely my own work;
5. I have acknowledged all main sources of help;
6. Where the thesis is based on work done by myself jointly with others, I have made clear exactly what was done by others and what I have contributed myself;
7. Parts of this work have been published in research journals. A list of publications is provided with this manuscript.

Signed:.....

Date:.....



# Acknowledgements

I would like to give my thanks to Dr. Harold M.H. Chong, Dr. Robert J. K. Wood, and Dr Jurgita Zekonyte for the opportunity and the support they had given me throughout this project.

It would be impossible to thank everyone else that has contributed directly or indirectly towards this PhD. However, in no particular order I would like to thank Dr. Kian Kiang for his expertise in all things related to photolithography, Dr. Owain Clark for training on all the plasma tools and help in developing new recipes, Mike Perry for continuously repairing clean room equipment, Richard S. Kean for both his technical expertise and fantastic sense of humour, Dr. Ioannis Zeimpekis for his help with setting up the KOH tank, Dr. Antulio Tarazona and Dr. Tess De Leon for help with the HWCVD depositions, Dr Taha Ben Masaud for help with the RTA, Swe Zin Oo for training on the Raman spectroscopy, Dr Maurits de Planque for help with the agarose hydrogels, Chirenjeevi Krishnan for the company in the measurement lab, and Dr Marek E Schmidt, Sheng Ye, Graham S. Wood and Zhao Chun for the good times at the PG.

Lastly, and especially, I would like to thank my partner, Katja Gauci, who put up with all the long hours and missed holidays.



# List of abbreviations

<b>AFM</b>	Atomic Force Microscopy
<b>Al</b>	Aluminium
<b>Ar</b>	Argon
<b>B</b>	Bending
<b>B/S</b>	Back side
<b>BFP</b>	Biomembrane force probe
<b>BHF</b>	Buffered hydrofluoric acid
<b>BNC</b>	Bayonet Neill–Concelman
<b>BOX</b>	Buried oxide
<b>C</b>	Compression
<b>CAD</b>	Computer aided design
<b>CD</b>	Cytodetacher
<b>CHF<sub>3</sub></b>	Trifluoromethane
<b>CTA</b>	Classic thermal annealing
<b>DC</b>	Direct Current
<b>DI</b>	Deionized
<b>DMM</b>	Digital multimeter
<b>DRIE</b>	Deep reactive-ion etching
<b>DUT</b>	Device under test
<b>F/S</b>	Front side
<b>FBD</b>	Free-body-diagram
<b>FBD</b>	Free body diagram
<b>F-D</b>	Force Displacement
<b>FEA</b>	Finite element analysis
<b>FNA</b>	Fuming nitric acid
<b>GA</b>	Genetic Algorithm
<b>GF</b>	Gauge Factor
<b>HF</b>	Hydrofluoric
<b>HRFS</b>	High resolution force spectroscopy
<b>HWCVD</b>	Hot Wire Chemical Vapour Deposition
<b>IC</b>	Integrated circuit
<b>ICP</b>	Inductively coupled plasma
<b>IPA</b>	Isopropyl alcohol
<b>KOH</b>	Potassium hydroxide
<b>LMA</b>	Levenberg-Marquardt Algorithm
<b>LPCVD</b>	Low Pressure Chemical Vapour Deposition
<b>LTLM</b>	Linear Transmission Line Method
<b>MA</b>	Micropipette aspiration
<b>MEMS</b>	Micro electromechanical sensors

<b>MI</b>	Microindenters
<b>MN</b>	Microneedle
<b>mPAD</b>	Embedded particle tracking microfabricated post array detector
<b>MT</b>	Magnetic Tweezers
<b>MTC</b>	Magnetic Twisting Cytometry
<b>MTC</b>	Magnetic twisting cytometry
<b>NCG</b>	Nano-crystalline graphite
<b>NI</b>	Nanoindenters
<b>O<sub>2</sub></b>	Dioxygen
<b>OS</b>	Optical Stretcher
<b>OT</b>	Optical Tweezers/trap
<b>PBS</b>	Phosphate buffered saline
<b>PC</b>	Personal computer
<b>PCB</b>	Printed circuit board
<b>PECVD</b>	Plasma Enhanced Chemical Vapour Deposition
<b>PLA</b>	Polyactide
<b>PR</b>	Photoresist
<b>QC</b>	Quasi Concertina
<b>QCM</b>	Quartz Crystal Microbalance
<b>RIE</b>	Reactive ion etching
<b>RTA</b>	Rapid thermal annealing
<b>SA</b>	Spectrum analyser
<b>SC</b>	Substrate composition
<b>SD</b>	Substrate deformation
<b>SEM</b>	Scanning Electron Microscope
<b>SF<sub>6</sub></b>	Sulfur hexafluoride
<b>SG</b>	Savitzky-Golay
<b>Si</b>	Silicon
<b>Si<sub>3</sub>N<sub>4</sub></b>	Silicon nitride
<b>SiO<sub>2</sub></b>	Silicon Oxide
<b>SIP</b>	Single in-line package
<b>SLA</b>	Stereolithography
<b>SOI</b>	Silicon on insulator
<b>SPM</b>	Scanning probe microscopy
<b>T</b>	Tension
<b>TC</b>	Optimised self-sensing cantilever
<b>TLM</b>	Transmission Line Method
<b>WHB</b>	Wafer Handle Block
<b>2D</b>	Two dimension

## List of symbols

$A$	Cross-sectional area
$\hat{A}$	Fitting parameter
$C_H$	Hooge noise property of amplifier
$C_J$	Johnson noise property of amplifier
$D$	Theoretically derived coefficient
$d_{max\_n}$	Total deflection before fracture
$d_{min}$	Minimum resolvable displacement
$E$	Young's modulus
$E_i$	Young's modulus - indenter
$E_{poly}$	Young's modulus - polysilicon
$E_r$	Reduced elastic modulus
$E_S$	Young's modulus - sample
$E_{Si}$	Young's modulus - crystalline Si
$F$	Force
$f$	Frequency
$f_0$	First mode resonant frequency
$f_{max}$	Maximum frequency
$f_{min}$	Minimum frequency
$F_{min}$	Minimum resolvable force
$F_x$	Force applied in the x-direction
$F_y$	Force applied in the y-direction
$F_z$	Force applied in the z-direction
$Gain_{Amp}$	Amplifier gain
$GF$	Gauge factor
$h_c$	Contact depth
$h_f$	Final residual hardness impression
$h_{max}$	Total displacement
$h_s$	Displacement at the perimeter
$I$	Cross-section moment of inertia
$I_{c-Si}$	Intensity for the deconvoluted Raman peaks measured at the crystalline peaks
$I_{a-Si}$	Intensity for the deconvoluted Raman peaks measured at the amorphous peaks
$k$	Spring constant
$K$	Stiffness matrix for the complete system
$k_b$	Boltzmann's constant
$k_c$	Spring constant of commercial cantilever
$k_d$	Device spring constant
$k_x$	Spring constant in the x-direction

$k_y$	Spring constant in the y-direction
$k_z$	Spring constant in the z-direction
$k_{z,beam}$	Spring constant for beam in the z-direction
$l_p$	Length of crystalline Si grain
$l_{pr}$	Length of piezoresistor
$l_{sp}$	Length of suspended platform
$M$	Bending moment
$M_{beam}$	Beam moment
$m_{eq}$	Equivalent mass of suspended platform and beams
$M_{mass}$	Mass matrix for the complete system
$m_{sp}$	Mass of suspended platform
$m_{spring}$	Mass of springs
$n$	Dopant concentration
$N$	Total number of carriers in the piezoresistor
$n_{pr}$	Number of piezoresistors
$P$	Piezoresistance factor
$P_i$	Load applied by indenter
$P_{max}$	Maximum applied load
$q$	Electron charge
$r$	Radius of curvature
$R$	Resistance
$R_0$	Resistance of the piezoresistor in the nulled state
$R_1$	Resistance in bridge leg 1
$R_2$	Resistance in bridge leg 2
$R_3$	Resistance in bridge leg 3
$R_4$	Resistance in bridge leg 4
$r_{tip}$	Radius of tip
$S$	Gradient
$S_c$	Slope of displacement vs. actuation curve
$S_f$	Force sensitivity
$S_H$	Hooge noise spectral density
$S_J$	Johnson noise spectral density
$SIP$	Single in-line package
$t$	Thickness of beam
$T$	Absolute temperature of resistor
$t_{pr}$	Thickness of piezoresistor
$u$	Generalised eigenvector
$V_A$	Amplifier noise spectral density
$V_{bias}$	Bias voltage
$V_{Bridge}$	Bridge voltage
$V_H$	Hooge noise spectral density

$V_J$	Johnson noise spectral density
$V_{noise}$	Total noise spectral density
$V_{Output}$	Output voltage
$W$	Heat dissipated by piezoresistor
$w$	Width of beam
$w_p$	Width of depleted region
$w_{pr}$	Width of piezoresistor
$w_{sep}$	Separation between beams
$X_c$	Crystalline volume fraction
$Z$	Displacement in the z-direction
$\alpha$	Hooke factor
$\beta^*$	Efficiency factor
$\delta$	Deflection
$\Delta m_{bal.}$	Change in mass measured by the precision balance
$\delta_p$	Width of grain boundary
$\delta_x$	Deflection in the x - direction
$\delta_y$	Deflection in the y - direction
$\delta_z$	Deflection in the z - direction
$\varepsilon$	Longitudinal strain
$\theta$	Angle of deflection
$\lambda$	Generalised eigenvalue
$\mu$	Concentration dependent majority carrier mobility
$\nu$	Poisson's ratio
$\nu_i$	Poisson ratio for indenter
$\nu_s$	Poisson ratio for sample
$\xi$	Geometric constant
$\pi_l$	Longitudinal piezoresistance coefficients
$\pi_t$	Transverse piezoresistance coefficients
$\rho$	Resistivity
$\rho_b$	Resistivity - grain boundary barrier
$\rho_g$	Resistivity - crystalline Si grain
$\sigma_l$	Longitudinal stress
$\sigma_{poly}$	Stress in the polysilicon layer
$\sigma_{Si}$	Stress in the crystalline Si layer
$\sigma_t$	Transverse stress
$Y$	Relative resistance factor
$\omega$	Angular frequency



# List of publications

## Journals

- D. Grech, K. S. Kiang, J. Zekonyte, M. Stolz, R. J. K. Wood, and H. M. H. Chong, "Highly linear and large spring deflection characteristics of a Quasi-Concertina MEMS device," *Microelectronic Engineering*, vol. 119, pp. 75-78, 5/1/2014.
- D. Grech, A. Tarazona, M.T. De Leon, K. S. Kiang, J. Zekonyte, R. J. K. Wood and H. M. H. Chong, "Piezoresistive properties of doped polysilicon films deposited by hot-wire chemical vapour deposition", Manuscript in preparation. (2014)
- D. Grech, A. Tarazona, M.T. De Leon, K. S. Kiang, J. Zekonyte, R. J. K. Wood and H. M. H. Chong, "Characterisation of a Quasi-Concertina MEMS sensor with piezoresistive self-sensing", Manuscript in preparation. (2014)
- D. Grech, M. R. R. de Planque, A. Tarazona, K. S. Kiang, J. Zekonyte, R. J. K. Wood and H. M. H. Chong, "Mechanical characterisation of soft/bio materials with a self-sensing Quasi-Concertina MEMS sensor", Manuscript in preparation. (2014)

## Conferences

- Grech, David, Kiang, Kian Shen, Zekonyte, Jurgita, Stolz, Martin, Woods, Robert and Chong, Harold M.H. (2013) Highly linear and large spring deflection characteristics of a Quasi-Concertina MEMS device. In, *39th International Conference on Micro and Nano Engineering, 16 - 19 Sep 2013*.
- A. Tarazona, M.T. De Leon, D. Grech, I. Zeimpekis, S.Kai, H.M.H. Chong, P.Ashburn "Illustration of the industrial readiness of hot wire chemical vapor deposition (HWCVD) as part of standard micro-fabrication and high spec nanofabrication production lines," *accepted for presentation, 8th Hot-wire (Cat) Chemical Vapor Deposition Conference, 13-16 October 2014, Braunschweig, Germany, (2014)*



# Chapter 1

## Introduction

The scope of this project is the development of a force-displacement (F-D) MEMS sensor with nN/nm resolution, high linearity, high in-plane compliance and a high deflection range suitable for the measurement of soft bio polymeric materials and in-vivo measurement applications. The proposed sensor increases the measurement range thus enabling the capture of phenomena that would otherwise be lost with conventional narrow range measurement techniques. Furthermore, the high deflection range increases the resilience of the device to over travel thus making it ideal for in-vivo F-D measurements.

### 1.1 Motivation of the thesis

Traditionally the accurate measurement of the mechanical properties, such as the Young's modulus, strength, ductility and Poisson ratio, of a material was crucial for the successful design of products that are reliable, cost effective and for predicting the service life. In recent years, the same terminology used to determine a material's reaction to a physical force, the material's mechanical properties, and the techniques used to measure them, are being utilised to study the mechanics of biopolymers. This is of interest as it has been observed that the physiological state of biological tissue and its alterations due to the pathological state can be detected by measuring its mechanical properties. This has led to the opportunity to develop diagnostic devices and treatment for cancer, orthopaedic, cardiovascular and respiratory diseases [1-7].

Presently the mechanical properties of biopolymers with a high stiffness, such as polyactide (PLA), can be readily determined using a microindenter or nanoindenter. On the other hand, tools such as Microneedle (MN), Atomic Force Microscopy (AFM), Optical Tweezers (OT), Optical Stretcher (OS) and Magnetic Tweezers (MT) have been developed to measure the mechanical properties of biological cells which have extremely low stiffness [8, 9]. However, despite the numerous tools available there is hardly any overlap between the methods developed. In particular, techniques developed to study the response of a cell are restricted to small deformations (1-2  $\mu\text{m}$ ) or have a small force range ( $\sim 1$  nN) and the spring constant of microindenters and nanoindenters are typically too high to make any meaningful measurements on soft biological tissue. Thus cell response to larger deformations is still largely unknown [3, 10, 11]. Moreover, these techniques involve large measurement equipment, with some requiring intricate sample preparation such as staining, labelling, and sample coating, thus have limited potential for in-vivo applications. Some techniques also require high-powered lasers which may cause thermal damage to the biopolymers examined and inaccuracies due to laser reflection/refraction [3, 12].

## 1.2 Objectives

The main aim of this project is to develop an accurate force-displacement (F-D) sensor with a broad F-D range and suitable for adaptation for in-vivo measurements of biological tissue. The device is to be designed to take advantage of the relatively small size, high resolution, and batch fabrication capabilities of MEMS technology [13]; and to have the potential for an automated process which could offer increased measurement efficiency and repeatability [14]. To achieve this F-D MEMS sensor, the project has the following objectives:

1. Design and development of a novel Quasi Concertina (QC) spring to increase the linear and deflection range while maintaining a high out-of-plane and low-in-plane compliance. These features are absent in typical MEMS flexures but are essential when high accuracy over large out-of-plane deflections are required and are also necessary to increase the resilience of the device to over-travel for in-vivo applications. Key requirements for the QC spring are a spring constant  $< 6$  N/m, a deflection range  $> 1$  mm with a linearity  $< 20\%$ , linearity over  $100 \mu\text{m}$   $< 1\%$ , and a device size  $< 3$  mm x  $3$  mm x  $0.7$  mm.

2. Development of an accurate mechanical to electrical transduction mechanism for quasi-static measurements (1-10 Hz) to complement the QC spring concept. The method of transduction should allow the sensor to work without external lasers, magnetic fields, or optical microscopes, require minimum experiment setup expertise, no sample preparation and adaptable for in-vivo use. Key requirements for the F-D sensors are a force and displacement resolution in the nN and nm range respectively.
3. Development of a novel stiction-free process for the fabrication of the QC spring.
4. Development of hot wire chemical vapour deposition (HWCVD) polysilicon piezoresistors with a large gauge factor ( $> 40$ ), and a crystal volume  $> 95\%$ .
5. Establish a means to take measurements using the F-D MEMS sensor and build the necessary readout circuit, and electrical/mechanical interfaces.
6. Show proof of concept by using the F-D MEMS sensor to measure the stiffness of agarose hydrogels at different levels of concentration. Agarose is ideal for this purpose as it is a biopolymer synthesised from seaweed extracts which, at low concentrations, mimics the mechanical stiffness of soft biological tissue such as cartilage [15].

### **1.3 Organisation of the thesis**

This thesis is organised in the following format. Chapter 2 gives a literature review and begins with an overview of the measurement techniques used to characterise biopolymers. This is followed by an overview of linear and non-linear flexures, transduction and a detailed review of piezoresistive sensing. Chapter 3 presents the development of a novel highly linear and large displacement QC spring which is combined with a full Wheatstone bridge and optimised for high resolution. The chapter ends with the successful testing of a macroscale proof of concept prototype. In Chapter 4 the novel stiction-free fabrication process developed specifically for the fabrication of the QC sensor is presented. The mechanical and electrical characteristics of the devices fabricated are discussed in depth in Chapter 5, and in Chapter 6 the QC sensor is used to measure the stiffness of agarose hydrogels with mechanical properties similar to that of soft biological tissue. Finally, in Chapter 7 the conclusions and other possible applications for the QC MEMS sensor are discussed.

## References

- [1] K. A. Addae-Mensah and J. P. Wikswo, "Measurement techniques for cellular biomechanics in vitro," *Experimental Biology and Medicine*, vol. 233, pp. 792-809, Jul 2008.
- [2] M. L. Rodriguez, P. J. McGarry, and N. J. Sniadecki, "Review on Cell Mechanics: Experimental and Modeling Approaches," *Applied Mechanics Reviews*, vol. 65, Nov 2013.
- [3] O. Loh, A. Vaziri, and H. D. S. M. Espinosa, "The Potential of MEMS for Advancing Experiments and Modeling in Cell Mechanics," *Experimental Mechanics*, vol. 49, pp. 105-124, Feb 2009.
- [4] D. L. Bader and M. M. Knight, "Biomechanical analysis of structural deformation in living cells," *Medical & Biological Engineering & Computing*, vol. 46, pp. 951-963, Oct 2008.
- [5] K. J. Van Vliet, G. Bao, and S. Suresh, "The biomechanics toolbox: experimental approaches for living cells and biomolecules," *Acta Materialia*, vol. 51, pp. 5881-5905, Nov 25 2003.
- [6] S. E. Cross, Y. S. Jin, J. Rao, and J. K. Gimzewski, "Nanomechanical analysis of cells from cancer patients," *Nature Nanotechnology*, vol. 2, pp. 780-783, Dec 2007.
- [7] M. Lekka, "Atomic Force Microscopy a Tip for Diagnosing Cancer," *Nature Nanotechnology*, vol. 7, pp. 691-692, Nov 2012.
- [8] D. H. Kim, P. K. Wong, J. Park, A. Levchenko, and Y. Sun, "Microengineered Platforms for Cell Mechanobiology," *Annual Review of Biomedical Engineering*, vol. 11, pp. 203-233, 2009.
- [9] G. Bao and S. Suresh, "Cell and molecular mechanics of biological materials," *Nature Materials*, vol. 2, pp. 715-725, Nov 2003.
- [10] S. Yang and T. Saif, "Mechanical response of single living cells by bio-MEMS sensors," in *Micro Electro Mechanical Systems, 2004. 17th IEEE International Conference on. (MEMS)*, 2004, pp. 265-267.
- [11] J. Rajagopalan, A. Tofangchi, and M. T. A. Saif, "Highly Linear, Ultra Sensitive Bio-Mems Force Sensors with Large Force Measurement Range," *Mems 2010: 23rd Ieee International Conference on Micro Electro Mechanical Systems, Technical Digest*, pp. 88-91, 2010.
- [12] S. J. Park, M. B. Goodman, and B. L. Pruitt, "Analysis of nematode mechanics by piezoresistive displacement clamp," *Proceedings of the National Academy of Sciences of the United States of America*, vol. 104, pp. 17376-17381, Oct 30 2007.
- [13] J. Rajagopalan and M. T. A. Saif, "MEMS sensors and microsystems for cell mechanobiology," *Journal of Micromechanics and Microengineering*, vol. 21, May 2011.
- [14] J. Bronson, W. R., Gloria J., and R. Tran-Son-Tay, "A Feasibility Study On MEMS Test-Structures For Analysis Of Biological Cells and Tissues," presented at the Florida Conference on Recent Advances in Robotics, 2004
- [15] M. Ahearne, Y. Yang, A. J. El Haj, K. Y. Then, and K. K. Liu, "Characterizing the viscoelastic properties of thin hydrogel-based constructs for tissue engineering applications," *Journal of the Royal Society Interface*, vol. 2, pp. 455-463, Dec 22 2005.

## Chapter 2

### Literature Review

The sensor developed in this work was conceived to be particularly suited for the measurement of the mechanical properties of biopolymers; therefore, this chapter opens with a review of the current state of the art F-D techniques. As is frequently the case with MEMS sensors, and even more so when high linearity and large deflections are involved, flexures are a critical component of the device, hence current designs are thoroughly investigated. A section on transduction mechanisms, in which various techniques are scrutinised for their applicability to the sensor, and a review of piezoresistance and piezoresistive materials, is also included.

#### 2.1 F-D techniques

A vast array of techniques has been developed for the study of the mechanical properties of materials. Microindenters (MI) and nanoindenters (NI) are well established tools for the determining the mechanical properties, such as the hardness and Young's modulus, of metals, ceramics and hard polymers. Recently new techniques have been developed specifically to mechanically characterise softer materials such as polymers/biopolymers and to investigate the behaviour of biological cells. The technique used greatly depends on the F-D range of the phenomenon investigated. The two main categories of techniques used to measure the biomechanical properties of cells are referred to as active and passive [1-3]. In active or force-application techniques, the cells have a force applied to them and the mechanical reaction of the cells is recorded (Figure 2-1). Typical active techniques include Microneedle (MN), Atomic Force Microscopy (AFM), Optical Tweezers (OT), Optical Stretcher (OS), Magnetic

Tweezers (MT), Magnetic Twisting Cytometry (MTC), Quartz Crystal Microbalance (QCM), and MEMS techniques [2-8].

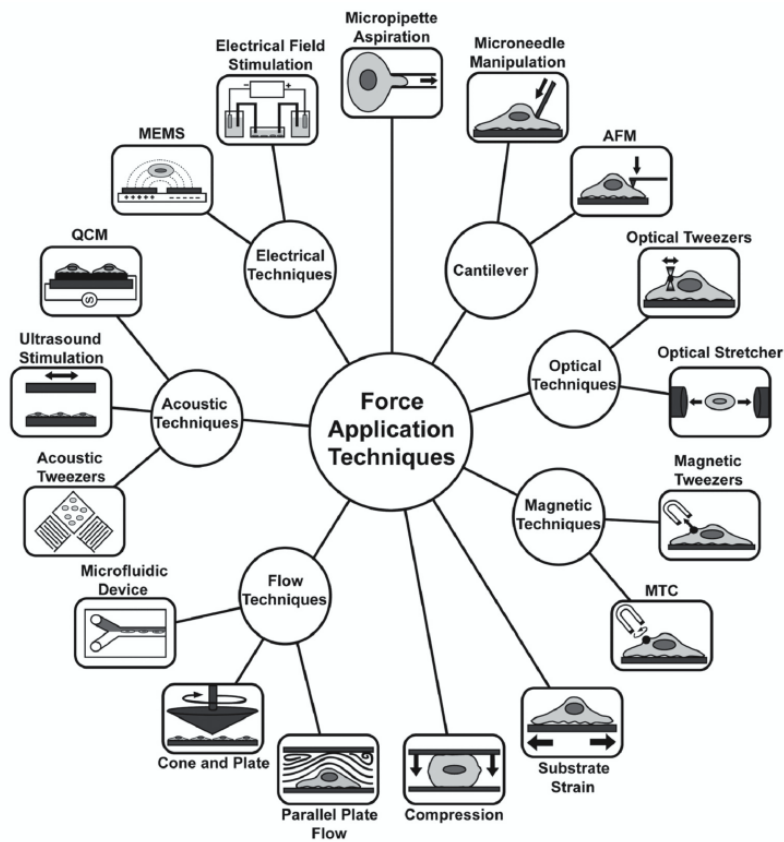


Figure 2-1: Force application or active techniques for biomechanical measurements. Adapted from [2].

In passive or force-sensing techniques, no force is applied to the cells and the traction forces generated by the cells are recorded (Figure 2-2).

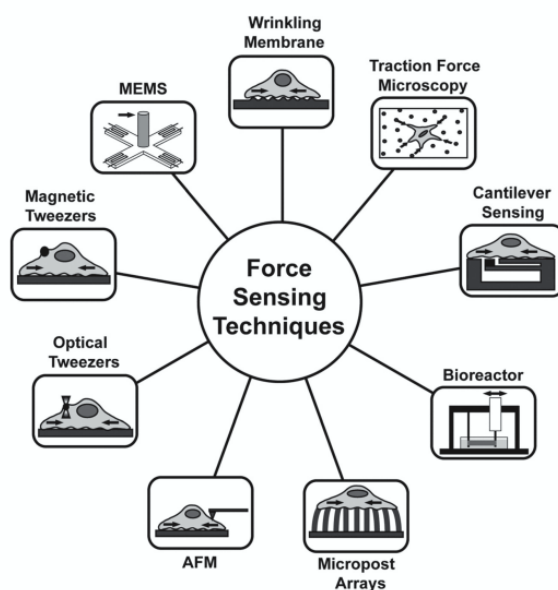


Figure 2-2: Force sensing or passive techniques for biomechanical traction measurements. Adapted from [2].

Typical passive techniques include Wrinkling Membranes, Traction Force Microscopy, Cantilever Sensing, Bioreactors, Micropost Arrays, AFM, OT, MT, and MEMS [2]. The active and passive techniques can be further subdivided into cell population techniques, which manipulate and measure the response of cell populations, and single cell or single molecule techniques, which measure the response to a mechanical stimulus of a single cell [2-6]. Measurement tools such as the AFM, OT, and MT are adaptable to performing active, passive, single cell, and cell population techniques.

These measurement tools have force and displacement range limitations which restricts the phenomena that can be investigated. Figure 2.3 shows the force-displacement range of the various techniques and includes details of conventional and non-conventional force-displacement instruments, the force range of biological events, and the displacement range of biological structures for comparison. Also included are the force and displacement range of the QC MEMS sensors developed in this work.

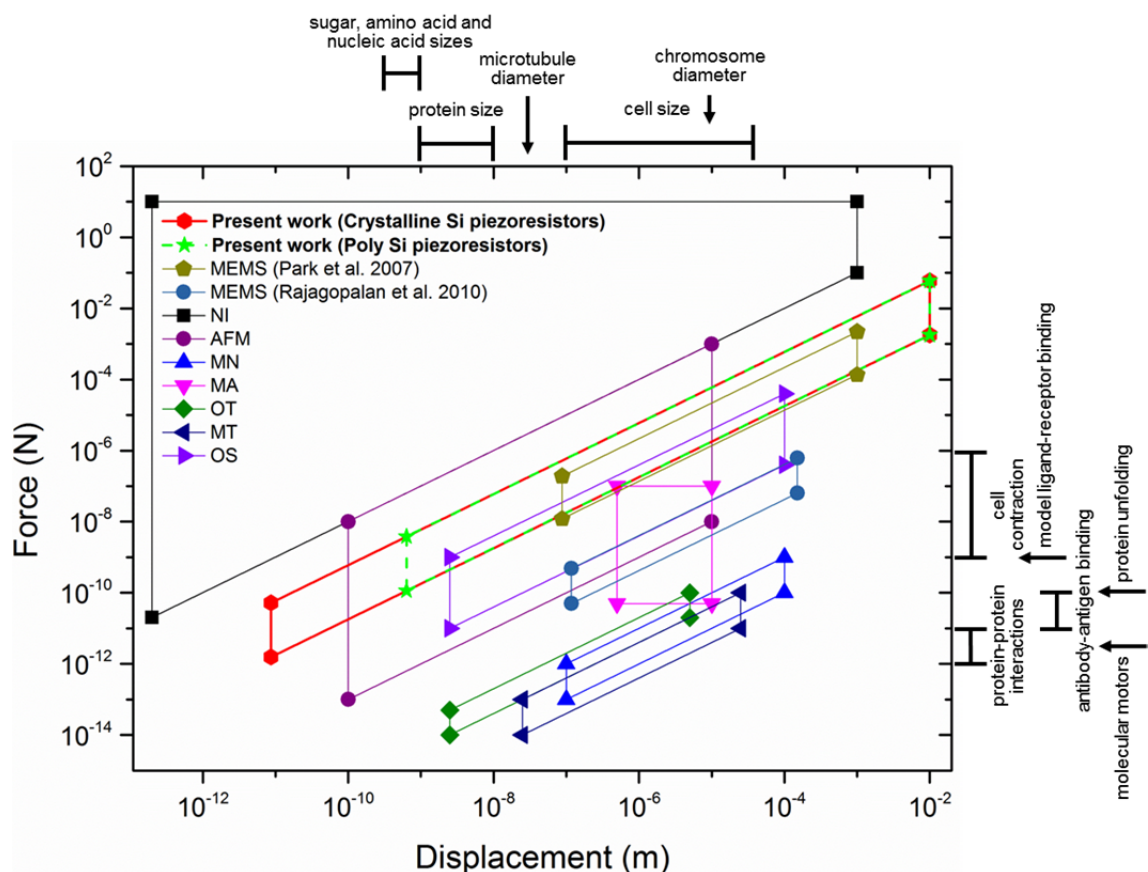
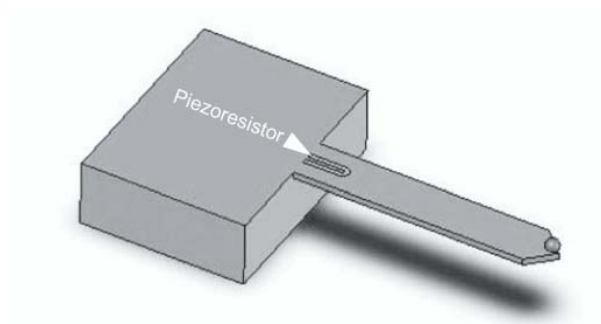


Figure 2-3: Range relevant to representative biological structures and processes. Adapted from [1-4, 6, 9-18].

The range of the two MEMS devices shown in Figure 2-3 were specifically developed for biological force-displacement measurements. The devices developed by

Park et al. [15, 18] were designed specifically to study how signals in the neuromuscular system relate to behaviour and to investigate force-sensing organs and sensory neurons. This required a F-D range that was unavailable in other existing measurement methods. The developed MEMS devices are highly optimised piezoresistive cantilevers with a quarter bridge configuration (Figure 2-4). The p-type crystalline piezoresistors used were boron ion implanted directly on to the Si cantilevers. To increase the linear range to  $> 100 \mu\text{m}$  the sensor employed relatively long cantilevers (2-6 mm) with a width and thickness of  $80\text{-}400 \mu\text{m}$  and  $15 \mu\text{m}$  respectively. The sensors were fabricated with spring constants of  $0.137\text{-}2.2 \text{ N/m}$ , and had a force resolution of  $12 \text{ nN}$  over a  $0.1 \text{ Hz}$  to  $100 \text{ kHz}$  bandwidth. Using this approach the displacement and linearity are limited by the length of the cantilever. Thus for larger linear deflections the length of the cantilever would need to be increased.



**Figure 2-4: Graphical representation of the piezoresistive cantilever developed by Park et al. to study how signals in the neuromuscular system relate to behaviour and to investigate force-sensing organs and sensory neurons [15].**

For the development of their measuring device, Rajagopalan et al. [6, 16] utilised a number (8 to 24) of flexible beams in a meander spring configuration to minimise the deflection in each beam thus increase the F-D linearity and reducing the spring constant. (Figure 2-5). The overall dimension of the device is  $3 \text{ mm} \times 4 \text{ mm} \times 150 \mu\text{m}$  with the beams having a width, thickness, and length of  $2\text{-}4 \mu\text{m}$ ,  $10\text{-}40 \mu\text{m}$ , and  $2\text{-}3 \text{ mm}$  respectively. The sensors were fabricated with spring constants of  $0.427 \times 10^{-3} - 4.135 \times 10^{-3} \text{ N/m}$ , can achieve a force resolution of  $50\text{-}500 \text{ pN}$  and have a displacement range of  $150 \mu\text{m}$  [6, 16]. Since the device is not self-sensing, an optical microscope is required to measure the displacement of the probe relative to a fixed reference. Furthermore, for accurate measurements contact between probe and fixed reference and contact between the springs and other components would need to be avoided. Thus this solution is not suitable for an in-vivo application.

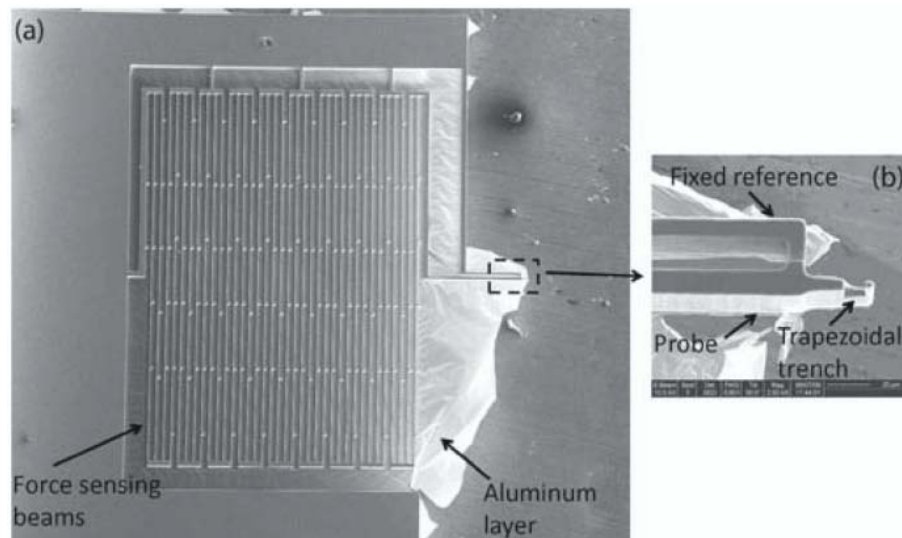


Figure 2-5: (a) SEM image of the F-D sensor developed by Rajagopalan et al. for biological studies, (b) magnified view of the probe and reference beam. Adapted from [16].

## 2.2 MEMS flexures

The flexure or spring is a fundamental component of a MEMS device. Typically it is responsible for the mechanical aspect of the device. The selection and design of the flexure type has a large impact on the range and linearity. Flexures are also used to confine motion to a particular plane and can be used to apply force, store energy and used in conjunction with other phenomena for transduction. Since frictional forces do not scale well, flexures are typically the preferred kinematic link for MEMS [19].

Since the fabrication of MEMS devices is presently achieved using technology developed for the semiconductors industry, most MEMS structures are limited to a 2D plane. This restricts the flexures used in MEMS to be composed of beams. Thus a thorough understanding of the linear and non-linear deflection of beams is necessary especially when large deflections are envisioned.

### 2.2.1 Linear and Non-linear Deflections

The fundamental equation for the determination of the deflection of a beam for an applied load was first published by L.Euler in 1744 in the appendix of his book *Des Curvis Elastics*. The theorem is known as the Euler – Bernoulli law since Jacob and Johann Bernoulli made contributions to the work [20].

The Euler-Bernoulli law is based on the determination of the exact shape of the deflected beam, referred to as *elastica*. The law states that, provided that the beam is made from a material that behaves elastically according to Hooke's law, and whose plane sections remain plane and perpendicular to the neutral axis, the bending moment is proportional to the change in curvature caused by the applied force. Mathematically this can be summarised as [20]:

$$\frac{1}{r} = \frac{M}{EI} \quad \text{Eq. 2-1}$$

where  $r$ ,  $M$ ,  $E$ , and  $I$  are the radius of curvature of the beam, bending moment, modulus of elasticity, and the cross-section moment of inertia respectively (Figure 2-6).

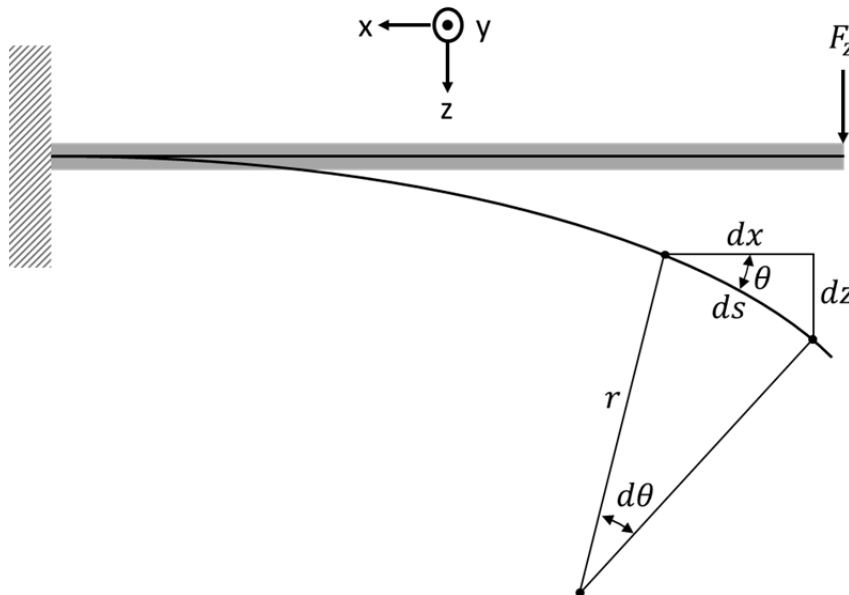


**Figure 2-6: Deflected cantilever beam showing the radius of curvature ( $r$ ) and the angle of deflection ( $\theta$ ).**

Using small angle approximations ( $\tan \theta \approx \theta$  for  $\theta < 5^\circ$  [21]) and Eq. 2-1 the basic differential equation for the deflection of a beam, with an angle of deflection,  $\theta$ , shown (Figure 2-6) can be derived as [22]:

$$\frac{d^2z}{dx^2} = \frac{M}{EI} \quad \text{Eq. 2-2}$$

This equation is referred to as the elementary or linear beam theory and, since small angle approximations were used in its derivation, it is only valid for small angles of deflection [20, 22].

**2.2.1.1 Linear Deflections – Small Angles**

In many MEMS applications the deflections are sufficiently small that Eq. 2.2 suffices.

**Table 2-1: Displacement equations for typical beam configuration derived using linear beam theory [23]**

Cantilever	Guided-end	Fixed-Fixed
$x = \frac{F_x l}{Et w}$	$x = \frac{F_x l}{Et w}$	$x = \frac{F_x l}{4Et w}$
$y = \frac{4F_z l^3}{Et w^3}$	$y = \frac{F_z l^3}{Et w^3}$	$y = \frac{F_z l^3}{16Et w^3}$
$z = \frac{4F_y l^3}{E w t^3}$	$z = \frac{F_y l^3}{E w t^3}$	$z = \frac{F_y l^3}{16E w t^3}$

Table 2-1 presents equations derived using this equation for the calculation of the deflection of the cantilever (Figure 2-7.a), the cantilever with a guided end (Figure 2-7.b), and the fixed-fixed or clamped-clamped beam (Figure 2-7.c).  $F_x, F_y, F_z$  are the forces applied to the beam in the x, y and z direction and  $l, w$  and  $t$  are the length, width and thickness of the beam respectively.

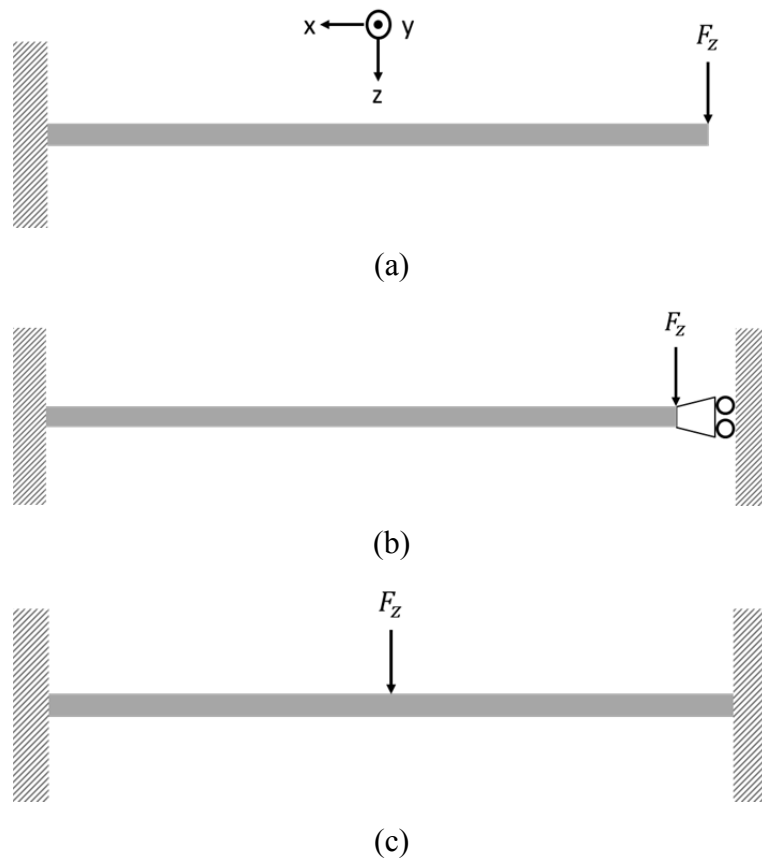


**Figure 2-7: Typical beam configurations (a) cantilever, (b) guided cantilever and (c) fixed-fixed beam.**

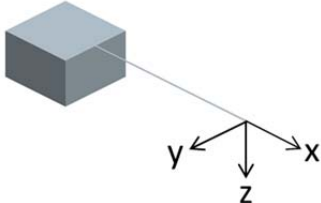
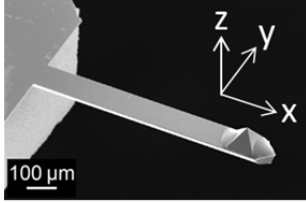
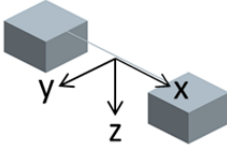
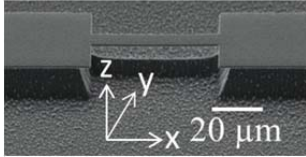
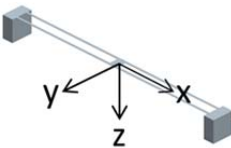
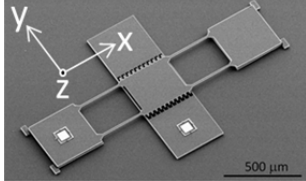
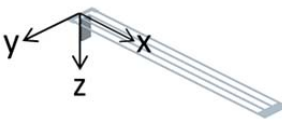
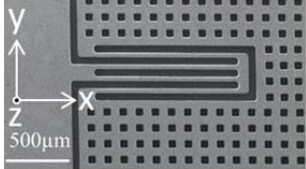
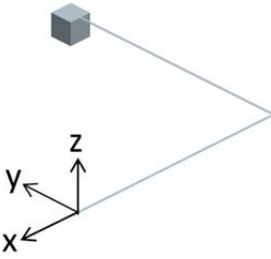
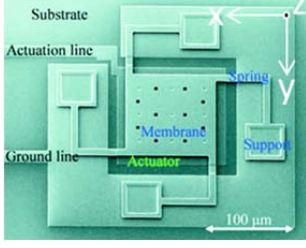
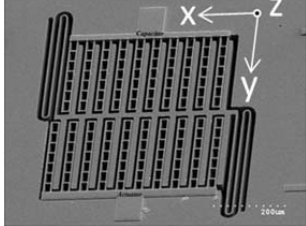
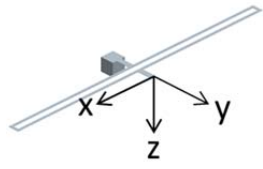
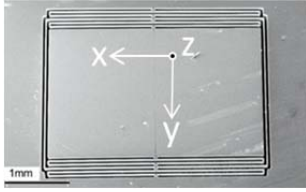
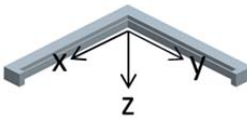
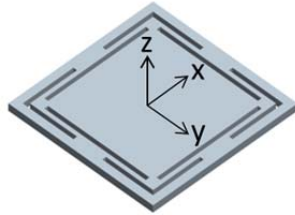
Once the deflection of the beam is known, the spring constant,  $k$ , can be calculated using Hooke's Law [24]:

$$k = \frac{F}{\delta} \quad \text{Eq. 2-3}$$

where  $\delta$  and  $F$  are the deflection and force applied to the beam respectively.

Table 2-2 shows images of a microfabricated cantilever, fixed-fixed beam and other more elaborate multi-beam flexures typically used in MEMS. For comparison the table includes the spring constants of these flexures relative to the spring constant of a cantilever with a force applied in the  $z$ -direction ( $k_{c,z}$ ). The spring constants were estimated with the finite element method (FEM) using commercial software (ANSYS). The models of the springs prepared for the analysis were assembled from beams with a length/width/thickness ratio of 100/1/0.1 respectively. The length, width and thickness of the beams in all in the models are the same. For instance, the cantilever and the fixed-fixed beam model are constructed from the same beam with the former fixed at one end while the latter is fixed at both ends. In the case of the hammock flexure, the two beams each have the same length as the cantilever and are connected at the centre with a small beam. On all the models the small interconnecting beams were designed to have negligible effect on the overall spring constant of the springs and can thus be ignored. The attributes listed in Table 2-2 should only be considered as a preliminary guide in spring selection. Methods to calculate the linear spring constants, and the non-linear spring constants, for these flexures are available elsewhere [23, 25-27]. In the table it can also be observed that the double folded, meander, and lateral springs all use multiple beams in series. This is typically done as it decreases the angle of deflection per beam thus increasing the overall linear range, and range of the spring. This will be discussed further in Chapter 3.

**Table 2-2: SEM Images and characteristics of typical flexures used in MEMS**

Flexure	Flexure Attributes	FEM Model	SEM/Model	Ref.
Cantilever (c)	$k_{c,x}/k_{c,z} = 2.8E-07$ $k_{c,y}/k_{c,z} = 1.0E-02$ $k_{z,c}/k_{c,z} = 1.0E+00$			[28]
Fixed-fixed beam (ff)	$k_{ff,x}/k_{c,z} = 6.3E-08$ $k_{ff,y}/k_{c,z} = 1.6E-04$ $k_{ff,z}/k_{c,z} = 1.6E-02$			[29]
Hammock (h)	$k_{h,x}/k_{c,z} = 7.7E-08$ $k_{h,y}/k_{c,z} = 7.9E-05$ $k_{h,z}/k_{c,z} = 7.8E-03$			[30]
Double Folded (df)	$k_{df,x}/k_{c,z} = 3.4E-07$ $k_{df,y}/k_{c,z} = 2.7E-03$ $k_{df,z}/k_{c,z} = 1.1E+00$			[31]
Crab-leg (cl)	$k_{cl,x}/k_{c,z} = 1.0E-02$ $k_{cl,y}/k_{c,z} = 4.0E-02$ $k_{cl,z}/k_{c,z} = 3.8E+00$			[32]
Meander (m)	$k_{m,x}/k_{c,z} = 2.1E-02$ $k_{m,y}/k_{c,z} = 4.3E-06$ $k_{m,z}/k_{c,z} = 2.0E+00$			[33]
Lateral Suspension (ls)	$k_{ls,x}/k_{c,z} = 2.6E-05$ $k_{ls,y}/k_{c,z} = 3.3E-04$ $k_{ls,z}/k_{c,z} = 3.7E-02$			[30]
Spring-Supported Diaphragm (sd)	$k_{sd,x}/k_{c,z} = 3.2E-06$ $k_{sd,y}/k_{c,z} = 3.2E-06$ $k_{sd,z}/k_{c,z} = 2.7E-01$			[26]

### 2.2.1.2 Non-Linear Deflections – Large Angles

For large angles of deflection the small angle assumption used to derive Eq. 2-2 is invalid. Thus the equation for the deflection of a beam is more accurately derived as [20, 22, 34]:

$$\frac{1}{r} = \frac{z''}{[1 + (z')^2]^{3/2}} \quad \text{Eq. 2-4}$$

which is a nonlinear differential equation for which an analytical solution does not exist [20, 35]. For applications that require large deflections, the non-linear equation is typically solved numerically using a computational software program such as MATLAB [35], or using a dedicated FEM engineering simulation software such as ANSYS. Figure 2-8 shows a comparison of the linear theory versus the non-linear solution [23, 36] for a cantilever with a load applied to its end. The non-linear solution deviates from the linear theory at small deflections clearly showing the limitations of Eq. 2-2.

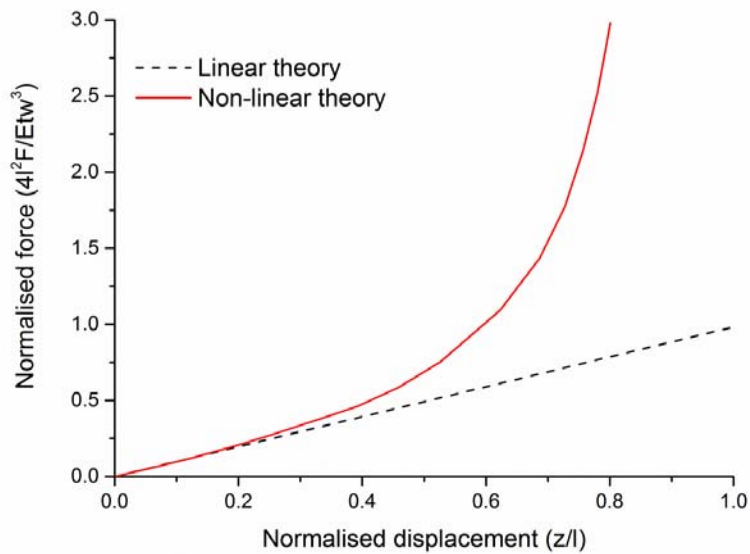


Figure 2-8: Comparison between linear beam theory and non-linear theory shows that they are approximately equal for only small deflections. Adapted from [23, 36].

## 2.3 Sensor Transduction Mechanisms

Transduction is the conversion of a signal from one physical phenomenon to another. Transduction in MEMS can occur between electrical, magnetic, mechanical, thermal, chemical or radiative signals. Figure 2-9 summarises the various transduction mechanisms typically used in MEMS. In sensors, the final transduction mechanism is typically to an electrical signal which is processed using a PC or similar to determine the measurand [37].

	Electrical	Magnetic	Mechanical	Thermal	Chemical	Radiative
Electrical		Ampere's Law	Electro-statics, Electro-phoresis	Resistive Heating	Electrolysis, Ionization	EM Transmission
Magnetic	Hall Effect, Mag. Resistance		Magneto-statics, Magneto-striction	Eddy Currents, Hysteretic Loss	Magnetic Separation	Magneto-optics
Mechanical	Variable Cap, Piezoresistive, Piezo-electricity	Magneto-striction		Friction	Phase Change	Tribo- Luminescence
Thermal	Thermo-electric	Curie Point	Thermal Expansion		Reaction Rate Ignition	Thermal Radiation
Chemical	Electro-chemical Potential	Chemo-magnetic	Phase Change	Combustion		Chemo- Luminescence
Radiative	Photo-conductor, EM Receiving	Magneto-optics	Radiation Hardening	Photo-thermal	Photochemical	

Figure 2-9: Common MEMS transduction mechanisms. Adapted from [37].

In a force-displacement sensor the most direct transduction mechanism is from a mechanical signal to an electrical signal. However, it is not necessary to go directly from the measured source energy to the final signal directly. For instance, the thermal cantilever force [38, 39], and Hall Effect sensors [40] use mechanical-thermal-electric and mechanical-magnetic-electric transduction mechanisms respectively. Multi-transduction systems typically increase the complexity of the sensor, and frequently require an external source, such as a magnetic field in the case of the Hall Effect sensor, thus a direct transduction mechanism is preferred. Capacitive, piezoelectric and piezoresistive sensing are examples of frequently used mechanical to electrical single transduction mechanisms used in force-displacement sensors. In capacitive sensing the change in capacitance that occurs when capacitor plates move relative to one another is used to measure displacement [22]. In piezoelectric sensing the displacement is

determined by monitoring the increase in charge in a piezoelectric material for a given change in mechanical stress. This technique can also employ the reverse phenomenon for actuation [41-50]. Commonly used piezoelectric materials are quartz (SiO<sub>4</sub>), Lead Zirconate Titanate (PZT), Zinc oxide (ZnO), and Aluminum Nitride (AlN) [51]. In a piezoresistive sensor, the displacement is measured by monitoring the change in electrical resistance in a piezoresistive material when subjected to a mechanical stress [52].

**Table 2-3: Critique of sensing systems proposed to measure sensor deflection. Adapted from [53].**

<b>Detection Scheme</b>	<b>Pros</b>	<b>Cons</b>
<b>Capacitive</b>	CMOS compatible Large dynamic range	Needs calibration upon change of dielectric constant of medium between plates Unsuitable in electrically conductive media
<b>Piezoelectric</b>	Self-actuation	DC leakage current makes static applications challenging Small output signal
<b>Piezoresistive</b>	Implementation of detection mechanism inside cantilever CMOS integration Can be used in any medium Large dynamic range Reliability; Well commercialized Implementation in large arrays	Needs a piezoresistive layer to be implemented over a stressed structural layer Thermal power dissipation in piezoresistors and thermal drift Generated heat can cause erratic beam deflection Associated noise of resistors

Table 2-3 lists the advantages and disadvantages of capacitive, piezoelectric, and piezoresistive sensors. The critical disadvantage that detracts from the suitability of capacitive sensing is that it is not amenable to applications in which the dielectric constant between the capacitive plates changes. Thus biomaterial measurements, which are frequently made in buffered solutions, would be inaccurate unless the device is pre-calibrated for the particular buffered solution. The main disadvantage with using piezoelectric sensing is that DC current leakage makes it inappropriate for quasi-static (1 to 10 Hz) measurements such as those investigated in this work. Piezoresistive sensing is unaffected by both the dielectric constant of the measurement medium and quasi-static measurements. Furthermore, Figure 2-10 shows a performance chart prepared from databases of existing MEM sensors and published literature which shows that piezoresistive sensing has a higher force resolution and force range when compared to capacitive and piezoelectric sensing [9]. Thus this work will use piezoresistive sensing as the transduction mechanism.

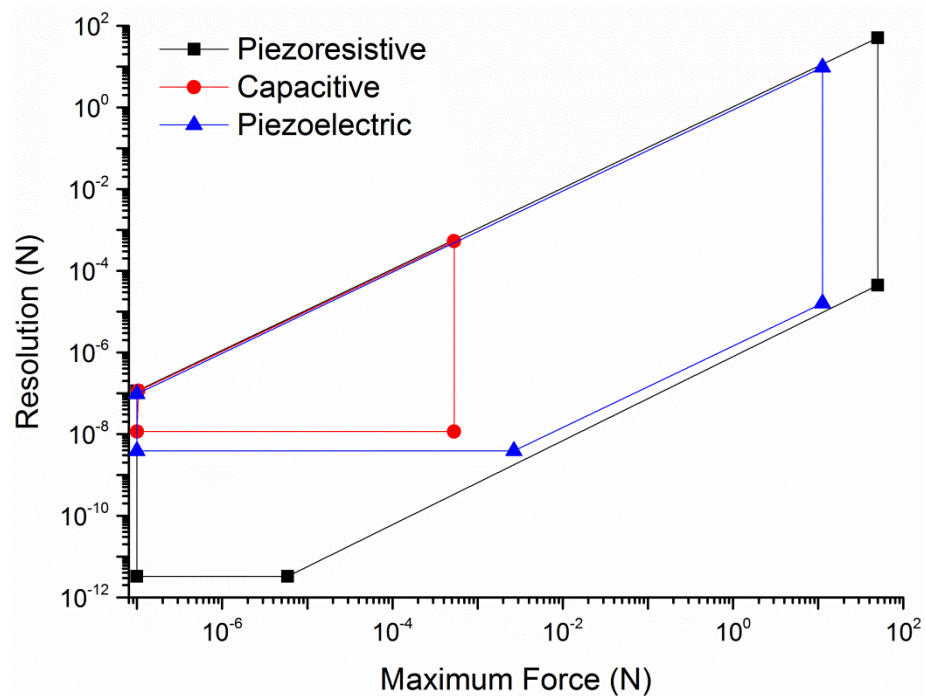


Figure 2-10: Force resolution versus maximum force for capacitive, piezoelectric and piezoresistive transduction mechanisms [9].

### 2.3.1 A review of piezoresistive transduction

The first reported change in resistance versus the elongation of iron and copper wires was made by Thomson (Lord Kelvin) in 1856 [53, 54], and confirmed by Tomlinson in 1876-1883. In the 1920's and 1930's Bridgman, Williams, Rolnick and Allen continued to research and measure the phenomenon in other materials including polycrystalline and amorphous conductors. The term piezoresistance was first used to refer to the phenomenon by Cookson in 1935 [54]. The first published use of piezoresistance was made in 1938 by Clark and Datwyler who used a metal wire piezoresistive sensor invented by Simmons in 1936 to measure strain in a stressed beam [54, 55]. The device became known as the strain gauge and Simmons and Ruge, who had also independently invented a similar device, were granted patents in the 1940's [54, 56-58]. In 1954, C.S. Smith reported large piezoresistivity in silicon and germanium [59], and in 1957 Mason and Thurston developed the first silicon based strain gauges with a sensitivity fifty times larger than that of the metal based strain gauges. The technology was soon adapted and developed into piezoresistive pressure sensors. Both the piezoresistive strain gauge and the piezoresistive pressure sensor became commercially available in the 1950's. These devices were the first to take

advantage of the fabrication methods developed for the semiconductors industry and are the first generation of the devices now commonly referred to as MEMS [54].

The basic principle of piezoresistive transduction can be seen in Ohm's Law:

$$R = \rho \frac{l}{A} \quad \text{Eq. 2-5}$$

where  $R$ ,  $\rho$ ,  $l$ , and  $A$  are the resistance, resistivity, length, and cross-sectional area of the conductor or semi-conductor respectively. The equation shows that a change to any of these parameters will result in a change in resistance. When a piezoresistive material is stressed, there is a change in the cross-sectional area of the material as a function of the longitudinal strain,  $\varepsilon$ , and its Poisson's ratio,  $\nu$ , known as the geometric effect. Furthermore, there is a change in volume, which changes the energy gap between the valence and conduction bands. Thus, there is a change in the number of carriers and hence a change in resistivity of the material [59]. This effect has been found to be larger in semiconductors than in metals and is referred to as the piezoresistive effect [59]. The combined geometric and piezoresistive effects change in resistance is given by [60]:

$$\frac{\Delta R}{R} = (1 + 2\nu)\varepsilon + \frac{\Delta\rho}{\rho} \quad \text{Eq. 2-6}$$

where  $(1+2\nu)\varepsilon$  is due to the geometric effect and  $\Delta\rho/\rho$  is the change in resistivity due to the piezoresistive effect.

The Gauge Factor (GF) is the relative change in resistance ( $\Delta R/R$ ) versus  $\varepsilon$  and is thus defined as [61]:

$$GF = \frac{\Delta R/R}{\varepsilon} \quad \text{Eq. 2-7}$$

The Poisson's ratio for crystalline Si is typically 0.06 to 0.36, thus the geometric effect would account for 1.12% to 1.36% of the change in resistance. In silicon, the change in resistivity ( $\Delta\rho/\rho$ ), is generally 50 to 100 times larger than the geometric effect [54], hence, the contribution of the geometric effect will be ignored in the present investigation.

The change in resistivity due to the piezoresistive effect is given as [22]:

$$\frac{\Delta R}{R} = \pi_l \sigma_l + \pi_t \sigma_t \quad \text{Eq. 2-8}$$

where  $\pi_l$ ,  $\sigma_l$ ,  $\pi_t$ , and  $\sigma_t$  are the longitudinal piezoresistance coefficients, longitudinal stress, transverse piezoresistance coefficients, and transverse stress respectively. The piezoresistors in this work are long, narrow, and thin (length>width>thickness), thus the transverse stress is negligible and will be ignored. Thus Eq. 2-8 becomes:

$$\frac{\Delta R}{R} = \pi_l \sigma_l \quad \text{Eq. 2-9}$$

The piezoresistive effect is generally taken to be linear to 0.1% for stresses below 15.3 MPa, and 1% for stresses below 139 MPa and needs to be taken into consideration when designing high accuracy piezoresistive devices [18, 62].

In semiconductors, the mechanical and electrical material properties are dependent on the orientation of the atomic lattice. Moreover, the piezoresistive effect is also dependent of the dopant concentration, and temperature. Values for the piezoresistive coefficients for crystalline silicon are available as data based on Smith’s work [59], a theoretical model [63], or an empirical fit [18, 64]. For this work the empirical fit method was used to determine the piezoresistive coefficients. For boron doped Si piezoresistors with concentrations  $> 10^{17} \text{ cm}^{-3}$  this is given as [62, 64]:

$$\pi_l = P\pi_0 \quad \text{Eq. 2-10}$$

where  $\pi_0 = 72 \times 10^{-11} \text{ Pa}^{-1}$  for  $\langle 110 \rangle$  p-type piezoresistors, and  $P$  is the piezoresistive factor given as [62, 64]:

$$P = \log\left(\frac{b}{n}\right)^a \quad \text{Eq. 2-11}$$

where  $a = 0.2014$  and  $b = 1.53 \times 10^{-22} \text{ cm}^{-3}$ , and  $n$  is the dopant concentration [62, 64].

### 2.3.1.1 Sensitivity

The conversion from a change in resistance to a change in voltage is typically achieved using one of the Wheatstone bridge configurations shown in Figure 2-11.

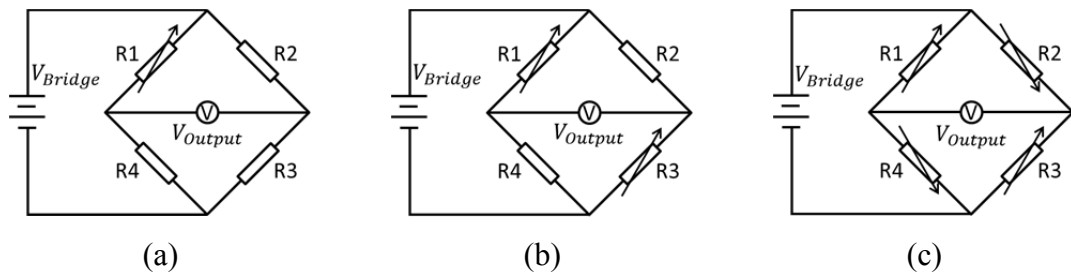


Figure 2-11: Typical Wheatstone bridge configurations (a) quarter bridge, (b) half bridge, and (c) full bridge.

In this representation  $V_{Bridge}$  is the DC supply and  $V_{Output}$  is the measured output. The relationship of  $V_{Output}$  relative to  $V_{Bridge}$  is given as [22]:

$$\frac{V_{Output}}{V_{Bridge}} = \frac{R_1 R_3 - R_2 R_4}{(R_1 + R_2)(R_3 + R_4)} \quad \text{Eq. 2-12}$$

The equation shows that if all the resistors are equivalent ( $R_1 = R_2 = R_3 = R_4 = R_0$ ) then  $V_{Output}/V_{Bridge}$  is equal to zero, a state referred to as a balanced or nulled bridge. Moreover, this is also significant since a change in resistance due to a change in temperature would, provided they all have the same thermal/resistive properties and are in the same environment, affect all the resistors equally. Thus, error due to temperature drift is mitigated.

The Wheatstone bridge can have a quarter, half, or full bridge configurations with 1, 2, or 4 active resistors (Figure 2-11.a-c). An active resistor can only be considered as such if it is a stress sensitive resistor, such as a piezoresistor or a strain gauge, and if it is positioned on a stressed member of the sensor. The full bridge configuration has four times and two times the sensitivity of a quarter and half bridge respectively and has a linear stress versus displacement output, thus it is the preferred configuration.

In a full bridge configuration the maximum  $V_{Output}/V_{Bridge}$  occurs when the resistance in  $R_1$  and  $R_3$  increases ( $+\Delta R$ ) and the resistance in  $R_2$  and  $R_4$  decreases ( $-\Delta R$ ) or the reverse. This is achieved by strategically placing the resistors  $R_1$  and  $R_3$  on a member with compressive/tensile stress, and resistors  $R_2$  and  $R_4$  on a member with the reverse and equal stress (tensile/compressive). This will be discussed in greater detail in Chapter 3. In such a scenario [22]:

$$\frac{\Delta R_1}{R_1} = \frac{\Delta R_1}{R_0} = \pi_l \sigma_l \quad \text{Eq. 2-13}$$

thus:

$$R_1 = R_3 = (1 + \pi_l \sigma_l) R_0 \quad \text{Eq. 2-14}$$

and:

$$\frac{\Delta R_2}{R_2} = \frac{\Delta R_2}{R_0} = -\pi_l \sigma_l \quad \text{Eq. 2-15}$$

thus:

$$R_2 = R_4 = (1 - \pi_l \sigma_l) R_0 \quad \text{Eq. 2-16}$$

Substituting Eq. 2-14 and Eq. 2-16 into Eq. 2.12 gives [22]:

$$\frac{V_{Output}}{V_{Bridge}} \approx \pi_l \sigma_l \quad \text{Eq. 2-17}$$

Using Eq. 2.6, 2.9, and 2.13 the overall force sensitivity,  $S_f$ , can be calculated for a full Wheatstone bridge as:

$$S_f = \frac{\Delta V}{F} \approx \frac{\pi_l \sigma_l V_{bridge} \beta^* \gamma}{F} \quad \text{Eq. 2-18}$$

where  $\Delta V$ ,  $F$ ,  $\gamma$ , are the change in voltage, the applied force, the ratio of the piezoresistive resistance to the total measured resistance in the circuit respectively.  $\beta^*$  is an efficiency factor which for a uniformly doped piezoresistor with finite thickness is given as [52]:

$$\beta^* = P \left( 1 - \frac{t_{pr}}{t} \right) \quad \text{Eq. 2-19}$$

where  $t$ ,  $t_{pr}$  are the thickness of the beam, and the thickness of the piezoresistor respectively.

### 2.3.1.2 Noise

Piezoresistors have three main sources of noise that hinder the performance of the device. These are Johnson, Hooge and the amplifier noise.

#### Johnson Noise

Johnson noise, or white noise, is a thermal noise that is independent of frequency and gives a fluctuating zero average voltage across the terminals of an electrical resistor. The noise power spectral density ( $V^2/Hz$ ) for a single resistor due to Johnson noise is [22]:

$$\overline{S^2_J} = 4k_b TR \quad \text{Eq. 2-20}$$

where  $k_b$ ,  $T$ , and  $R$  are the Boltzmann's constant ( $1.38065e^{-23} \text{ m}^2\text{Kgs}^{-2}\text{K}^{-1}$ ), the absolute temperature of the resistor, and resistance respectively. The resistance of a uniformly doped piezoresistor is calculated using Eq. 2-5 for which the resistivity can be calculated using [65]:

$$\rho = \frac{1}{q\mu n} \quad \text{Eq. 2-21}$$

where  $q, \mu$  and  $n$  are the electron charge, the concentration dependent majority carrier mobility, and the dopant concentration respectively. In a Wheatstone bridge, the total Johnson noise is equivalent to that of a single resistor. For a frequency range of  $f_{min}$  to  $f_{max}$  the Johnson noise power is [62]:

$$\overline{V^2}_J = 4k_bTR(f_{max} - f_{min}) \quad \text{Eq. 2-22}$$

### Hooge Noise

Hooge noise is the dominant 1/f noise in silicon piezoresistors [62]. It is a result of fluctuations in conductance with a power spectral density proportional to  $f^{-\gamma}$ , where  $\gamma = 1.0 \pm 0.1$ . Thus, unlike Johnson noise, 1/f noise is dependent on the frequency. Hooge noise has been found to be related to the process variables, independent of the resistance and inversely proportional to the total number of carriers ( $N$ ) in the piezoresistor [64, 65]. Annealing has been observed to reduce the Hooge noise level, while plasma processes, such as reactive ion etching, have been found to increase it [64]. The voltage power spectral density for the Hooge noise of a single piezoresistor is [62]:

$$\overline{S^2}_H = \alpha \frac{V_{bias}^2}{Nf} \quad \text{Eq. 2-23}$$

where  $f$ , and  $V_{bias}$  are the frequency and bias voltage ( $V_{bias} = V_{Bridge}/2$ ) respectively.  $\alpha$  is an experimentally determined value dependent on the crystal lattice quality called the Hooge factor [64, 66, 67], and  $N$  is the total number of carriers in the piezoresistor calculated using [62]:

$$N = nl_{pr}w_{pr}t_{pr} \quad \text{Eq. 2-24}$$

where  $l_{pr}$ ,  $w_{pr}$ , and  $t_{pr}$  are the length, width, and thickness of the piezoresistor respectively. The integrated voltage power due to 1/f noise is [65]:

$$\overline{V^2}_H = \frac{\alpha V_{bridge}^2}{4N} \text{Log}(f_{max}/f_{min}) \quad \text{Eq. 2-25}$$

### Amplifier Noise

The signal from the Wheatstone bridge is typically amplified using a low noise instrumentation amplifier. This adds another source of noise. The amplifier voltage noise can be approximated as [62]:

$$\overline{V_A^2} = C_J^2(f_{max} - f_{min}) + C_H^2 \text{Log}(f_{max}/f_{min}) \quad \text{Eq. 2-26}$$

where  $C_J$  and  $C_H$  are the Johnson and Hooge voltage noise properties of the amplifier used.

#### 2.3.1.3 Force Resolution

Using the values for each noise source, the root mean square voltage noise of the uncorrelated noise sources system can be estimated. For this application the uncorrelated noise sources include the Johnson Noise for a single piezoresistor, the Hooge Noise for each piezoresistor, and the amplifier noise. The root mean square voltage noise is found using [62]:

$$\overline{V_{noise}} = \sqrt{V_J^2 + V_H^2 + V_A^2} \quad \text{Eq. 2-27}$$

and the minimum resolvable force ( $F_{min}$ ) for the device can be determined using [62]:

$$F_{min} = \frac{\overline{V_{noise}}}{S_f} \quad \text{Eq. 2-28}$$

#### 2.3.1.4 Power Dissipation

The heat dissipated (W) by a single piezoresistor can be calculated using [62]:

$$W = \frac{V_{bridge}^2}{4R} \quad \text{Eq. 2-29}$$

The working temperature of the device depends on how efficiently the heat is dissipated into the measurement medium via convection and into the bulk of the device, and its packaging via conduction. An elevated temperature decreases the piezoresistive coefficient, increases the thermal noise, and may ultimately damage the piezoresistor [62]. Thus, the heat dissipated by the piezoresistors needs to be limited while the heat the sensor can dissipate needs to be encouraged.

### 2.3.1.5 Deposition of piezoresistive materials

The predominant piezoresistive material used in MEMS is p-type or n-type doped silicon. Crystalline Si piezoresistors in MEMS are typically introduced into the device using dopant implantation techniques such as ion implantation, and diffusion or growth techniques such as epitaxial. Typically p-n junctions are used to isolate the piezoresistors from the bulk silicon. These have a tendency to cause current leakage which increases with temperature and may cause the device to fail at temperatures exceeding 100°C. Thus for high temperature applications silicon on insulator (SOI) substrates are preferred. Polysilicon and amorphous Si piezoresistors are generally deposited using Low Pressure Chemical Vapour Deposition (LPCVD), Plasma Enhanced Chemical Vapour Deposition (PECVD), or Hot Wire Chemical Vapour Deposition (HWCVD). The low piezoresistive coefficient of amorphous silicon is typically considered insufficient for MEMS applications. Crystalline Si exhibits the highest piezoresistive coefficients; however, the equipment required for the fabrication of such devices was not available for this work. Thus the performances of the devices developed in this work will be calculated for both crystalline Si and polysilicon piezoresistors; however, the devices fabricated for proof of concept will use polysilicon piezoresistors. The remainder of this chapter will focus on the properties and fabrication methods of polysilicon piezoresistors [60, 61].

#### Polysilicon

Polysilicon is composed of different grains of crystalline Si. This results in the crystals having different planar orientations relative to one another. The structure formed by the different crystalline Si grains can be either random crystals or columnar (Figure 2-12) and is dependent on processing. The grain boundaries, which is the interface between the randomly orientated crystals, result in defects which decrease the electrical and thermal conductivity of the polysilicon [68].

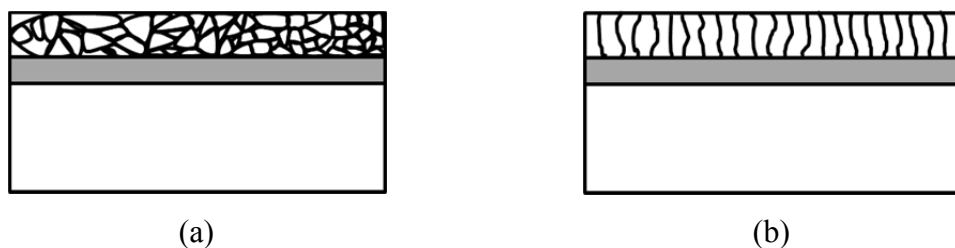
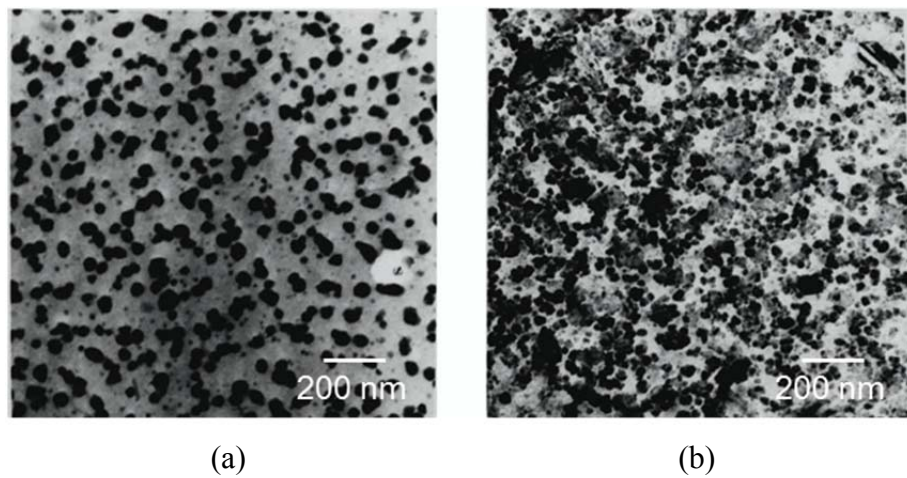
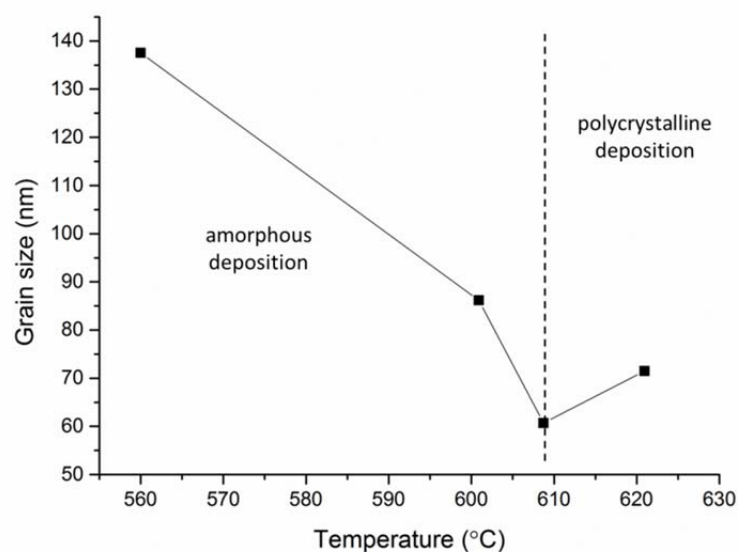


Figure 2-12: Two polysilicon structures: (a) random crystal or, (b) column structure. Adapted from [68].

Polysilicon piezoresistors can be deposited on a variety of insulators, thus they do not rely on p-n junctions for isolation. This negates issues associated with leakage currents. The gauge factor for polysilicon piezoresistors is dependent on the doping concentration, and on the fabrication method and is always less than that of crystalline Si [60, 68]. It has been observed that when polysilicon is deposited below a certain critical temperature ( $\sim 609^\circ\text{C}$ ) with LPCVD, it results in amorphous silicon with crystalline Si grains. Moreover, as the deposition temperature is decreased further (Figure 2-13), the grain size of the crystalline Si remains unchanged ( $\sim 60$  nm) but the grain density decreases [61].



**Figure 2-13: Examples of two polysilicon films deposited at (a)  $560^\circ\text{C}$  and (b)  $601^\circ\text{C}$ . In both cases, the grain size was approximately 60 nm. The image shows that the deposition at  $560^\circ\text{C}$  has less crystalline Si grains, thus there is a greater distance between the crystals. This allows the crystals to grow further when annealed. Adapted from [68].**



**Figure 2-14: Grain size as a function of deposition temperature. After LPCVD deposition, samples were implanted with boron and annealed at  $1000^\circ\text{C}$  for 30 min. Adapted from [68].**

It has also been observed that by annealing the amorphous/polysilicon at  $\leq 1000^\circ\text{C}$ , the crystalline Si crystals consume the amorphous silicon to form larger grains (Figure 2-14). This crystal growth continues until only a thin grain boundary between the crystals remains. This is beneficial as larger crystal grains increase the gauge factor of the resulting polysilicon. Once the grain boundaries are formed anneals above  $1000^\circ\text{C}$  are required for continued grain growth [68].

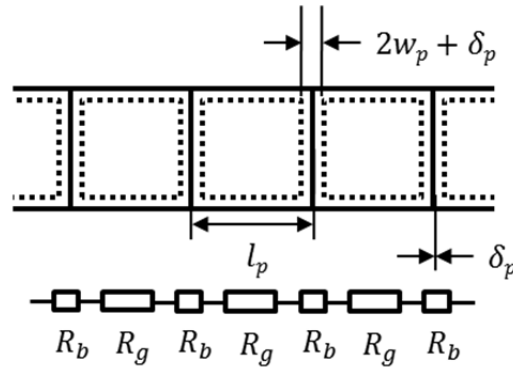


Figure 2-15: Simple electrical model for polysilicon [68].

The current theory explaining the piezoresistance in polysilicon [68-72] models it as a series of crystalline Si grains and grain boundary resistors in series (Figure 2-15) with the resultant resistivity equivalent to [68]:

$$\rho = \left[ \frac{L - (2w + \delta)}{L} \right] \rho_g + \left[ \frac{2w + \delta}{L} \right] \rho_b \quad \text{Eq. 2-30}$$

where  $\rho_g$ ,  $\rho_b$  are the crystalline Si grain and the grain boundary barrier resistivity and  $l_p$ ,  $w_p$ , and  $\delta_p$  are the length of the crystalline Si grain, width of the depleted region and width of the grain boundary respectively as defined in Figure 2-15.

Research has shown that the formation of grain boundaries during deposition increases the number of traps, thus a higher barrier and greater width. The effect of the deposition temperature on the grain boundary can be seen in the decrease in resistivity of polysilicon deposited at  $560^\circ\text{C}$  versus  $610^\circ\text{C}$  for the same boron doping concentration (Figure 2-16). The process used for deposition can increase the barrier width, which increases  $\rho_b$ , at the detriment of the performance of the piezoresistor.

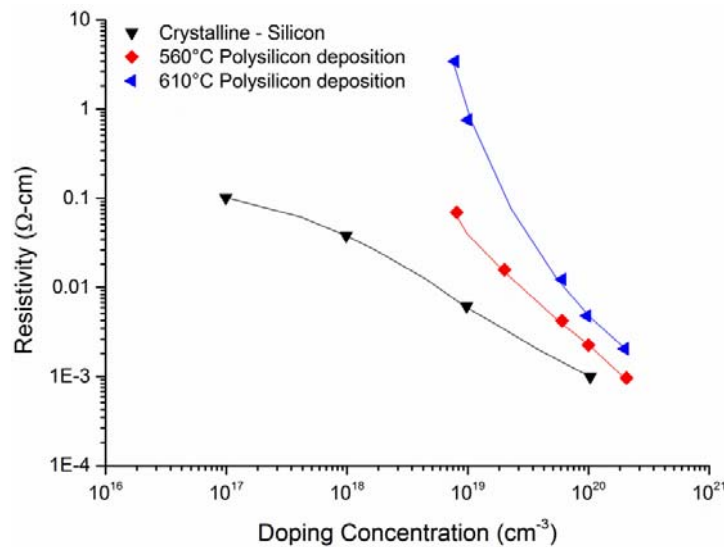


Figure 2-16: Resistivity versus boron doping concentration for crystalline Si, polysilicon deposited at 560°C and polysilicon deposited at 610°C. Adapted from [61].

Figure 2-17 shows the gauge factor for p-type and n-type polysilicon versus the deposition temperature. The piezoresistors were deposited using LPCVD and annealed at 1000°C. The graph indicates that the gauge factor is at a maximum when the deposition temperature is at a minimum.

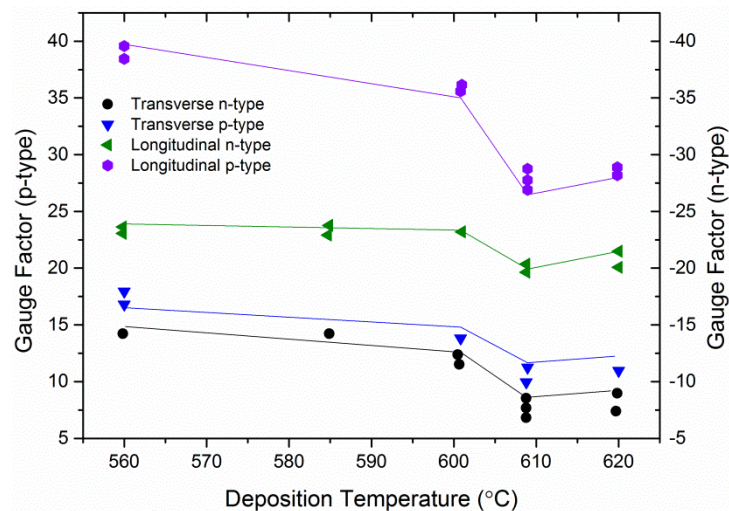


Figure 2-17: Gauge Factor as a function of deposition temperature. All films were annealed at 1000 °C after implantation. Adapted from [68].

Figure 2-18 shows the gauge factor for p-type and n-type polysilicon versus doping concentration. The polysilicon was deposited using LPCVD at a temperature of 560°C and annealed at 1000°C. The graph indicates that a longitudinal p-type piezoresistor provides the largest gauge factor of 40 at a doping concentration of  $1.63 \times 10^{19} \text{ cm}^{-3}$ . Thus to achieve the highest possible sensitivity, polysilicon piezoresistors with similar attributes will be required.

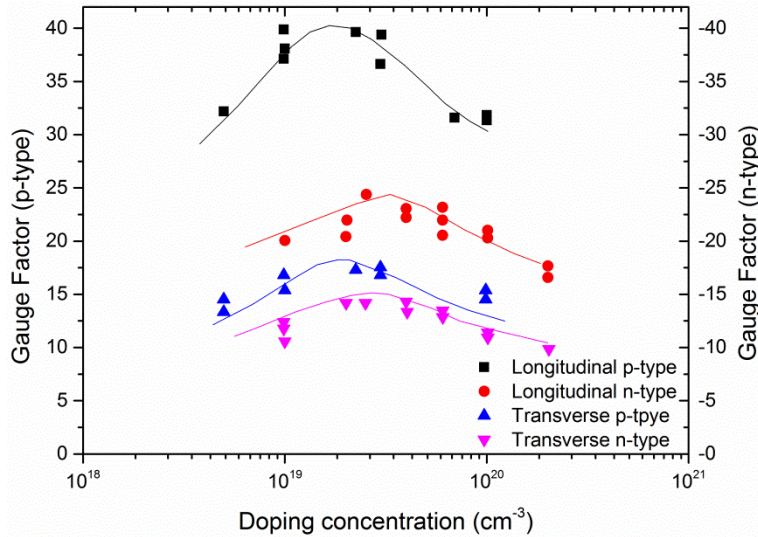


Figure 2-18: Graph of gauge factor as a function of doping concentration for both boron and phosphorus doped material. All films were deposited at 560°C. Adapted from [61].

### The Effect of Stress Transformation

When polysilicon is used in a piezoresistive application, it is typically deposited on to a crystalline Si structure with an intermediate dielectric between the two layers (Figure 2.19).

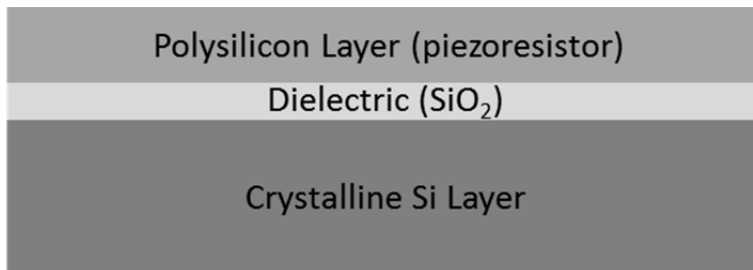


Figure 2-19: Layers which make up a polycrystalline piezoresistive device.

This introduces a crystalline Si to dielectric to polysilicon mechanical interface. Since the thickness of both the dielectric and the polysilicon layers are both generally much thinner than that of the crystalline Si layer, the strain at this interface can be considered to be that of the crystalline Si layer. This results in a polysilicon stress,  $\sigma_{poly}$ , equivalent to [60]:

$$\sigma_{poly} = \frac{E_{poly}}{E_{Si}} \sigma_{Si} \quad \text{Eq. 2-31}$$

where  $E_{poly}$ ,  $E_{Si}$ ,  $\sigma_{Si}$  and are the Young's modulus of the polysilicon and crystalline Si layers, and the stress in the crystalline Si layer respectively. Since  $E_{Si}$  is greater

than  $E_{poly}$  this effect reduces the sensitivity of the piezoresistor and needs to be taken into account when designing a MEMS sensor using piezoresistive polysilicon [60].

## 2.4 Conclusions

This chapter begins with an introduction to the F-D measurement systems used to investigate biological tissue and cells. These techniques typically have a restricted F-D range which limits the phenomena that can be investigated. The MEMS sensors previously developed to increase the F-D range of these measurement techniques include a piezoresistive cantilever and a meander spring design. In the piezoresistive cantilever approach the displacement and linearity range are controlled by the length of the beam. In the meander spring approach the linearity range is increased by using multiple beams in series. This design used an optical microscope to measure the deflections relative to a fixed reference point thus is not suited for an in-vivo application.

Since the type of spring used is a critical component of any MEMS sensor, a comprehensive overview of the flexures typically used was presented and includes a review on linear and non-linear beam theory. From this it was shown that the F-D of a beam is linear for only small angles of deflection and that the linear range can be extended by using a number of beams in series since this reduces the angle of deflection per beam. This approach is used in the double folded, meander and lateral suspension spring design and will be applied to the spring developed in this work.

An overview of the different transduction mechanisms and a summary of their attributes was also provided. This study indicated that piezoresistive sensing was the most opportune for the application, thus a thorough review was included. From this overview it established that a full Wheatstone bridge configuration using crystalline Si piezoresistors would give the highest force resolution. However, since the equipment required for depositing crystalline Si piezoresistors was not available a polysilicon alternative was investigated. The literature reviewed indicated that the gauge factor of LPCVD polysilicon is enhanced by using a low deposition temperature. This results in a polysilicon with a low grain density which when annealed permits the growth of large grains which exhibit a higher gauge factor. A maximum gauge factor of 40 has been achieved using this method when the polysilicon was doped with boron. In this work a

similar technique will be used on HWCVD polysilicon for which a gauge factor has not been previously reported.

The force resolution of piezoresistive transduction is directly related to the doping concentration, size of the piezoresistors, geometry of the stressed beam, and the bias voltage. Due to parameter coupling, which is most notable between the Hooge noise, Johnson noise and the gauge factor a straightforward approach to determining the optimal values of these parameters is not possible. Thus an optimisation scheme is developed in Chapter 3.

## References

- [1] K. A. Addae-Mensah and J. P. Wikswo, "Measurement techniques for cellular biomechanics in vitro," *Experimental Biology and Medicine*, vol. 233, pp. 792-809, Jul 2008.
- [2] M. L. Rodriguez, P. J. McGarry, and N. J. Sniadecki, "Review on Cell Mechanics: Experimental and Modeling Approaches," *Applied Mechanics Reviews*, vol. 65, Nov 2013.
- [3] O. Loh, A. Vaziri, and H. D. S. M. Espinosa, "The Potential of MEMS for Advancing Experiments and Modeling in Cell Mechanics," *Experimental Mechanics*, vol. 49, pp. 105-124, Feb 2009.
- [4] K. J. Van Vliet, G. Bao, and S. Suresh, "The biomechanics toolbox: experimental approaches for living cells and biomolecules," *Acta Materialia*, vol. 51, pp. 5881-5905, Nov 25 2003.
- [5] S. Kasas and G. Dietler, "Probing nanomechanical properties from biomolecules to living cells," *Pflugers Archiv-European Journal of Physiology*, vol. 456, pp. 13-27, Apr 2008.
- [6] J. Rajagopalan, A. Tofangchi, and M. T. A. Saif, "Highly Linear, Ultra Sensitive Bio-Mems Force Sensors with Large Force Measurement Range," *Mems 2010: 23rd IEEE International Conference on Micro Electro Mechanical Systems, Technical Digest*, pp. 88-91, 2010.
- [7] S. Yang and M. T. A. Saif, "Microfabricated Force Sensors and Their Applications in the Study of Cell Mechanical Response," *Experimental Mechanics*, vol. 49, pp. 135-151, Feb 2009.
- [8] S. Yang and T. Saif, "Mechanical response of single living cells by bio-MEMS sensors," in *Micro Electro Mechanical Systems, 2004. 17th IEEE International Conference on. (MEMS)*, 2004, pp. 265-267.
- [9] D. J. Bell, T. J. Lu, N. A. Fleck, and S. M. Spearing, "MEMS actuators and sensors: observations on their performance and selection for purpose," *Journal of Micromechanics and Microengineering*, vol. 15, pp. S153-S164, Jul 2005.
- [10] CSM. (22 June). *CSM Instruments SA*. Available: [http://www.csm-instruments.com/en/webfm\\_send/51](http://www.csm-instruments.com/en/webfm_send/51)
- [11] (22 June). *Micro Materials Limited*. Available: <http://www.micromaterials.co.uk/the-nano-test/nanoindentation/>
- [12] Agilent. (22 June). *Agilent Nano Indenter G300 - Data Sheet*. Available: <http://cp.literature.agilent.com/litweb/pdf/5990-4178EN.pdf>
- [13] Agilent. (22 June). *The Cypher™ Atomic Force Microscope*. Available: <http://www.asylumresearch.com/Products/Cypher/CypherProduct.shtml#Specs>

- [14] Bruker. *Dimension Icon - Technical Details*. Available: <http://www.bruker.com/products/surface-analysis/atomic-force-microscopy/dimension-icon/technical-details.html>
- [15] S. J. Park, M. B. Goodman, and B. L. Pruitt, "Analysis of nematode mechanics by piezoresistive displacement clamp," *Proceedings of the National Academy of Sciences of the United States of America*, vol. 104, pp. 17376-17381, Oct 30 2007.
- [16] J. Rajagopalan, A. Tofangchi, and M. T. A. Saif, "Linear High-Resolution BioMEMS Force Sensors With Large Measurement Range," *Microelectromechanical Systems, Journal of*, vol. 19, pp. 1380-1389, 2010.
- [17] A. Noy, *Handbook of molecular force spectroscopy*. New York, NY: Springer, 2008.
- [18] S.-J. Park, *Development of piezoresistive microcantilever based force feedback system for analysis of mechanosensation in caenorhaditis elegans nematodes*, 2009.
- [19] W. T. Pike and S. Kumar, "Improved design of micromachined lateral suspensions using intermediate frames," *Journal of Micromechanics and Microengineering*, vol. 17, pp. 1680-1694, Aug 2007.
- [20] D. G. Fertis. (2006). *Nonlinear Structural Engineering With Unique Theories and Methods to Solve Effectively Complex Nonlinear Problems*.
- [21] J. Bird and ebrary Inc. (2010). *Higher engineering mathematics (6th ed.)*. Available: <http://site.ebrary.com/lib/yale/Doc?id=10408211>
- [22] S. D. Senturia, *Microsystem design*. Boston: Kluwer Academic Publishers, 2000.
- [23] G. K. Fedder, "Simulation of Microelectromechanical Systems," PhD., University of California at Berkeley, 1994.
- [24] J. Carvill, *Mechanical engineer's data handbook*: Butterworth-Heinemann, 2003.
- [25] J. J. Allen, *Micro electro mechanical system design*. Boca Raton: Taylor & Francis/CRC Press, 2005.
- [26] N. Mohamad, P. Iovenitti, and T. Vinay, "High sensitivity capacitive MEMS microphone with spring supported diaphragm - art. no. 68001T," *Device and Process Technologies for Microelectronics, Mems, Photonics and Nanotechnology Iv*, vol. 6800, p. 248, 2008.
- [27] W. C. Young, R. G. Budynas, A. M. Sadegh, and R. J. Roark, *Roark's formulas for stress and strain*, 8th ed. New York ; London: McGraw-Hill, 2012.
- [28] N. Kawasegi and N. Morita, *Three-Dimensional Lithography Using Combination of Nanoscale Processing and Wet Chemical Etching*, 2013.
- [29] J. Hees, N. Heidrich, W. Pletschen, R. E. Sah, M. Wolfer, O. A. Williams, *et al.*, "Piezoelectric actuated micro-resonators based on the growth of

- diamond on aluminum nitride thin films," *Nanotechnology*, vol. 24, Jan 18 2013.
- [30] S. Kumar, "Design and Fabrication of Micromachined Silicon Suspensions," PhD., Optical and Semiconductor Device Group, Imperial College London, 2007.
- [31] Y. Gerson, D. Schreiber, H. Grau, and S. Krylov, "Meso scale MEMS inertial switch fabricated using an electroplated metal-on-insulator process," *Journal of Micromechanics and Microengineering*, vol. 24, Feb 2014.
- [32] F. C. Tabak, E. C. M. Disseldorp, G. H. Wortel, A. J. Katan, M. B. S. Hesselberth, T. H. Oosterkamp, *et al.*, "MEMS-based fast scanning probe microscopes," *Ultramicroscopy*, vol. 110, pp. 599-604, May 2010.
- [33] P. Monajemi, "Analytical design of polymer-encapsulated radio frequency microelectromechanical devices," *Journal of Micro/Nanolithography, MEMS, and MOEMS*, vol. 11, pp. 021207-1-021207-10, 2012.
- [34] R. Frisch-Fay, *Flexible bars*. London: Butterworths, 1962.
- [35] T. Belendez, C. Neipp, and A. Belendez, "Large and small deflections of a cantilever beam," *European Journal of Physics*, vol. 23, pp. 371-379, May 2002.
- [36] K. E. Bisshopp, Drucker, D.C., " Large Deflections of Cantilever Beams," *Q. Appl. Math.*, pp. 272-5, 1945.
- [37] J. W. Judy, "Microelectromechanical systems (MEMS): fabrication, design and applications," *Smart Materials & Structures*, vol. 10, pp. 1115-1134, Dec 2001.
- [38] W. P. King, T. W. Kenny, and K. E. Goodson, "Comparison of thermal and piezoresistive sensing approaches for atomic force microscopy topography measurements," *Applied Physics Letters*, vol. 85, pp. 2086-2088, Sep 13 2004.
- [39] K. J. Kim, K. Park, J. Lee, Z. M. Zhang, and W. P. King, "Nanotopographical imaging using a heated atomic force microscope cantilever probe," *Sensors and Actuators a-Physical*, vol. 136, pp. 95-103, May 1 2007.
- [40] D. W. Lee, T. Ono, and M. Esashi, "Cantilever with integrated resonator for application of scanning probe microscope," *Sensors and Actuators a-Physical*, vol. 83, pp. 11-16, May 22 2000.
- [41] S. Stucklin, M. R. Gullo, T. Akiyama, and M. Scheidiger, "Atomic Force Microscopy for Industry with the Akiyama-Probe Sensor," *2008 International Conference on Nanoscience and Nanotechnology*, pp. 79-82, 240, 2008.
- [42] T. Akiyama, N. F. de Rooij, U. Staufer, M. Detterbeck, D. Braendlin, S. Waldmeier, *et al.*, "Implementation and characterization of a quartz tuning fork based probe consisted of discrete resonators for dynamic mode atomic force microscopy," *Review of Scientific Instruments*, vol. 81, pp. -, Jun 2010.

- [43] T. Akiyama, K. Suter, N. F. de Rooij, A. Baumgartner, A. E. Gildemeister, T. Ihn, *et al.*, "Scanning probe with tuning fork sensor, microfabricated silicon cantilever and conductive tip for microscopy at cryogenic temperature," *Japanese Journal of Applied Physics Part 1-Regular Papers Brief Communications & Review Papers*, vol. 45, pp. 1992-1995, Mar 2006.
- [44] T. Akiyama, U. Staufer, and N. F. de Rooij, "Self-sensing and self-actuating probe based on quartz tuning fork combined with microfabricated cantilever for dynamic mode atomic force microscopy," *Applied Surface Science*, vol. 210, pp. 18-21, Mar 31 2003.
- [45] H. Hida, M. Shikida, K. Fukuzawa, A. Ono, K. Sato, K. Asaumi, *et al.*, "Development of self-vibration and -detection AFM probe by using quartz tuning fork," *Transducers '07 & Eurosensors Xxi, Digest of Technical Papers, Vols 1 and 2*, pp. U775-U776, 2616, 2007.
- [46] H. Hida, M. Shikida, K. Fukuzawa, A. Ono, K. Sato, K. Asaumi, *et al.*, "Fabrication and characterization of AFM probe with crystal-quartz tuning fork structure," *Proceedings of the 2005 International Symposium on Micro-NanoMechatronics and Human Science*, pp. 97-101, 324, 2005.
- [47] H. Hida, M. Shikida, K. Fukuzawa, S. Murakami, K. Sato, K. Asaumi, *et al.*, "Fabrication of a quartz tuning-fork probe with a sharp tip for AFM systems," *Sensors and Actuators a-Physical*, vol. 148, pp. 311-318, Nov 4 2008.
- [48] S. Horowitz, T. Nishida, L. Cattafesta, and M. Sheplak, "Development of a micromachined piezoelectric microphone for aeroacoustics applications," *Journal of the Acoustical Society of America*, vol. 122, pp. 3428-3436, Dec 2007.
- [49] S. H. Lee, S. S. Lee, J. J. Choi, J. U. Jeon, and R. Ko, "Fabrication of a high-aspect-ratio nano tip integrated micro cantilever with a ZnO piezoelectric actuator," *Advances in Nondestructive Evaluation, Pt 1-3*, vol. 270-273, pp. 1095-1100, 2004.
- [50] S. H. Lee, S. S. Lee, J. J. Choi, J. U. Jeon, and K. Ro, "Fabrication of a ZnO piezoelectric micro cantilever with a high-aspect-ratio nano tip," *Microsystem Technologies-Micro-and Nanosystems-Information Storage and Processing Systems*, vol. 11, pp. 416-423, May 2005.
- [51] S. Beeby, *MEMS mechanical sensors*. Boston: Artech House, 2004.
- [52] S. J. Park, J. C. Doll, and B. L. Pruitt, "Piezoresistive Cantilever Performance-Part I: Analytical Model for Sensitivity," *Journal of Microelectromechanical Systems*, vol. 19, pp. 137-148, Feb 2010.
- [53] K. Naeli, "Optimization of Piezoresistive Cantilevers for Static and Dynamic Sensing Applications," Doctor of Philosophy, School of Electrical and Computer Engineering, Georgia Institute of Technology, Atlanta, Georgia 2009.
- [54] A. A. Barlian, W. T. Park, J. R. Mallon, A. J. Rastegar, and B. L. Pruitt, "Review: Semiconductor Piezoresistance for Microsystems," *Proceedings of the IEEE*, vol. 97, pp. 513-552, Mar 2009.

- [55] D. Clark and G. Datwyler, "Stress-strain relations under tension impact loading," *American Society for Testing and Materials*, vol. 39, p. 98, 1938.
- [56] E. E. Simmons, "Method and apparatus for making strain gauges," 2344647, March 21, 1944, March 21, 1944.
- [57] E. E. Simmons, "Strain gauge and method for making same," USA Patent 2350073, May 30, 1944, May 30, 1944.
- [58] A. C. Ruge, "Strain gage," Jun. 6, 1944, Jun. 6, 1944.
- [59] C. S. Smith, "Piezoresistance Effect in Germanium and Silicon," *Physical Review*, vol. 94, pp. 42-49, 1954.
- [60] M.-H. Bao, *Analysis and design principles of MEMS devices*. Amsterdam ; Oxford: Elsevier, 2005.
- [61] P. J. French, "Polysilicon: a versatile material for microsystems," *Sensors and Actuators a-Physical*, vol. 99, pp. 3-12, Apr 30 2002.
- [62] J. C. Doll, S. J. Park, and B. L. Pruitt, "Design optimization of piezoresistive cantilevers for force sensing in air and water," *Journal of Applied Physics*, vol. 106, Sep 15 2009.
- [63] Y. Kanda, "Piezoresistance Effect of Silicon," *Sensors and Actuators a-Physical*, vol. 28, pp. 83-91, Jul 1991.
- [64] J. A. Harley and T. W. Kenny, "1/f noise considerations for the design and process optimization of piezoresistive cantilevers," *Journal of Microelectromechanical Systems*, vol. 9, pp. 226-235, Jun 2000.
- [65] J. C. Doll, "Advances in High Bandwidth Nanomechanical Force Sensors with Integrated Actuation," Doctor of Philosophy, Department of Mechanical Engineering, University of Stanford, California, 2012.
- [66] J. R. Mallon, A. J. Rastegar, A. A. Barlian, M. T. Meyer, T. H. Fung, and B. L. Pruitt, "Low 1/f noise, full bridge, microcantilever with longitudinal and transverse piezoresistors," *Applied Physics Letters*, vol. 92, Jan 21 2008.
- [67] F. N. Hooge, T. G. M. Kleinpenning, and L. K. J. Vandamme, "Experimental Studies on 1-F Noise," *Reports on Progress in Physics*, vol. 44, pp. 479-532, 1981.
- [68] F. P.J, "Polysilicon: a versatile material for microsystems," *Sensors and Actuators A: Physical*, vol. 99, pp. 3-12, 2002.
- [69] P. J. French and A. G. R. Evans, "Piezoresistance in polysilicon," *Electronics Letters*, vol. 20, p. 999, 1984.
- [70] P. J. French and A. G. R. Evans, "Piezoresistance in polysilicon and its applications to strain gauges," *Solid-State Electronics*, vol. 32, pp. 1-10, 1989.
- [71] P. J. a. E. French, A G R, "Polycrystalline silicon as a strain gauge material," vol. 19, pp. 1055-1058, 1986.

- [72] P. J. French and A. G. R. Evans, "Polycrystalline silicon strain sensors," *Sensors and Actuators*, vol. 8, pp. 219-225, 1985.

## Chapter 3

### Design, Simulation and Optimisation

In this chapter a self-sensing QC MEMS F-D sensor for measuring the mechanical properties of biopolymers is developed. Initially the focus is on the mechanical spring structure which gives the device a low in-plane and high out-of-plane compliance with a large and linear deflection range. Analytical equations are derived for the out-of-plane spring constant, first mode resonant frequency, and the F-D linearity. In the subsequent section the self-sensing properties of the device are developed and optimised. Numerical analysis is then used to verify the derived analytical equations, investigate the self-sensing readout versus the angle of actuation and determine the total deflection before fracture. The chapter ends with the characterisation of a large scale proof of concept self-sensing QC sensor prototype.

#### 3.1 Mechanical Design

The spring in accelerometers [1], gyroscopes [2], optical mirrors [3], and biosensors [4] is a critical component that affects the overall accuracy, output linearity, and operation range of such MEMS devices. The basic spring types used in MEMS (Figure 3-1) are the cantilever, double clamped beam, hammock, crab-leg, and the folded spring [5]. However, in circumstances where a large linear and travel range is required a meander spring [6] is typically used, and a lateral suspension [1] is used when the in-plane compliance also needs to be much greater than the out-of-plane compliance. For applications that require the out-of-plane compliance to be much

greater than the in-plane compliance, the spring-supported diaphragm [7] would be a suitable choice for small deflections; however, there is still little work done on a flexure type spring that can in addition also give a high linear and large deflection range in the out-of-plane direction.

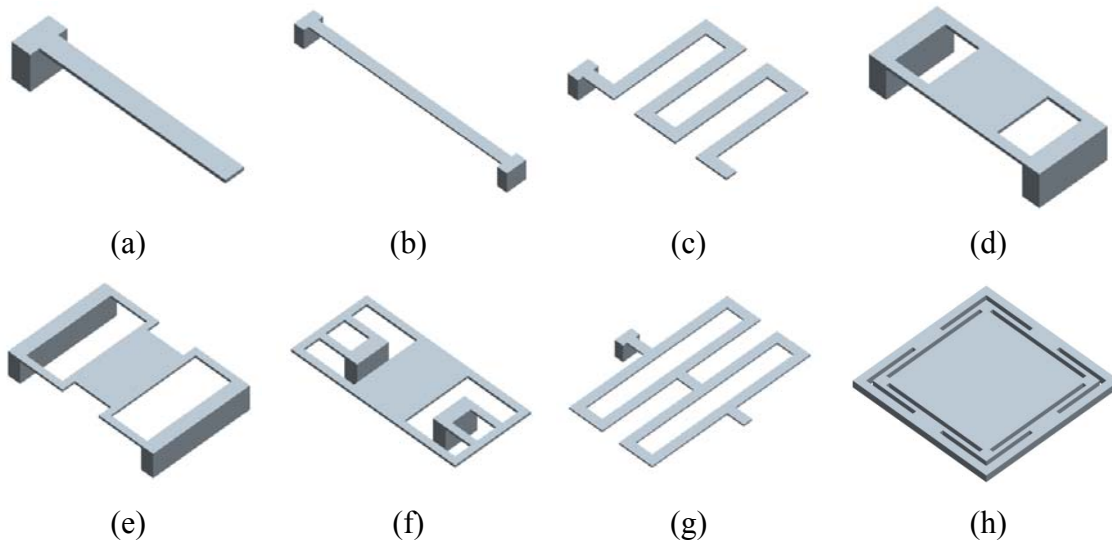


Figure 3-1: MEMS spring types (a) Cantilever, (b) Double Clamped Beams, (c) Meander [6], (d) Hammock [5], (e) Crab-leg [5], (f) Folded [5], (g) Lateral Suspension [1], and (h) Spring-Supported Diaphragm [7].

The following section outlines the design rationale of the QC spring. This will be followed by the analytical determination of the out-of-plane spring constants, the first-mode resonant frequency and the F-D linearity.

### 3.1.1 Design Rationale

The design of the QC spring is based on three approaches. The first is that using a number of beams in series increases the linear and deflection range. This is demonstrated in the design of the lateral suspension [1].

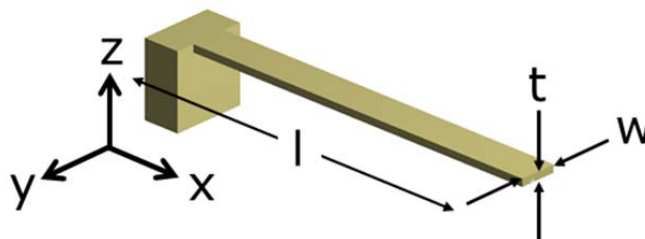


Figure 3-2: Geometric parameters of a cantilever.

The second approach is that the compliance of a cantilever beam in bending with a thickness significantly less than its width will be greatest when a force applied to its

end is applied perpendicular across its width. This can be demonstrated analytically using the cantilever shown in Figure 3-2 for which the spring constant,  $k_z$  is determined using [8]:

$$k_z = \frac{F_z}{\delta_z} = \frac{Ewt^3}{4l^3} \quad \text{Eq. 3-1}$$

where  $w$ ,  $t$ ,  $l$ ,  $F_z$ ,  $\delta_z$ , and  $E$  are the width, thickness, length, force applied in the z-direction, deflection and elastic modulus of the beam respectively. Similarly the spring constant,  $k_y$ , is given by [8]:

$$k_y = \frac{F_y}{\delta_y} = \frac{Et w^3}{4l^3} \quad \text{Eq. 3-2}$$

where  $F_y$  is the force applied in the y-direction, and  $\delta_y$  is the deflection of the beam respectively. Comparing the equations for  $k_z$  and  $k_y$  gives:

$$k_y = k_z \frac{w^2}{t^2} \quad \text{Eq. 3-3}$$

This shows that provided  $w$  is greater than  $t$ ,  $k_y$  will be greater than  $k_z$ .

The third approach is that the compliance of a beam in tension or compression is significantly less than that of a beam in bending. This can be shown analytically by putting the beam into tension or compression (depending on the orientation of the force) by applying a force in the x-direction,  $F_x$ . In this case the spring constant,  $k_x$ , is determined using [8]:

$$k_x = \frac{F_x}{\delta_x} = \frac{Ewt}{l} \quad \text{Eq. 3-4}$$

where  $\delta_x$  is the deflection in the x direction. Comparing the equations for  $k_z$  and  $k_x$  gives:

$$k_x = k_z \frac{4l^2}{t^2} \quad \text{Eq. 3-5}$$

This proves that  $k_x$  will always be greater than  $k_z$  in such an application. Thus, the out-of-plane compliance is greater than the in-plane compliance.

Using these equations as a guide the QC spring shown in Figure 3-3 was developed. In the QC spring a platform is suspended with beams oriented such that a

relatively high compliance, high linear range, and high deflection range is achieved in the  $z$  out-of-plane direction. The deflection of the platform is restricted in the  $x/y$  in-plane direction by having interconnected beams on each of the four sides of the platform.

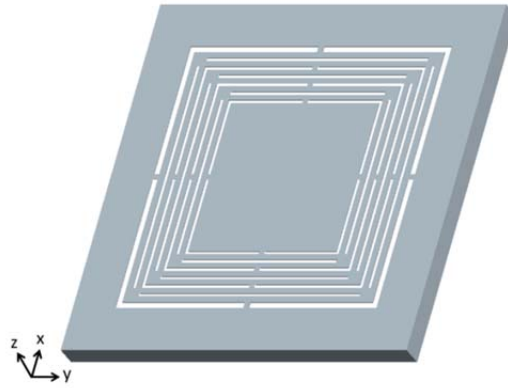


**Figure 3-3: A model of the Quasi-Concertina (QC) Spring developed in this work.**

For clarification, Figure 3-4.a shows the QC spring with a force,  $F_x$ , applied in an in-plane direction. The spring can be simplified by concentrating on one set of beams restrained as shown in Figure 3-4.b. This can be simplified further by replacing the beams with springs as shown in Figure 3-4.c. Thus the beams in the device go into bending (B), tension (T), or compression (C) when an in-plane load is applied. As discussed earlier, the beams in bending will have a minor effect on the in-plane compliance.

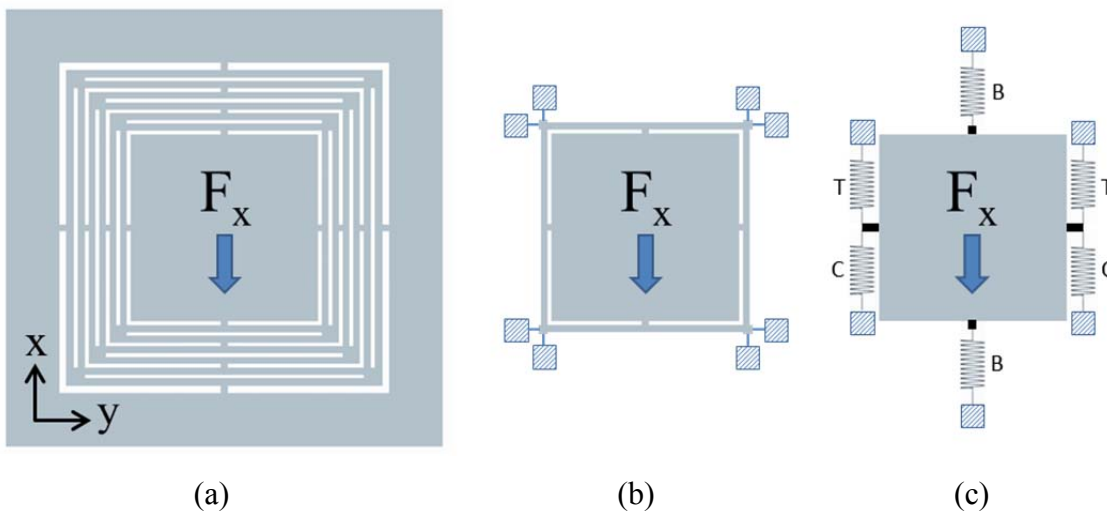


**Figure 3-4: (a) Top view of a QC spring with an in-plane force ( $F_x$ ) applied to the suspended platform, (b) the spring is simplified by taking only one set of beams into consideration, and (c) the deflection of the suspended platform is restrained by beams that bend (B) which have high compliance, and beams that go into tension (T) and compression (C) which have a low compliance.**

However, the beams in tension and compression will substantially decrease the in-plane compliance of the spring. In contrast, Figure 3-5.a shows the QC spring with a force,  $F_z$ , applied in an out-of-plane direction. In this case the beams will bend, thus the spring will have a higher compliance in the out-of-plane direction than in the in-plane direction.

### 3.1.2 Out-of-plane Spring Constant

To analytically determine the total spring constant for the device in the z out-of-plane direction, the suspended platform of the QC spring shown in Figure 3-5.a is displaced by an applied force,  $F_z$ , in the z-direction.

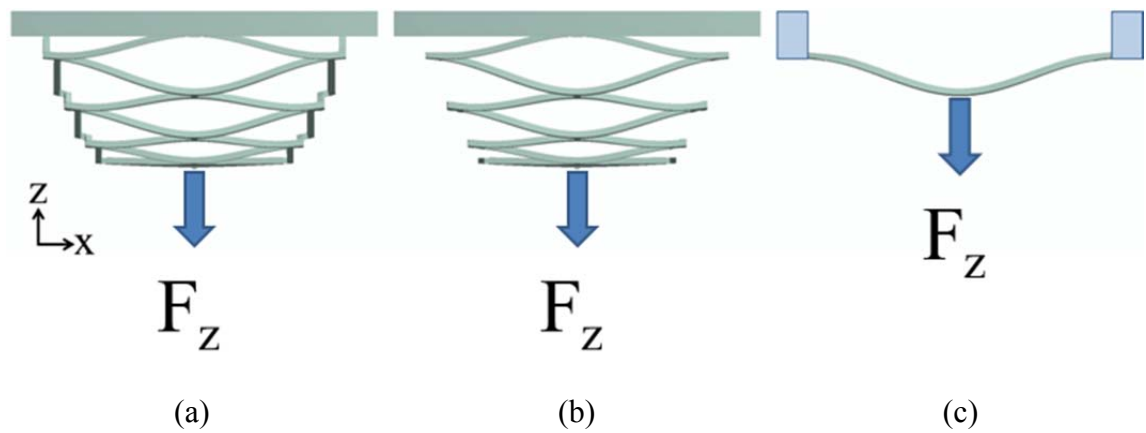


Figure 3-5:(a) QC spring with a force,  $F_z$ , applied to the platform, (b) the spring is simplified by ignoring the beam sets on three of the four sides leaving the set shown and an applied load of,  $F_z/4$  and (c) the beam is simplified further by focusing on just one beam.

In Figure 3-5.b the spring is simplified by ignoring the beam sets on three of the four sides. Since only one of the four spring sets in parallel now remains, a quarter of the originally applied load is required to achieve the same deflection, thus the applied load becomes  $F_z / 4$ . Further simplification is made by considering each beam in the set equivalent to a double clamped beam (Figure 3-5.c). Using Bernoulli-Euler beam theory the equation for the spring constant for the beam,  $k_{z,beam}$ , was derived as [8]:

$$k_{z,beam} = \frac{16Ewt^3}{l^3} \quad \text{Eq. 3-6}$$

where  $w$  is the width,  $t$  is the thickness, and  $l$  is the length of the beam. By calculating the spring constant for each beam in series, the equivalent spring constant for the set was determined using [9]:

$$1/k_{z,series} = 1/k_{z,beam 1} + 1/k_{z,beam 2} \dots \quad \text{Eq. 3-7}$$

and by multiplying by 4, for the 3 spring sets in parallel ignored earlier, the total spring constant of the flexure is obtained.

### 3.1.3 First-mode resonant frequency

A simple analytical method to estimate the first-mode resonant frequency,  $f_0$ , of the QC spring is possible by ignoring the mass of the springs and taking into consideration only the mass of the suspended platform,  $m_{sp}$ . Figure 3-6 shows the simplified representation of the QC spring.

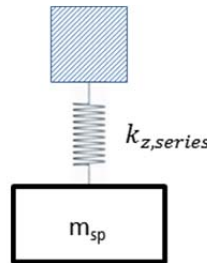


**Figure 3-6: A simplified representation of the QC spring with the mass of the springs ignored and only the mass of the suspended platform taken into consideration. This facilitates the analytical calculation of the first-mode resonant frequency of the spring.**

The  $f_0$  is then calculated using [10]:

$$f_0 = \frac{1}{2\pi} \sqrt{\frac{k_{z,series}}{m_{sp}}} \quad \text{Eq. 3-8}$$

Since the mass of the springs in the QC spring are a considerable part of the overall mass of the device, not taking the beams into consideration will result in an over estimation of the  $f_0$ . An increase in accuracy is possible by including the mass of the springs using the method developed by Galloni et al. [10] in which  $f_0$  is calculated using:

$$f_0 = \frac{1}{2\pi} \sqrt{\frac{k_{z,series}}{m_{eq}}} \quad \text{Eq. 3-9}$$

where  $m_{eq}$  is the equivalent mass of the suspended platform and beams, and is calculated using [10]:

$$m_{eq} = m_{sp} + m/D \quad \text{Eq. 3-10}$$

where  $m$  is the mass of the springs, and  $D$  is a theoretically derived coefficient [10] found in Table 3-1.

Table 3-1: Values for the coefficient  $D$  [10].

$m/m_{sp}$	$D$
0	3.00
0.2	2.96
0.5	2.92
1.0	2.85
2.0	2.76
5.0	2.64
$\infty$	2.467

An alternative numerical approach to calculate  $f_0$  is possible by considering each beam set as a discrete mass connected to massless springs as shown in Figure 3-7.a. Figure 3-7.b shows the free body diagram (FBD) for the suspended platform and beams. Using FBDs for each mass and Newton's second law, the equations of motion for each discrete mass can be determined. These are then used to form an equation of motion matrix for the device with the form:

$$M_{mass} \frac{d^2 Z}{dt^2} + KZ = 0 \quad \text{Eq. 3-11}$$

where  $M_{mass}$  is the mass matrix,  $K$  is the stiffness matrix for the complete system, and  $Z$  is the displacement matrix of the mass. By considering that the solution has oscillatory characteristics of the form  $Z\omega \sin\omega t$  the above equation can be rewritten as:

$$-M_{mass} Z \omega^2 \sin\omega t + KZ \sin\omega t = 0 \quad \text{Eq. 3-12}$$

and simplified to:

$$KZ = \omega^2 M_{mass} Z \quad \text{Eq. 3-13}$$

where  $\omega$  is the angular frequency, and:

$$Ku = \lambda M_{mass} u \quad \text{Eq. 3-14}$$

where  $u$  is a vector and  $\lambda$  is a scalar that satisfy the matrix equation and are called the 'generalised eigenvectors' and 'generalised eigenvalues' of the equation respectively.

Solutions for the generalised eigenvectors and eigenvalues of the equation are found numerically using MATLAB (code in Appendix 1) and  $f_0$  is calculated using [11]:

$$f_0 = \frac{\sqrt{\lambda}}{2\pi} \quad \text{Eq. 3-15}$$

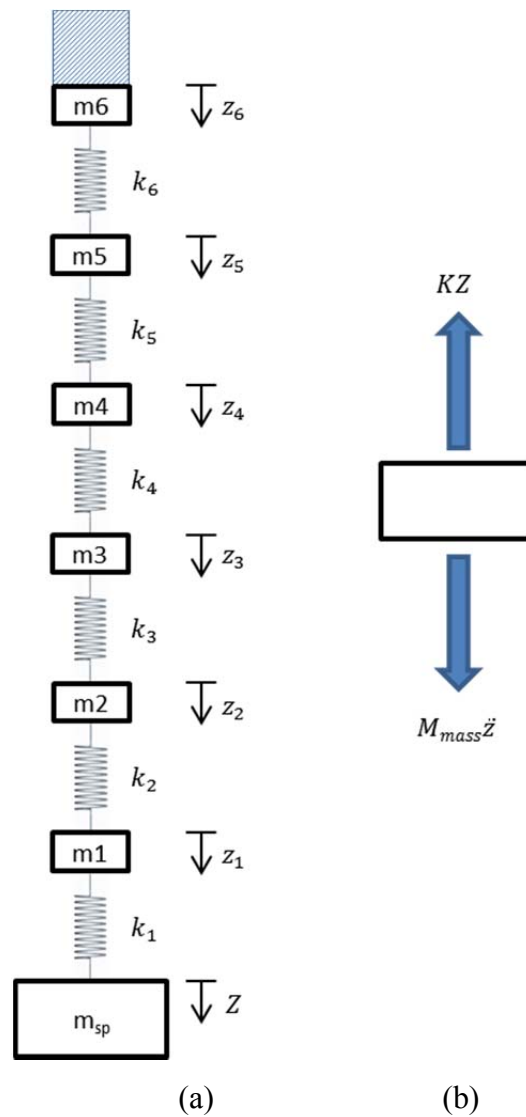
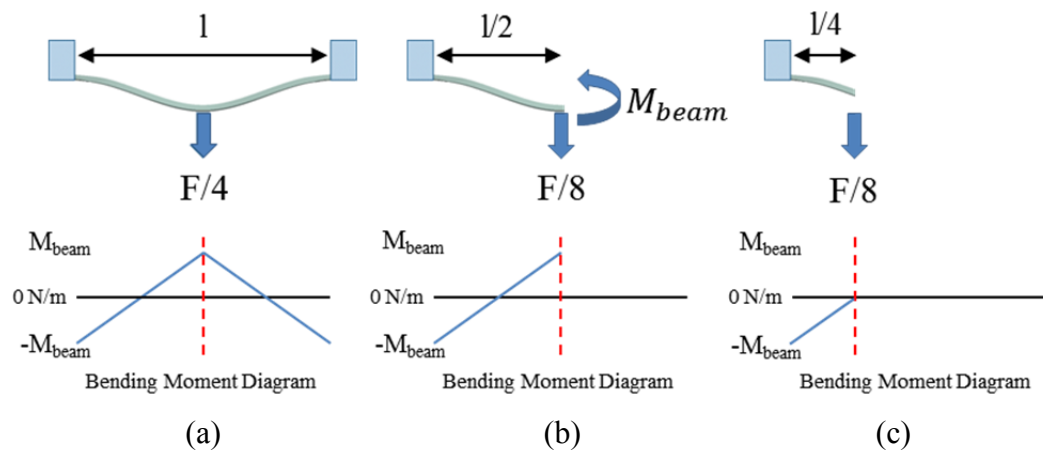


Figure 3-7: (a) A simplified representation of a QC spring with 6 beam sets. Each beam set is replaced by massless spring and a discrete mass, and (b) a FBD showing the resultant forces acting on the suspended platform.

### 3.1.4 Linearity

The linear characteristics of the device are determined by deconstructing the beam discussed in Figure 3-5.c. The beam is shown again in Figure 3-8.a with the addition of the bending moment diagram. The bending moment diagram indicates that the beam can

be simplified further by replacing the right hand side of the beam with a moment,  $M_{beam}$ , and force,  $F/8$ , as shown in Figure 3-8.b.



**Figure 3-8:** To investigate the linearity of the spring versus the deflection further simplification is necessary. (a) Simplified beam, (b) through symmetry the right hand side of the device is ignored leaving a cantilever with a load of  $F/8$  and a moment  $M_{beam}$ , (c) additional simplification is possible by considering only half the remaining beam which leaves a cantilever of length  $l/4$  and a load of  $F/8$ .

The bending moment diagram also indicates that further simplification is possible by focusing on the beam where the moment is equal to zero. This occurs at  $l/4$  (Figure 3-8.c). This leaves a cantilever with a load  $F/8$  applied to its end.

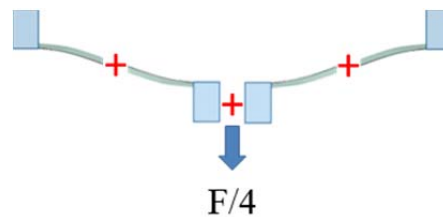


**Figure 3-9:** The double clamped beam can be simplified to two beams in series of length  $l/4$ , in parallel with two identical cantilevers in series

Thus a full beam can be considered equivalent to two cantilevers in series, of length  $l/4$ , in parallel with two identical cantilevers in series as shown in Figure 3-9. The force-displacement characteristics of the complete device can now be calculated using differential equations for the nonlinear behaviour of cantilevers as derived by Belendez [12]. The equations were solved numerically using MATLAB (code in Appendix 1).

## 3.2 Electrical Design

To sense the deflection of the suspended platform a piezoresistive transduction mechanism was integrated into the sensor. Piezoresistive sensing typically uses a

quarter, half, or full Wheatstone bridge circuit. These have one, two, or four active piezoresistors respectively with the balance being made up of passive resistors (Figure 3-10). The full bridge is generally the preferred configuration as it has 4, and 2 times more sensitivity versus the quarter and half bridge respectively. In the full bridge configuration, the change in resistance in piezoresistors R1 and R3 must be countered by an opposite change in resistance on the remaining piezoresistors (R2 and R4) as indicated by the arrows in Figure 3-10.c.

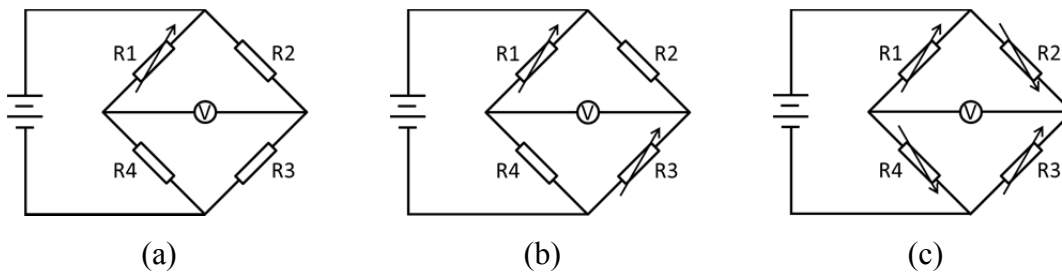


Figure 3-10: (a) Quarter, (b) half, and (c) full Wheatstone bridge configurations.

A typical configuration used in MEMS to accomplish this takes advantage of the almost equal but opposite polarity of the piezoresistive coefficients of p-type crystalline Si for longitudinal and transverse stress [13, 14]. The drawback of this configuration is that the magnitude of the change in resistance in the transverse piezoresistor is highly dependent on the accurate positioning of the piezoresistor relative to the device which makes photolithographic alignment critical to the performance of the device [13]. Moreover, if this approach was used in this application, the increase in the width of the beams required to accommodate the transverse piezoresistors would result in a larger device.

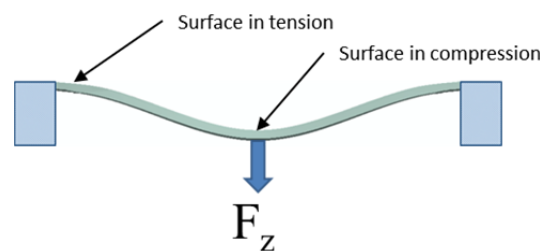


Figure 3-11: Areas in compression and in tension of a double clamped beam with a central load.

In this work an alternative approach is taken by strategically positioning the piezoresistors on the beams in areas that are in compression or in tension as shown in Figure 3-11. With this arrangement piezoresistors in tension will have an equal and opposite change in resistance as the piezoresistors in compression. One of the difficulties with full Wheatstone bridge circuits is balancing the bridge. In this

application a bridge is balanced, or nulled, when the voltage output is 0 V when there is no load applied to the sensor and this occurs when [13]:

$$\frac{V_{Output}}{V_{Bridge}} = \frac{R_1 R_3 - R_2 R_4}{(R_1 + R_2)(R_3 + R_4)} = 0 \quad \text{Eq. 3-16}$$

This requirement was met by using identical piezoresistors (in geometry and resistance) for each leg of the Wheatstone bridge. To ensure that the piezoresistors remain identical following fabrication, each of the four piezoresistors have been divided into two equal piezoresistors in series and positioned over two beams orthogonal to one another as shown in Figure 3-12. This has no net effect on the circuit; however, any photolithography misalignment (lateral or rotational) affects each of the piezoresistors equally thus the bridge would continue to remain balanced.

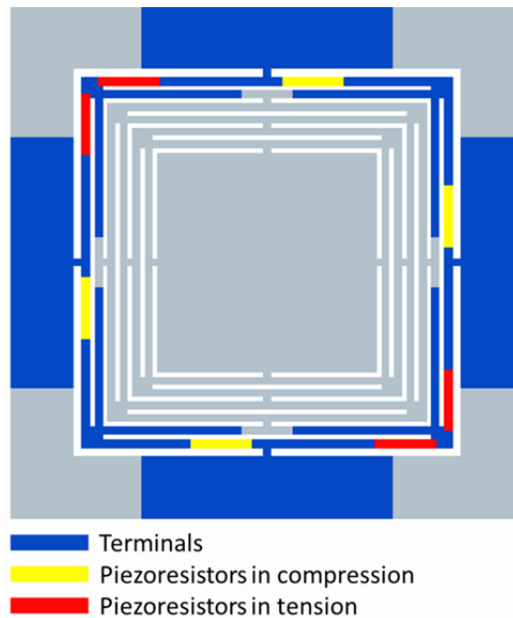


**Figure 3-12: Top view of a QC sensor with piezoresistors for self-sensing. The beams are in compression and in tension in the areas indicated only when a load is applied directly into the page. The piezoresistors are positioned in areas that are in compression and in tension to fulfil the requirements of a full Wheatstone bridge. The piezoresistors in each leg are divided into two equal parts and positioned over two beams orthogonal to one another. This feature allows any photolithographic misalignment to effect each piezoresistors leg equally, thus the bridge remains balanced.**

### 3.3 Optimisation

In the following section the performance of the QC MEMS sensor is enhanced through optimisation.

### 3.3.1 Optimisation Algorithm

With the mechanical and electrical characteristics quantified, the performance of the device can now be optimised for a high force resolution versus a low piezoresistor power. It is essential to limit the power as this will dissipate as heat and will thus increase the temperature of the device which reduces the piezoresistive coefficient, increases the noise, and limits the use of the device in applications involving temperature sensitive materials such as biopolymers.

The optimisation process involves selecting the values from a parameter set to achieve the best force resolution versus the power. The parameter set consist of physical, manufacturing and design constraints that are related to the performance of the sensor. The parameter set was based on the following considerations:

- Piezoresistor maximum length must be less than 25% of the length of the outermost beam. This is necessary since the change in resistance in a piezoresistor larger than this will diminish as the stress in the beam changes in polarity (tension to compression or the reverse). For example, a piezoresistor that is 50% the length of the beam will have equal areas in tension as in compression thus the change in resistance will become nulled.
- Piezoresistor thickness must be less than 0.6  $\mu\text{m}$ . This thickness was selected as a practical polysilicon deposition thickness limit.
- A p-type doping concentration range of  $1 \times 10^{17} \text{ cm}^{-3}$  and  $1 \times 10^{20} \text{ cm}^{-3}$ . The largest piezoresistive coefficient is observed within this range. P-type doping was selected as it has a larger gauge factor in polysilicon than n-type doping [15].
- Beam and beam separation widths must be greater than 10  $\mu\text{m}$  to permit the use of conventional photolithography microfabrication techniques with an alignment tolerance of  $\pm 1 \mu\text{m}$ .
- Device structure thickness of 4.5  $\mu\text{m}$  due to the availability of SOI wafers with the device layer of this thickness.
- The minimum and maximum suspended platform width/length,  $l_{sp}$ , was selected to be 500-1500  $\mu\text{m}$ . This would permit the installation of a probe for device characterisation and biopolymer measurements.
- Spring constants of 4.5 N/m and 0.18 N/m based on the sensing applications.
- Quasi-static frequency range (1-10 Hz).

- Crystalline silicon or polysilicon piezoresistors. Due to the unavailability of equipment for epitaxial deposition, diffusion or ion implantation necessary for single crystal silicon piezoresistors, HWCVD polysilicon piezoresistors will be used in the fabricated devices. However, the potential theoretical performance of self-sensing QC sensors using crystalline silicon piezoresistors will still be evaluated.
- Maximum power per piezoresistor is limited to less than 1 mW. This will reduce the potential damage to the piezoresistor, and decrease the rise in temperature which would otherwise limit the use of the device in temperature sensitive applications such as biopolymers.

Table 3-2 shows the design correlation matrix of a typical piezoresistor used in a self-sensing cantilever application [16]. The matrix shows the interdependence of the various parameters. The interdependence of the parameters shown in the matrix are also valid for the QC sensor developed in this work and were thus used for the optimisation of the device.

**Table 3-2: Design correlation matrix for a self-sensing cantilever. The matrix shows the effect of an increase in a parameter, relative to the other parameters, on the performance of the sensor with (↑), (↓) and (–) indicating an increase, decrease and no substantial effect respectively. Adapted from [16].**

	$S_D$ (V/m)	$S_F$ (V/N)	$V_H$ (V/√Hz)	$V_J$ (V/√Hz)	$W$ (W)	$f_o$ (Hz)	$k$ N/m
$l$ (m)	↓	↑	–	–	–	↓	↓
$w$ (m)	–	↓	–	–	–	–	↑
$t$ (m)	↑	↑	–	–	–	↑	↑
$l_{pr}$ (m)	↑	↑	↓	↑	↓	–	–
$w_{pr}$ (m)	–	–	↓	↓	↑	–	↑
$t_{pr}$ (m)	↑	↑	↑	–	↑	–	–
$n$ (cm <sup>-3</sup> )	↓	↓	↓	↓	↑	–	–
$V_{Bridge}$ (V)	↑	↑	↑	–	↑	–	–

In previous work analytical [16-19] and numerical [16, 20-23] methods have been used to optimise piezoresistive devices. In the analytical method functions are derived

for the desired qualities of the sensor using the parameter set. Next, using these functions the gradient versus the parameter set is calculated which, depending on the size of the parameter set, can become cumbersome [16].

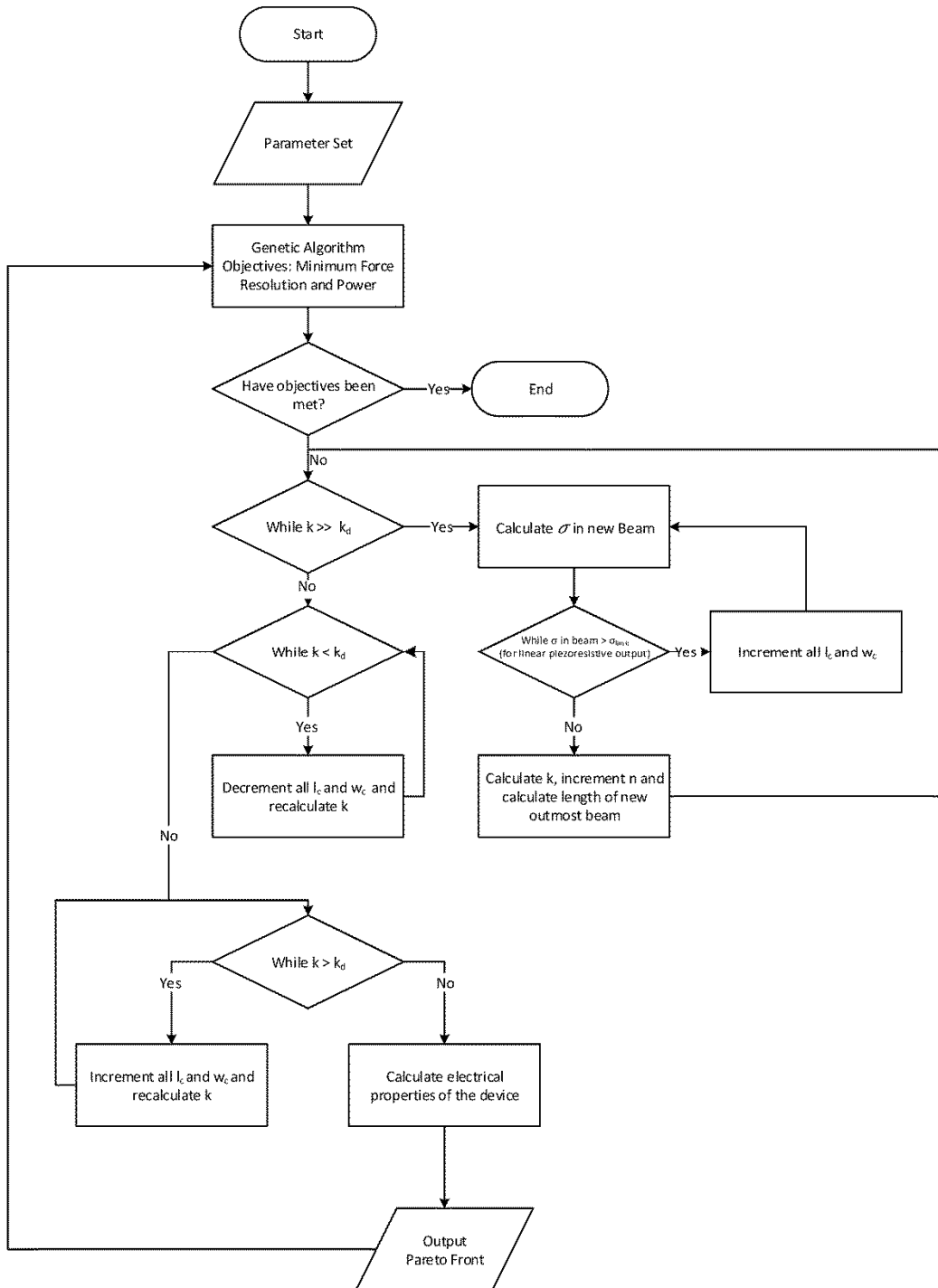


Figure 3-13: Flow chart showing the process used to optimise the QC MEMS sensor.

In the alternative approach the relationship between the optimisation requirements, the objective, and the parameter set are established automatically numerically. In this work a numerical method called the Genetic Algorithm (GA) has been used for the optimisation of the QC MEMS sensor.

The GA mimics the natural evolutionary process by evolving the solutions to a function for a given range of constraints (parameter set) towards better solutions. It does this by randomly selecting an initial population from a parameter set. The fittest individuals, the “parents”, of this population are selected based on a fitness function and combined to produce the next generation of individuals, the “offspring”, which share attributes taken from the parents. To ensure mutation, which will permit a diverse search of the gene space as occurs in nature, a small population of the least fit individuals are also added to the new offspring. This process continues over the whole population over a large number of iterations giving a final population with a high fitness score and which will converge to an optimal solution [24, 25].

Figure 3-13 shows the flow chart for the process developed to optimise the QC MEMS sensor. The process was automated using MATLAB. The objective of the process is to find the parameter sets that give the highest force resolution,  $F_{\min}$ , for the least power dissipated.

The process begins with the GA selecting the initial population from the provided parameter set. Next, the number of beam sets of the device is calculated. This is accomplished through a program loop which adds a new set of beams until the calculated spring constant is within a rough tolerance. A second embedded program loop increases the width of each subsequent beam set to ensure that the maximum stress in the beams is less than the stress requirement for a 99% linear piezoresistive readout for the selected displacement range [26-28]. The spring constant is then refined through an incremental change in the width of each beam until a tighter tolerance is achieved. Next, the electrical characteristics are calculated for the developed geometry and the current population. The GA continues to evolve the solution until a predetermined number of iterations have been computed.

Figure 3-14 shows the graphs prepared for the optimisation of QC 5 (Table 3-4) using the output from the optimisation program developed in this work (Appendix 1). The upper and lower values of the parameter set are shown in Table 3-3. The graphs

show the final converging solutions found by the GA after the stipulated number of iterations have been computed. Each data point represents a possible optimised design solution. The solution selected and recorded in Table 3-4 is marked in red on each graph.

**Table 3-3: Upper and lower values of the parameter set variables used during the GA process used to optimise the graphs in Figure 3-14 and 3-15.**

<b>Parameter</b>	<b>Lower Boundary</b>	<b>Upper Boundary</b>
$l_{pr}/l$ (%)	0	25
$t_{pr}$ (m)	$0.1 \times 10^{-6}$	$0.6 \times 10^{-6}$
$V_{Bridge}$ (V)	0.1	2
$n$ ( $cm^{-3}$ )	$1 \times 10^{17}$	$1 \times 10^{20}$
$w$ (m)	$10 \times 10^{-6}$	$20 \times 10^{-6}$
$t$ (m)	$4.5 \times 10^{-6}$ ;	$4.5 \times 10^{-6}$
$w_{sep}$ (m)	$10 \times 10^{-6}$	$20 \times 10^{-6}$
$l_{sp}$ (m)	$500 \times 10^{-6}$	$1500 \times 10^{-6}$
$k$ (N/m)	0.18	0.18
Piezoresistive material	Crystalline silicon	Crystalline silicon

The power versus force resolution graph (Figure 3-14.a) shows the primary scope of the optimisation procedure which was to find solutions that give the highest force resolution for the lowest power/heat dissipation. The solutions shown meet the less than 1 mw criteria thus are all valid for the application with  $F_{min} = 20$  pN being the most attractive for the application. The graph indicates that the force resolution increases with an increase in power. This is expected since  $V_{Bridge}$  is directly related to both the sensitivity of the device (Eq. 2-23) and the power (Eq. 2-29). This is further confirmed in the bridge voltage versus force resolution graph shown in Figure 3-14.b which shows a similar trend.

The graph in Figure 3-14.c shows the relationship between the number of beam sets and the force resolution. The trend shows that for the constraints applied, the best resolution would be achieved with fewer (15-16) beam sets. This indicates that a compromise between the best resolution, linearity and deflection would need to be taken. In Figure 3-14.d the grouping of the solutions indicates that for this application a beam width of  $\sim 15$   $\mu m$  is optimal. Similar trends are seen in Figures 3-15.a-d where 0.475  $\mu m$ , 0.13  $\mu m$ , 1150  $\mu m$ , and 19  $\mu m$  are optimal solutions for  $t_{pr}$ ,  $l_{pr}/l$ ,  $l_{sp}$ ,  $l_{sep}$  respectively.

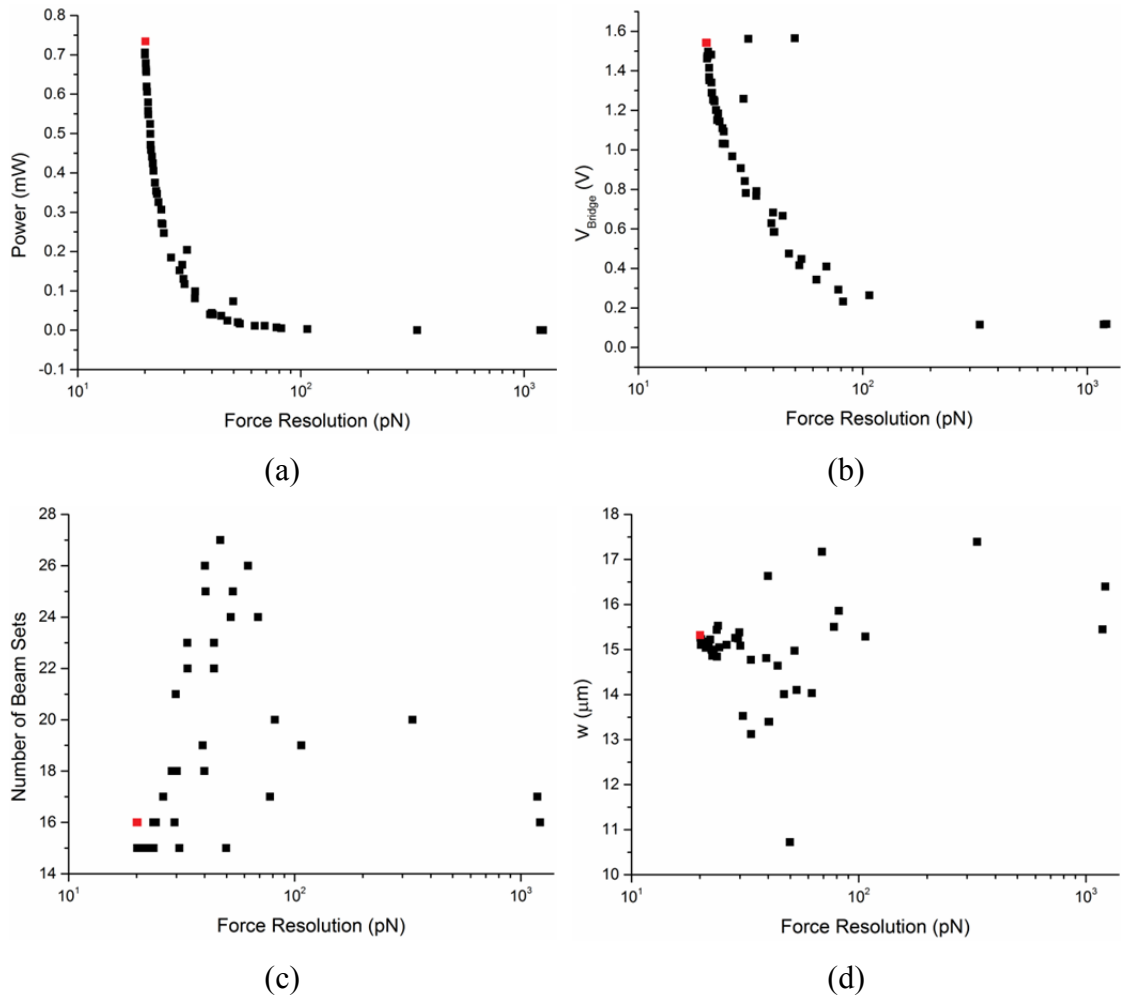


**Figure 3-14: GA output graphs for QC 5 (a) Power vs.  $F_{\text{min}}$ , (b)  $V_{\text{Bridge}}$  vs.  $F_{\text{min}}$  (c) Number of beam sets vs.  $F_{\text{min}}$ , and (d)  $w$  vs.  $F_{\text{min}}$ . Each data point represents a possible design solution. The data point in red represents the solution selected.**

Table 3-4 shows the characteristics of 7 devices optimised using the scheme outlined. QC 1 to 3 have polysilicon piezoresistors. These sensors have a force-displacement of 3803 pN/634 pm, 775 pN/4306 pm, and 858 pN/4767 pm respectively. QC 4 to 6 were optimised for crystalline silicon piezoresistors and have a force-displacement resolution of 52 pN/19 pm, 20 pN/111 pm, 19 pN/106 pm respectively. TC 1 is an optimised self-sensing cantilever with a force-displacement resolution of 802 pN/3236 pm, and was included to study the piezoresistance of the HWCVD polysilicon piezoresistors independently from the QC sensor.

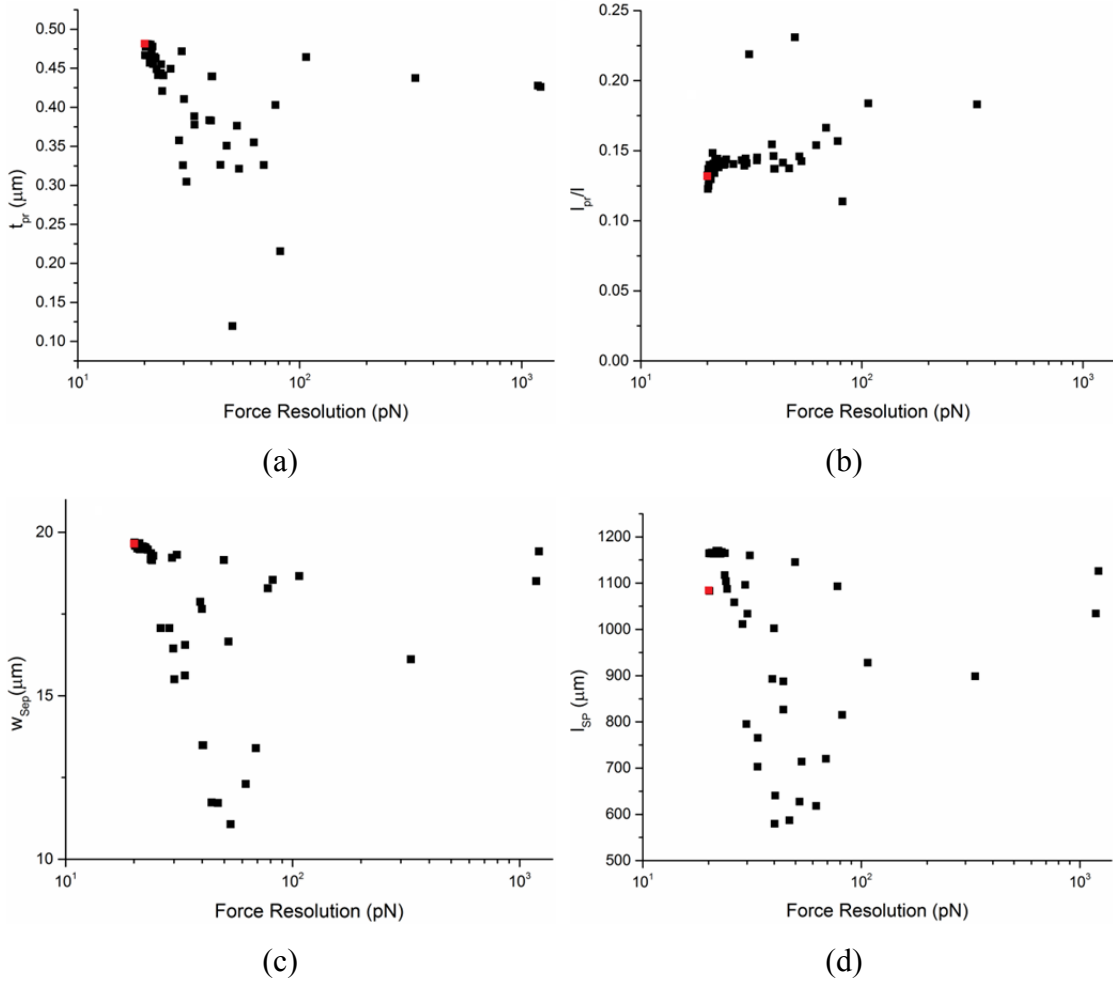


**Figure 3-15: GA output graphs for QC 5 (a)  $t_{pr}$  vs.  $F_{min}$ , (b)  $I_{pr}/l$ , vs.  $F_{min}$  (c)  $w_{sep}$  sets vs.  $F_{min}$ , and (d)  $I_{sp}$  vs.  $F_{min}$ . The data point in red represents the solution selected.**

Table 3-4: Characteristics of 6 optimised QC MEMS sensors

Property	Definition	QC 1s	QC 2s	QC 3s	QC 4s	QC 5s	QC 6s	TC 1s
<b>Silicon Type</b>	Polysilicon/Crystalline	Poly	Poly	Poly	Crystalline	Crystalline	Crystalline	Poly
<b>F<sub>min</sub> (pN)</b>	Min. force resolution	4200	775	858	52	20	19	809
<b>d<sub>min</sub> (pm)</b>	Min. displ. resolution	933	4306	4767	9	111	106	3236
<b>S<sub>F</sub> (V/N)</b>	Force sensitivity	22	348	332	960	1760	1990	25
<b>V<sub>noise</sub> (V)</b>	Total noise	5.87x10 <sup>-8</sup>	2.70x10 <sup>-7</sup>	2.85x10 <sup>-7</sup>	4.99x10 <sup>-8</sup>	3.54x10 <sup>-8</sup>	3.84x10 <sup>-8</sup>	2.03x10 <sup>-8</sup>
<b>V<sub>H</sub> (V)</b>	Hooqe noise	5.55x10 <sup>-8</sup>	2.68x10 <sup>-7</sup>	2.83x10 <sup>-7</sup>	4.72x10 <sup>-8</sup>	3.08x10 <sup>-8</sup>	3.42x10 <sup>-8</sup>	1.00x10 <sup>-8</sup>
<b>V<sub>J</sub> (V)</b>	Johnson noise	1.39x10 <sup>-8</sup>	1.51x10 <sup>-8</sup>	1.48x10 <sup>-8</sup>	9.15x10 <sup>-9</sup>	1.11x10 <sup>-8</sup>	1.11x10 <sup>-8</sup>	1.19x10 <sup>-8</sup>
<b>k<sub>d</sub> (N/m)</b>	Spring constant	4.50	0.18	0.18	6.00	0.18	0.18	0.25
<b>V<sub>Bridge</sub> (V)</b>	Bridge voltage bias	0.39	1.00	1.00	1.49	1.54	1.81	0.39
<b>R (kΩ)/piezo</b>	Resistance	0.924	1.550	1.480	0.563	0.834	0.830	0.920
<b>W (mW)</b>	Power/piezoresistor	0.12	0.13	0.17	0.99	0.71	0.99	0.04
<b>No. Beam Sets</b>	No. of beam sets	6	17	27	2	16	18	N/A
<b>t (μm)</b>	Thickness of beam	4.5	4.5	4.5	4.5	4.5	4.5	4.5
<b>t<sub>pr</sub> (μm)</b>	Thickness of piezoresistor	0.58	0.50	0.50	0.56	0.48	0.50	0.58
<b>I<sub>pr</sub>/I<sub>Beam</sub></b>	Length of piezo/length beam	0.13	0.13	0.13	0.15	0.13	0.14	0.41
<b>n (cm<sup>-3</sup>)</b>	Doping concentration	4.5x10 <sup>19</sup>	6.0x10 <sup>19</sup>	6.0x10 <sup>19</sup>	5.0x10 <sup>19</sup>	5.4x10 <sup>19</sup>	5.6x10 <sup>19</sup>	4.5x10 <sup>19</sup>

### 3.3.2 Piezoresistor Positioning

In the optimisation process the change in resistance versus the applied force calculations are based on a piezoresistor with one end constrained at the centre of the beam as shown in Figure 3-16. The magnitudes of the change in resistance of the remaining piezoresistors are assumed to be identical. Thus, while the position of the central piezoresistors, which are considered here as being in compression, has been established, the position of the piezoresistors in tension still needs to be determined.

The main objective in positioning the piezoresistors in tension is to ensure that they have an equal and opposite change in resistance as the piezoresistors in compression when the suspended platform is deflected. Thus the change in magnitude of  $R_1$  and  $R_3$  in equation 2-12 versus the displacement is equal to the change in magnitude of  $R_2$  and  $R_4$  which results in a linear relationship between  $V_{Output}$  and the deflection. To accomplish this, a parametric numerical analysis was prepared using commercial software (Coventorware). In the analysis, the change in resistance is calculated numerically for the piezoresistor when positioned at different locations along a deflected beam (Figure 3-16). Initially the change in resistance is calculated for when the piezoresistor has one end at the centre of the beam. This corresponds to a displacement of 0  $\mu\text{m}$  from the centre of the beam (Figure 3-17) and the piezoresistor is in compression. Next, the piezoresistor is continuously offset by 10  $\mu\text{m}$ , until it is no longer on the beam ( $\sim 900 \mu\text{m}$  in Figure 3-17), and the change in resistance for each incremented position is calculated. Representative results for such a study are shown in Figure 3-17. The graph indicates that the change in resistance increases linearly, as it goes from being in compression to being in tension, until one end of the piezoresistor reaches the end of the beam ( $\sim 600 \mu\text{m}$ ). At this point the change in resistance decreases until there is no change in resistance. This is expected as the piezoresistor would not be in contact with the beam at this position.

Using the graph on Figure 3-17 the ideal location of the piezoresistor in tension is determined by selecting an offset from the centre that gives a change in resistance that is equal and opposite to the change in resistance of the piezoresistor in compression. For example, in Figure 3-17, when the piezoresistors is at 0  $\mu\text{m}$  it is in compression and has a change in resistance of  $-4.5 \times 10^{-5}\%$ . Thus the piezoresistor in tension needs to be

positioned 600  $\mu\text{m}$  away from the centre to have an equal and opposite change in resistance (i.e.  $+4.5 \times 10^{-5}\%$ ).

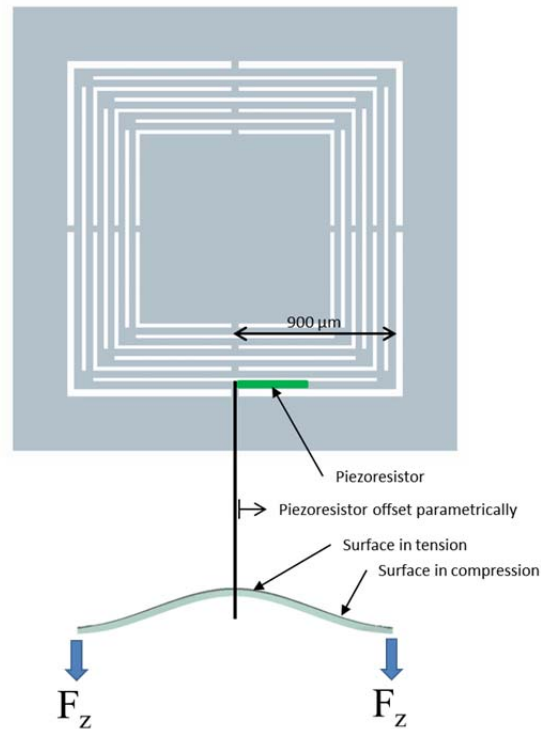


Figure 3-16: QC sensor top view and cross-sectional view showing the piezoresistor offset direction. Using a parametric numerical analysis the piezoresistor is incrementally offset along the beam. The percentage change in resistance is calculated at each offset.

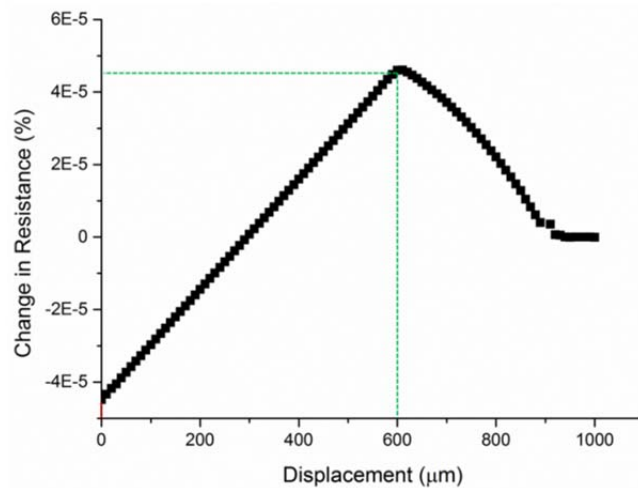


Figure 3-17: Piezoresistive percentage change in resistance versus the piezoresistor offset from the centre of the beam (from compression to tension). To ensure a linear relationship between  $V_{Output}$  and the displacement, the percentage change in resistance needs to be equal and opposite between the piezoresistors in tension and in compression. The graph can be used to determine the position of the piezoresistors. For example if the piezoresistors in compression is positioned at 0  $\mu\text{m}$ , i.e. has a change in resistance of  $-4.5 \times 10^{-5}\%$ , the piezoresistor in tension would need to be positioned at 600  $\mu\text{m}$  where the change in resistance is equal and opposite that of the piezoresistor in compression (i.e. at  $+4.5 \times 10^{-5}\%$ ).

### 3.4 Simulation

The calculations used during the optimisation of the QC MEMS are based on the analytical analysis presented earlier in the chapter. In this section the analytical calculations for the spring constant and first mode resonant frequency are validated using a numerical analysis software package (ANSYS). In addition, the total deflection before fracture and the readout accuracy versus the angle of actuation is also investigated.

#### 3.4.1 Mechanical properties

To determine the spring constant numerically, a force is applied perpendicularly to the centre of the suspended platform and the resulting deflection obtained using ANSYS is recorded. The spring constant is then calculated using Eq. 2-3. The spring constants obtained numerically and analytically are presented in Table 3-5. The spring constant calculated numerically for QC 1, 2, and 3, and TC 1 are within 2.5%, 5.6%, 5.3%, and 0 % respectively of the results obtained analytically. Since QC 4, 5, and 6 were optimised to establish the resolution of the QC sensor with crystalline piezoresistors and the equipment required to fabricate these sensors is not available, these were not included in the present study.

Table 3-5: Comparison of the spring constants obtained analytically and numerically for QC-1 to 3.

	QC 1	QC 2	QC 3	TC 1
Spring constant - Analytical	6.00 N/m	0.18 N/m	0.18 N/m	0.28 N/m
Spring constant - Numerical	5.85 N/m	0.17 N/m	0.19 N/m	0.28 N/m

The total deflection before fracture,  $d_{\max_n}$ , was determined numerically by increasing the applied load until the ultimate tensile strength of the device (Si) was reached. Due to the large beam deflections a non-linear analysis was used. Figure 3-18 shows a simulation of the deflection of QC 2 as a result of the applied load. The results in Table 3.6 indicate that a total deflection before fracture of as much as 8.3 mm is possible with QC 3.

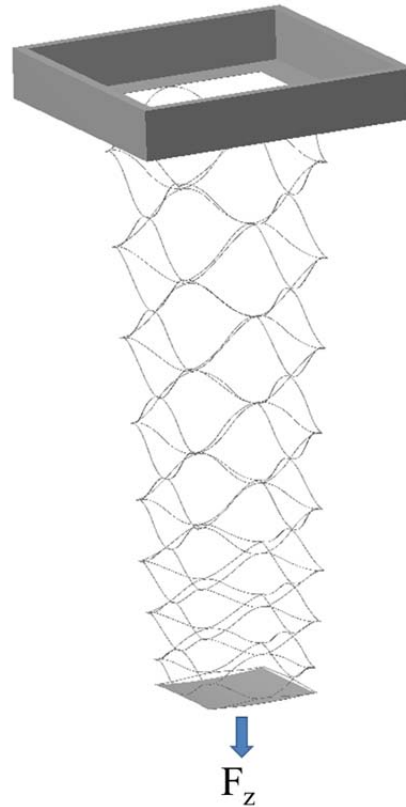


**Figure 3-18: Numerical analysis of a QC 2 spring with a load applied to the platform. The simulation shows that deflections as large as 8300  $\mu\text{m}$  are possible with a QC spring.**

**Table 3-6: Results for the total deflection before fracture determined numerically for QC 1 to 3.**

	QC 1	QC 2	QC 3
$d_{\text{max}_n}$ ( $\mu\text{m}$ )	1100	8000	8300

In addition to the analytical calculations discussed earlier, the first fundamental frequencies of the devices were also determined numerically using ANSYS. The results were found to be within 11% of the analytical and numerical methods (MATLAB) that included the mass of the beams, and within 33 % of the method which ignored the mass of the beams. The results are shown in Table 3-7.

**Table 3-7: Calculated resonance frequencies for QC 1, 2 and 3 using analytical and numerical methods.**

$f_0$	QC 1	QC 2	QC 3
Analytical (spring mass ignored)	6030 Hz	563 Hz	973 Hz
Analytical (spring mass included)	4747 Hz	475 Hz	654 Hz
Analytical/Numerical (MATLAB)	4840 Hz	480 Hz	620 Hz
Numerical (ANSYS)	4889 Hz	535 Hz	656 Hz

### 3.4.2 Sensor readout error versus angle of actuation

To investigate the QC sensor readout versus the angle of actuation, 1  $\mu\text{N}$  loads were applied to the centre of the suspended platform. The direction of the load was varied (0-45°) relative to the perpendicular for each measurement (Figure 3-19) and the resultant stress at each piezoresistor was obtained numerically using commercial software (ANSYS). Using Eq. 2-17 the  $V_{\text{Output}}/V_{\text{Bridge}}$  was calculated.

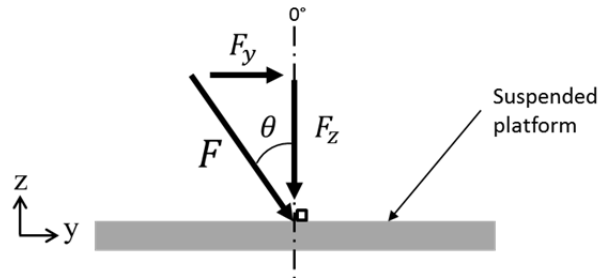


**Figure 3-19: Direction of actuation of the suspended platform for the QC MEMS sensor readout versus the angle of actuation analysis.**

Figures 3-20.a, 3-20.c, and 3-20.e show the total applied force versus the  $V_{\text{Output}}/V_{\text{Bridge}}$  for QC 1 to 3 respectively. The results indicate that when the applied force is at 45°, the maximum measurement discrepancy is ~29% (Table 3-8). In Figures 3-20.b, 3-20.d, and 3-20.f the  $V_{\text{Output}}/V_{\text{Bridge}}$  is plotted versus the out-of-plane component ( $F_z$ ) of the applied force. Since the resulting plots have the same gradient for each angle of actuation the following can be concluded:

- The discrepancy in the measurements is a result of a decrease in the out-of-plane force (the measurand), and not a direct result of the angle of actuation
- In-plane forces do not affect the output of the device

**Table 3-8: Summary of  $V_{\text{Output}}/V_{\text{Bridge}}$  % discrepancy versus the angle application.**

Angle of Actuation	0°	15°	25°	35°	45°
QC 1	0.00%	3.37%	9.24%	17.86%	28.98%
QC 2	0.00%	3.50%	9.40%	18.09%	29.29%
QC 3	0.00%	3.43%	9.44%	18.16%	29.37%

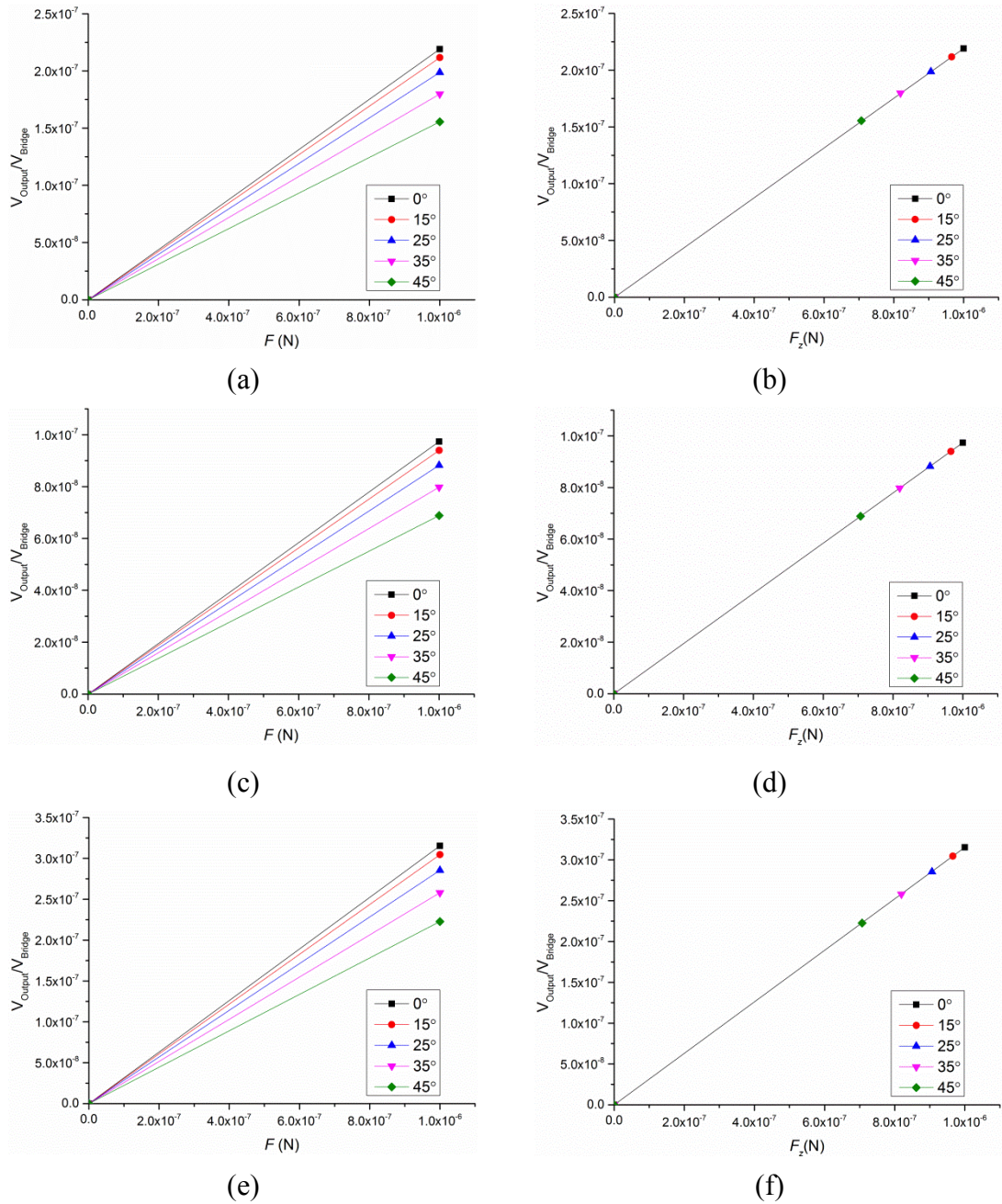


**Figure 3-20: Graphs for  $V_{\text{Output}}/V_{\text{Bridge}}$  versus an applied force with an 0-45° angle of incidence and  $V_{\text{Output}}/V_{\text{Bridge}}$  versus the out-of-plane component of an applied force with 0-45° angle of incidence for (a-b) QC 1, (c-d) QC 2, and (e-f) QC 3 respectively.**

### 3.5 Macroscale Prototype

A macroscale prototype was fabricated as a proof of concept to validate the analytical and numeric analysis used to develop the design. The prototype QC structure was fabricated using Stereolithography (SLA) rapid prototyping. In lieu of piezoresistors, strain gauges (Omega SGD-1.5/120-LY13) with a gauge factor of 2 were bonded to the beams using cyanoacrylate (Figure 3-21). Two strain gauges (R2 and R4)

were located at the centre of the outer beams and numerical analysis (ANSYS) was used to position the balance of the strain gauges (R1 and R3) as explained earlier. The resistors were wired as shown in Figure 3-10.c (full Wheatstone bridge).

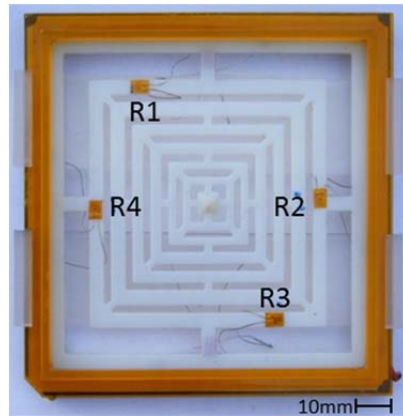


**Figure 3-21: The macroscale prototype was fabricated using Stereolithography (SLA) rapid prototyping. Strain gauges were bonded to the beams to mimic the piezoresistors.**

To characterise the prototype the Wheatstone bridge was connected to a power supply (Agilent-U8001A1), an amplifier (Maxim MAX1452), and a digital multimeter (Agilent 34410A) as shown in Figure 3-22. The device was actuated using a translation stage with Vernier head which was mounted directly above the device (Figure 3-23). The stage was lowered in increments of 0.5 mm and the output voltage was recorded using the digital multimeter (DMM).

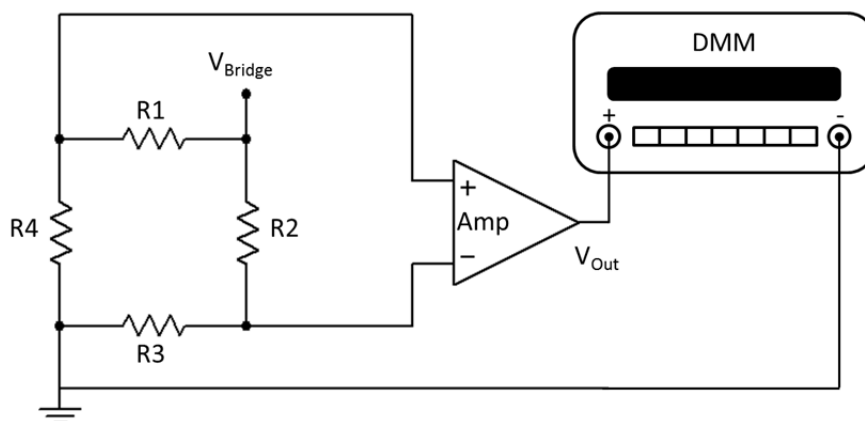


**Figure 3-22: Circuit used the test the macroscale prototype.**

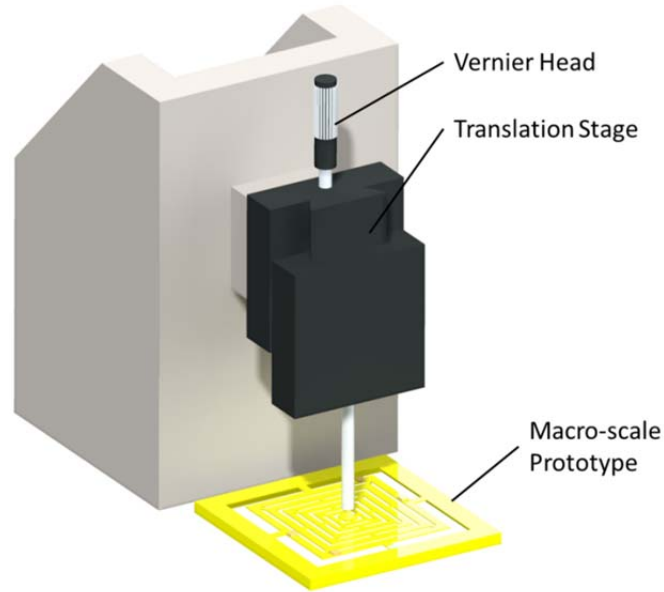


**Figure 3-23: A translation stage with Vernier head was used to actuation the macroscale prototype during characterisation.**

Using the measured output voltage, the strain in the beams was calculated for each incremental displacement by substituting Eq. 2-7 and Eq. 2-9 into Eq. 2-17 and solving for  $\varepsilon$  which gives:

$$\varepsilon = \frac{V_{output}}{GF Gain_{Amp} V_{Bridge}} \quad \text{Eq. 3-17}$$

where  $V_{output}$ ,  $GF$ ,  $Gain_{Amp}$ ,  $V_{Bridge}$  are the output voltage, gauge factor of the strain gauges, gain of the amplifier and the voltage supplied to the Wheatstone bridge respectively. Since [29]:

$$E = \frac{\sigma}{\varepsilon} \quad \text{Eq. 3-18}$$

and the beam stress is equivalent to [30] :

$$\sigma = \frac{3Fl}{4wt^2} \quad \text{Eq. 3-19}$$

Thus the total force detected by the prototype for four identical beams is:

$$\text{Total Force} = \frac{(4E\varepsilon wt^2)}{3l} \times 4 \quad \text{Eq. 3-20}$$

The resulting forces were then plotted versus the displacement and compared to the values obtained using numerical analysis (ANSYS), and the analytical calculations. Figure 3.24 shows that the linear fit of the output from the macroscale prototype is in

good agreement with the results from the numerical analysis and similar to results obtained analytically.

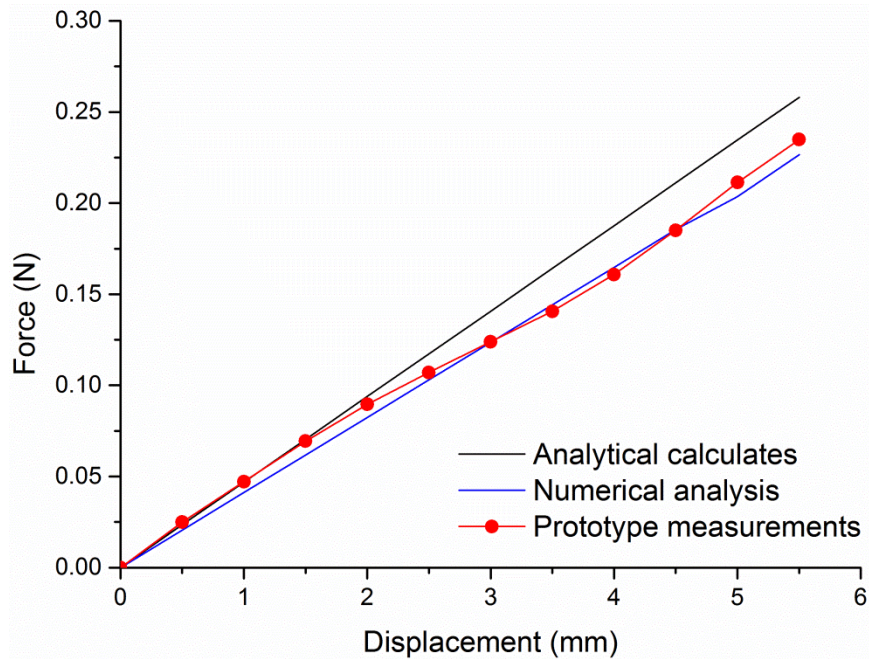


Figure 3-24: Force-displacement characteristics of the macroscale model using measurements from the prototype, analytical calculations and numerical analysis.

The closer agreement with the numerical results is reasonable since the 3D CAD model used to fabricate the structure was also used in the numerical analysis, thus every detail was included in the analysis. In contrast, details such as radii between adjacent beams were ignored in the analytical calculations.

### 3.6 Conclusions

In this chapter the development details of the QC F–D sensor are presented. The chapter begins with the design rationale behind the QC spring and followed by the derivation of the analytical equations for the spring constant, first fundamental frequency and linearity of the device. These estimates confirmed the high deflection and high linearity attributes of the QC spring.

To enable self-sensing, piezoresistors were integrated into the QC spring to form a full Wheatstone bridge circuit. The piezoresistors were strategically positioned to promote piezoresistor to QC beam alignment during fabrication. The size of the beams and the piezoresistors and the doping concentration of the piezoresistors was optimised using code developed for the application. The code implemented a GA to determine

parameter solutions for the optimal force resolution versus the power. Using this scheme a force resolution of as much as 775 pN and 19 pN was obtained for devices using polysilicon and crystalline piezoresistors respectively. This meets the nN resolution criteria stipulated for the device in Chapter 1.

A further optimisation procedure was conducted numerically to determine the location of the piezoresistors in tension versus the piezoresistors in compression. This ensures that the Wheatstone bridge gives a linear voltage output versus the displacement of the platform. Thus the sensor is designed to have a high level of both mechanical and electrical linearity.

A numerical analysis was conducted to confirm the analytical calculations. This study confirmed that the spring constant and first fundamental frequency were within 5.6% and 11% respectively of the numerical analysis. The total deflection before fracture for QC 1, QC 2, and QC 3 was estimated numerically to be 1.1 mm, 8 mm, and 8.3 mm respectively. These high levels of deflection increase the resilience of the sensor for in-vivo applications and allows for a large displacement range for passive measurement techniques.

A numerical analysis conducted to estimate the impact of a force applied at an angle relative to the suspended structure indicated that only the perpendicular force vector would be measured. The results indicate that when a force is applied at a 45° relative to the suspended structure the maximum expected error would be 30%. This feature is desirable for sensors used in-vivo applications where it would be difficult to orient the sensor relative to the tissue being measured.

Finally, a macroscale prototype fabricated using a rapid prototyped QC spring and conventional metal strain gauges was successfully tested thus further validating the concept.

## References

- [1] W. T. Pike and S. Kumar, "Improved design of micromachined lateral suspensions using intermediate frames," *Journal of Micromechanics and Microengineering*, vol. 17, pp. 1680-1694, Aug 2007.
- [2] M. Kraft, "Micromachined inertial sensors: the state-of-the-art and a look into the future.," *Measurement & Control*, vol. 33, pp. 164-168, Jul 2000.
- [3] Y. H. Bai, J. T. W. Yeow, P. Constantinou, S. Damaskinos, and B. C. Wilson, "A 2-D Micromachined SOI MEMS Mirror With Sidewall Electrodes for Biomedical Imaging," *Ieee-Asme Transactions on Mechatronics*, vol. 15, pp. 501-510, Aug 2010.
- [4] J. L. Arlett, E. B. Myers, and M. L. Roukes, "Comparative advantages of mechanical biosensors," *Nature Nanotechnology*, vol. 6, pp. 203-215, Apr 2011.
- [5] J. W. Gardner, V. K. Varadan, and O. O. Awadelkarim, *Microsensors, MEMS, and smart devices*. Chichester ; New York: J. Wiley, 2001.
- [6] G. Barillaro, A. Molfese, A. Nannini, and F. Pieri, "Analysis, simulation and relative performances of two kinds of serpentine springs," *Journal of Micromechanics and Microengineering*, vol. 15, pp. 736-746, Apr 2005.
- [7] P. I. Norizan Mohamad, Thurai Vinay, "Modelling and Optimisation of a Spring-Supported Diaphragm Capacitive MEMS Microphone," *Scientific Research Publishing*, vol. 2 pp. 762-770, 2010.
- [8] A. Bedford, W. L. Fowler, and K. lynkaran, *Engineering mechanics. Statics*, SI ed. Singapore ; London: Pearson/Prentice Hall, 2005.
- [9] J. J. Allen, *Micro electro mechanical system design*. Boca Raton: Taylor & Francis/CRC Press, 2005.
- [10] E. E. Galloni and M. Kohen, "Influence of the mass of the spring on its static and dynamic effects," *American Journal of Physics*, vol. 47, pp. 1076-1078, 1979.
- [11] W. T. Thomson, *Theory of vibration with applications*, 4th ed ed. Cheltenham: Nelson Thornes Ltd., 2003.
- [12] T. Belendez, C. Neipp, and A. Belendez, "Large and small deflections of a cantilever beam," *European Journal of Physics*, vol. 23, pp. 371-379, May 2002.
- [13] S. D. Senturia, *Microsystem design*. Boston: Kluwer Academic Publishers, 2000.
- [14] J. R. Mallon, A. J. Rastegar, A. A. Barlian, M. T. Meyer, T. H. Fung, and B. L. Pruitt, "Low 1/f noise, full bridge, microcantilever with longitudinal and transverse piezoresistors," *Applied Physics Letters*, vol. 92, Jan 21 2008.
- [15] P. J. French, "Polysilicon: a versatile material for microsystems," *Sensors and Actuators a-Physical*, vol. 99, pp. 3-12, Apr 30 2002.
- [16] J. C. Doll, "Advances in High Bandwidth Nanomechanical Force Sensors with Integrated Actuation," Doctor of Philosophy, Department of Mechanical Engineering, University of Stanford, California, 2012.
- [17] J. A. Harley and T. W. Kenny, "1/F noise considerations for the design and process optimization of piezoresistive cantilevers," *Journal of Microelectromechanical Systems*, vol. 9, pp. 226-235, Jun 2000.

- [18] X. M. Yu, J. Thaysen, O. Hansen, and A. Boisen, "Optimization of sensitivity and noise in piezoresistive cantilevers," *Journal of Applied Physics*, vol. 92, pp. 6296-6301, Nov 15 2002.
- [19] O. Hansen and A. Boisen, "Noise in piezoresistive atomic force microscopy," *Nanotechnology*, vol. 10, pp. 51-60, Mar 1999.
- [20] A. Perez-Cruz, A. Dominguez-Gonzalez, I. Stiharu, and R. A. Osornio-Rios, "Optimization of Q-factor of AFM cantilevers using genetic algorithms," *Ultramicroscopy*, vol. 115, pp. 61-67, Apr 2012.
- [21] J. C. Doll, S. J. Park, and B. L. Pruitt, "Design optimization of piezoresistive cantilevers for force sensing in air and water," *Journal of Applied Physics*, vol. 106, Sep 15 2009.
- [22] S. J. Park, J. C. Doll, and B. L. Pruitt, "Piezoresistive Cantilever Performance-Part I: Analytical Model for Sensitivity," *Journal of Microelectromechanical Systems*, vol. 19, pp. 137-148, Feb 2010.
- [23] S. J. Park, J. C. Doll, A. J. Rastegar, and B. L. Pruitt, "Piezoresistive Cantilever Performance-Part II: Optimization," *Journal of Microelectromechanical Systems*, vol. 19, pp. 149-161, Feb 2010.
- [24] D. K. Chaturvedi, *Modeling and simulation of systems using MATLAB and Simulink*. Boca Raton: CRC Press, 2010.
- [25] R. Wilcock and M. Kraft, "Genetic Algorithm for the Design of Electro-Mechanical Sigma Delta Modulator MEMS Sensors," *Sensors*, vol. 11, pp. 9217-9232, Oct 2011.
- [26] K. Matsuda, K. Suzuki, K. Yamamura, and Y. Kanda, "Nonlinear piezoresistance effects in silicon," *Journal of Applied Physics*, vol. 73, pp. 1838-1847, 1993.
- [27] J. M. Chen and N. C. MacDonald, "Measuring the nonlinearity of silicon piezoresistance by tensile loading of a submicron diameter fiber using a microinstrument," *Review of Scientific Instruments*, vol. 75, pp. 276-278, 2004.
- [28] S.-J. Park, *Development of piezoresistive microcantilever based force feedback system for analysis of mechanosensation in caenorhaditis elegans nematodes*, 2009.
- [29] J. Carvill, *Mechanical engineer's data handbook*: Butterworth-Heinemann, 2003.
- [30] E. Oberg and C. J. McCauley, *Machinery's handbook : a reference book for the mechanical engineer, designer, manufacturing engineer, draftsman, toolmaker and machinist*, 29th ed. New York: Industrial Press, 2012.



## Chapter 4

### Fabrication

This chapter discusses the process used to fabricate the QC sensor. It begins with a brief account of the initial unsuccessful device release trials attempted using inductively coupled plasma (ICP) Si etch and hydrofluoric (HF) vapour release techniques. These trials demonstrated the challenges in fabricating large and thin suspended structures with a small spring constant such as the QC sensor. Subsequently, the complete process, including the release process developed specifically to overcome the shortcomings of the earlier techniques, and the devices fabricated using this process are presented.

#### 4.1 Initial Trials

The fabrication of the suspended multi-beam QC sensor required the development of a new technique since initial attempts with conventional fabrication techniques gave unsatisfactory results. The difficulties encountered were mainly observed during the removal of the Wafer Handle Block (WHB) which releases the suspended structure following frontside fabrication. In this section only the unsuccessful device release techniques will be discussed. The details for the frontside fabrication will be included with the process finally used to successfully fabricate the complete device.

##### 4.1.1 Device release trial 1 – ICP Si etch

In the first attempt to fabricate the QC sensor, a silicon on insulator (SOI) wafer with a 4.5  $\mu\text{m}$  device layer, 575  $\mu\text{m}$  handle and a 2  $\mu\text{m}$  buried oxide (BOX) layer was used. After frontside (f/s) fabrication a 3  $\mu\text{m}$  thick layer of  $\text{SiO}_2$  was deposited on the

backside (b/s) of the wafer using plasma-enhanced chemical vapour deposition (PECVD). A 6  $\mu\text{m}$  thick layer of photoresist (AZ2070, MicroChemicals) layer was deposited on the b/s using spin coating, and patterned using standard photolithography techniques. The photoresist mask was then transferred on to the  $\text{SiO}_2$  layer using reactive ion etching (RIE) and acted as a hard mask (Fig. 4.1).

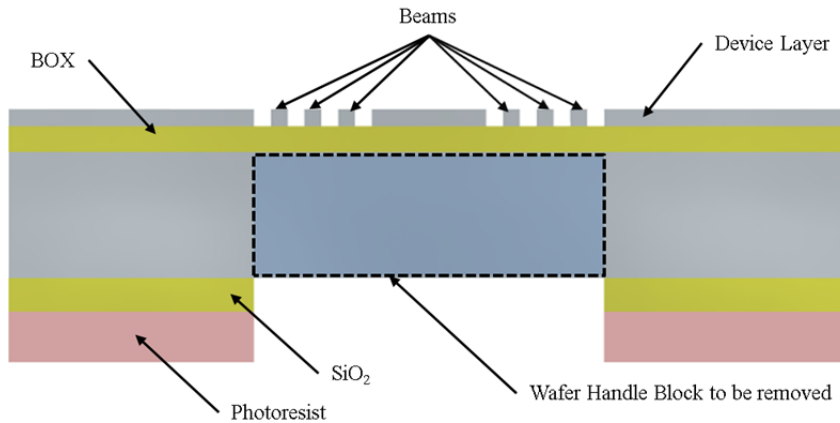


**Figure 4-1: Cross-section of the DRIE release**

The wafer was loaded into an ICP and deep reactive-ion etching (DRIE) of the Si was initiated to remove the WHB. The process intent was that whilst micro-loading would result in the centre of the WHB to etch to the BOX layer first, a continued dry etch would eventually consume the residual Si along the perimeter of the WHB cavity releasing the devices before the BOX, photoresist and  $\text{SiO}_2$  were completely etched away. However, during the trials (Figures 4.2 and 4.3) the devices were damaged before the WHB was completely removed. This occurred regardless of the high Si etch selectivity ( $\text{SiO}_2:\text{Si} - 1:300$ , photoresist: $\text{Si} - 1:100$ ) of the DRIE process used. Increasing the thickness of the BOX layer was considered to improve the performance. However, the thickness of the  $\text{SiO}_2$  hard mask was limited to 3  $\mu\text{m}$  to avoid layer cracking or delamination due to deposition related stress. Moreover, increasing the photoresist thickness would have promoted carbonisation during the DRIE etch, thus further development of this process was not pursued.

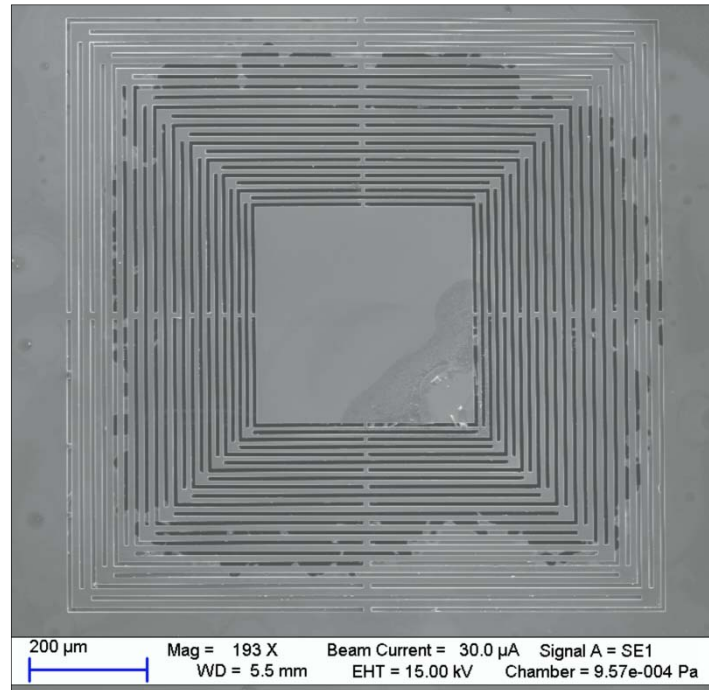


**Figure 4-2: Scanning Electron Microscope image of the top view of a partially released QC sensor fabricated using an ICP Si etch to remove the WHB. The outline of the un-etched Si along the perimeter of the structure can be seen through the beams. In the centre the BOX layer has been breached and the top layer of the structure shows evidence of being etched. If this etch was continued, the suspended structure would have been damaged.**

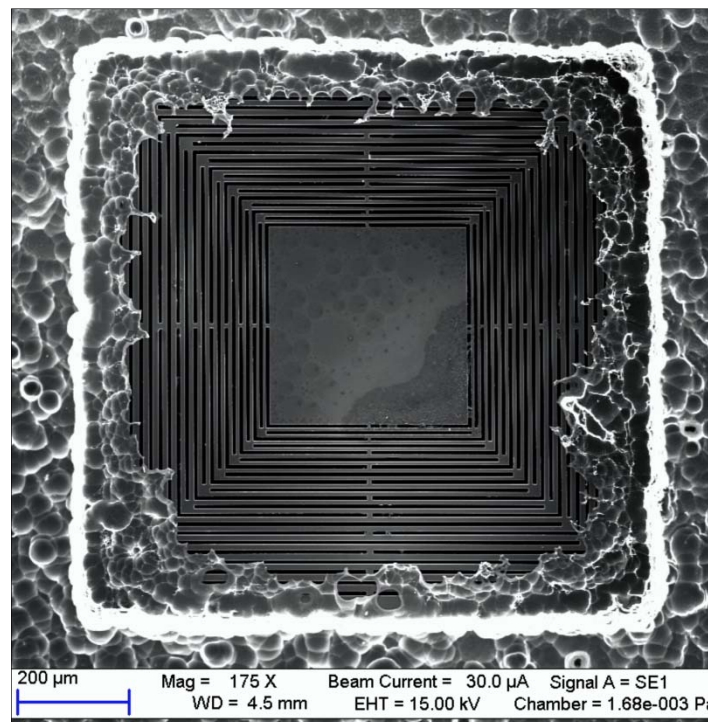


**Figure 4-3: Scanning Electron Microscope image of the bottom view of the device shown in Figure 4.2. The un-etched Si can be seen along the perimeter. The image also shows that the BOX etch-stop, the photoresist and SiO<sub>2</sub> hard mask have been completely etched away.**

### 4.1.2 Device release trial 2 – Hydrofluoric vapour etch

The next attempt was based on the Dicing Free process developed by Sari et al. for the release of MEMS sensors and actuators [1]. This technique is also based on SOI wafers technology. In this process, following frontside fabrication, the device is semi-released using trenches etched into the wafer handle using DRIE. The device remains temporarily attached to the WHB and the wafer handle through the BOX layer (Figure 4.4). Next, HF vapour is used to strategically semi etch the BOX layer via release holes provided in the device layer (Figure 4.5). This should release the device from the WHB and the wafer handle (Figure 4.6). However, notwithstanding the success by Sari et al. on devices with a 50  $\mu\text{m}$  device layer; attempts to release the QC sensor with a 4.5  $\mu\text{m}$  thick device layer were unsuccessful. It is likely that the low spring constant (0.18-6 N/m), the high device deflection (greater than  $>1$  mm) and the large surface of the suspended platform made stiction unavoidable when using this technique (Figure 4-7).

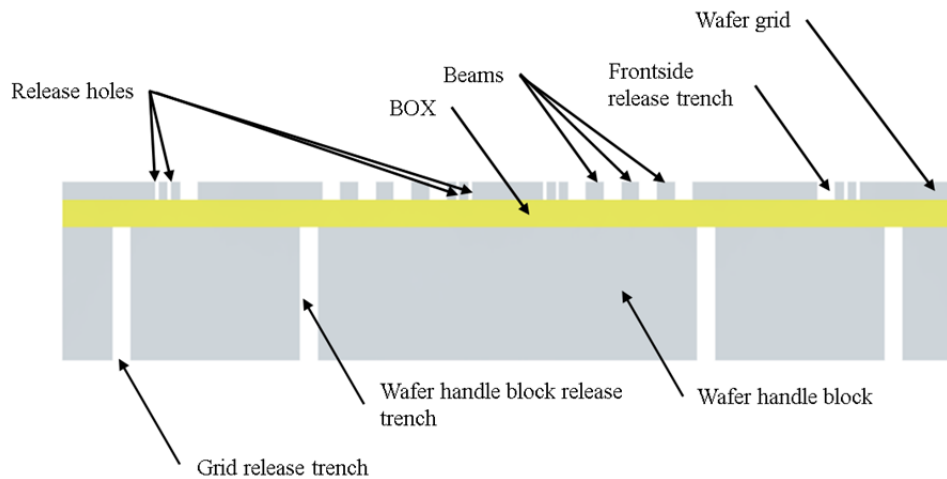


Figure 4-4: Cross-section schematic of the Dicing Free process - post trench DRIE pre HF vapour release.



Figure 4-5: Cross-section schematic of the Dicing Free process - post vapour HF release, pre WHB removal, and pre wafer grid separation.



Figure 4-6: Cross-section schematic of the Dicing Free process - post WHB removal and post separation from grid

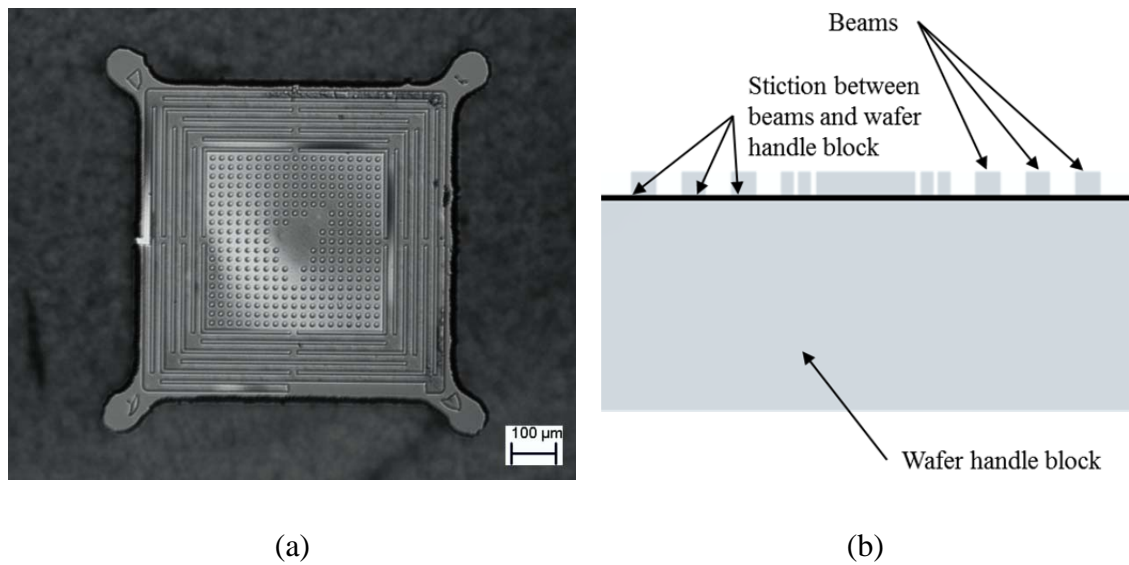


Figure 4-7: (a) Microscope image of the top view of a device fabricated using the Dicing Free process, and (b) a graphical representation of the cross-section showing the suspended structure and beams of the device attached to the WHB through stiction.

## 4.2 QC Fabrication Process

The process used for the successful fabrication of the QC sensor will be outlined next. The process has been subdivided into the following main sections: wafer preparation, backside semi-release, defining the suspended structure, defining the piezoresistors, defining the electrical contact terminals, and sensor release. The process is also summarised in Table 4.1 and the process recipes are available in Appendix 2.

## 4.2.1 Wafer Preparation

The microfabrication process developed for the fabrication of the QC sensor is based on a double sided polished SOI wafer having a device layer of 4.5  $\mu\text{m}$ , a BOX layer of 2  $\mu\text{m}$  and a handle of 575  $\mu\text{m}$ .

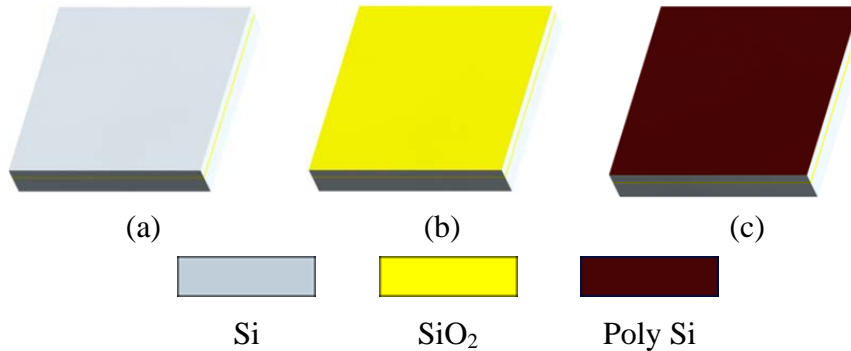


**Figure 4-8:** The fabrication process begins with a(a) SOI wafer clean, (b) PECVD deposition of  $\text{SiO}_2$  on the f/s and (c), HWCVD deposition of doped polysilicon on the f/s.

The process begins with a thorough wafer clean (Figure 4-8.a). This is followed by 200 nm of  $\text{SiO}_2$  deposited on the device layer (Figure 4-8.b) using PECVD (Plasmalab System 100) and with 500 nm of amorphous silicon with a p-type (Boron) doping concentration of  $4.5 \times 10^{19} \text{ cm}^{-3}$  which was deposited at  $550^\circ\text{C}$  using HWCVD (Figure 4-8.c). The wafer was annealed in a tube furnace at  $430^\circ\text{C}$  for 2 hours to release hydrogen entrapped during the deposition process. Failure to do this would have caused the polysilicon to blister at higher anneal temperatures. A second anneal at  $1000^\circ\text{C}$  for 30 minutes converted the amorphous silicon to a polysilicon [2]. The complete anneal temperature profile is included in Appendix 2.

## 4.2.2 Backside Semi-Release

Following a wafer clean, 500 nm of PECVD silicon nitride ( $\text{Si}_3\text{N}_4$ ) was deposited on both sides of the wafer (Figure 4-9.a). The  $\text{Si}_3\text{N}_4$  layer acts as a hard mask for a potassium hydroxide (KOH) wet etch, thus needed to be void of any pinholes or defects; consequently an LPCVD  $\text{Si}_3\text{N}_4$ , which typically has less pinholes, would have been preferred.

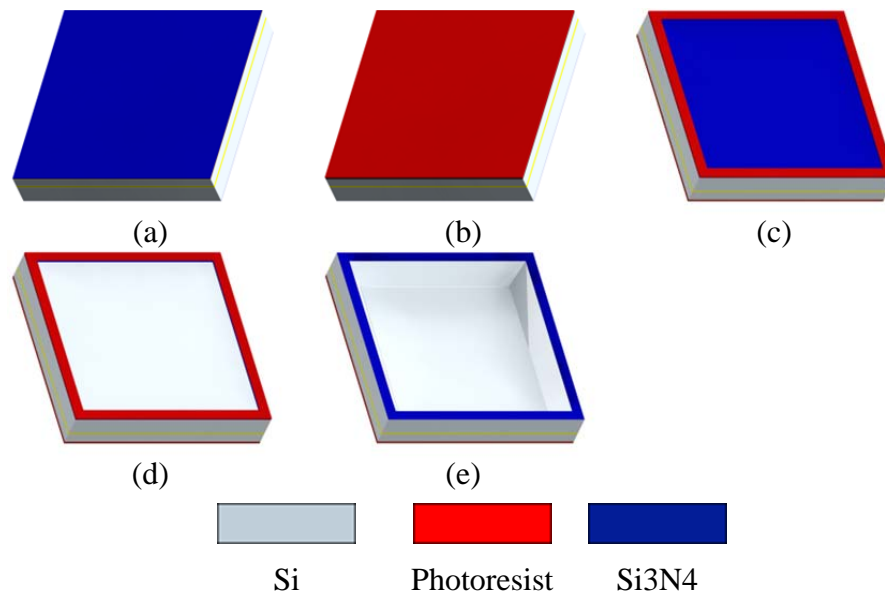


**Figure 4-9:** The semi-release process involves (a) PECVD deposition of  $\text{Si}_3\text{N}_4$  on f/s and b/s, (b) protective coating of photoresist on the f/s, (c) photoresist and release photo-lithography on the b/s, (d) RIE of the  $\text{Si}_3\text{N}_4$  layer on the b/s and a (e) KOH wet etch.

A protective coating of photoresist 6  $\mu\text{m}$  thick (AZ9260 – diluted for spray coating, MicroChemicals) was applied to the frontside of the wafer (Figure 4-9.b), and 3  $\mu\text{m}$  of photoresist (AZ2070 – diluted for spray coating, MicroChemicals) was deposited on the backside. In both instances, the photoresist was applied using a spray coater (EVG150 Automated Resist Processing System) since the lower angular acceleration of the chuck was found to cause less damage to the  $\text{Si}_3\text{N}_4$  hard mask. The backside release pattern was next transferred on to the photoresist using photo-lithography (Figure 4-9.c), and transferred onto the  $\text{Si}_3\text{N}_4$  hard mask using RIE (Plasmalab 80 plus) (Figure 4-9.d). The photoresist was then stripped using FNA and the wafer was wet etched to a depth of 475  $\mu\text{m}$  in a KOH solution with a concentration of 40% and a temperature of 70°C (Figure 4-9.h). This left ~100  $\mu\text{m}$  of the WHB to be removed at a later stage. The deciding factor for leaving 100  $\mu\text{m}$  of Si was due to preliminary trials which showed that a thinner membrane would lose structural integrity and buckle. This would form a convex surface making spinning or spray coating photoresist uniformly difficult and would furthermore cause proximity errors during photo-lithography.

At this stage, due to the large semi-release cavities that were introduced into the b/s following the KOH etch, the wafer is unable to hold a vacuum. Thus to enable the spray coater to secure the wafer on to the loading arm and chuck, it was mounted onto a carrier wafer and fastened with Kapton tape. Similarly, the ICP uses a mechanical clamp to secure the wafer in the chamber. This could fracture a weakened wafer, thus

the wafer was temporarily reinforced by bonding it onto a carrier wafer using vacuum oil (Fomblin). In each instance, the carrier wafer was removed once the process was complete and the wafer cleaned using acetone and IPA (isopropyl alcohol).

### 4.2.3 Defining the Suspended Structure

Subsequent to the KOH etch the  $\text{Si}_3\text{N}_4$  hard mask is no longer required on the frontside of the wafer. Thus this was removed using RIE ( $\text{CHF}_3/\text{O}_2$ ) (Figure 4-10.a). The frontside was now spray-coated with 3  $\mu\text{m}$  of photoresist (AZ2070 – diluted for spray coating, MicroChemicals), the suspended structure mask was aligned to the backside of the wafer using a top and bottom side mask aligner (EVG 620TB) and the pattern was transferred onto the photoresist using photo-lithography (Figure 4-10.b).

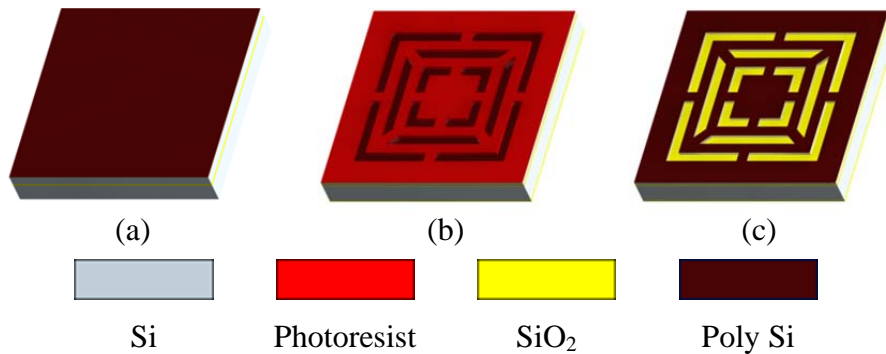


**Figure 4-10:** To define the suspended structure the (a)  $\text{Si}_3\text{N}_4$  on the f/s is removed using RIE, (b) photoresist and the structure photo-lithography is applied to the f/s and (c) the polysilicon/ $\text{SiO}_2$ /Si is etched using ICP.

The pattern was then transferred onto the wafer with an ICP polysilicon etch ( $\text{SF}_6/\text{Ar}$ ),  $\text{SiO}_2$  etch ( $\text{CHF}_3/\text{O}_2$ ), and Si etch ( $\text{SF}_6/\text{Ar}$ ). An ellipsometer (Woollam Md2000D) was used to confirm that each layer was completely etched before proceeding to etch the next layer (Figure 4-10.c), and the BOX layer was used as a final etch-stop.

### 4.2.4 Defining the Piezoresistors

To establish the piezoresistors, the frontside of the wafer was spray-coated with 3  $\mu\text{m}$  of photoresist (AZ9260 – diluted for spray coating), the mask was aligned to the suspended structure and the pattern transferred using photo-lithography (Figure 4-11a). The wafer was loaded into the ICP and the surplus polysilicon was etched ( $\text{SF}_6/\text{Ar}$ ) away (Figure 4-11.b).

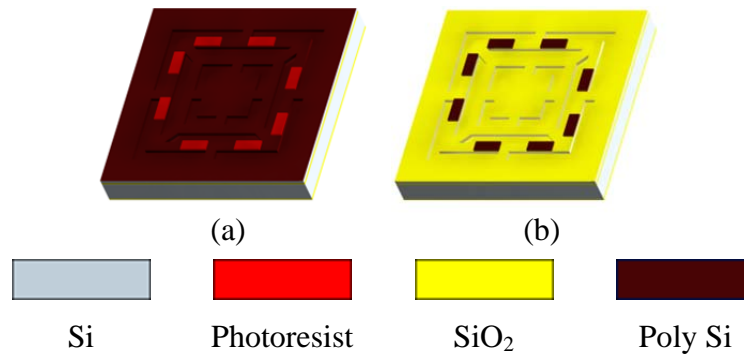


Figure 4-11: The piezoresistors are defined by (a) applying photoresist and piezoresistor photo-lithography on the f/s and a (b) polysilicon ICP etch.

#### 4.2.5 Defining the Electrical Contact Terminals

The process for creating the electrical contact terminals began with the deposition of 500 nm of aluminium (Figure 4-12.a) using an Electron Beam Physical Vapor Deposition (LAB 700, Leybold). The wafer was next spray-coated with 3  $\mu\text{m}$  of photoresist (AZ9260 – diluted for spray coating), the electrical contact terminal mask aligned to the piezoresistors and the pattern transferred using photo-lithography (Figure 4-12.b). The wafer was wet etched in an aluminium etchant (Type A) until all surplus aluminium was etched away (Figure 4-12.c). The contact terminals were then annealed at 425°C for 30 minutes in a tube furnace to improve the ohmic contact resistance [3].

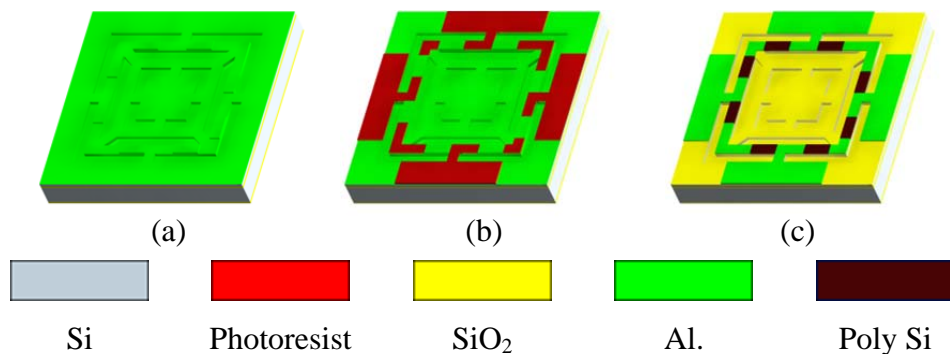


Figure 4-12: : The terminals are defined by (a) Al deposition on the f/s, (b) applying photoresist and terminal photo-lithography and a (c) Al wet etch.

#### 4.2.6 Sensor Release

To release the suspended structure the wafer was diced into individual devices, rinsed in DI water,  $\text{N}_2$  blow dried, mounted on to a glass carrier wafer, loaded into an ICP and the remaining 100  $\mu\text{m}$  of the Si WHB was etched ( $\text{SF}_6/\text{Ar}$ ) away (Figure 4-13.a-b). The devices were then transferred onto a Si carrier wafer, loaded into a RIE and the BOX layer was removed using a  $\text{SiO}_2$  dry etch ( $\text{CHF}_3/\text{Ar}$ ). Finally the devices were



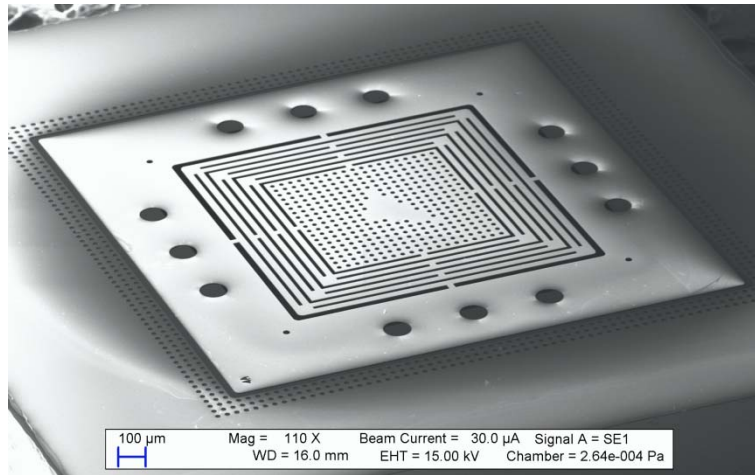
No.	Fig. ref.	Step	Properties	Notes
1	4-8.a	Wafer clean	FNA, RCA-1, BHF, RCA-2	Recipe in Appendix
2	4-8.b	PECVD - SiO <sub>2</sub> (f/s)	Thickness – 200 nm	Recipe in Appendix
3	4-8.c	HWCVD of doped polysilicon (f/s)	Thickness – 500 nm Dopant – Diborane Deposition Temperature – 550°C Doping concentration – $4.5 \times 10^{19} \text{ cm}^{-3}$	N/A
4		HWCVD doped polysilicon anneal – Tube furnace	430°C for 120 min. 1000°C for 30 min.	Profile in Appendix
5		Wafer clean	FNA, RCA-1, BHF 20:1, RCA-2	Recipe in Appendix
6	4-9.a	PECVD deposition of Si <sub>3</sub> N <sub>4</sub> (f/s) and backside (b/s)	Gases: SiH <sub>4</sub> /N <sub>2</sub> /N <sub>2</sub> O Thickness – 400 nm	Recipe in Appendix
7	4-9.b	Protective PR (f/s)	Thickness – 3000 nm PR type – AZ9260 (spray)	Recipe in Appendix
8	4-9.c	PR backside release Photo-lithography (b/s), Mask 1	Thickness – 3000 nm PR type – AZ2070 (spray)	Recipe in Appendix Mask in Appendix
9	4-9.d	RIE of Si <sub>3</sub> N <sub>4</sub> (f/s)	Etch depth – 400 nm	Recipe in Appendix
10		PR strip	FNA – 15 min.	N/A
11	4-9.c	KOH wet etch (b/s)	40% @ 70°C KOH concentration Depth – ~475 μm	N/A
12	4-10.a	RIE of Si <sub>3</sub> N <sub>4</sub> (f/s)	Etch depth – 400 nm	Recipe in Appendix
13	4-10.b	PR and structure Photo-lithography (f/s), Mask 2	Thickness – 3000 nm PR type – AZ2070 (spray)	Mask in Appendix
14	4-10.c	ICP of polysilicon/SiO <sub>2</sub> /Si (f/s)	Polysilicon – 500 nm, SiO <sub>2</sub> – 200 nm, Si – 5000 nm	Recipe in Appendix
15		Wafer clean	Acetone/IPA rinse O <sub>2</sub> Plasma asher – 10 min.	To remove vacuum oil used to mount wafer
16	4-11.a	PR and piezoresistor Photo-lithography (f/s), Mask 3	Thickness – 3000 nm PR type – AZ9260 (spray)	Recipe in Appendix Mask in Appendix
17	4-11.b	ICP polysilicon (f/s)	Etch depth: 500 nm	Recipe in Appendix
18		Wafer clean	Acetone/IPA rinse O <sub>2</sub> Plasma asher – 10 min.	To remove vacuum oil
19		RIE native oxide etch (f/s)	Time – 10 seconds	Recipe in Appendix
20	4-12.a	Al deposition (f/s)	EBPVD	N/A
21	4-12.b	PR and terminal Photo-lithography (f/s), Mask 4	Thickness – 3000 nm PR type – AZ9260 (spray)	Recipe in Appendix Mask in Appendix
22	4-12.c	Al wet etch	Etch time – 1 min.	Al. etchant Type A
23		Anneal - Tube Furnace	425°C for 30 minutes	N/A
24		Wafer clean	Acetone/IPA rinse, N <sub>2</sub> dry, O <sub>2</sub> plasma for 5 min.	N/A
25		Dice and DI water rinse	N/A	N/A
	4-13.a	Dicing	N/A	N/A
26	4-13.b	ICP Si etch to BOX (b/s)	Si etch depth – ~100 μm	Recipe in Appendix
27	4-13.c	RIE SiO <sub>2</sub> etch to Si (b/s)	SiO <sub>2</sub> etch depth – 2 μm	Recipe in Appendix
28	4-13.d	RIE SiO <sub>2</sub> etch (f/s)	SiO <sub>2</sub> etch: SiO <sub>2</sub> – 200 nm	Recipe in Appendix

Table 4.1: The details of the process used to fabricate the QC sensor.

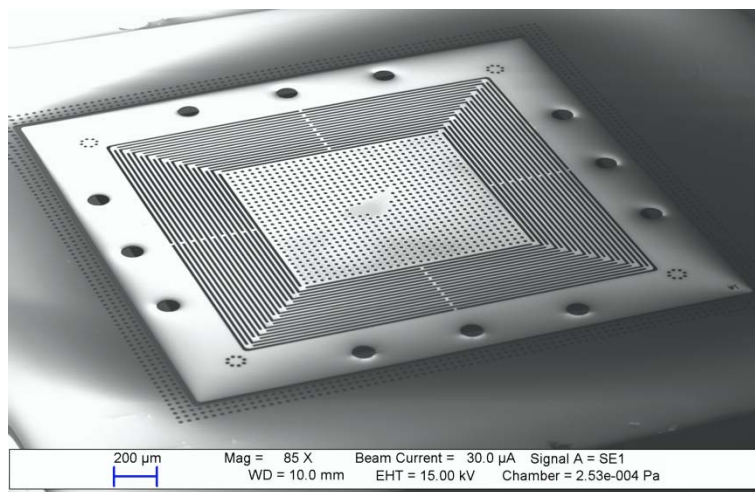
## 4.2.7 Fabricated Devices

To ensure that the outlined fabrication process was feasible, an initial trial to fabricate QC springs (QC 1, QC 2 and QC 3) was attempted without the polysilicon piezoresistors and terminals. Figure 4-15 shows the Scanning Electron Microscope (SEM) images of the QC springs fabricated using this process. There were no difficulties encountered during the fabrication and no noticeable discrepancies in the length and width of the beams of the fabricated devices.

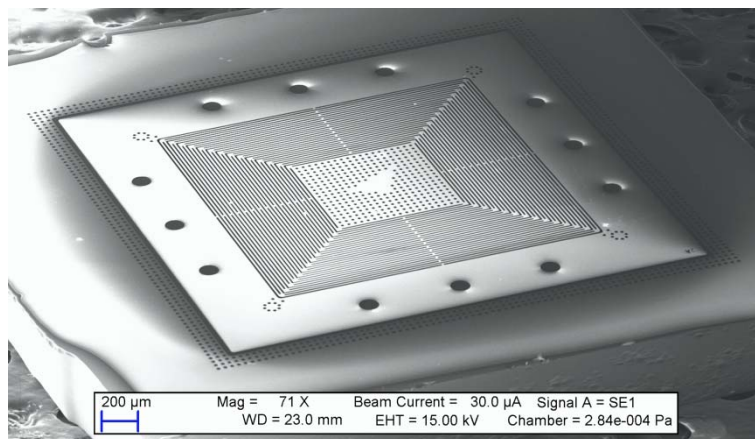
Having established that stiction was no longer an issue; the full process was used to fabricate QC sensor (QC 1s) and large self-sensing cantilevers (TC 1s) with piezoresistive sensing (Figure 4-16) where the 's' denotes that the device is a sensor. TC 1s was fabricated as it would allow the piezoresistive properties of the HWCVD polysilicon to be evaluated independently of the QC spring. Again there were no discrepancies in the width and length of the beams and no difficulties were encountered in the release of the suspended structure; however, discolouration was noted on the frontside of the TC 1s devices after the final Si/SiO<sub>2</sub> dry etches used to release the device. This indicated that, despite the frontside of the device being placed face down onto the platen of the ICP/RIE, it was not sufficiently masked. Thus the fabrication process needs to be amended to include a protective mask on the frontside of the device prior to the final backside etch. This would also protect the piezoresistors from the plasma which has been found to increase the Hooge factor [4]. In addition it was noted that there was a 3 µm misalignment between the piezoresistors and the Al terminals (Figure 4-16.c). However, since there was no misalignment between the piezoresistors and the beams it was determined that this would have no effect on the performance of the device. SEM images of other devices fabricated using this process are also included in Appendix 2.



(a)

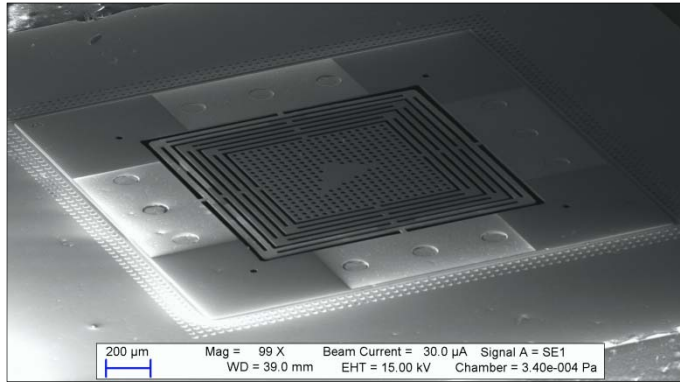


(b)

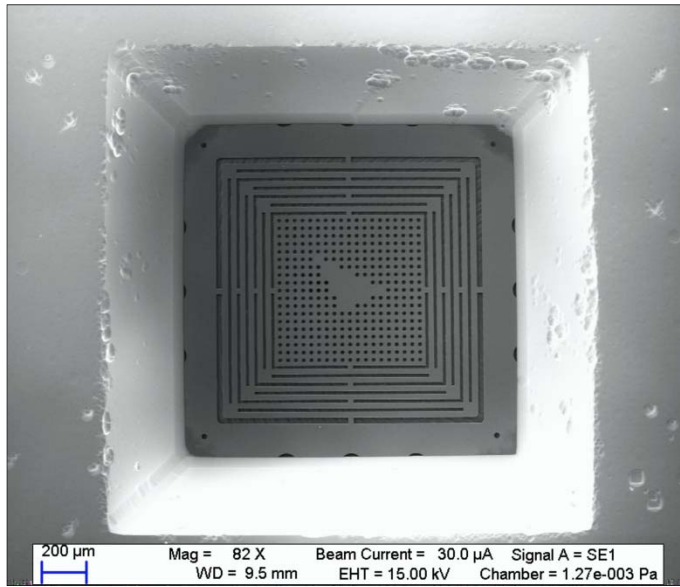


(c)

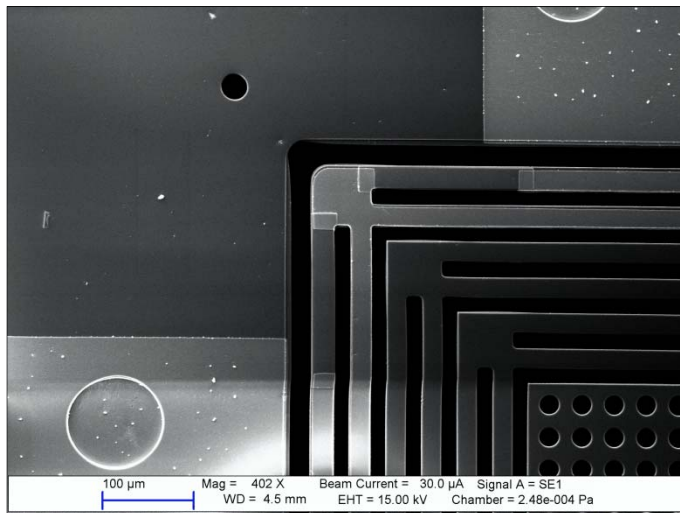
Figure 4-15: SEM images of QC springs (a) QC 1, (b) QC 2 and (c) QC 3 microfabricated using the process outlined in this chapter.



(a)



(b)



(c)

**Figure 4-16: SEM image of (a) an isometric view (b) bottom view and (c) close up of beams with integrated piezoresistors and terminals of an QC MEMS sensor (QC 1s).**

### 4.3 Conclusions

In this chapter the challenges encountered and the development of a novel fabrication process for the QC sensor was presented. The critical area was found to be the release of the suspended structure from the WHB. Initial trials using an ICP Si etch and the Dicing Free technique were unsatisfactory due to micro-loading and stiction respectively. However, trials using a KOH wet etch to partially etch the WHB prior to frontside fabrication, and a dry etch following frontside fabrication was shown to successfully release the suspended structure by avoiding micro-loading and stiction altogether. The fabrication process outline in this chapter was used to successfully fabricate QC springs (QC 1, QC 2, and QC 3) without piezoresistive sensing and MEMS sensors QC 1s and TC 1s with piezoresistive sensing.

The process outlined in this work is adaptable to other suspended devices which are prone to stiction. A further improvement to the process would be the addition of a mask on the frontside of the device prior to the final backside release. This would inhibit frontside etching, observed as discolouration of the piezoresistors on TC 1s, which indicated that the piezoresistors had thinned. This mask would also protect the piezoresistors from plasma which can cause an increase in the Hooge factor.

### References

- [1] I. Sari, I. Zeimpekis, and M. Kraft, "A dicing free SOI process for MEMS devices," *Microelectronic Engineering*, vol. 95, pp. 121-129, 2012.
- [2] P. J. French, "Polysilicon: a versatile material for microsystems," *Sensors and Actuators a-Physical*, vol. 99, pp. 3-12, Apr 30 2002.
- [3] S. D. Senturia, *Microsystem design*. Boston: Kluwer Academic Publishers, 2000.
- [4] J. C. Doll, S. J. Park, and B. L. Pruitt, "Design optimization of piezoresistive cantilevers for force sensing in air and water," *Journal of Applied Physics*, vol. 106, Sep 15 2009.



## **Chapter 5**

### **Characterisation**

In this chapter the fabricated QC spring (QC 1, QC 2, and QC 3) and the MEMS sensors QC 1s and TC 1s are characterised. The characterisation of the cantilever (TC 1s) is also included as this allows for the piezoresistive properties of the HWCVD polysilicon to be investigated independently from the QC sensor. The initial measurements are performed to characterise the mechanical properties of the QC springs and cantilever and to compare them to the analytical and numerical analysis. The characterisation involves the measurement of the spring constant, first mode resonant frequency, linearity, and maximum deflection. Next, the electrical noise characteristics, sensitivity, and the resolution of the sensors are established. Finally the crystal volume, grain size, gauge factor and Hooge factor, of the HWCVD polysilicon piezoresistors are determined.

#### **5.1 Mechanical characterisation**

In the following section the mechanical properties of the QC springs and cantilever are characterised. The F-D mode of an AFM microscope was used to establish the spring constants at deflections less 5  $\mu\text{m}$ , and a F-D jig was used to investigate the linearity, maximum deflection and confirm the spring constant. The first resonant frequency of the QC springs was determined using a laser Doppler vibrometer.

## 5.1.1 Spring Constant, Linearity and Maximum Deflection

### Measurements

To obtain highly accurate spring constant measurements F-D curves were recorded using an AFM microscope (Multimode 5, Veeco) set in F-D mode. This was achieved with a modified cantilever-on-cantilever method [1]. The setup was altered for the measurements such that a commercial cantilever was used as the optical lever rather than the device under test (DUT) as in the original setup (Figure 5-1). This was done as it was more practical to have QC spring on the AFM microscope's sample stage. The commercial cantilevers used had a nominal spring constant,  $k_c$ , of 3 N/m (Budget Sensor, Multi75) for QC 1s, and 0.2 N/m (Budget Sensor, ContAL) for QC 2 and 3 and TC 1s. This ensured that for accuracy  $k_c$  was similar to the spring constant,  $k$ , of the DUT measured ( $0.3 k_c < k < 3.0 k_c$ ) as was recommended by Gibson et al. [2]. The spring constant provided by the cantilever manufacturer can be out of tolerance by as much as 200% [3]. Thus, for accuracy,  $k_c$  was measured using the thermal noise method [1, 4] which yields a spring constant uncertainty of better than 25% [1]. Furthermore, the total deflections were limited to  $\leq 5 \mu\text{m}$  as this was the maximum travel of the piezoelectric actuator (J scanner) installed on the AFM microscope. This also ensured that the cantilevers operated within their linear range.

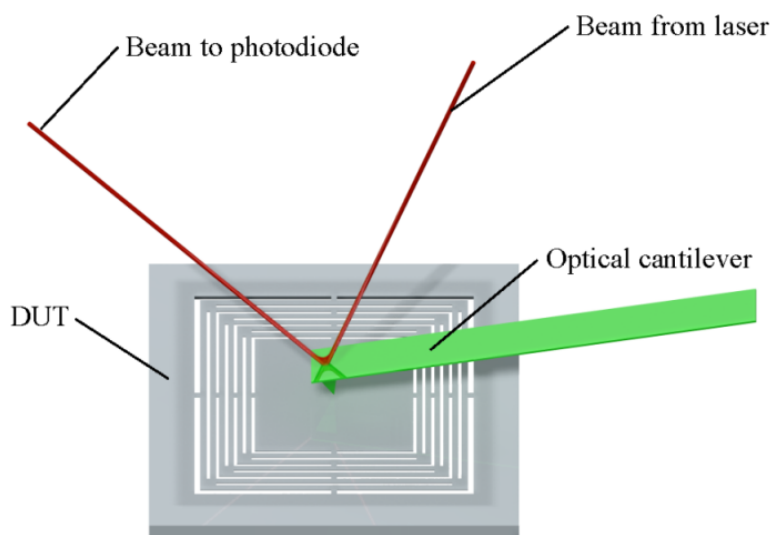
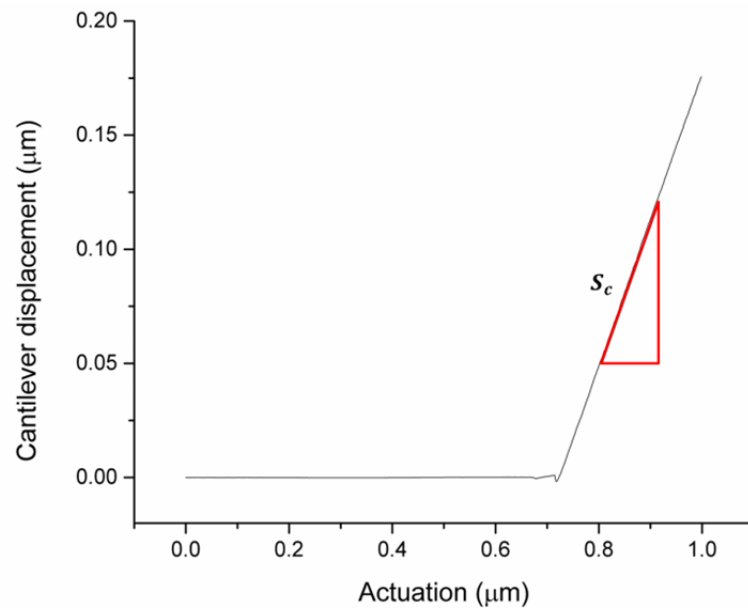


Figure 5-1: The schematic shows the set-up of the cantilever-on-cantilever method as it was adapted to measure the spring constant of the QC spring.

Prior to the measurements, the sensitivity of the optical lever system was calibrated for each cantilever used. This was accomplished by deflecting the optical lever by a known displacement against a stainless steel disc. The relative compliance of the disc was negligible compared to that of the optical cantilever, thus was ignored. The actuation and recording of the photodiode voltage versus the displacement were controlled automatically using the AFM's software and the resultant gradient of the data collected is equivalent to the displacement sensitivity of the setup.

During the measurements, the optical cantilever is pushed against the centre of the suspended platform of the QC sensor or against the edge of the cantilever if TC 1s was being tested. The resultant optical cantilever deflection versus the total actuation data were recorded using the AFM's software. A representative curve is shown in Figure 5-2.



**Figure 5-2: Representative graph for the DUT spring constant measurement. Measurements were made with the AFM microscope in the F-D mode and using the modified cantilever-on-cantilever method.**

The gradient of the curve,  $S_c$ , was used to calculate the spring constant for the DUT using:

$$k = k_c / (1/S_c - 1) \cos^2 \theta \quad \text{Eq. 5-1}$$

where  $\theta$  is the angle to the horizontal of the optical cantilever as mounted on the AFM (typically  $11^\circ$ ). The derivation for Eq. 5-1 is provided in Appendix 3. To measure the linearity and maximum deflection of the QC sensor, deflections greater than  $5 \mu\text{m}$  were

required. For this purpose a F-D jig (Figure 5-3), which consisted of a precision balance positioned directly beneath a Vernier micrometre head, was utilised.

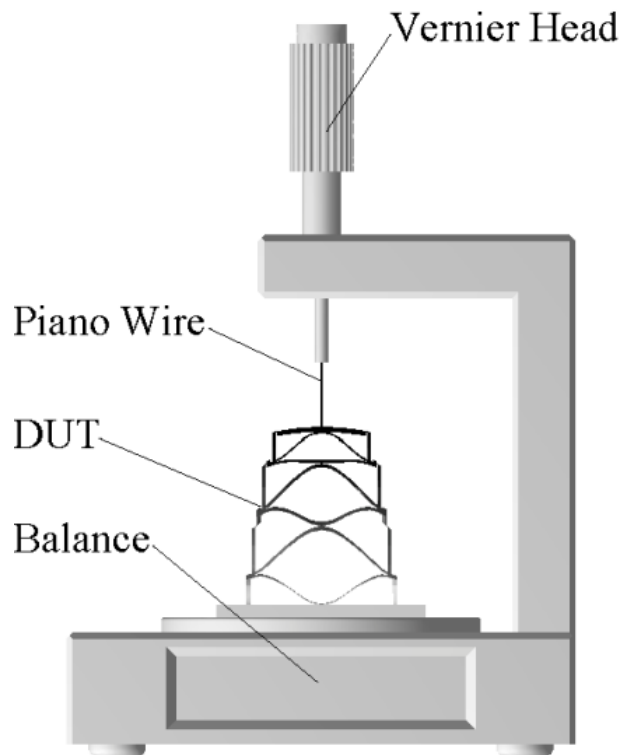
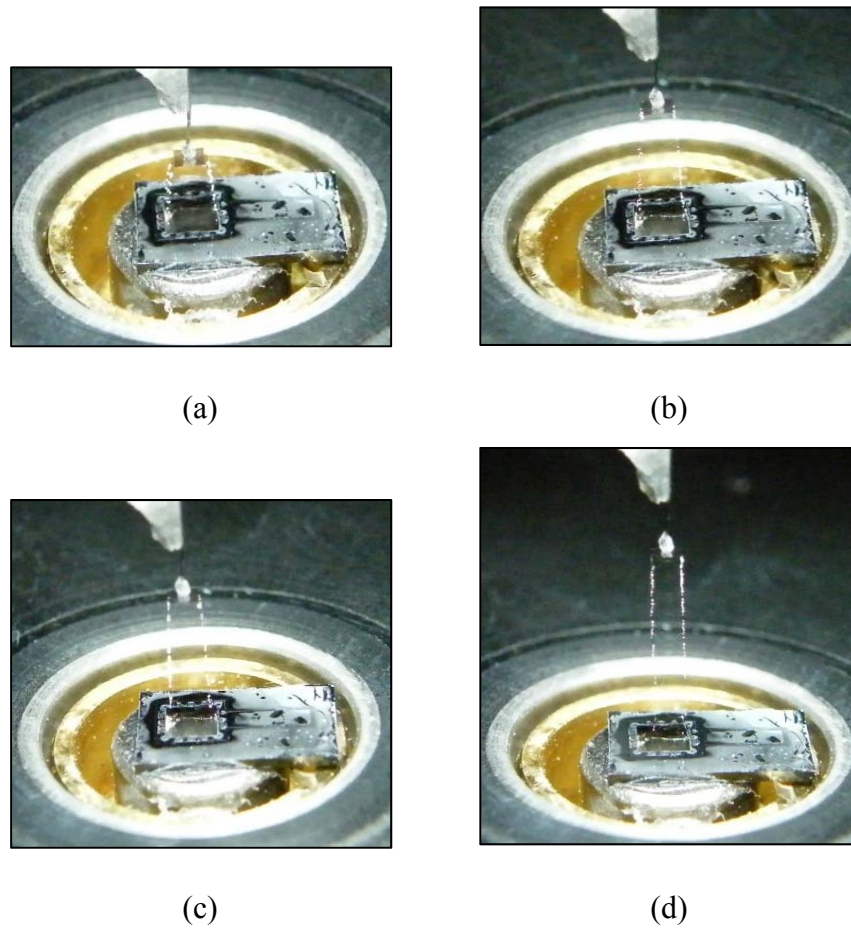


**Figure 5-3: Schematic of the F-D jig used for the mechanical out-of-plane characterisation of the QC spring. The DUT is mounted on a precision balance directly beneath a Vernier micrometre head using a cyanoacrylate adhesive. The suspended structure of the DUT (shown deflected and not to scale) is connected to the Vernier micrometre head with flexible piano wire fixed at both ends using a cyanoacrylate adhesive.**

The QC spring was mounted onto the precision balance using a cyanoacrylate adhesive and the Vernier micrometre head was connected to the suspended platform of the QC spring with flexible piano wire fixed at both ends using a cyanoacrylate adhesive. To make the measurements the suspended platform was deflected using the Vernier micrometre head (Figure 5-4). The change in mass,  $\Delta m_{bal.}$ , measured by the balance was converted to the force,  $F$ , required to deflect the QC spring using [5]:

$$F = \Delta m_{bal.}g \quad \text{Eq. 5-2}$$

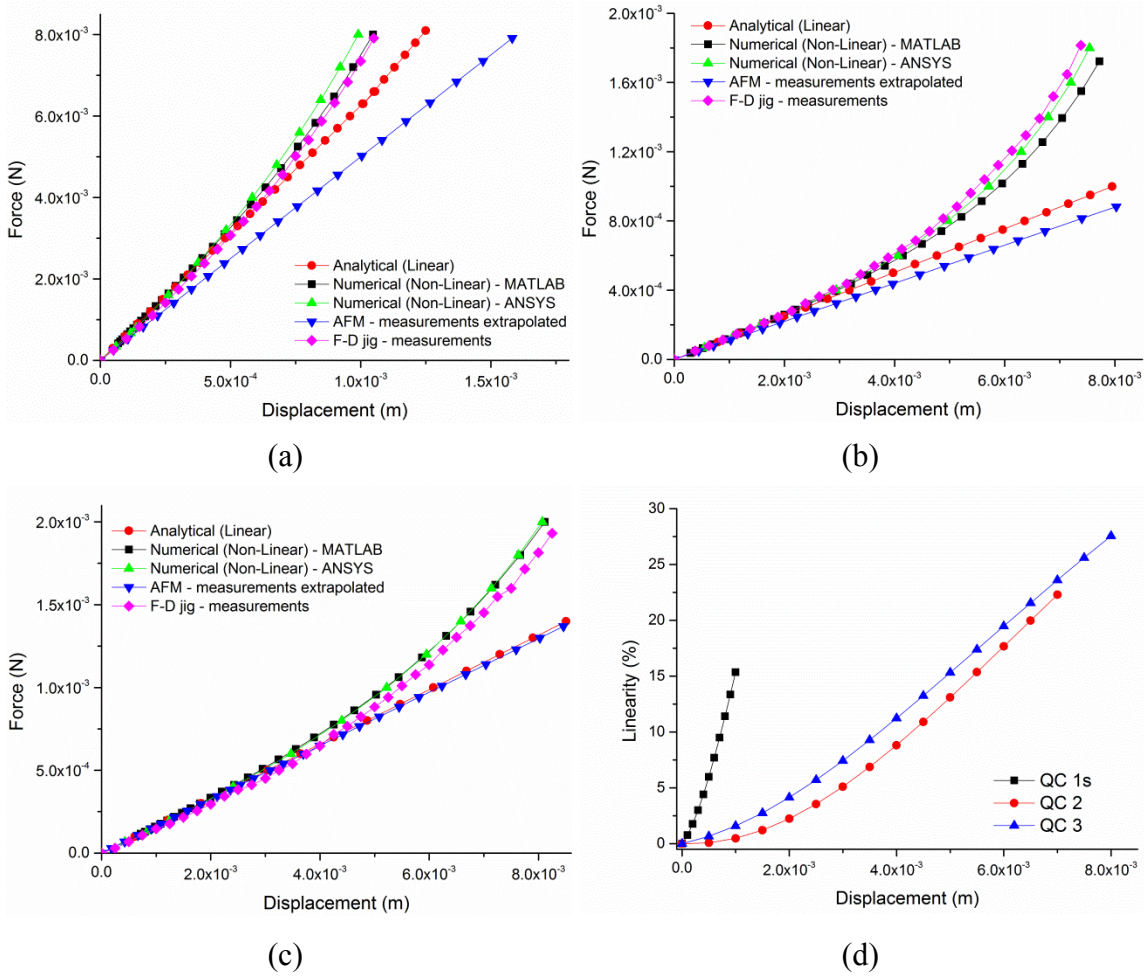
where  $g$  is the acceleration due to gravity. Initial measurements were conducted to < 60% of the theoretical maximum deflection of the DUT and repeated four times. Finally the maximum deflection was measured by deflecting the spring until it fractured. TC 1s was not tested on the F-D jig since deflections greater than 5  $\mu\text{m}$  were already approaching the linear limit of the device.



**Figure 5-4:** The images show the QC 2 DUT mounted onto the precision balance. The suspended platform is bonded to a short piece of piano wire which is attached to the Vernier micrometre head (not shown). Using the Vernier the suspended platform is pulled away from the device. The force required for each incremental deflection is calculated from the change in mass displayed on the balance.

Figures 5-5.a-c shows the data obtained from the AFM, F-D jig, analytical calculations, and numerical analysis for the three different QC springs. The gradients represent the spring constants of the QC springs being evaluated. The spring constants measured with the AFM microscope in F-D mode were 4.69 N/m, 0.105 N/m, 0.162 N/m and 0.280 N/m for QC 1s, QC 2, QC 3 and TC1s respectively. Using the F-D jig measurements it was established that linearity of QC 1s, QC 2 and QC 3 was 0.76%/15.35%, 0.48%/22.3%, and 0.65%/27.6% up to deflections of 100  $\mu\text{m}$ /1000  $\mu\text{m}$ , 100  $\mu\text{m}$ /7250  $\mu\text{m}$ , and 100  $\mu\text{m}$ /8000  $\mu\text{m}$  respectively (Figure 5-5.d).

The results also show that a total deflection before fracture of as much as 1000  $\mu\text{m}$ , 7250  $\mu\text{m}$ , and 8000  $\mu\text{m}$  is possible for QC 1s, 2, and 3 respectively. The complete results for QC 1s, 2 and 3 and TC 1s are summarised in Table 5-1.



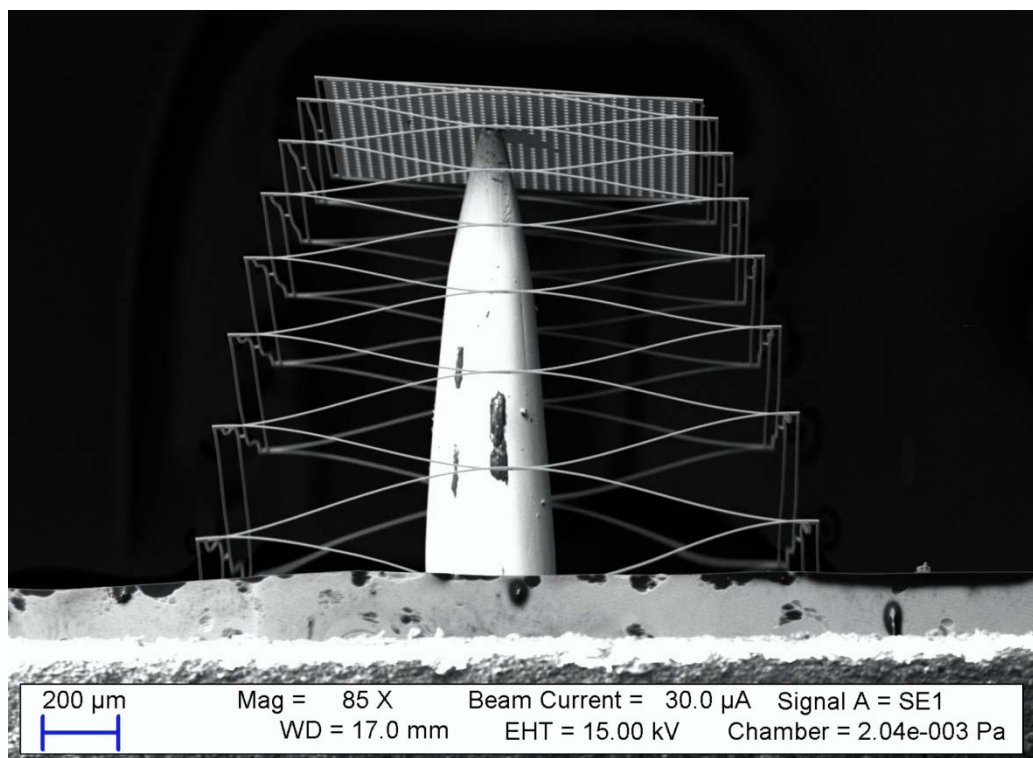
**Figure 5-5: Force-displacement graphs for (a) QC 1s, (b) QC 2, and (c) QC 3 based on analytical, numerical (MATLAB and ANSYS), extrapolated AFM measurement, and F-D jig measurement results. (d) The graph shows the linearity % versus displacement for QC 1, QC 2, and QC 3.**

Figure 5-6 and 5-7 show the SEM images of the QC springs deflected by  $\sim 1300 \mu\text{m}$  and  $\sim 575 \mu\text{m}$  respectively. The shape of the deflected beams is analogous to those used in the analytical calculations (Figure 3-5) and obtained from the FEA simulations (Figure 3-18). This justifies the approach used in the analytical solution and verifies the numerical analysis solution.

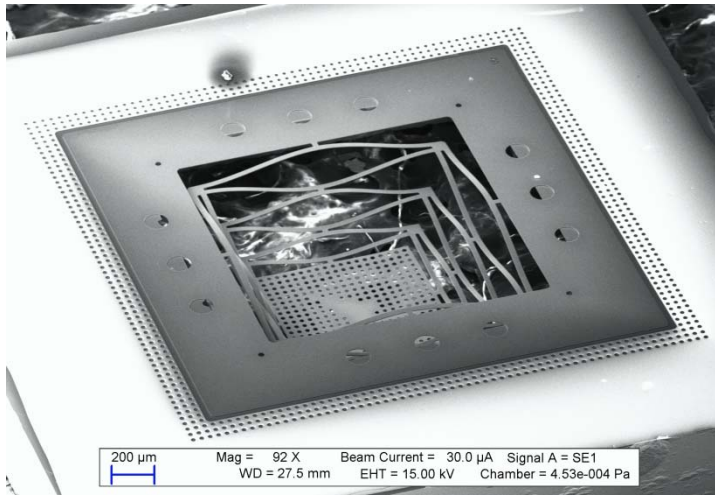
**Table 5-1: Spring constant, linear range, total deflection before fracture, for QC 1s, 2 and 3, and TC 1s using analytical analysis, numerical analysis, AFM, and F-D jig.**

Property	QC 1s	QC 2	QC 3	TC 1s
k – Analytical (N/m)	6.30	0.125	0.165	0.28
k – Numerical (MATLAB) (N/m)	6.32	0.130	0.166	n/a
k – Numerical (ANSYS) (N/m)	5.66	0.166	0.168	0.28
k - Measured with AFM (N/m)	4.69	0.105	0.162	0.28
k - Measured with F-D jig (N/m)	5.50	0.129	0.156	n/a
% Linearity at 100 $\mu\text{m}$	0.76	0.48	0.65	n/a
% Linearity at maximum deflection	15.35	22.3	27.6	n/a
Total Deflection ( $\mu\text{m}$ )	1000	7250	8000	n/a

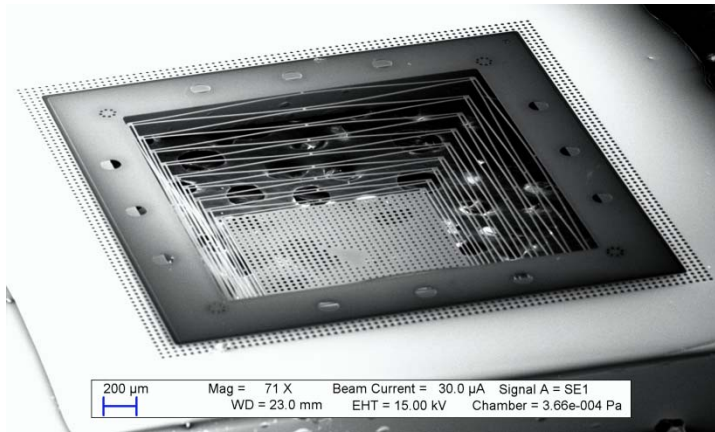
From the graphs in Figure 5-5.a to c, it is observed that the various methods used to determine the F-D characteristics of each spring are in good agreement at low deflections. This confirms their validity for determining the behaviour of the springs at low displacements. However, at increased deflections the analytical data and extrapolated AFM measurements on the force-displacement graphs remain linear, while the numerical analysis (MATLAB and ANSYS) data and F-D jig measurements show a non-linear increase in the spring constant.



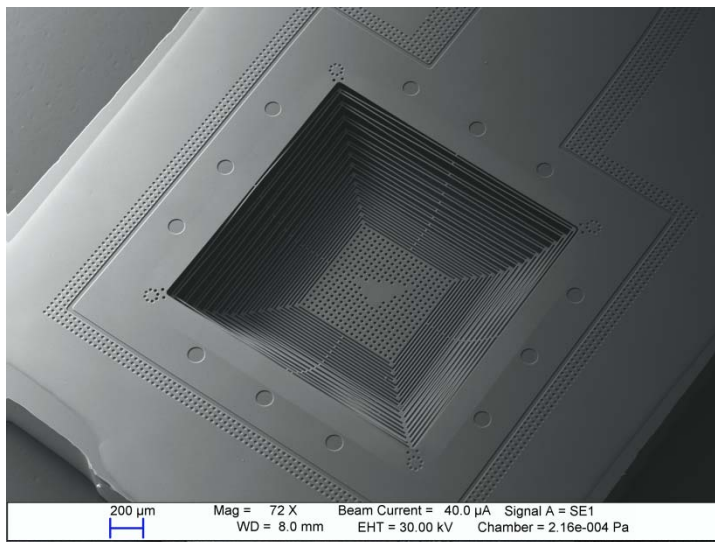
**Figure 5-6: SEM image of a deflected QC 2. The device was mounted on a soft vinyl block using cyanoacrylate adhesive. A metal pin inserted into the vinyl was used to deflect the suspended platform away from the device and the vinyl block as shown. The shape of the deflected beams is analogous to those seen in the numerical analysis simulations and of the double clamped beams in series used in the analytical model.**



(a)



(b)



(c)

**Figure 5-7: An SEM image of (a) QC 1s, (b) QC 2, and (c) QC 3 spring deflected by 575  $\mu\text{m}$ . These images show that the beams bend as shown in the numerical analysis simulations. This also confirms that the beams can be considered to be double-clamped beams in series as was used in the analytical calculations.**

This is expected as Bernoulli-Euler elementary beam theory used for the analytical calculations is linear and the AFM force-displacement measurements were extrapolated linearly from the spring constants obtained at low deflections ( $\leq 5 \mu\text{m}$ ). Unlike the numerical analysis, these methods do not take into account the non-linear behaviour which occurs at higher deflections. This explains why the F-D jig measurements are in better agreement with the numerical analysis data at higher deflections. The agreement between the commercial software numerical analysis (ANSYS) and the numerical analysis developed in this work using MATLAB justifies the four identical cantilevers in series approach used to determine the non-linear behaviour of the QC spring as discussed in Chapter 3. In Figure 5-5.a the difference between the gradients of the analytical and AFM extrapolated data is 26%. This is most likely due to the inherent uncertainty in the cantilever-on-cantilever method used for the AFM measurements which can be as much as 30% [1]. The spring constant measurements for the TC 1s are in good agreement with the analytical and numerical analysis.

### 5.1.2 Resonant frequencies

The first-mode resonant frequencies of the QC springs were determined using a laser Doppler vibrometer (Polytec MSA 400). The laser Doppler vibrometer calculates the amplitude and frequency using the Doppler shift of a laser beam reflected off the vibrating surface off the DUT. For the measurements, the DUT was mounted on to a shaker jig using double sided tape. The shaker jig was electrically connected to the vibrometer and the laser beam was focused onto the centre of the suspended platform. During the measurements, the DUT was vibrated using a frequency sweep and the amplitude of the vibrations were detected and recorded by the vibrometer. The peaks in the measurements corresponded to the resonant frequency of the DUT.

The first mode resonant frequency for QC 1s, 2 and 3 was measured as 4548 Hz, 375 Hz, and 672 Hz respectively. These results are within 6%, 21%, 3% of that calculated analytically and within 7%, 30%, 2% of the value obtained numerically (Table 5-2).

**Table 5-2: First-mode resonant frequencies for QC 1s, 2, and 3 using analytical, numerical and laser Doppler vibrometer measurements**

Property	QC 1s	QC 2	QC 3
Analytical (spring mass ignored)	6030 Hz	563 Hz	973 Hz
Analytical (spring mass included)	4747 Hz	475 Hz	654 Hz
Numerical (MATLAB)	4840 Hz	480 Hz	620 Hz
Numerical (ANSYS)	4889 Hz	535 Hz	656 Hz
Measured	4548 Hz	375 Hz	672 Hz

The measured resonant frequencies for QC 1s and QC 2 are lower than those obtained analytically and numerically. A similar trend was observed on the spring constants as measured with the AFM microscope. This may indicate that the spring constant of these devices was reduced due a reduction in beam thickness from over etching during the fabrication process. However, the general agreement between the measurements and the analytically and numerically determined first-mode of resonance frequency further justifies the approach used to analyse the mechanical performance of the QC springs.

## 5.2 Electrical Characterisation

In the following section the electrical properties of the sensors are characterised. The section begins with a verification that the contacts are ohmic using the Linear Transmission Line Method (LTLM). This is followed with the details of the electrical test circuit and adapters used for interfacing with the DUT and amplifying the signal. A spectrum analyser (SA) was used to measure the noise characteristics of the sensors and the sensitivity was determined using the F-D mode of an AFM microscope and the F-D jig. Using this data, the force and displacement resolution of the devices was established.

### 5.2.1 Contact resistance and doping concentration

To ensure that the metallisation between the piezoresistive polysilicon and the aluminium terminals had resulted in contacts that are ohmic, the electrical contact

resistance needed to be established. It was also necessary to establish that the contact resistance was not significant when compared to the resistance of the piezoresistors. This was critical as the contact resistance does not contribute towards the change in piezoresistive sensing resistance versus a load applied to the sensor, thus a large contact resistance reduces the sensors sensitivity. Furthermore, a large contact resistance increases both the Johnson noise, through the increased resistance, and the Hooge Noise, through regions of high current density [6]. A LTLM, with mesa etched structure such that current flow only occurs between the contact pads, was employed to measure the contact resistance.

The graph in Figure 5-8.a represents the electrical current (I) versus a bias voltage (V) for the different gap spacing, while the graph in Figure 5-8.b shows the resistance versus the gap spacing as measured on the LTLM test structure. The IV graph indicates that the current is a linear function of the applied voltage, thus the contact between the piezoresistors and the terminals is ohmic. From Figure 5-8.b the specific contact resistance was calculated to be  $5.83 \times 10^{-5} \Omega\text{-cm}^2$ . This results in a device resistance per contact of  $11.5 \Omega$  and  $0.3 \Omega$  for QC 1s and TC 1s respectively. The contact resistance of TC 1s is noticeably smaller than the other sensors. This is due to the larger contact area between the piezoresistor and the terminals on TC 1s.

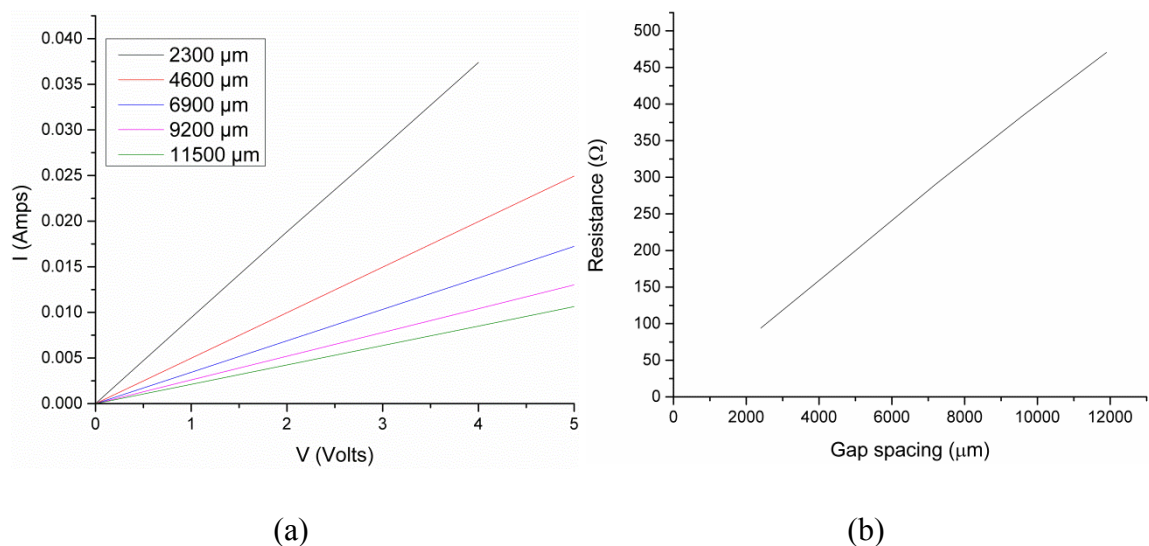


**Figure 5-8: (a) Typical I-V characteristics and (b) resistance versus the gap spacing showing a linear ohmic relationship of the metallised aluminium on polysilicon contacts.**

These contact resistances are small ( $< 4\%$ ) when compared to the resistance per piezoresistor ( $\sim 1 \text{ k}\Omega$ ), thus the metallisation of the contacts was considered acceptable.

From the LTM data, the sheet resistance for the polysilicon was calculated as 82  $\Omega/\square$  which is within 15% of the value measured (70  $\Omega/\square$ ) using a four point probe (RM3000, Jandel). This gives a calculated resistivity of 0.0048  $\Omega\text{-cm}$ , and an estimated doping concentration of  $4.5 \times 10^{19} \text{ cm}^{-3}$ .

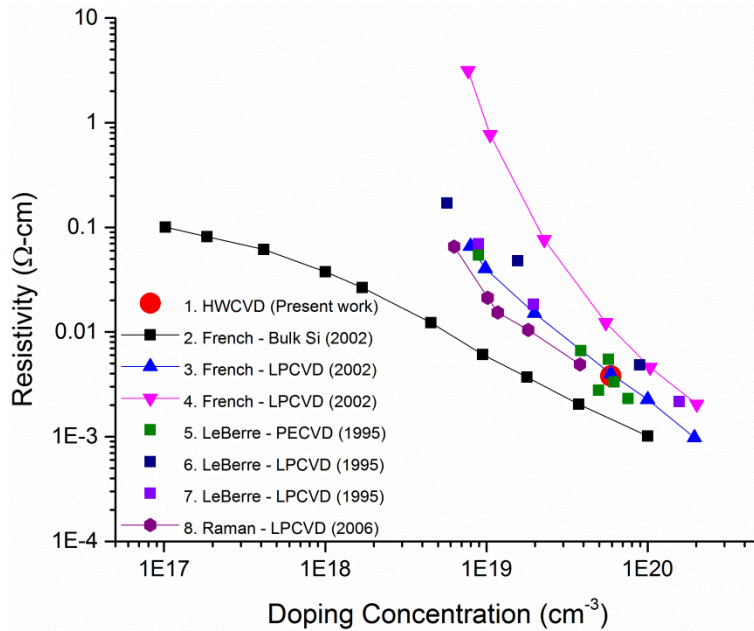


Figure 5-9: Resistivity as a function of the doping concentration for crystalline silicon, LPCVD polysilicon from published literature, and HWCVD polysilicon from this work. Adapted from [7-9].

Table 5-3: Deposition temperatures and annealing details for the HWCVD polysilicon characterised in this work and silicon/polysilicon from published data

No.	Author	Deposition		Anneal		
		Method	Temp.(°C)	Method	Temp.(°C)	Time (min.)
1.	Present work	HWCVD	550	CTA	1000	30
2.	French (2002)	Bulk Si	N/A	N/A	N/A	N/A
3.	French (2002)	LPCVD	560	CTA	1000	30
4.	French (2002)	LPCVD	610	CTA	1000	30
5.	LeBerre (1995)	PECVD	320	RTA	1100	0.33
6.	LeBerre (1995)	LPCVD	620	CTA	950	30
7.	LeBerre (1995)	LPCVD	620	RTA	1100	0.33
8.	Raman (2006)	LPCVD	620	CTA	1000	20

The values obtained for the HWCVD polysilicon are shown in Figure 5-9 together with published data for LPCVD polysilicon with classic thermal annealing (CTA) and rapid thermal annealing (RTA) [7-9]. Table 5-3 gives a summary of the deposition temperatures and annealing details of the silicon and polysilicon obtained from the

published data. The measured resistivity is similar to values obtained by French et al. [7] using LPCVD with a deposition temperature of 560°C with a classic thermal anneal at 1000°C for 30 minutes.

## 5.2.2 Electrical Test Circuit

The schematic in Figure 5-10 shows the circuit used to power, amplify and null the Wheatstone bridge on the DUT. The circuit was designed such that experiments could be performed using the +15/-15 V voltage source typically available on AFM microscopes or using lead-acid batteries. This was necessary since typical laboratory quality mains powered regulated power supplies were found to have noise levels that were too high for this application. All the components on the circuit were powered directly by the input voltage with the exception of the Wheatstone bridge which used an adjustable 2 V via a voltage regulator (U1 – ADR420). The voltage regulator reduced the voltage noise and ensured a constant bias voltage which is critical when using batteries. The Wheatstone bridge voltage bias was adjusted using a potential divider (R6 and R7) which was buffered using an operational amplifier (U2A – TL074).

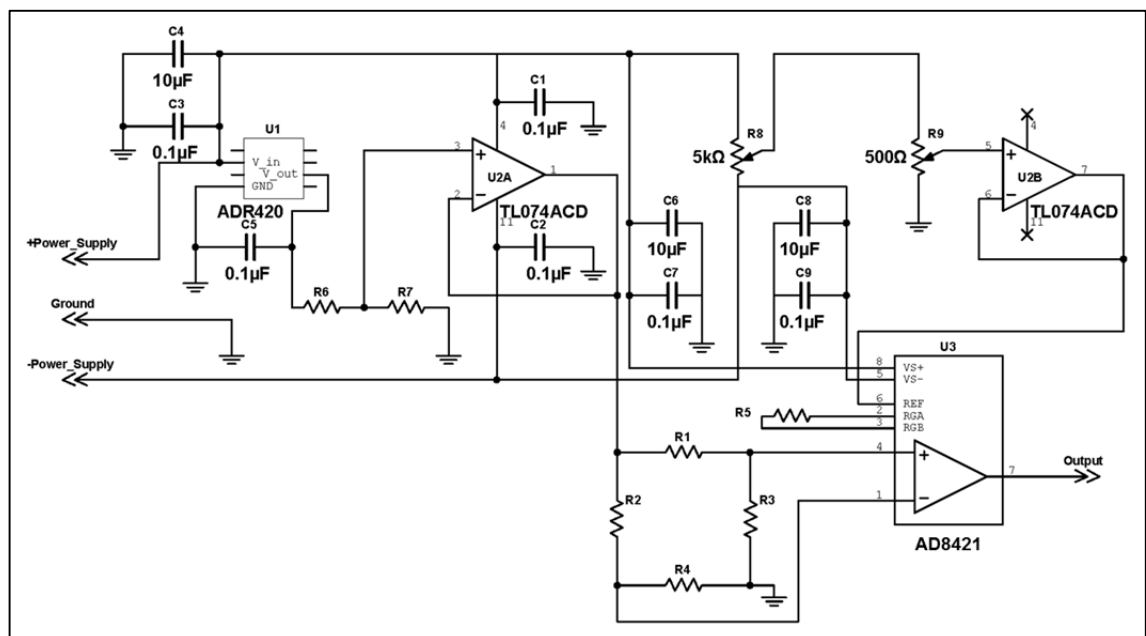


**Figure 5-10: Signal amplification schematic.** Resistors R1 to R4 represent the piezoresistive Wheatstone bridge. R5 is the gain adjustment resistor, R6 and R7 are the adjustable potential divider for the bridge bias voltage, and R8 and R9 are coarse and fine potentiometers for the amplifier reference voltage used to null the bridge. U1, U2A/B, and U3 are a voltage regulator, operational amplifiers (used here as buffers), and a precision instrumentation amplifier respectively, and C1 to C9 are decoupling capacitors.

To minimize noise, metal film resistors were used for the potential divider and connected using gold plated IC single in-line package (SIP) sockets to allow for quick voltage adjustment. The output from the Wheatstone bridge was amplified via a precision instrumentation amplifier (U3 – AD8421). Any initial Wheatstone bridge voltage offset, caused by the bridge not being perfectly balanced, was nulled by offsetting the precision instrumentation amplifier’s reference voltage. The reference voltage was manipulated using two voltage dividers buffered with an operational amplifier (U2B – TL074). The coarse voltage adjustment was done using a 5 k $\Omega$  (R8) potentiometer and refined using the 500  $\Omega$  potentiometer (R9). Both potentiometers were wire wound and connected off-board via a screened cable to reduce noise during reference voltage adjustments [10]. With exception to the coarse and fine reference voltage adjustment potentiometers, all the components in the schematic were assembled on to a printed circuit board (PCB). The DUT were mounted onto purposely made connectors using Crystalbond. Each leg of the Wheatstone bridge was connected to the pins using wire bonding (Figure 5-11).

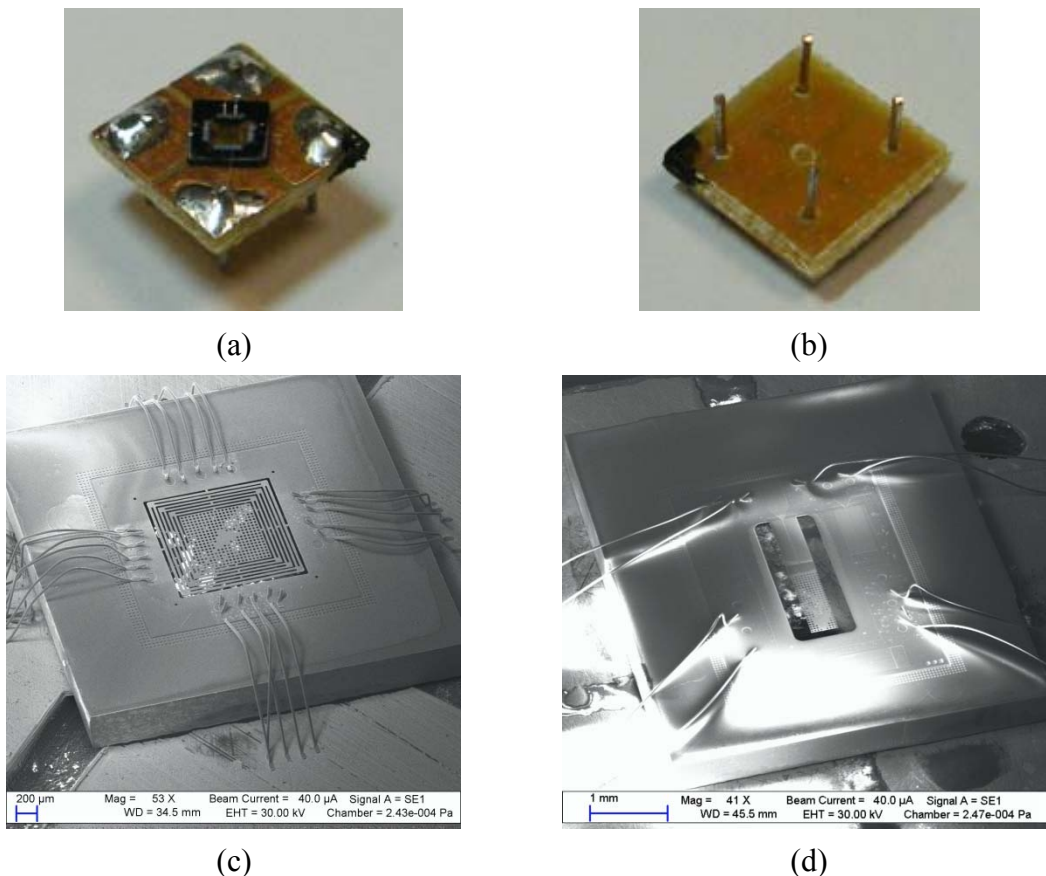


**Figure 5-11: (a) QC 1s mounted onto a connector using Crystalbond and connected electrically using wire bonding, (b) pin side of the DUT connector. (c) SEM images of QC 1s (d) and TC 1s mounted and wire bonded to the DUT connector.**

The PCB was designed such that the DUT could be plugged directly on to the PCB using gold plated SIP sockets. The mounted DUT was located in close proximity to the precision amplifier to reduce pre-amplification noise. External connections to the PCB were made via a 5-way connector for +PS, -PS, ground, output and spare. The coarse and fine reference voltage potentiometers were connected using a 4-way connector for +PS, -PS, ground, and reference voltage.

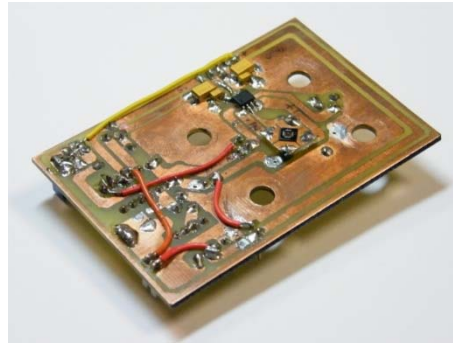


**Figure 5-12: Bottom view of the PCB with the DUT inserted in the socket.**

Depending on the experiment, the PCB was electrically connected directly to a AFM microscope, or to a breakout box (Figure 5-13) which was used to connect the PCB to instruments with BNC connections such as a digital multimeter (DMM) or a spectrum analyser (SA). The breakout box also allows connection to a battery based power supply.

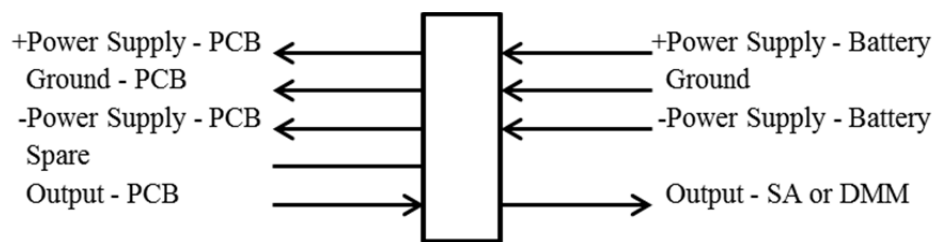


**Figure 5-13: Breakout box for connecting the PCB with the DUT to a battery and a SA or DMM.**

An AFM adapter (Figure 5-14) was fabricated to directly interface the PCB and DUT with the AFM microscope. The resulting AFM adapter, PCB, and DUT assembly substitutes the AFM microscope's laser head during DUT electrical AFM based F-D measurements. The PCB was assembled on to the AFM adapter using four spring loaded screws. These secured the PCB to the AFM adapter but allowed for the PCB to be moved relative to the AFM adapter. This permitted manual DUT to sample alignment; however, the assembly was firm enough to permit accurate measurements to

be made. Figure 5-15 shows the PCB assembled into the AFM adapter and Figure 5-16 shows the complete assembly.

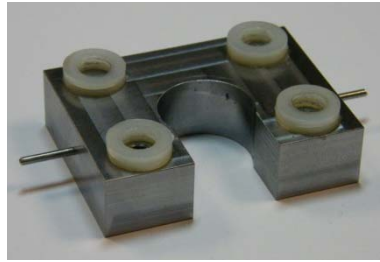


**Figure 5-14: AFM adapter fabricated to interface the DUT and PCB to the AFM microscope.**

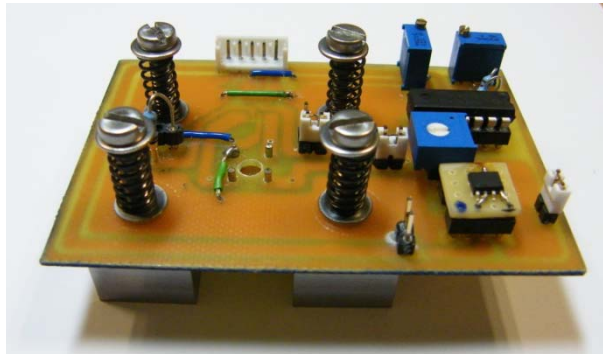


**Figure 5-15: The DUT and PCB assembled on to the AFM adapter using four spring loaded screws. This allowed for course adjustment of the position of the DUT relative to the sample stage.**

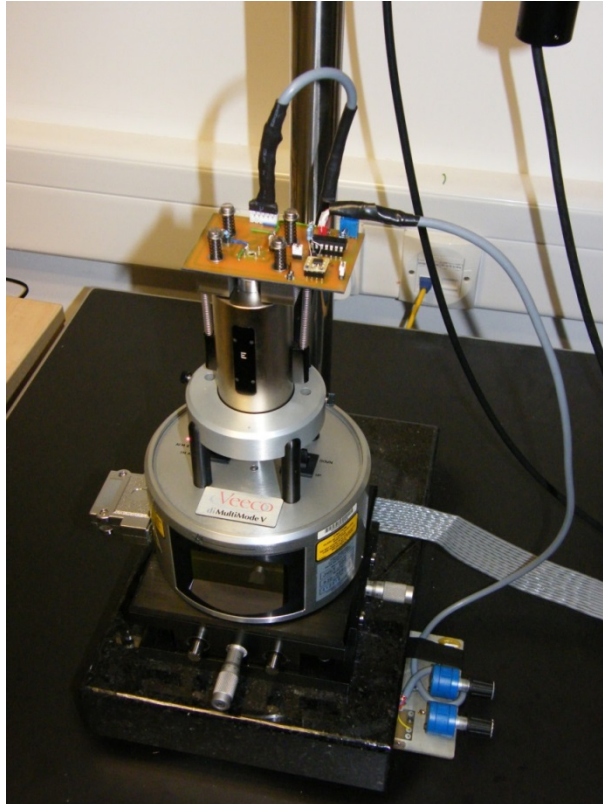


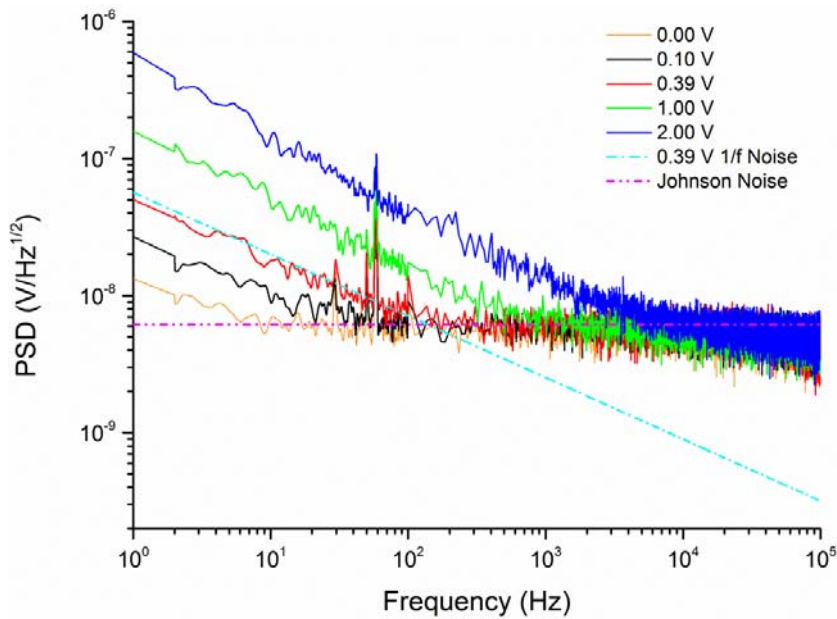
**Figure 5-16: The complete DUT, PCB, AFM adapter and coarse and fine reference voltage adjustment potentiometers assembled on to an AFM microscope.**

### 5.2.3 Electrical Noise Characterisation

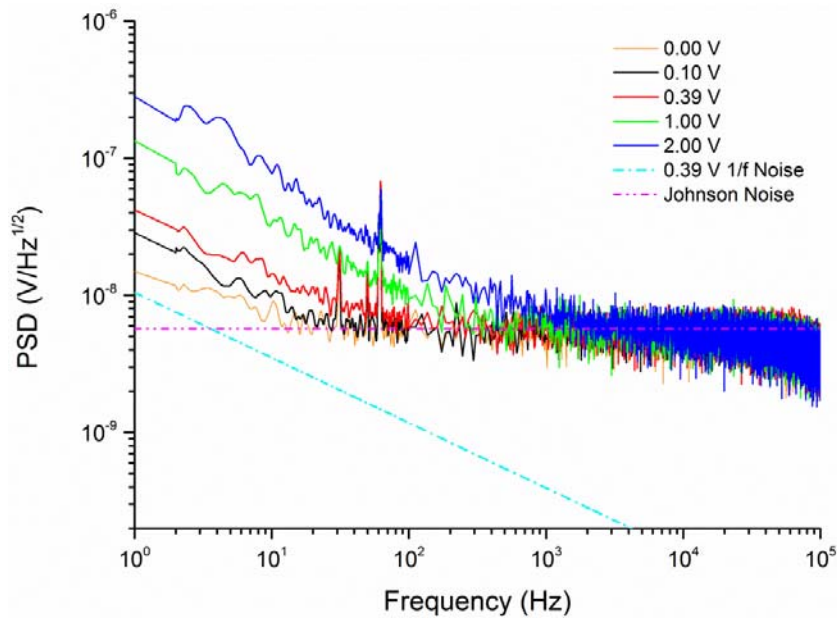
To characterise the electrical noise properties of the piezoresistors the DUT were assembled into the PCB and AFM adapter (Figure 5-15), placed inside a shielded aluminium enclosure and connected to the breakout box. The PCB was connected to a  $\pm 12$  V lead acid battery and the output from the DUT was connected to a SA (E4443A, Agilent) via the breakout box. This setup was then used to perform a noise spectrum analysis on the DUT within a 1 Hz to 100 kHz range and for different bridge voltages. Figure 5-17.a and Figure 5-17.b shows the noise power spectral density (PSD) versus the frequency for QC 1s and TC 1s respectively.

The noise spectra for both QC 1s and TC 1s show a similar trend with the gradient of the noise decreasing to 0 as the frequency increases. This occurs as Hooge noise is frequency dependant and is the dominant noise at lower frequencies in this application. At higher frequencies the Johnson noise, which is independent of both the frequency and the bridge voltage, becomes the dominant noise source. Since Hooge noise is also bridge voltage dependant, the increase in noise at higher bridge voltages is expected; however, it should not be present when the bridge voltage is at 0.0 V. The deviation from the mean Johnson noise at low frequencies when the bridge voltage is 0.0 V is most likely amplifier noise. The graphs also include the estimated Hooge (at 0.39 V) and Johnson noise. Figure 5-17.a shows that the estimates are in good agreement with the noise measured on QC 1s; however, Figure 5-17.b shows that while the estimated Johnson noise for TC 1s is in good agreement with the measurements, the estimated Hooge Noise is not. It is likely that this is a result of a decrease in the piezoresistor thickness due to over etching, or an increase in the Hooge factor due to a fabrication process such as dry etching [6]. Other factors may also include temperature fluctuations or thermomechanical coupling due to erratic cantilever heat dissipation. A similar phenomenon was observed by Park et al. [11]. These increased levels of noise will have a detrimental effect on the performance of TC 1s.

In both QC 1s and TC 1s a gradual decrease in noise after  $10^4$  Hz is observed. Since the Johnson noise is not frequency related, the noise at these frequencies should have remained constant. This phenomenon was due to a decrease in the amplifier's gain at these frequencies and is reported on the amplifiers data sheet. Furthermore, the spikes seen at less than 100 Hz are mains noise which is still detectable despite the shielded cables and box, and the battery power supply.



(a)



(b)

Figure 5-17: Noise spectra of (a) QC 1s and (b) TC 1s.

### 5.2.4 Determining the Sensitivity

To measure the voltage versus force and displacement sensitivity, the sensors were assembled into an AFM microscope using the PCB and AFM adapter assembly. Both the power supply and the DUT output connections were made directly to the microscope. The complete setup was controlled through the microscope's F-D mode software without any additional changes. To null the DUT's voltage output, the coarse and fine potentiometers were adjusted until both the vertical and sum voltages displayed were zeroed. This departs from the conventional AFM microscopes setup procedure in that the sum voltage typically needs to be maximised to ensure that the laser beam reflected off the optical cantilever is centred on the photodiode. Unlike the conventional AFM microscope's setup, this zeroing procedure takes seconds to accomplish. Moreover, removing and reinserting the DUT into the PCB does not require recalibration. To actuate the devices, a  $\text{\O} 100 \mu\text{m} \times 2 \text{mm}$  length of piano wire was bonded perpendicularly to a metal disc ( $\text{\O} 10 \text{mm} \times 0.5 \text{mm}$ ) using cyanoacrylate adhesive (Figure 5-18). Once cured the disc was loaded on to the microscope's sample stage.

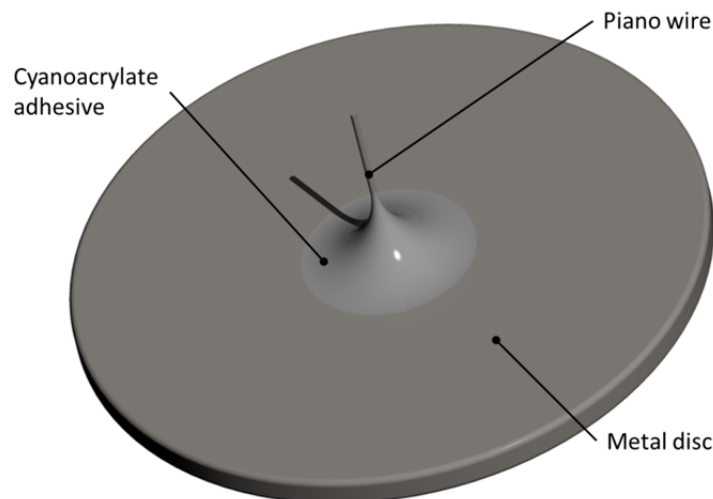


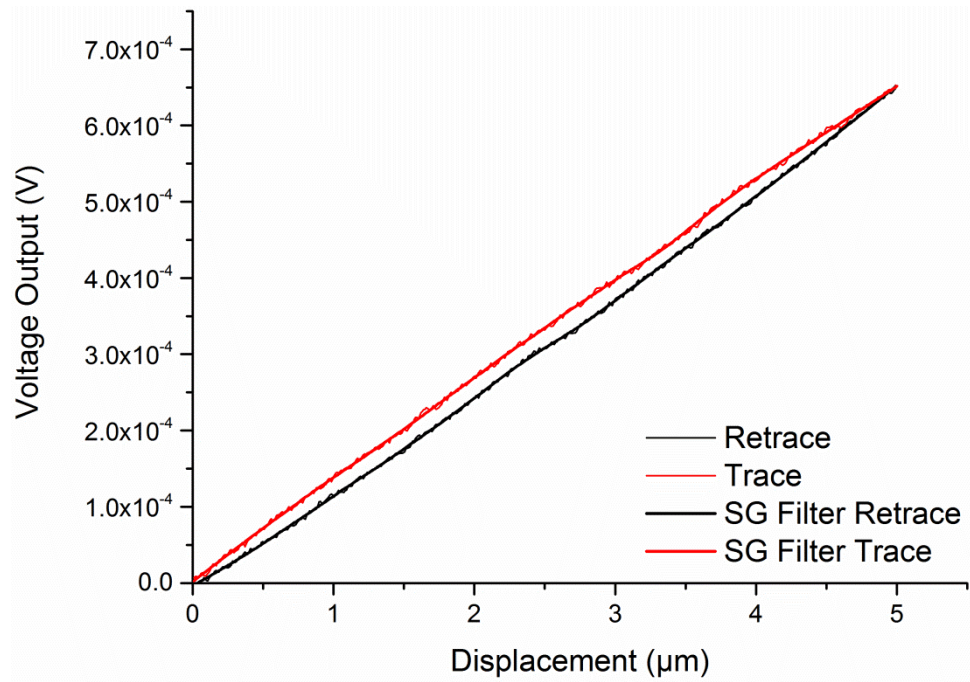
**Figure 5-18:** A rendered model of the metal disc with an affixed  $\text{\O} 100 \mu\text{m} \times 2 \text{mm}$  length of piano wire which was mounted on the AFM microscope's sample stage and used to deflect the suspended platform.

Before taking measurements, the tip of the piano wire was positioned at the centre of the suspended platform for QC 1s, or at the end of the cantilever for the TC 1s. Using the AFM microscope's software the metal disc with protruding piano wire was automatically raised until contact with the sensor was made. Actuating the DUT with the tip of the piano wire was assumed to be equivalent to actuating the device using an

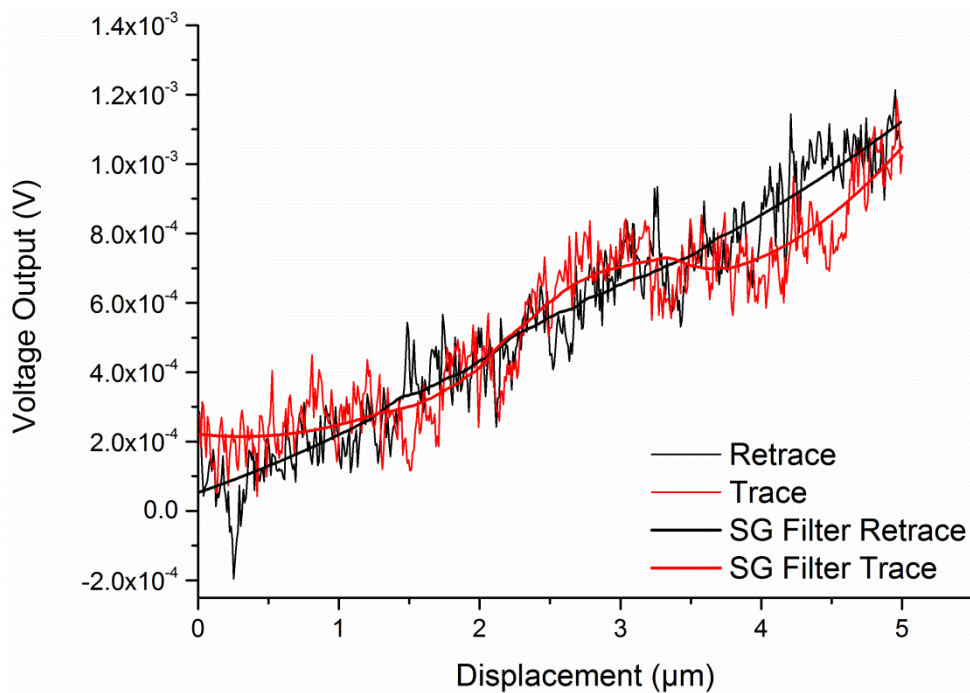
infinitely hard surface. Thus the compliance of the piano wire was ignored when the sensitivity was calculated. Using the microscope's '*calibrate deflection sensitivity*' software option the DUT was actuated by 5  $\mu\text{m}$  and the voltage versus displacement was recorded for multiple measurements for various bias voltages. A representative output curve is shown in Figure 5-19.a/b for QC 1s and TC 1s respectively. The figures show the original curves (Trace/Retrace) together with a second group of curves (SG Filter) which were generated by smoothing the noise in the original curves using a Savitzky-Golay digital filter using commercial software (OriginPro, OriginLab).

The output curves from QC 1s have a high signal to noise ratio thus the smoothing filter has a negligible effect on the output. The Trace and Retrace are not completely linear which suggests a hysteresis of 3.82%. The cause for this could be either from the QC 1s or from the AFM microscope's piezoelectric stack. At a deflection of 5  $\mu\text{m}$  the piezoelectric stack is approaching its limit of travel thus this is a potential explanation for the hysteresis. It is also possible that this was caused by deflections in the piano wire used to actuate the device. The signal to noise ratio on TC 1s was low, thus the digital filter could not smoothen the signal. The gradient of the curves represents the displacement sensitivity of the devices.

The QC sensors have a displacement range larger than the maximum 5  $\mu\text{m}$  z-direction travel of the AFM microscope used. Thus to obtain the voltage versus force-displacement curves for larger displacements, a method similar to the linearity and maximum displacement measurements used earlier was employed. To achieve this, the DUT/PCB/AFM adapter assembly was mounted directly beneath a Vernier micrometer head and the suspended platform was connected to it via a length of piano wire bonded at either end using cyanoacrylate adhesive. The amplified output from the PCB was connected to a DMM which was interfaced to a PC for recording the measurements. Lead-acid batteries were used to provide a  $\pm 12$  V power supply to reduce noise levels and increase measurement accuracy.

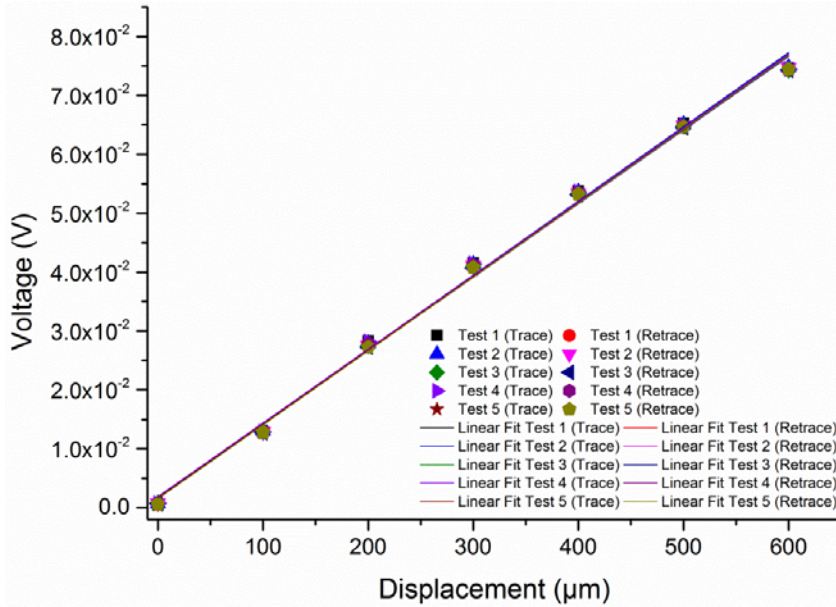


(a)

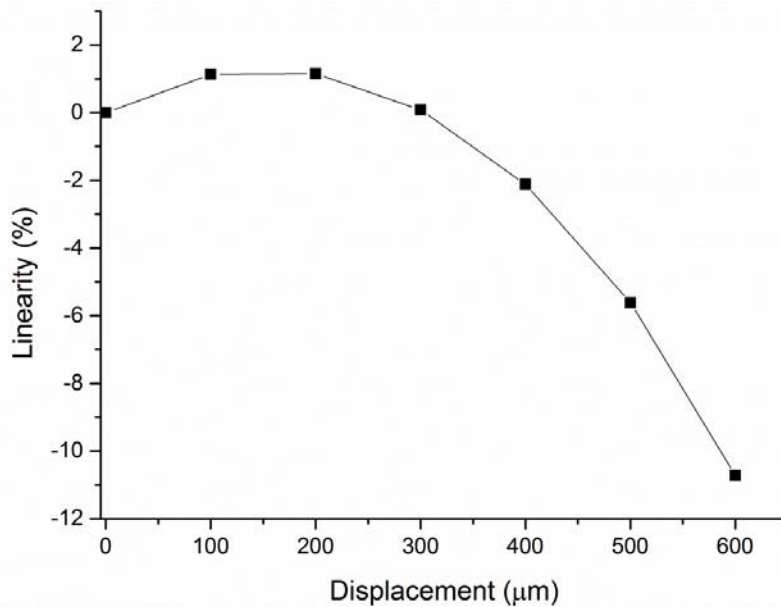


(b)

**Figure 5-19: Representative calibration sensitivity curves for (a) QC 1s and (b) TC 1s measured using an AFM microscope in F-D measurement mode. The curves have been smoothed using Savitzky-Golay digital filters. The curve for QC 1s shows hysteresis which may be due to the piezoelectric stack approaching its end of travel or deflections in the piano wire used to actuate it. The curve for TC 1s displays a poor signal to noise ratio.**



(a)

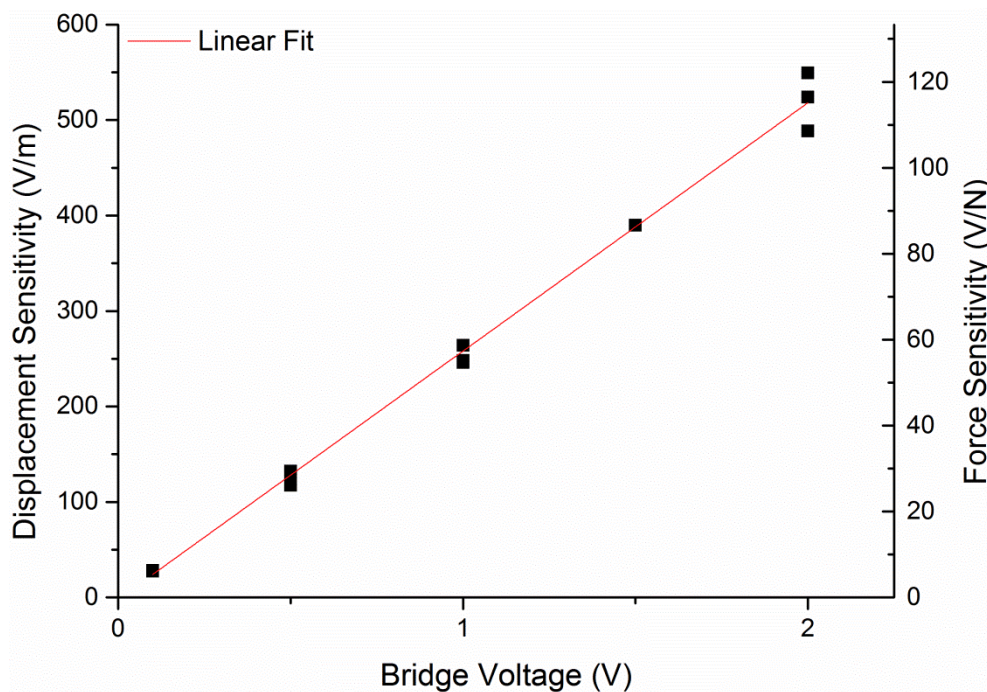


(b)

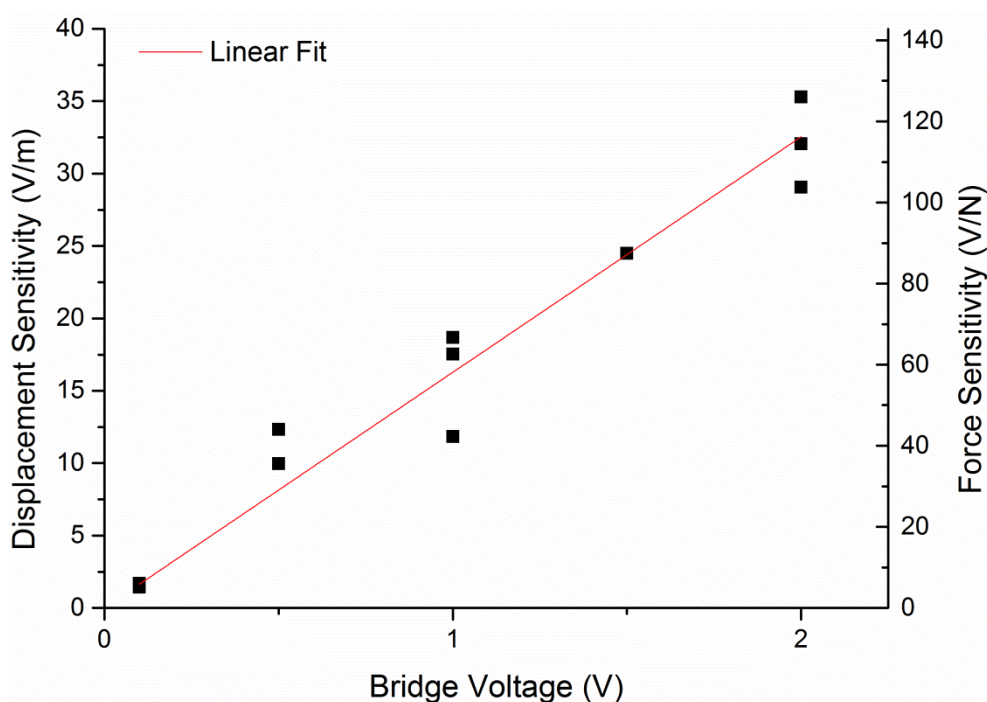
**Figure 5-20: (a) Representative calibration sensitivity curves for QC 1s for deflections as large as 600  $\mu\text{m}$ . Measurements were made using the DUT/PCB/AFM adapter assembly with the suspended platform connected to a Vernier micrometre via a short piece of piano wire in a setup similar to the F-D jig. (b) Representative Linearity % versus the deflection of QC 1s.**

Once the adhesive was fully cured, the output measured by the DMM was zeroed using the coarse and fine potentiometers. To perform the measurements, the QC sensor was deflected in increments of 100  $\mu\text{m}$  to a total deflection of 600  $\mu\text{m}$  and returned to 0  $\mu\text{m}$  also in increments of 100  $\mu\text{m}$ . This procedure was repeated 5 times to confirm the results and investigate the sensor's hysteresis. A 100 output voltages were recorded for

each displacement, and the procedure was repeated for various bridge voltages. Representative results are shown in Figure 5-20.a..



(a)



(b)

**Figure 5-21: Displacement and force sensitivity versus the bridge voltage for (a) QC 1s, (b) TC 1s. The data for the graphs was extracted from the micro and macro (QC 1s only) calibration sensitivity measurements.**

Although the deflections used are 120 times larger than those used in the AFM microscope sensitivity tests, the graph indicates that measured hysteresis in the 5 repeat

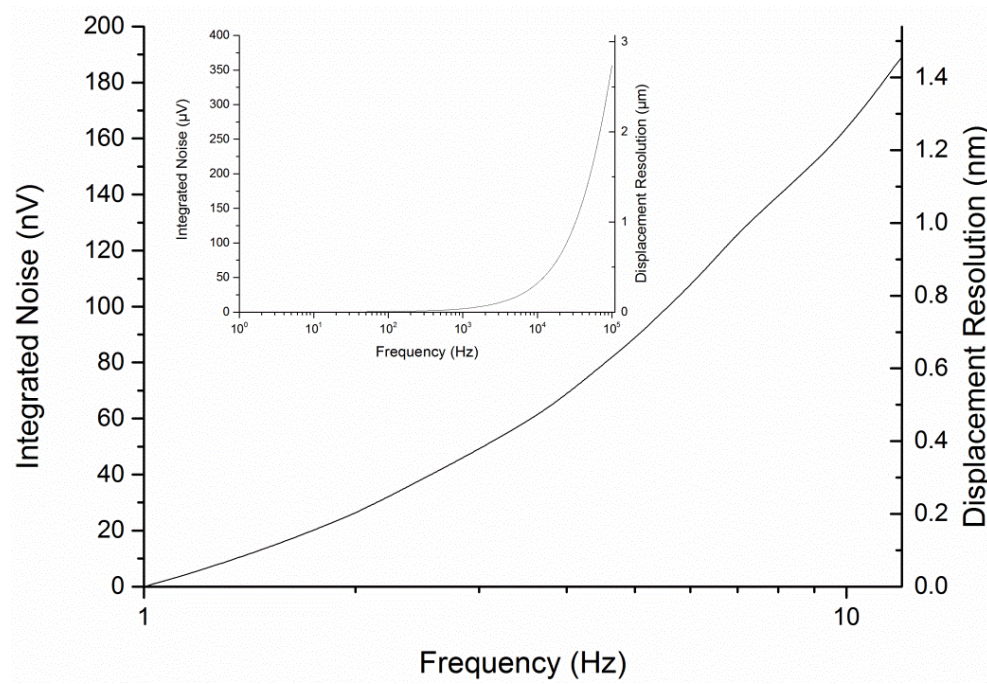
loading and unloading cycles is 0.73%. This is significantly less than the 3.82% hysteresis measured during the AFM microscope sensitivity tests. This supports the argument that the hysteresis observed during the AFM sensitivity tests originated from the test method and not from the device. Figure 5-20.b indicates that the linearity % at 600  $\mu\text{m}$  is -10.7%. During the mechanical measurements the F-D linearity % at 600  $\mu\text{m}$  was +7.7%. This suggests that mechanical and electrical nonlinearities could compensate for one another and that the actual linearity of the device is better than these figures

Figures 5-21.a/b shows the displacement and force sensitivity versus the bridge voltage for QC 1s and TC 1s. The graphs were plotted using data collected from the micro and macro (for QC 1s only) calibration sensitivity curves. The curves indicate that the sensitivity of the sensors varies linearly versus a change in the bridge voltage. This is in agreement with Eq. 2-14 which shows that the force sensitivity,  $S_f$ , is directly proportional to the bridge voltage. The data points for QC 1s have a better linear fit due to the higher signal to noise ratio of the device. At a bridge voltage of 0.39 V, QC 1s and TC 1s have a force sensitivity of 22.4 V/N and 25.3 V/N which is within 2% and 1% of the estimates respectively.

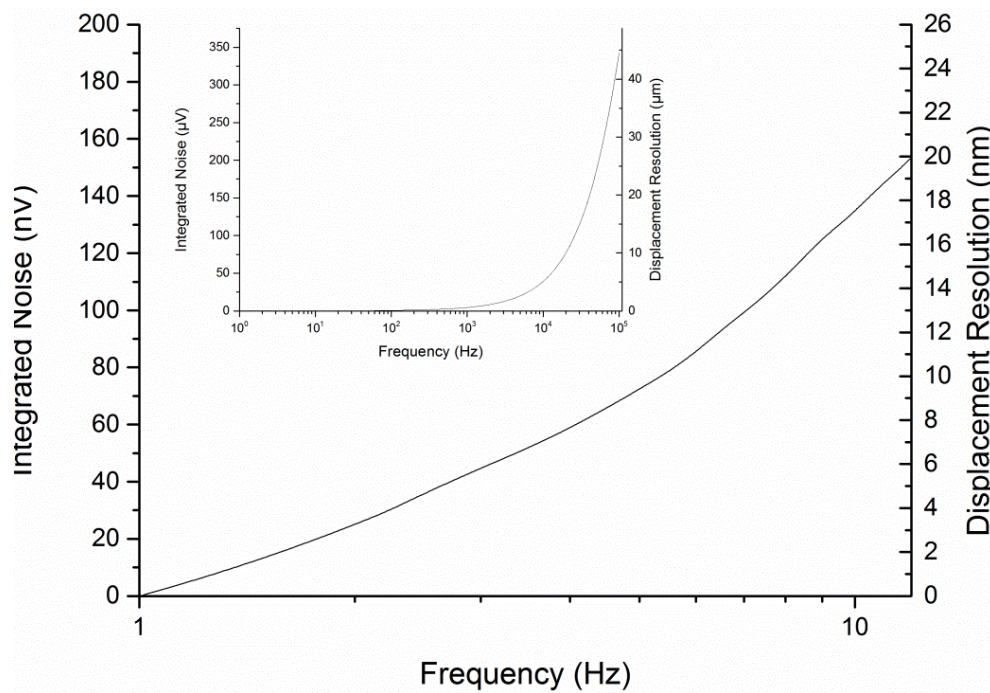
## **5.2.5 Minimum Force and Displacement Resolution**

Using the data collected from the noise spectra analysis and the displacement and force sensitivity measurements, the minimum detectable displacement and force of the sensors can be finally established.

Figure 5-22.a/b shows a representative integrated noise and minimal displacement resolution versus the frequency for measurements made with a bridge voltage of 0.39 V for QC 1s and TC 1s respectively. These indicate that the minimal F-D detectable at 10 Hz is 5.4 nN/1.2 nm and 4.7 nN/17 nm for QC 1s and TC 1s respectively. This results in a displacement resolution that is 29% and 581% higher for QC 1s and TC 1s respectively than the analytical estimates.



(a)



(b)

Figure 5-22: Representative integrated noise and minimal displacement resolution versus the frequency for measurements made with a bridge voltage of 0.39 V for (a) QC 1s and (b) TC 1s

## 5.3 Characterisation of the HWCVD Polysilicon

### Piezoresistors

In the following section the properties of the HWCVD polysilicon piezoresistors are determined. The crystal volume and grain size are estimated using Raman Spectroscopy and AFM imaging while the gauge factor and Hooge factor are calculated from the electrical and mechanical data obtained earlier in the chapter.

#### 5.3.1 Raman Spectroscopy

The polysilicon piezoresistors deposited using HWCVD was analysed using Raman spectroscopy (Renishaw inVia laser Raman spectrometer). The excitation laser used had a 532 nm wavelength and the microscope objective was set to a 20x magnification. The measurements were taken with the laser excitation light intensities set to 0.5%, 1%, 5% and 10%. From the Raman spectroscopy obtained, the crystal volume and thin film quality was determined. In addition, an indication of the grain size and thin film stress was also obtained. Figure 5-23 shows the Raman spectroscopy and deconvolution of the Raman spectrum of the HWCVD polysilicon thin film. The peaks used for the deconvolution are a narrow peak centred at  $520\text{ cm}^{-1}$  and broader peaks centred at  $510\text{ cm}^{-1}$  and  $480\text{ cm}^{-1}$ . A Gaussian profile was chosen for the fit. These peaks are attributed to the crystalline silicon (c-Si) phase, the defective part of the crystalline phase, and the amorphous silicon (a-Si) phase respectively. Also shown is the Raman spectroscopy of a bulk silicon sample and the cumulative fit of the deconvoluted peaks for comparison.

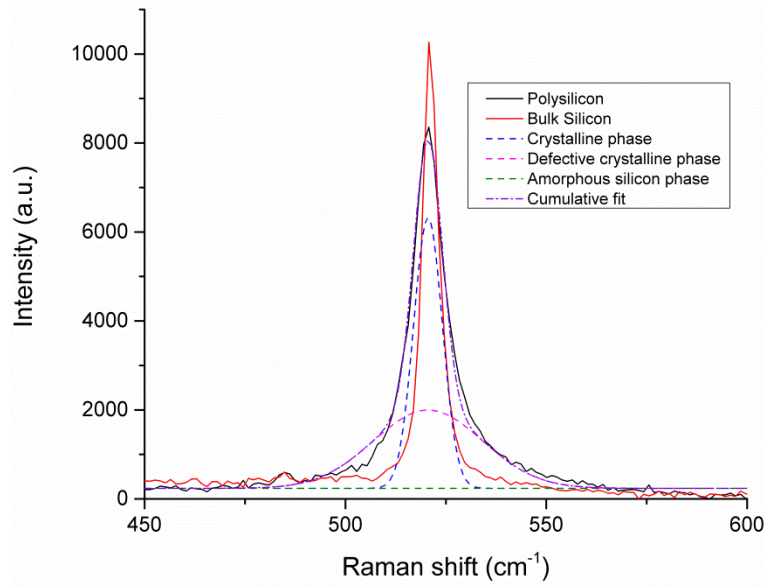


**Figure 5-23: A representative Raman spectroscopy and deconvolution of the Raman spectrum of the HWCVD polysilicon piezoresistors.**

The occurrence of the peaks and Full Width at Half Maximum (FWHM) of the HWCVD polysilicon, crystalline phase, defective crystalline phase, and the bulk silicon are  $520.75 \text{ cm}^{-1}/14.82 \text{ cm}^{-1}$ ,  $520.75 \text{ cm}^{-1}/7 \text{ cm}^{-1}$ ,  $520.66 \text{ cm}^{-1}/35 \text{ cm}^{-1}$ , and  $520.66 \text{ cm}^{-1}/5 \text{ cm}^{-1}$  respectively. The crystal volume fraction,  $X_c$ , is calculated using [12]:

$$X_c = \frac{I_{c-si}}{I_{c-si} + I_{a-si}} \quad \text{Eq. 5-3}$$

where  $I_{c-si}$  and  $I_{a-si}$  are the intensities for the deconvoluted Raman peaks measured at the crystalline silicon peaks (including the defective crystalline peaks), and the amorphous peak respectively [12].

The cumulative fit compares well with the original Raman spectroscopy as does the width of the c-Si to the bulk Si. This indicates that the deconvolution curves are accurate and can be used to indicate the different phases present in the material. The curves indicate a definite presence of a crystalline and defective crystalline phase; however, an amorphous phase was not detected, thus, Eq. 5-2 suggests the polysilicon crystal volume approaches 100%. Similar results were obtained at the different laser excitation light intensities used. Furthermore the symmetry of the polysilicon and small curved shoulders also suggests a highly microcrystalline silicon and the absence of a peak shift indicates that the stress in the material is low [13]. This is a good indicator that the annealing process was sufficient to convert any a-Si into c-Si and that the grain boundaries formed are small in comparison to the size of the c-Si grains.

### 5.3.2 AFM

To obtain an estimate of the grain sizes of the thin film HWCVD polysilicon piezoresistors an AFM microscope (Multimode 5, Veeco) was used to image the surface topography. The images obtained were made in contact mode with a sharp AFM tip (ContAl-G, Budget Sensor).

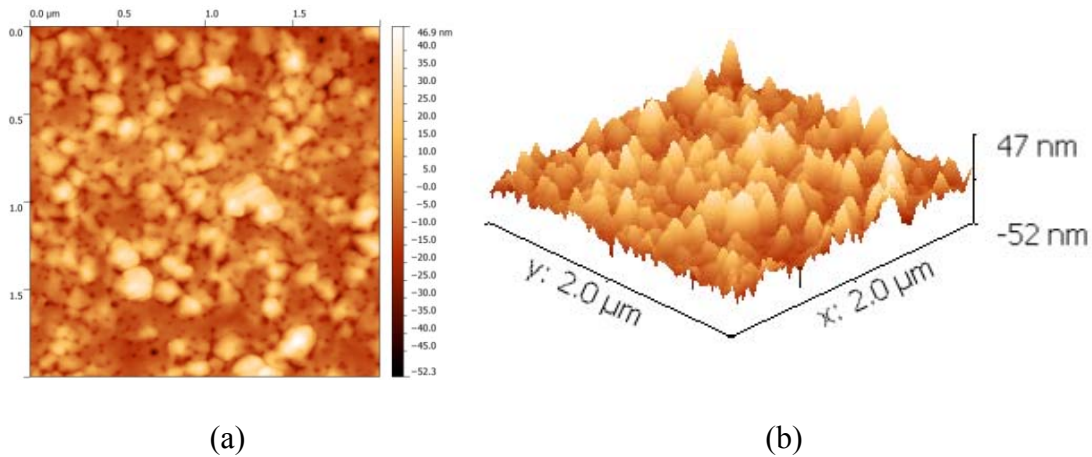


**Figure 5-24: (a) AFM surface imaging and (b) AFM 3D surface topography of the HWCVD polysilicon piezoresistors taken at a resolution of 2944 x 2944 pixels in contact mode using a sharp AFM tip with a nominal tip radius of 10 nm.**

The images obtained (Figure 5-24) indicate the surface roughness on the 600 nm thick piezoresistors was  $<100$  nm. To estimate the grain size, an analysis was performed on the images with the Watershed algorithm available on the Gwyddion modular software for scanning probe microscopy (SPM). The resultant grain marking is shown in Figure 5-25 and indicates that the polysilicon comprises large 100 nm to 200 nm equivalent disc diameter grains combined with random smaller 20 nm to 40 nm equivalent disc diameter grains.

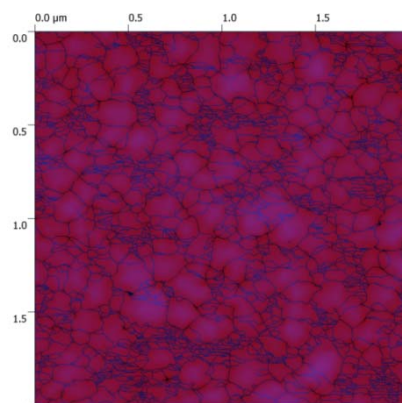


**Figure 5-25: HWCVD polysilicon grains as determined by the Watershed algorithm.**

The graph in Figure 5-26 shows the average of the larger c-Si grains versus the deposition temperature presented in this work. The graph also shows the grain size versus deposition temperatures for samples deposited using LPCVD and annealed at 1000°C for 30 minutes as published by French et.al [7].

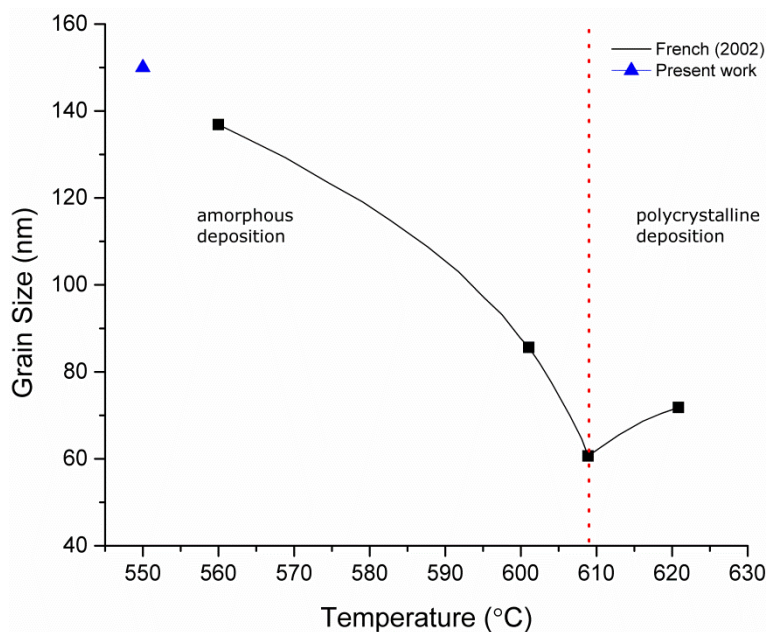
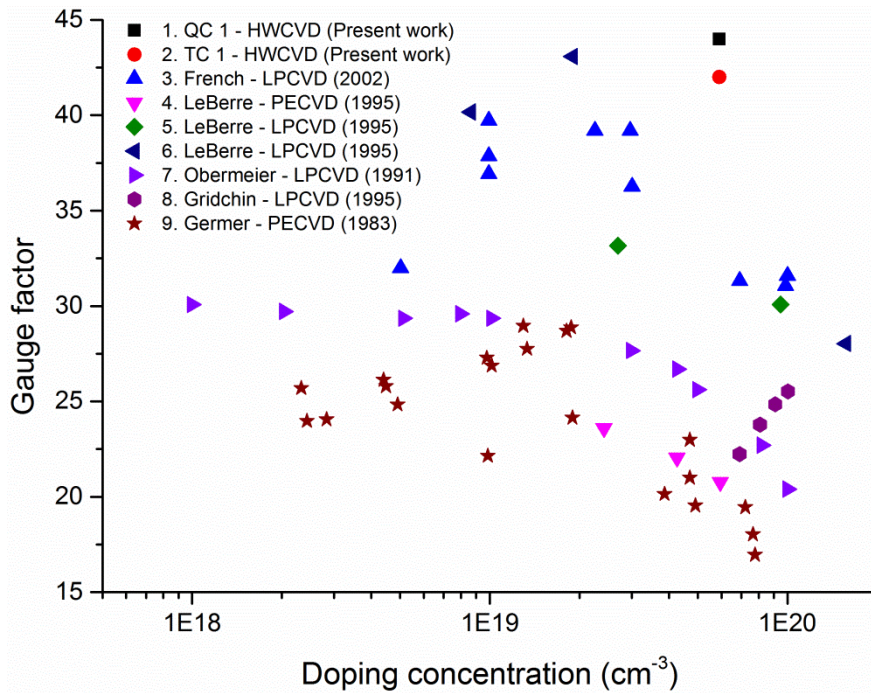


Figure 5-26: Polysilicon grain size versus deposition temperature. Adapted from [7].

By extrapolating the values from the reported data to 550°C the average grain size could be estimated to be ~150 nm. This is equivalent to the average large grain size measured in this work for the HWCVD polysilicon deposited at a temperature of 550°C.

### 5.3.3 Determining the Gauge Factor

Figure 5-27 shows the gauge factors versus the doping concentration estimated for piezoresistors mounted on the QC 1s and TC 1s sensors. The graph includes published data for polysilicon piezoresistors deposited using LPCVD and PECVD with various deposition temperatures and anneals. Table 5-4 provides further detail for the piezoresistors from the published work.



**Figure 5-27: Doping concentraion versus gauge factor for various polysilicon deposition technecques. Adapted from [7, 8, 14-16].**

The measured longitudinal gauge factor for the HWCVD polysilicon piezoresistors was 44 and 42 for the QC 1s and TC 1s sensors respectively. The difference between the two values is marginal, which is expected since there is no correlation between the geometry of the device and the gauge factor. The difference between the two values is thus attributed to measurement error.

**Table 5-4: Anneal details for the data presented in Figure 5-28. Adapted from [7, 8, 14-16].**

No.	Author	Deposition		Anneal		
		Method	Temp.(°C)	Method	Temp.(°C)	Time (min.)
1.	Present work	HWCVD	550	CTA	1000	30
2.	Present work	HWCVD	550	CTA	1000	30
3.	French (2002)	LPCVD	560	CTA	1000	30
4.	LeBerre (1995)	PECVD	320	RTA	1100	0.33
5.	LeBerre (1995)	LPCVD	620	CTA	950	30
6.	LeBerre (1995)	LPCVD	620	RTA	1100	0.33
7.	Obermeier (1991)	LPCVD	N/A	CTA	1000	30
8.	Gridchin (1995)	LPCVD	625	None	N/A	N/A
9.	Germer (1983)	PECVD	300	Laser	N/A	N/A

The measurements made on the HWCVD polysilicon shows the gauge factor to be comparable to a  $\leq 560^\circ\text{C}$  or  $\geq 620^\circ\text{C}$  deposition temperature LPCVD polysilicon with an anneal temperature  $\geq 1000^\circ\text{C}$  or  $\geq 1100^\circ\text{C}$  respectively and regardless if the annealing is CTA or RTA. It can also be ascertained that the piezoresistive qualities of the HWCVD polysilicon is superior to that of PECVD which the data shows to have a gauge factor  $< 30$  regardless of deposition temperature or of the anneal temperature.

### 5.3.4 Determining the Hooge Factor

The Hooge factor,  $\alpha$ , for the HWCVD polysilicon piezoresistors was determined using the noise spectral analysis data (Figure 5-17). The data was fitted to a  $y = ax^b$  type curve where  $a$  is the gradient of the curve where the Hooge noise is dominant. The Hooge factor was then calculated using:

$$\alpha = \frac{4a^2N}{V_{Bridge}^2 n_{pr}} \quad \text{Eq. 5-4}$$

where  $n_{pr}$  is the number of piezoresistors on the device. The fitted values for  $\alpha$  were  $1.4 \times 10^{-3}$  to  $9.8 \times 10^{-3}$  and  $2.7 \times 10^{-2}$  to  $5.6 \times 10^{-2}$  for the QC 1s and the TC 1s devices respectively. The Hooge factor used for the performance estimates for the polysilicon piezoresistors was  $1.8 \times 10^{-3}$  which is within the range of Hooge factors measured from QC 1s; however, this is a magnitude smaller than those measured on TC 1s.

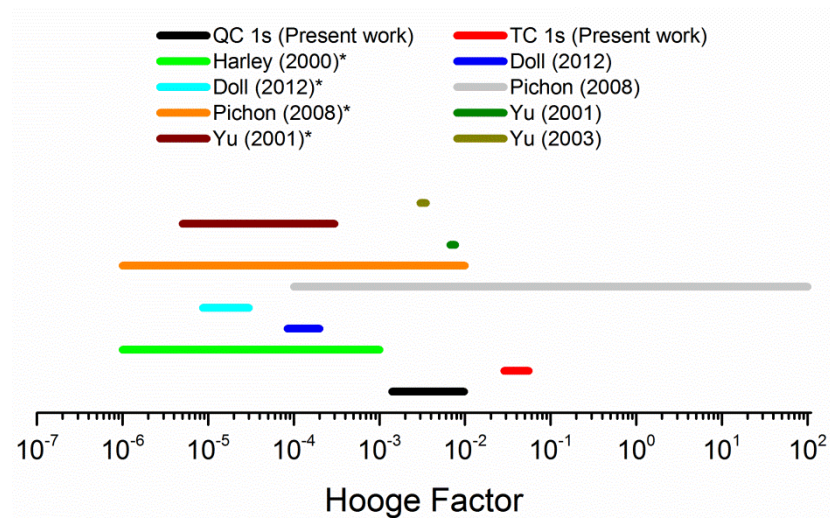


Figure 5-28: The range of the Hooge factor measured in this work for HWCVD polysilicon and as reported in published work for LPCVD polysilicon and crystalline Si (\*) [10, 17-20].

The measured Hooge factors are graphically compared to reported data for polysilicon and crystalline Si materials [10, 17-20] in Figure 5-28. The figure shows that the measured Hooge factor for the HWCVD polysilicon is comparable to the range of the reported data for LPCVD polysilicon. Although the polysilicon used for the piezoresistors in QC 1s and the TC 1s was from the same deposition process, and annealed together, the measured Hooge factor range for the two devices is different. This was likely due to the TC 1s noise anomalies observed and discussed in section 5.2.3 which indicated higher than estimated levels of noise.

## 5.4 Conclusions

In this chapter the mechanical and electrical properties of the fabricated QC sensors and springs were characterised. The self-sensing cantilever, TC 1s, which was fabricated with the QC sensors, was also characterised such that the piezoresistive properties of the HWCVD polysilicon could be measured independently of the QC sensor. The spring constant of QC 1s, 2, and 3 and TC 1s were measured using an AFM microscope in F-D mode. The linearity and range of travel of the QC springs was measured using a F-D jig and the first resonant frequencies were measured using laser Doppler vibrometer. The measured results for the mechanical characteristics of the springs were in good agreement with the analytical and numerical estimates made in Chapter 3 and established that the spring can have a F-D linearity as little as 0.48% at a deflection of 100  $\mu\text{m}$  and a total deflection before fracture of as much as 8000  $\mu\text{m}$  with a F-D linearity of 27.6%.

To begin the electrical characterisation of the device, emphasis was made to ensure that the contact between the aluminium terminals and the piezoresistors was ohmic. This analysis was also used to confirm the sheet resistance measured using the four point probe and that the resistivity of the HWCVD piezoresistors was similar to that obtained using LPCVD in published literature.

The force and displacement sensitivity of the sensors was determined using the F-D mode of an AFM microscope. The sensitivity for the QC sensor was further confirmed for large displacements using the F-D jig. The results from these measurements showed that the sensitivity for QC 1s and TC 1s were within 2 % of the

estimates. However the signal to noise ratio of TC 1s was poor when compared to QC 1s. Using the data from the sensitivity measurements the  $V_{Output}$  versus deflection hysteresis and linearity was estimated to be 0.73% and -10.7% respectively at a displacement of 600  $\mu\text{m}$ . The non-linearity measured in the electrical measurements have the opposite polarity to those measured in the mechanical measurements. This suggests that these will compensate to improve the actual linearity of the sensor. This also indicates that there is an opportunity to investigate if it is possible to cancel the nonlinearities to a greater degree.

A noise analysis of the devices at different values of  $V_{Bridge}$  was performed using a spectrum analyser. The noise analysis for the QC 1s was in good agreement with the estimates as were the estimates for the Johnson noise on TC 1s. However, the Hooge noise measurements for TC 1s did not agree with the estimates. This confirmed the poor signal to noise ratio observed during the force displacement sensitivity analysis. This is likely due to an increase in the Hooge factor due to dry etch processes, the piezoresistive thinning observed during the fabrication of the device (Chapter 4), or temperature fluctuations or thermomechanical coupling due to erratic cantilever heat dissipation. Using the data obtained from the sensitivity and the noise analysis, the minimum force and displacement resolution at 10 Hz was determined to be 5.4 nN/1.2 nm and 4.7 nN/17 nm for QC 1s and TC 1s respectively. This results in a force resolution that is 29% and 581% higher for QC 1s and TC 1s respectively than the analytical estimates. Thus the resolution of QC 1s is within the objectives.

Using Raman spectroscopy, the crystal volume was established to ensure that the annealing process had converted the amorphous silicon to polysilicon. The crystal volume of the polysilicon was found to be approaching 100%. This was further confirmed using an AFM microscope to image the surface topography of the piezoresistors and by performing a Watershed analysis to estimate the average grain size of the polysilicon. The estimated grain size was found to be  $\sim 150$  nm which is similar to what would be expected for polysilicon piezoresistors deposited at  $\leq 560^\circ\text{C}$  using a LPCVD and annealed at  $\geq 1000^\circ\text{C}$ . Based on the data collected the gauge factor of the piezoresistors on QC 1s and TC 1s is 44 and 42 respectively. The minor difference is attributed to experimental error. The gauge factor is comparable to p-type polysilicon piezoresistors deposited using LPCVD and is at the higher limit of the maximum gauge factor possible for polysilicon. A gauge factor for p-type HWCVD piezoresistors has

not been previously reported. Thus the objective of developing a HWCVD polysilicon with a crystal volume > 95% and gauge factor >40 has been met.

The noise spectrum analysis data was also used to determine the Hooge factor for the HWCVD polysilicon piezoresistors. These were estimated to be  $1.4 \times 10^{-3}$  to  $9.8 \times 10^{-3}$  and  $2.7 \times 10^{-2}$  to  $5.6 \times 10^{-2}$  for the piezoresistors on QC 1s and the TC 1s respectively. The difference in these values explains why the signal to noise ratio of TC 1s was poor when compared to the QC 1s sensor and the large discrepancy between the measured and the analytically calculated force displacement resolution.

Based on the characterisation of QC 1s and TC 1s in this chapter, all the objectives for this project have been fulfilled with exception to the proof of concept measurements on biopolymers which will be conducted in Chapter 6

## References

- [1] M.-S. Kim, J.-H. Choi, J.-H. Kim, and Y.-K. Park, "Accurate determination of spring constant of atomic force microscope cantilevers and comparison with other methods," *Measurement*, vol. 43, pp. 520-526, 2010.
- [2] C. T. Gibson, G. S. Watson, and S. Myhra, "Determination of the spring constants of probes for force microscopy/spectroscopy," *Nanotechnology*, vol. 7, pp. 259-262, Sep 1996.
- [3] BudgetSensor. (2014, 19 September). *Contact-G*. Available: [http://www.budgetsensors.com/contact\\_mode\\_afm\\_probes.html](http://www.budgetsensors.com/contact_mode_afm_probes.html)
- [4] J. L. Hutter and J. Bechhoefer, "Calibration of Atomic-Force Microscope Tips (Vol 64, Pg 1868, 1993)," *Review of Scientific Instruments*, vol. 64, pp. 3342-3342, Nov 1993.
- [5] J. Carvill, *Mechanical engineer's data handbook*: Butterworth-Heinemann, 2003.
- [6] J. C. Doll, S. J. Park, and B. L. Pruitt, "Design optimization of piezoresistive cantilevers for force sensing in air and water," *Journal of Applied Physics*, vol. 106, Sep 15 2009.
- [7] P. J. French, "Polysilicon: a versatile material for microsystems," *Sensors and Actuators a-Physical*, vol. 99, pp. 3-12, Apr 30 2002.
- [8] M. Leberre, M. Lemiti, D. Barbier, P. Pinard, J. Cali, E. Bustarret, *et al.*, "Piezoresistance of Boron-Doped Pecvd and Lpcvd Polycrystalline Silicon Films," *Sensors and Actuators a-Physical*, vol. 46, pp. 166-170, Jan-Feb 1995.
- [9] M. S. Raman, T. Kifle, E. Bhattacharya, and K. N. Bhat, "Physical model for the resistivity and temperature coefficient of resistivity in heavily doped

- polysilicon," *Ieee Transactions on Electron Devices*, vol. 53, pp. 1885-1892, Aug 2006.
- [10] J. C. Doll, "Advances in High Bandwidth Nanomechanical Force Sensors with Integrated Actuation," Doctor of Philosophy, Department of Mechanical Engineering, University of Stanford, California, 2012.
- [11] S. J. Park, J. C. Doll, A. J. Rastegar, and B. L. Pruitt, "Piezoresistive Cantilever Performance-Part II: Optimization," *Journal of Microelectromechanical Systems*, vol. 19, pp. 149-161, Feb 2010.
- [12] T. M. B. Masaud, A. Tarazona, E. Jaberansary, X. Chen, G. T. Reed, G. Z. Mashanovich, *et al.*, "Hot-wire polysilicon waveguides with low deposition temperature," *Optics Letters*, vol. 38, pp. 4030-4032, 2013/10/15 2013.
- [13] C. Droz, "Thin Film Microcrystalline Silicon Layers and Solar Cells: Microstructure and Electrical Performances," Institute of Microtechnology, University of Neuchatel, Neuchâtel, 2003.
- [14] W. Germer and W. Tödt, "Low-cost pressure/force transducer with silicon thin film strain gauges," *Sensors and Actuators*, vol. 4, pp. 183-189, 1983.
- [15] E. Obermeier and P. Kopystynski, "Polysilicon as a material for microsensor applications," *Sensors and Actuators A: Physical*, vol. 30, pp. 149-155, 1// 1992.
- [16] V. A. Gridchin, V. M. Lubimsky, and M. P. Sarina, "Piezoresistive properties of polysilicon films," *Sensors and Actuators A: Physical*, vol. 49, pp. 67-72, 6// 1995.
- [17] J. A. Harley and T. W. Kenny, "1/F noise considerations for the design and process optimization of piezoresistive cantilevers," *Journal of Microelectromechanical Systems*, vol. 9, pp. 226-235, Jun 2000.
- [18] X. M. Yu, X. L. Jiang, J. Thaysen, O. Hansen, and A. Boisen, "Noise and sensitivity in polysilicon piezoresistive cantilevers," *Chinese Physics*, vol. 10, pp. 918-923, Oct 2001.
- [19] L. Pichon, A. Boukhenoufa, and C. Cordier, "Low frequency noise in polysilicon thin film transistors: effect of the laser annealing of the active layer," *Physica Status Solidi C - Current Topics in Solid State Physics*, Vol 5, No 10, vol. 5, pp. 3271-3275, 2008.
- [20] X. M. Yu, D. C. Zhang, C. S. Wang, X. F. Du, X. B. Wang, and Y. Ruan, "Chemical sensors based on piezoresistive cantilever array," *Chinese Physics Letters*, vol. 20, pp. 1637-1640, Sep 2003.



## Chapter 6

### Towards Biosensing Applications

In this chapter the feasibility of using the QC sensor as a tool for the characterisation of biological tissue is explored. The investigation of the mechanics of biological tissue has been at the forefront of the development of diagnostic tools and treatment of orthopaedic, cardiovascular, respiratory diseases over the last few decades [1]. These studies have revealed that the physiological state and alterations due to pathological state, such as cancer and osteoarthritis, can be correlated to the mechanical properties of the cell [2-7].

There are several techniques available to the researcher for determining the mechanical properties of biological cells and tissue. These include substrate deformation (SD), substrate composition (SC), embedded particle tracking microfabricated post array detector (mPAD), magnetic twisting cytometry (MTC), cytodetacher (CD), micropipette aspiration (MA), optical stretcher (OS) microneedle (MN), biomembrane force probe (BFP), optical or laser tweezers/traps (OT), magnetic tweezers (MT), high resolution force spectroscopy (HRFS) and AFM. The interested reader is referred to [2, 8-10] for further details regarding these techniques. From these the techniques, the AFM has been the most adaptable and has been used to investigate the mechanical properties at both the tissue level (heart, lung, bone, cartilage, blood vessel, skeletal and cardiac muscles) and at the cellular level. This was possible because the forces imparted on to the specimen can be readily customised by changing the spring constant of the optical lever. Commercially available spring constants are in the 0.01 - 450N/m range, which allows for a vast range of possible probing forces [8, 11]. However, the actual available force range for a given setup is greatly reduced by the

range of the photodiode and the linear limit of the optical lever. This deflection limit may prevent complete phenomena from being investigated. The difficulties encountered are further exacerbated by sample damage caused by laser heating, and laser reflection/refraction error in experiments performed in an aqueous environment which is typically required to keep a cell's normal function [9, 12].

The QC sensor presented in this work does not use a laser, thus specimen damage and errors due to reflection/refraction are completely avoided. Moreover, the sensor does not use a photodiode which would limit the measurement range. Instead, the QC sensor uses a spring design which features a high range of linearity and deflection. This allows the device to make accurate measurements over a wide range of forces and displacements. Figures 6-1 and Figure 6-2 compare the F-D range of the QC sensor to the other techniques used to probe biological tissue. Figure 6-1 shows that the force range of QC 1s to 6s greatly increases the range of the measurements possible. Moreover, Figure 6-2 shows that the displacement range of QC 1s, 2s and 3s almost includes the combined range of all the other techniques. This provides an opportunity for measurements that were previously not possible with the other techniques. A further advantage is that the QC sensor is not as cumbersome as the conventional desktop AFM, and can thus be used in otherwise difficult to access areas or used in combination with other tools such as the SEM, or in-vivo.

In this chapter the potential of the QC MEMS sensor as a tool for the characterisation of biopolymers is determined. This is achieved by establishing whether it can detect differences in agarose hydrogels samples prepared with different concentrations of agarose and determine their Young's modulus. Agarose hydrogels were used as they exhibit mechanical properties of the same magnitude as that found in biological cells (Figure 6-3) [13].

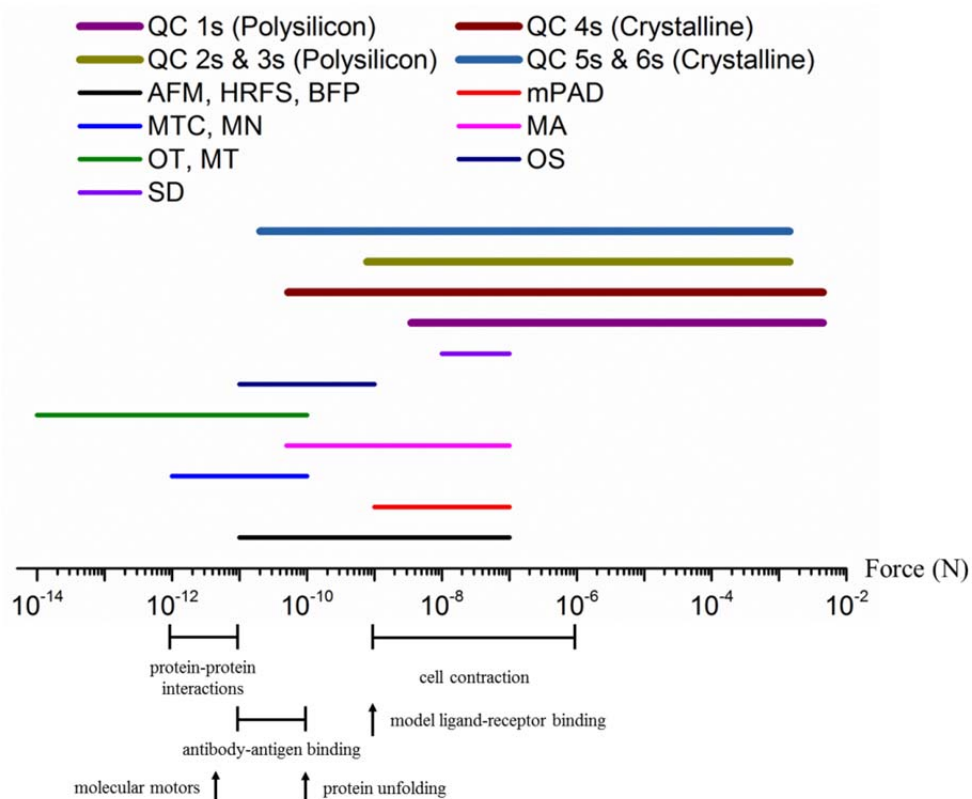


Figure 6-1: Experimental techniques including sensors developed in this work versus the force range and biological events. Adapted from [1, 8-10, 14, 15].

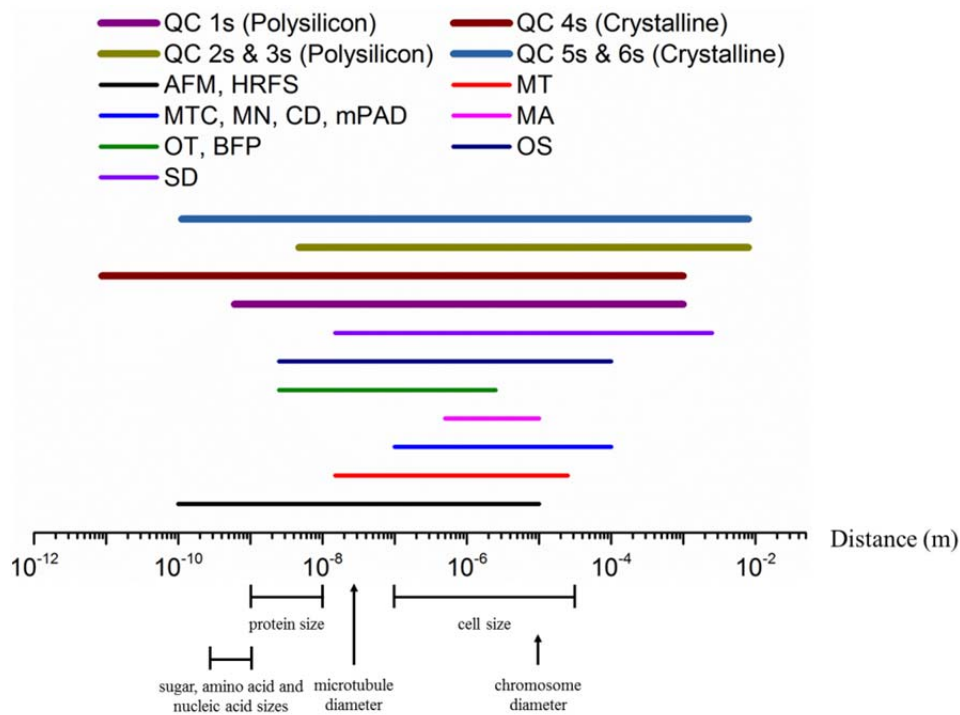


Figure 6-2: Experimental techniques including sensors developed in this work versus the displacement range and dimensions of biological structures. Adapted from [1, 8-10, 15].

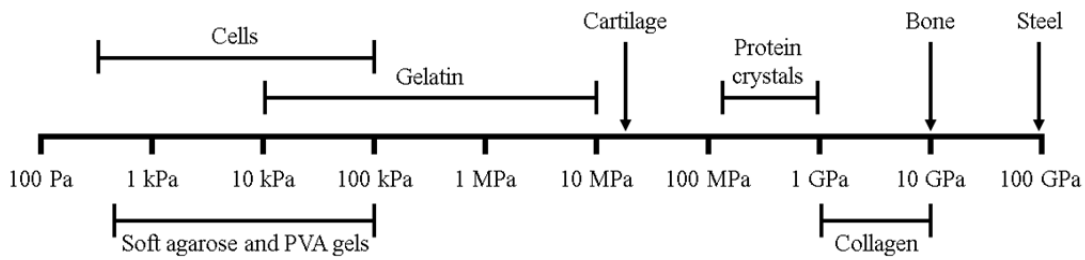


Figure 6-3: Young's modulus of several biomaterials. Adapted from [2, 13].

## 6.1 Materials and methods

Laboratory grade agarose and ultra-pure deionized (DI) water were used to prepare six agarose gel samples with weight to weight ratios of 1 to 6%. The agarose/DI water solutions were prepared beforehand in glass flasks and sealed to avoid evaporation. To avoid sample dehydration, which would lead to the sample hardening, each sample was heated to form a gel immediately before testing. To gel the samples, thoroughly stirred agarose/DI water solutions were heated in a microwave for 20 seconds, stirred and heated again until the solution became a clear gel. The gel was then poured into a mould that was fabricated by cyanoacrylate bonding O-rings onto a thick aluminium block which provided a heat-sink. This encouraged the gels to cool and cure at a faster rate thus reducing the dehydration of the sample before testing. The total time between heating and testing was less than ten minutes. The samples measured 8 mm in diameter and had a thickness of 1 mm.

To prepare the QC sensor for indentation testing, a probe was affixed to the QC sensor's suspended platform using cyanoacrylate adhesive. The probe was fashioned from a 100  $\mu\text{m}$  diameter x 3 mm length of piano wire cut using wire cutters. Typically the tips of indenters are made from materials with a Young's modulus much greater than that of the material being tested. Materials such as diamond and sapphire are customary. This ensures that the compliance of the sample is much greater than that of the tip, thus the compliance of the indenter becomes negligible. At this stage the probe mounted on the QC sensor is made from carbon steel which is significantly harder than the material being tested. However, since the probe was cut with wire cutters, the tip was wedge shaped and needed to be modified into a spherical shape. This was necessary since indentation testing on soft polymers, such as agarose hydrogels, is typically performed using spherical tips to reduce sample damage by minimising the plastic deformation and stress concentration which would otherwise occur if a sharp or flat tip

is used [16]. To form a parabolic tip on the probe, the QC sensor with probe was assembled into the AFM adapter and onto an AFM microscope. A small amount of cyanoacrylate adhesive gel was placed on to a metal disc and loaded on to the AFM's sample stage. The QC sensor was lowered using the AFM microscope's macro actuation until the end of the probe was immersed into the gel and then immediately retrieved. This formed a parabolic bead at the tip of the probe with a diameter of  $\sim 200$   $\mu\text{m}$ . The adhesive was allowed to cure for 24 hours prior to use to ensure complete hardening. The cured cyanoacrylate adhesive parabolic tip has a Young's modulus of 1.2 GPa [17] which is still significantly greater than that of the agarose gels being measured. Thus the probe's compliance can still be ignored from the calculations. Figure 6-4 shows the QC sensor with the attached probe and parabolic tip.

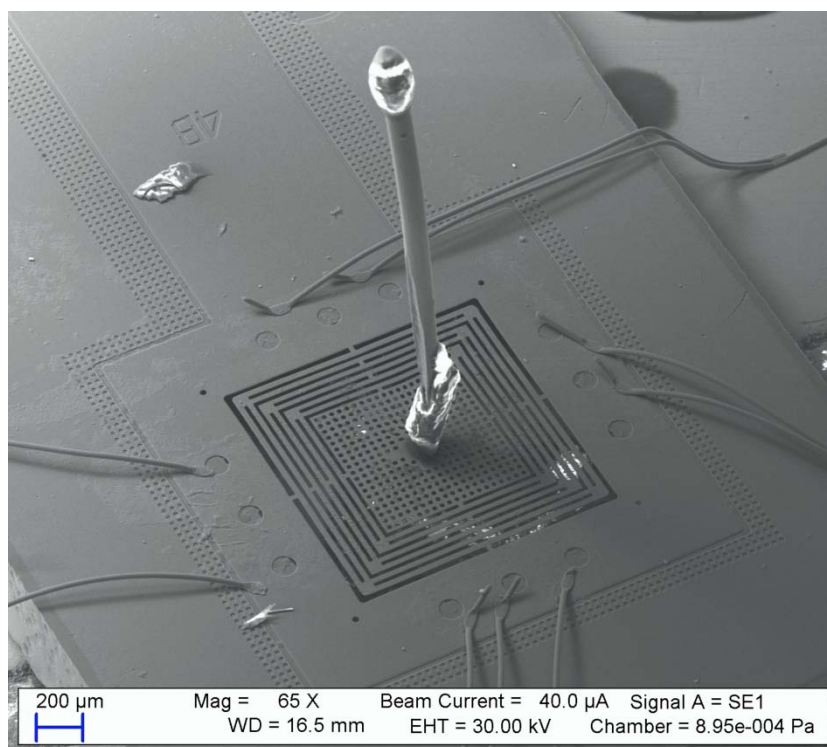


**Figure 6-4: QC MEMS F-D sensor with probe attached.**

### 6.1.1 Indentation

Prior to testing, the sensitivity of the QC MEMS was calibrated on a stainless steel disc. The disc is infinitely hard relative to the DUT, thus the resultant probe penetration depth was ignored from the sensitivity calculations and the gradient of the voltage to displacement curve obtained during the calibration measurements was equivalent to the sensitivity of the QC sensor.

During sample stiffness testing, the applied maximum load was limited by restricting the maximum deflection of the probe to 250 nm. This is equivalent to a maximum force of 1125 nN. The indentation depth was < 10% the sample thickness thus complies with Bueckle’s indentation depth limit [18]. All samples were tested at 1 Hz and 1025 data points for each deflection were recorded. Figure 6-7 shows representative F-D curves for the hydrogel samples.

### 6.1.2 Determining Young’s Modulus

To determine the Young’s modulus from the data collected, the unloading curves were modelled using the power law relation as outlined by Oliver and Pharr [19]:

$$P_i = \hat{A} (h_{max} - h_f)^{m_i} \quad \text{Eq. 6-1}$$

where  $P_i$  is the applied load and  $\hat{A}$ , and  $m_i$  are fitting parameters with  $m_i = 1.5$  when spherical indenters are used [20].  $h_{max}$ , and  $h_f$  (Figure 6-5 and 6-6) are the total displacement and the final residual hardness impression respectively; however,  $h_f$  can also be used as a fitting parameter. The fitting parameters were found using the Levenberg-Marquardt Algorithm (LMA) for non-linear curve fitting. The unloading curves were used in the analysis as these can be considered to be completely elastic.

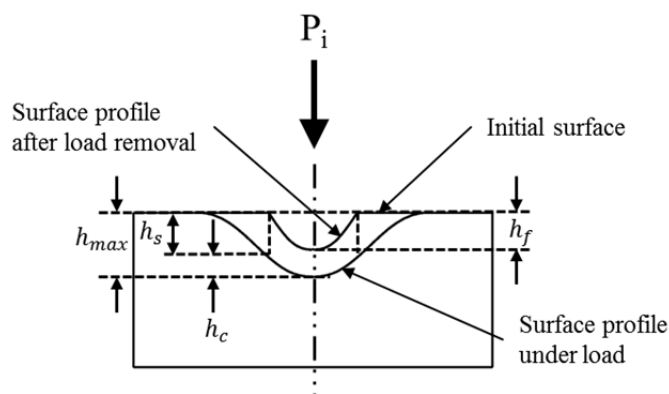
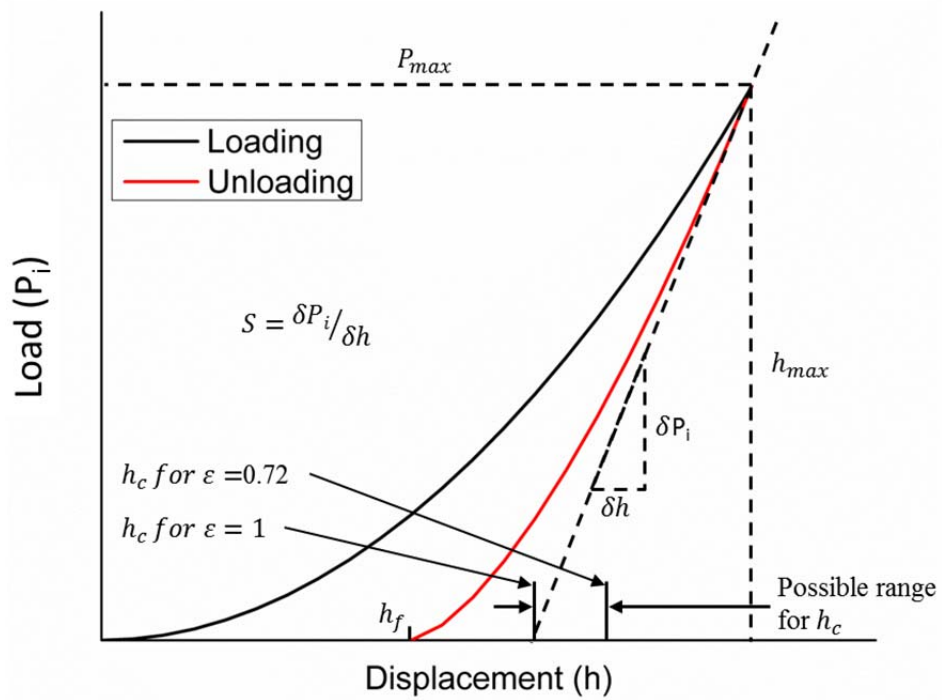


Figure 6-5: A schematic showing the surface profile before and after the application of the load. The various variables used in the calculations are also included. Adapted from [19].



**Figure 6-6:** A schematic representation of the load versus displacement for a single loading and unloading of the indenter. The graphical representation of the various variables used in the calculations is also included. Adapted from [19].

Using the top 25% of the resultant curve, the slope  $S$  (Figure 6-6), was found and used to determine the reduced Elastic Modulus,  $E_r$ , using [19]:

$$E_r = \frac{\sqrt{\pi} S}{2 \sqrt{A}} \quad \text{Eq. 6-2}$$

where  $A$  is the projected contact area. In this work, the deflections (250 nm) are relatively small when compared to the radius of the indenter tip (100  $\mu\text{m}$ ), thus the parabolic tip was considered as spherical at the point of contact and the project contact area function was calculated using [21]:

$$A = \pi (2r_{tip}h_c - h_c^2) \quad \text{Eq. 6-3}$$

where  $r_{tip}$  is the radius of the tip and  $h_c$  is the contact depth shown in Figure 6-5 and Figure 6-6 and calculated using [19]:

$$h_c = h_{max} - h_s \quad \text{Eq. 6-4}$$

where  $h_{max}$  is the maximum deflection, equal to the trigger deflection, and  $h_s$  is the displacement at the perimeter of the contact and can be calculated using [19]:

$$h_s = \frac{\xi P_{max}}{S} \quad \text{Eq. 6-5}$$

where  $\xi$  is a geometric constant equal to 0.73 for conical indenters, 0.75 for paraboloid of revolution, and 1.0 for flat punches [19]. The sample's Young's Modulus,  $E_s$ , was finally calculated from the  $E_r$  using [19]:

$$\frac{1}{E_r} = \frac{(1 - \nu_s^2)}{E_s} + \frac{(1 - \nu_i^2)}{E_i} \quad \text{Eq. 6-6}$$

where  $E_i$  is the Young's modulus for the indenter and  $\nu_s$  and  $\nu_i$  are the Poisson ratio for the sample and indenter respectively. Since the water content of agarose hydrogels was high, it was considered as incompressible, thus  $\nu_s$  was taken as 0.5 [22]. Also, given that the Young's modulus of the cyanoacrylate tip is 1.2 GPa [17], and therefore much greater than that of the agarose gel tested, Eq. 6-6 was simplified to:

$$E_s = \frac{E_r}{(1 - \nu_s^2)} \quad \text{Eq. 6-7}$$

## 6.2 Results and discussion

Figure 6-7 shows representative F-D curves obtained for the different concentrations of agarose hydrogels measured. These curves indicate a gradual decrease in indentation depth and an increase in gradient versus an increase in agarose concentrations as would be expected.

From similar curves generated over multiple indentation measurements the average and standard deviation Young's modulus were calculated and are shown graphically in Figure 6-8. The Young's modulus for the 1% to 6% (in 1% steps) agarose concentrations as measured with the QC sensor are  $19 \pm 9$  kPa,  $50 \pm 16.4$  kPa,  $60 \pm 15$  kPa,  $71 \pm 26$  kPa,  $96 \pm 20$  kPa, and  $114 \pm 33$  kPa respectively. Despite the standard deviation being as large as 33 kPa, the average results indicate a linear relationship between the Young's modulus and the agarose concentration. This is in agreement with the measurements made by Ahearne [23], for low concentrations of agarose (0.4% to 1.2%). These measurements disagree with measurements made by Normand et al. [24] for higher concentrations of agarose (0.3% to 10 %); however, the results obtained by Normand et al. have been previously disputed by Park et al. [25].

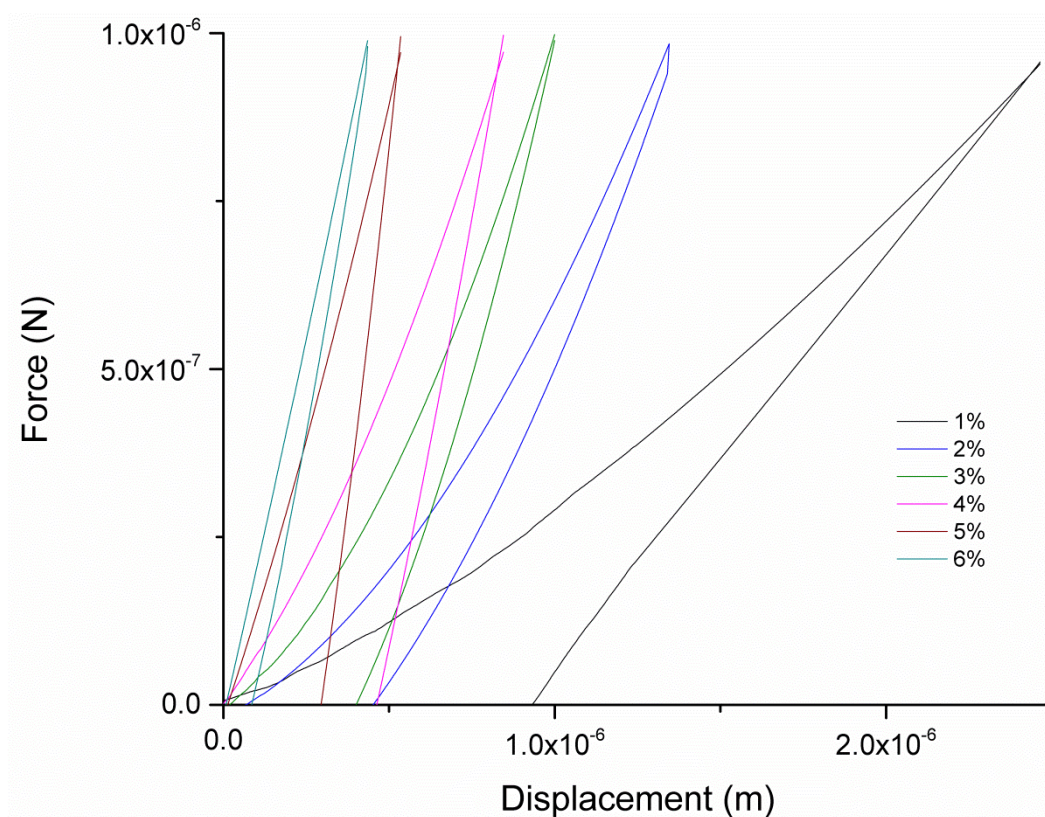


**Figure 6-7: Representative indents in 1% to 6% agarose hydrogels made using the QC F-D MEMS sensor modified to include probe with a  $\sim 200$   $\mu\text{m}$  diameter parabolic bead tip.**

Figure 6-9 shows data reported in literature for the Young's modulus versus agarose concentrations. For clarity, values reported as reduced modulus [21, 24] were converted to Young's modulus using Eq. 6-7, and the measurement reported by Salerno [26] was revised to reflect a Poisson ratio of 0.5 as was used throughout this work. The data indicates two main data groups with the Young's modulus as measured by Ebenstein [21], and Normand [24] peaking higher than the rest at higher agarose concentrations. Figure 6-10 focuses on the lower values of the same data. This graph indicates that the measurements made with the QC sensor fall between the two extremes of the reported measurement data.

The spread of Young's modulus versus the agarose concentration in the reported data is significant. This could stem from differences in the materials used and sample preparation methods more than from the different techniques, equipment and tips used in the measurements. For instance, many different grades of agarose exist and some of the reported data used phosphate buffered saline (PBS) for their hydrogel preparation [23, 27] rather than DI water. Other observations include heating using a microwave [21, 26] versus a heated water bath [28], sample hydration by submersion, droplets,

foam [21, 27-29] versus refrigerated storage [21, 24], versus left in a dust free environment [26] or combinations of all of these. Since submerging in water at ambient temperature causes agarose to swell [30], and prolonged exposure to the ambient and refrigeration cause the agarose to dehydrate, which has been shown to drastically alter the Young's modulus of hydrogels [21, 31], caution needs to be taken when comparing measured data to reported measurements. It was for this reason that samples in this work were heated, moulded, cooled, and tested in less than ten minutes.

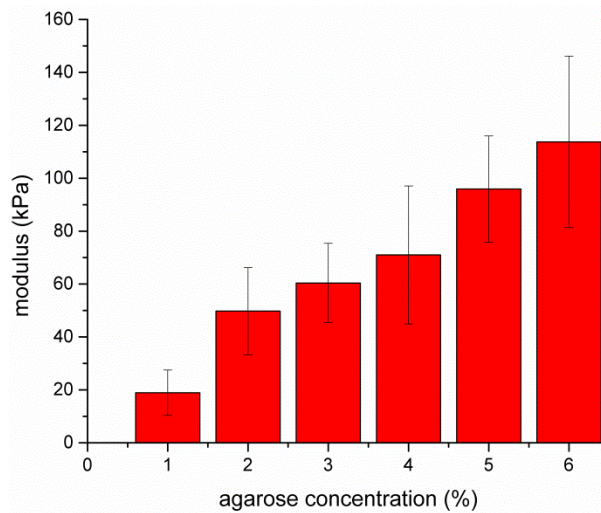


**Figure 6-8: Average Young's modulus versus various levels of agarose concentrations measured using the QC MEMS F-D sensor. The graph shows an increase in the Young's modulus for each incremental increase in agarose concentration. The error bars represent the range of values measured.**

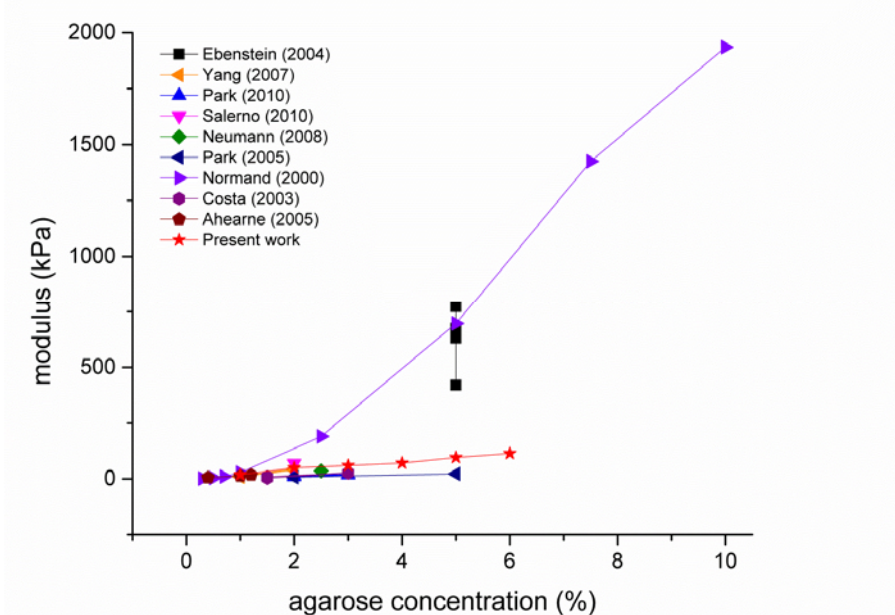


**Figure 6-9: Young's Modulus versus various levels of agarose concentrations from published data and measurements made using the QC MEMS F-D sensor. The graph indicates that the data is distributed into two main groups. Published data from [13, 21, 23, 24, 26, 27, 29, 31, 32].**

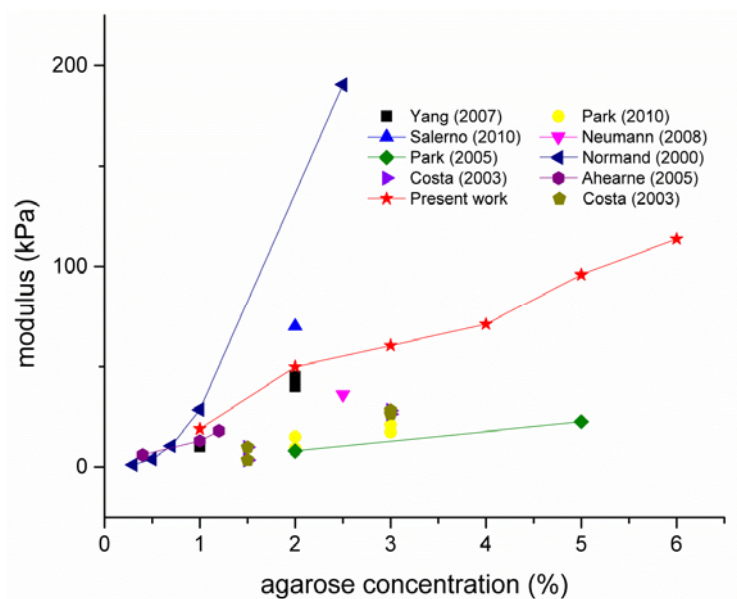


**Figure 6-10: Young's Modulus versus various levels of agarose concentrations from published data and measurements made using the QC MEMS F-D sensor. This is the same data as shown in Figure 6-9; however, the agarose concentration was limited to 6% to magnify the distribution of the measurements at lower concentrations. This graph indicates that the measurements made using the QC MEMS F-D sensor falls between the extremes of the published data. Published data from [13, 23, 24, 26, 27, 29, 31, 32].**

### 6.3 Conclusions

Devices such as the QC sensor are essential for the fundamental investigation of the mechanics of biological cells and tissue. The QC sensor enables measurements to be made over a broader range of displacements and forces which could enable capturing phenomena that would otherwise be missed. In this chapter, a QC sensor was adapted to perform indentation testing on soft agarose hydrogels. Agarose hydrogels are frequently used to mimic biological tissue. To enable the QC sensor to make these measurements, a probe with a parabolic tip was attached to the suspended platform. Indentation tests were carried out on hydrogel samples with different levels of agarose content. The measurements were made using a conventional desktop AFM microscope with the QC sensor replacing the AFM head. The measurements made using the QC sensor showed that the device was able to differentiate between the different agarose concentrations and determine the Young's modulus to be  $19 \pm 9$  kPa,  $50 \pm 16.4$  kPa,  $60 \pm 15$  kPa,  $71 \pm 26$  kPa,  $96 \pm 20$  kPa, and  $114 \pm 33$  kPa for 1% to 6% (in 1% steps) agarose concentrations respectively. The values obtained for the Young's modulus are within the range of reported data, thus confirming the potential use of the QC sensors as a tool for the characterisation of biopolymers thus fulfilling the last objective of this project.

## References

- [1] K. A. Addae-Mensah and J. P. Wikswo, "Measurement techniques for cellular biomechanics in vitro," *Experimental Biology and Medicine*, vol. 233, pp. 792-809, Jul 2008.
- [2] S. Kasas and G. Dietler, "Probing nanomechanical properties from biomolecules to living cells," *Pflügers Archiv-European Journal of Physiology*, vol. 456, pp. 13-27, Apr 2008.
- [3] G. Bao and S. Suresh, "Cell and molecular mechanics of biological materials," *Nature Materials*, vol. 2, pp. 715-725, Nov 2003.
- [4] D. H. Kim, P. K. Wong, J. Park, A. Levchenko, and Y. Sun, "Microengineered Platforms for Cell Mechanobiology," *Annual Review of Biomedical Engineering*, vol. 11, pp. 203-233, 2009.
- [5] D. L. Bader and M. M. Knight, "Biomechanical analysis of structural deformation in living cells," *Medical & Biological Engineering & Computing*, vol. 46, pp. 951-963, Oct 2008.
- [6] M. Lekka, "Atomic Force Microscopy a Tip for Diagnosing Cancer," *Nature Nanotechnology*, vol. 7, pp. 691-692, Nov 2012.
- [7] H. T. Nia, I. S. Bozchalooi, Y. Li, L. Han, H. H. Hung, E. Frank, *et al.*, "High-Bandwidth AFM-Based Rheology Reveals that Cartilage is Most Sensitive to High Loading Rates at Early Stages of Impairment," *Biophysical Journal*, vol. 104, pp. 1529-1537, Apr 2 2013.
- [8] K. J. Van Vliet, G. Bao, and S. Suresh, "The biomechanics toolbox: experimental approaches for living cells and biomolecules," *Acta Materialia*, vol. 51, pp. 5881-5905, Nov 25 2003.
- [9] O. Loh, A. Vaziri, and H. D. S. M. Espinosa, "The Potential of MEMS for Advancing Experiments and Modeling in Cell Mechanics," *Experimental Mechanics*, vol. 49, pp. 105-124, Feb 2009.
- [10] M. L. Rodriguez, P. J. McGarry, and N. J. Sniadecki, "Review on Cell Mechanics: Experimental and Modeling Approaches," *Applied Mechanics Reviews*, vol. 65, Nov 2013.
- [11] F. M. Serry, "Improving the Accuracy of AFM Force Measurements: The Thermal Tune Solution to the Cantilever Spring Constant Problem," *Bruker Application Note*, 2010.
- [12] S. J. Park, M. B. Goodman, and B. L. Pruitt, "Analysis of nematode mechanics by piezoresistive displacement clamp," *Proceedings of the National Academy of Sciences of the United States of America*, vol. 104, pp. 17376-17381, Oct 30 2007.

- [13] T. Neumann, "Determining the elastic modulus of biological samples using atomic force microscopy," *JK Instruments Application Report*, 2008.
- [14] (22 June). *Micro Materials Limited*. Available: <http://www.micromaterials.co.uk/the-nano-test/nanoindentation/>
- [15] A. Noy, *Handbook of molecular force spectroscopy*. New York, NY: Springer, 2008.
- [16] D. M. Ebenstein and L. A. Pruitt, "Nanoindentation of biological materials," *Nano Today*, vol. 1, pp. 26-33, Aug 2006.
- [17] H. Helbawi, L. C. Zhang, and I. Zarudi, "Difference in subsurface damage in indented specimens with and without bonding layer," *International Journal of Mechanical Sciences*, vol. 43, pp. 1107-1121, Apr 2001.
- [18] I. M. Khan, L. Francis, P. S. Theobald, S. Perni, R. D. Young, P. Prokopovich, *et al.*, "In vitro growth factor-induced bio engineering of mature articular cartilage," *Biomaterials*, vol. 34, pp. 1478-1487, 2013.
- [19] W. C. Oliver and G. M. Pharr, "An Improved Technique for Determining Hardness and Elastic-Modulus Using Load and Displacement Sensing Indentation Experiments," *Journal of Materials Research*, vol. 7, pp. 1564-1583, Jun 1992.
- [20] M. R. Vanlandingham, S. H. McKnight, G. R. Palmese, R. F. Eduljee, J. W. Gillespie, and R. L. McCulough, "Relating elastic modulus to indentation response using atomic force microscopy," *Journal of Materials Science Letters*, vol. 16, pp. 117-119, Jan 15 1997.
- [21] D. M. Ebenstein and L. A. Pruitt, "Nanoindentation of soft hydrated materials for application to vascular tissues," *Journal of Biomedical Materials Research Part A*, vol. 69A, pp. 222-232, May 1 2004.
- [22] V. T. Nayar, J. D. Weiland, C. S. Nelson, and A. M. Hodge, "Elastic and viscoelastic characterization of agar," *Journal of the Mechanical Behavior of Biomedical Materials*, vol. 7, pp. 60-68, Mar 2012.
- [23] M. Ahearne, Y. Yang, A. J. El Haj, K. Y. Then, and K. K. Liu, "Characterizing the viscoelastic properties of thin hydrogel-based constructs for tissue engineering applications," *Journal of the Royal Society Interface*, vol. 2, pp. 455-463, Dec 22 2005.
- [24] V. Normand, D. L. Lootens, E. Amici, K. P. Plucknett, and P. Aymard, "New insight into agarose gel mechanical properties," *Biomacromolecules*, vol. 1, pp. 730-738, Win 2000.
- [25] G. Yang, J. Tang, S. Kato, Q. Zhang, L. C. Qin, M. Woodson, *et al.*, "Magnetic nanowire based high resolution magnetic force microscope probes (vol 87, pg 123507, 2005)," *Applied Physics Letters*, vol. 87, pp. -, Nov 28 2005.

- [26] M. Salerno, S. Dante, N. Patra, and A. Diaspro, "AFM Measurement of the Stiffness of Layers of Agarose Gel Patterned With Polylysine," *Microscopy Research and Technique*, vol. 73, pp. 982-990, Oct 2010.
- [27] H. M. M. Y. Costa Kevin D., Hung Clark T., "MULTI-SCALE MEASUREMENT OF MECHANICAL PROPERTIES OF SOFT SAMPLES WITH ATOMIC FORCE MICROSCOPY," presented at the Summer Bioengineering Conference, 2003.
- [28] H. Haga, S. Sasaki, M. Morimoto, K. Kawabata, E. Ito, K. Abe, *et al.*, "Imaging elastic properties of soft materials immersed in water using force modulation mode in atomic force microscopy," *Japanese Journal of Applied Physics Part 1-Regular Papers Short Notes & Review Papers*, vol. 37, pp. 3860-3863, Jun 1998.
- [29] Y. Yang, P. O. Bagnaninchi, M. Ahearne, R. K. Wang, and K. K. Liu, "A novel optical coherence tomography-based micro-indentation technique for mechanical characterization of hydrogels," *Journal of the Royal Society Interface*, vol. 4, pp. 1169-1173, Dec 22 2007.
- [30] Y. Huang and J. L. Yang, "Novel Colloidal Forming of Ceramics," *Novel Colloidal Forming of Ceramics*, pp. 1-385, 2011.
- [31] S. J. Park, M. B. Goodman, and B. L. Pruitt, "Measurement of mechanical properties of *Caenorhabditis elegans* with a piezoresistive microcantilever system," *2005 3rd IEEE/EMBS Special Topic Conference on Microtechnology in Medicine and Biology*, pp. 400-403, 2005.
- [32] S.-J. Park, *Development of piezoresistive microcantilever based force feedback system for analysis of mechanosensation in caenorhaditis elegans nematodes*, 2009.

## Chapter 7

### Conclusions, Future work and Possible Applications

#### 7.1 Conclusions

In this work, a novel F-D MEMS sensor with nN/nm resolution, high linearity, high out-of-plane compliance, low in-plane compliance and a large deflection range for the analysis of biopolymers was realised. To achieve this, a novel QC spring with integrated full Wheatstone bridge for piezoresistive self-sensing was developed.

The QC spring and integrated piezoresistors were optimised to achieve nN/nm resolution with polysilicon piezoresistors, and minimise the heat dissipated. Furthermore it was shown that pN/pm resolution is theoretically possible with crystalline piezoresistors.

Initial attempts to fabricate the device using conventional methods resulted in over etching and stiction during the release of the suspended structure. To circumvent these issues a novel fabrication process was developed. This process used a KOH wet etch to semi release the device prior to frontside fabrication, and a dry etch to fully release the device post frontside fabrication. Using the developed fabrication process QC springs, QC sensors, and self-sensing cantilevers were fabricated.

The mechanical characterisation of the sensors has shown that the spring constant, linearity, deflection limit and first resonate frequency to be in good agreement with the analytical and numerical measurements and established that the spring can have a F-D linearity as little as 0.48% at a deflection of 100  $\mu\text{m}$  and a total deflection before

fracture of as much as 8000  $\mu\text{m}$  with a F-D linearity of 27.6%. The electrical characterisation of the device showed that the sensitivity is in agreement with the analytical calculations. The force and displacement resolution at 1-10 Hz was determined to be 5.4 nN/1.2 nm and 4.7 nN/17 nm for QC 1s and TC 1s respectively. This is 29% and 581% higher than the estimated resolution of QC 1s and TC 1s respectively. The  $V_{Output}$  versus deflection hysteresis and linearity of QC 1s was estimated to be 0.73% and -10.7% respectively at a displacement of 600  $\mu\text{m}$ .

The characterisation of the HWCVD polysilicon piezoresistors using Raman spectroscopy indicated that the polysilicon crystal volume approached 100% and had low levels of stress. This is a good indicator that the annealing process was sufficient to convert any amorphous silicon into polysilicon and that the grain boundaries formed are small in comparison to the size of the crystalline silicon grains. Images produced using AFM and processed using a Watershed algorithm estimated the grain size of the polysilicon to approach 150 nm. This is comparable to what would be expected from a low temperature ( $\leq 560^\circ\text{C}$ ) polysilicon deposition using LPCVD with a high temperature ( $\geq 1000^\circ\text{C}$ ) anneal.

Using the sensitivity measurements the gauge factor of the piezoresistors on QC 1s and TC 1s was calculated to be 44 and 42 respectively. The minor difference is attributed to experimental error. The measured gauge factor for the HWCVD polysilicon is comparable to p-type polysilicon piezoresistors deposited using LPCVD and is at the higher limit of the maximum gauge factor possible for polysilicon. A gauge factor for p-type HWCVD piezoresistors had not been previously reported.

Based on the noise analysis the calculated Hooke factor for QC 1s and TC 1s are different by an order of magnitude. It is unlikely that this discrepancy is due to a variation in the quality of the polysilicon since the piezoresistors for both devices were deposited together on to the same wafer. It is however possible that a decrease in the piezoresistors thickness occurred during the release of the suspended structure. This was more likely to occur on TC 1s due to the lower spring constant of the device. The decrease in piezoresistors thickness would have increased the Hooke noise. Thus the Hooke factor for TC 1s, which was therefore calculated with a piezoresistor thickness greater than the actual thickness, was overestimated. The increased Hooke noise also explains the lower than estimated F-D resolution measured for TC 1s. This indicates

that the process outlined in this project needs to be amended to include a protective mask for the frontside during the backside dry etch used to release the suspended structure.

To validate the QC sensors applicability for the F-D characterisation of biopolymers, the QC sensor was fitted with an indentation probe and used to measure the stiffness of agarose hydrogels with different concentrations of agarose. The measured values showed the expected linear relationship between the compliance and the agarose content. Furthermore, the measured Young's modulus,  $E$ , was found to be in good agreement with published data for similar measurements.

In this work, a QC sensor for the measurement of the mechanical properties of biopolymers was successfully developed, optimised, designed, fabricated, characterised and tested. In particular the novel QC sensor comprises the following features:

- QC spring capable of a 1% linear range at deflections  $>100\ \mu\text{m}$ , deflections  $>8\ \text{mm}$  with a linearity  $< 30\%$ , high out-of-plane compliance, and low in-plane compliance
- Implementation of a full Wheatstone bridge for accurate F-D sensing
- nN/nm resolution with polysilicon piezoresistors, and a theoretical pN/pm resolution with crystalline piezoresistors
- HWCVD polysilicon piezoresistors with a high gauge factor as large as 44
- Adaptable for in-vivo measurements
- A stiction free fabrication process

## 7.2 Future work

Future work on the QC sensor would include exploring other ideas to improve the performance of the sensor. One such idea is using circular beams as shown in Figure 7-1. This would decrease the stress concentrations in the beams thus increase the deflection limit of the device. Another possibility is increasing the sensitivity and thus the resolution of the device. This work has already shown that pN/pm resolution is theoretically possible using epitaxial piezoresistors; however, this can be improved further using the giant piezoresistive effect in Si nanowires [1]. The addition of a microfabricated tip would also improve the performance and scope of the device.

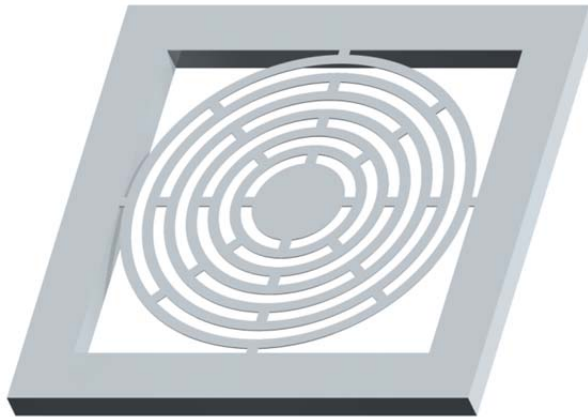


**Figure 7-1: QC sensor with circular beams. This may decrease the stress concentrations thus increase the deflection limit further.**

In addition to developing the sensor further, the adaptation of the device for different applications is also worthy of investigation. The following are some ideas which could take advantage of the high resolution, linearity and measurement range of the QC sensor.

The resolution, size and in-plane compliance of the QC sensor makes it ideal for in-vivo F-D measurements. Possible applications are the early detection of cancer cells [2] and osteoarthritis [3] for which a correlation between the Young's modulus and the pathological state has been established. Figure 7-2.a shows a possible embodiment of a diagnostic tool for the in-vivo early detection of osteoarthritis. The diagnostic tool head is connected to a tube which would contain the power and output wires and a second tube used to supply Ringer's solution to inflate a balloon. This would allow for the sensor to be stabilised during measurements. To use the device, it would be inserted into the joint during keyhole surgery and once positioned over the cartilage to be examined, the balloon would be inflated and F-D measurements taken (Figures 7-2.b and 7-3). A similar device has already been developed by Imer et al. [4]; however, the device used a piezoresistive cantilever. Due to the higher deflections possible, the QC sensor would increase the resilience of the device thus making it better suited for the application.

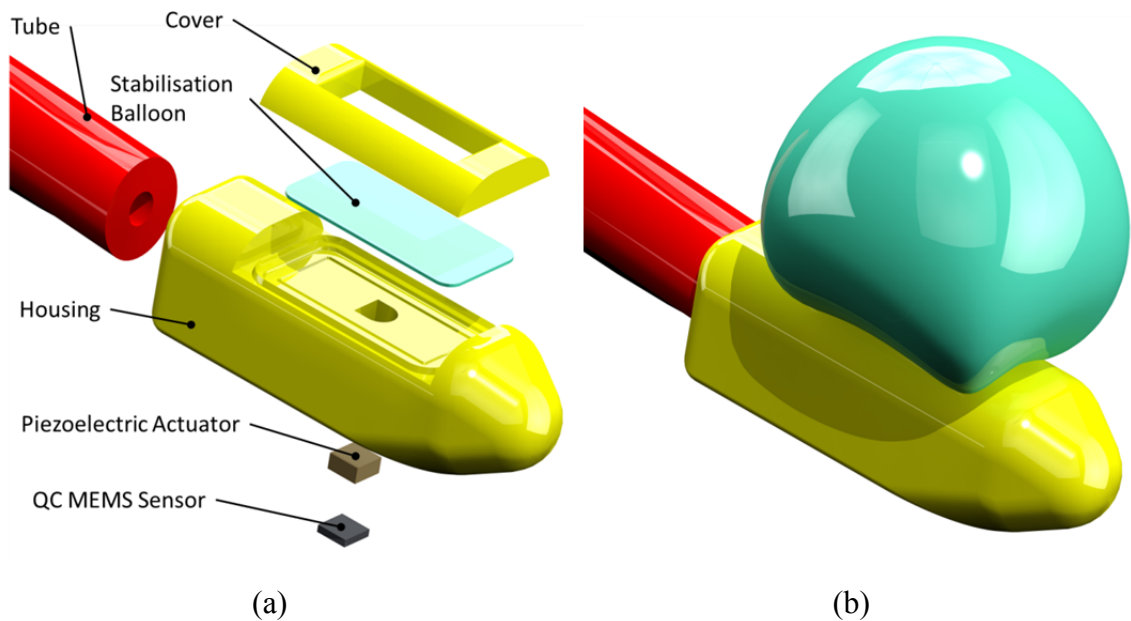


**Figure 7-2: (a) An exploded view and (b) an assembled view with stabilisation diaphragm inflated of a diagnostic tool for the early detection of osteoarthritis.**



**Figure 7-3: A view of the diagnostic tool for the early detection of osteoarthritis inserted into the knee.**

Another potential application for the QC sensor is for high-speed imaging. Using multiple piezoresistive sensors in parallel to increase the imaging speed is not novel [5, 6]; however, using the QC sensor would increase the out-of-plane range of the measurements thus permitting the imaging of surfaces with large changes in topography.

A further application is a high accuracy, high linearity and large range flow meter. In this application, the QC sensor is integrated into a tube as shown in Figure 7-4. The suspended platform features an orifice designed to suit the viscosity of the fluid or gas measured for the sensitivity required. The flow rate would be determined by monitoring the deflection of the suspended platform. Similar applications could also include

molecular mass sensors, extreme force accelerometers, optical mirrors, and pressure sensors.

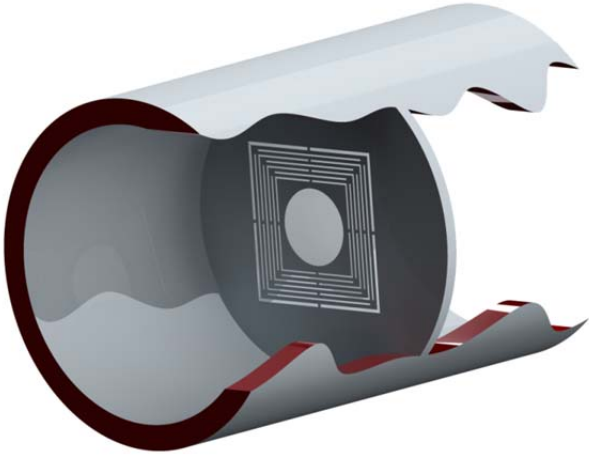


**Figure 7-4: A QC sensor adapted as a high accuracy, linearity and large range flow meter.**

## References

- [1] R. R. He and P. D. Yang, "Giant piezoresistance effect in silicon nanowires," *Nature Nanotechnology*, vol. 1, pp. 42-46, Oct 2006.
- [2] M. Lekka, "Atomic Force Microscopy a Tip for Diagnosing Cancer," *Nature Nanotechnology*, vol. 7, pp. 691-692, Nov 2012.
- [3] H. T. Nia, I. S. Bozchalooi, Y. Li, L. Han, H. H. Hung, E. Frank, *et al.*, "High-Bandwidth AFM-Based Rheology Reveals that Cartilage is Most Sensitive to High Loading Rates at Early Stages of Impairment," *Biophysical Journal*, vol. 104, pp. 1529-1537, Apr 2 2013.
- [4] R. Imer, "Development of a scanning force microscope for in-vivo, minimally invasive inspection of human knee cartilage.," Doctor of Science, Institut de Microtechnique, Université de Neuchâtel, Neuchâtel, Switzerland, 2008.
- [5] S. C. Minne, S. R. Manalis, and C. F. Quate, "Parallel atomic force microscopy using cantilevers with integrated piezoresistive sensors and integrated piezoelectric actuators," *Applied Physics Letters*, vol. 67, pp. 3918-3920, Dec 25 1995.
- [6] S. C. Minne, G. Yaralioglu, S. R. Manalis, J. D. Adams, J. Zesch, A. Atalar, *et al.*, "Automated parallel high-speed atomic force microscopy," *Applied Physics Letters*, vol. 72, pp. 2340-2342, May 4 1998.



## Appendix 1

### QC first resonant frequency Solver – MATLAB Code

```

% QC first resonant frequency solver
% For: QC MEMS Device
% Author: David Grech
% Date: 23nd May 2013
% Revision date: 2 Sept 2014
% Finds F_0 for QC 1, QC 2 and QC 3 by
% function accordingly and
% selecting matrices accordingly

% Change function accordingly for QC 1, 2 and 3

% Use for QC 1
function [freqs,modes] =
compute_frequencies_thesis_2_Sept_2014(k1,k2,k3,k4,k5,k6,M,m1,m2,m3,m4,m5)

% Use for QC 2
% function [freqs,modes] =
%compute_frequencies_thesis_2_Sept_2014(k1,k2,k3,k4,k5,k6,k7,k8,k9,k10,k11,k12,k%13,k14,k15,k16
% ,k17,M,m1,m2,m3,m4,m5,m6,m7,m8,m9,m10,m11,m12,m13,m14,m1%5,m16)

% Use for QC 3
% function [freqs,modes] =
%compute_frequencies_thesis_2_Sept_2014(k1,k2,k3,k4,k5,k6,k7,k8,k9,k10,k11,k12,k%13,k14,k15,k16
% ,k17,k18,k19,k20,k21,k22,k23,k24,k25,k26,k27,M,m1,m2,m3,m4,m5,%m6,m7,m8,m9,m10,m11,m12,
% m13,m14,m15,m16,m17,m18,m19,m20,m21,m22,m23,%m24,m25,m26)

% Use this for QC 2
M = [ M, 0,0,0,0,0;
      0,m1,0,0,0,0;
      0,0,m2,0,0,0;
      0,0,0,m3,0,0;
      0,0,0,0,m4,0;
      0,0,0,0,0,m5] ;

```

```

K = [k1,-k1,      0,0,0,0;
     -k1,k1+k2,-k2, 0,0,0;
     0, -k2,k2+k3,-k3, 0,0;
     0,0, -k3,k3+k4,-k4, 0;
     0,0,0, -k4,k4+k5,-k5;
     0,0,0,0, -k5,k5+k6];

```

```
% Use this for QC 2
```

```

%M = [ M, 0,0,0,0,0,0,0,0,0,0,0,0,0,0,0,0;
%      0, m1, 0,0,0,0,0,0,0,0,0,0,0,0,0,0,0;
%      0,0, m2, 0,0,0,0,0,0,0,0,0,0,0,0,0,0;
%      0,0,0, m3, 0,0,0,0,0,0,0,0,0,0,0,0,0,0;
%      0,0,0,0, m4, 0,0,0,0,0,0,0,0,0,0,0,0,0,0;
%      0,0,0,0,0, m5, 0,0,0,0,0,0,0,0,0,0,0,0,0;
%      0,0,0,0,0,0, m6, 0,0,0,0,0,0,0,0,0,0,0,0,0;
%      0,0,0,0,0,0,0, m7, 0,0,0,0,0,0,0,0,0,0,0,0,0;
%      0,0,0,0,0,0,0,0, m8, 0,0,0,0,0,0,0,0,0,0,0,0,0;
%      0,0,0,0,0,0,0,0,0, m9, 0,0,0,0,0,0,0,0,0,0,0,0,0;
%      0,0,0,0,0,0,0,0,0,0, m10, 0,0,0,0,0,0,0,0,0,0,0,0,0;
%      0,0,0,0,0,0,0,0,0,0,0, m11, 0,0,0,0,0,0,0,0,0,0,0,0,0;
%      0,0,0,0,0,0,0,0,0,0,0,0, m12, 0,0,0,0,0,0,0,0,0,0,0,0,0;
%      0,0,0,0,0,0,0,0,0,0,0,0,0, m13, 0,0,0,0,0,0,0,0,0,0,0,0,0;
%      0,0,0,0,0,0,0,0,0,0,0,0,0,0, m14, 0,0,0,0,0,0,0,0,0,0,0,0,0;
%      0,0,0,0,0,0,0,0,0,0,0,0,0,0,0, m15, 0,0,0,0,0,0,0,0,0,0,0,0,0;
%      0,0,0,0,0,0,0,0,0,0,0,0,0,0,0,0, m16];

```

```

%K = [k1,-k1,      0,0,0,0,0,0,0,0,0,0,0,0,0,0,0,0;
%     -k1,k1+k2,-k2, 0,0,0,0,0,0,0,0,0,0,0,0,0,0,0;
%     0, -k2,k2+k3,-k3, 0,0,0,0,0,0,0,0,0,0,0,0,0,0,0;
%     0,0, -k3,k3+k4,-k4, 0,0,0,0,0,0,0,0,0,0,0,0,0,0,0;
%     0,0,0, -k4,k4+k5,-k5, 0,0,0,0,0,0,0,0,0,0,0,0,0,0,0;
%     0,0,0,0, -k5,k5+k6,-k6, 0,0,0,0,0,0,0,0,0,0,0,0,0,0,0;
%     0,0,0,0,0, -k6,k6+k7,-k7, 0,0,0,0,0,0,0,0,0,0,0,0,0,0,0;
%     0,0,0,0,0,0, -k7,k7+k8,-k8, 0,0,0,0,0,0,0,0,0,0,0,0,0,0,0;
%     0,0,0,0,0,0,0, -k8,k8+k9,-k9, 0,0,0,0,0,0,0,0,0,0,0,0,0,0,0;
%     0,0,0,0,0,0,0,0, -k9,k9+k10,-k10, 0,0,0,0,0,0,0,0,0,0,0,0,0,0,0;
%     0,0,0,0,0,0,0,0,0, -k10,k10+k11,-k11, 0,0,0,0,0,0,0,0,0,0,0,0,0,0,0;
%     0,0,0,0,0,0,0,0,0,0, -k11,k11+k12,-k12, 0,0,0,0,0,0,0,0,0,0,0,0,0,0,0;
%     0,0,0,0,0,0,0,0,0,0,0, -k12,k12+k13,-k13, 0,0,0,0,0,0,0,0,0,0,0,0,0,0,0;
%     0,0,0,0,0,0,0,0,0,0,0,0, -k13,k13+k14,-k14, 0,0,0,0,0,0,0,0,0,0,0,0,0,0,0;

```





## Non-Linear Deflection Calculator – MATLAB Code

```

% Cantilever non-linear deflection Calculation
%
% Author: David Grech
% Date: 17th Aug 2013
% Revised: 3rd Sept 2014
% Reference Paper: "Large and small deflections of a cantilever beam" -
% Belendez - 2002
%
% Use program to calculate the non-linear beam deflection of a cantilever.
% For a QC spring this program would be run for each beam set
% and the total deflection for the QC would be calculated from
% the sum of each run. Force used is 1/8 force applied to QC
%
clear; clear; clear all; close all; clc;
delete(gcf)
parpool
loop = 0;

% Enter device parameters here
F_Orig = 0.00050; % Total Maximum Force (N)on device/8;
F = F_Orig; % Intial Force (N)usedin calc;
L = (0.001286)/4; % Length (m) of beam;
E = 169*10^9; % Young's Modulus (Pa);
w = 8.45E-06; % width of beam (m);
t = 4.38E-06; % thickness of beam (m)
I = (w*t^3)/12; % Moment of inertia of beam;

%%%%%%%%%%%%%%

Q0_array = []; % array for Q0
alfa_array = []; % array for alfa
alfa_test_array = [];
alta_array = [];
betax_array = [];
neta_array = [];
deltax_array = [];
deltay_array = []; % array for deflection in y. The resultant non-linear deflection
F_array = [] ;

```

```

%%%%%%%%%%%%%%%%%%%%%%%%%%%%%%%%%%%%%%%%%%%%%%%%%%%%%%%%%%%%%%%%%%%%%%%%
%Loop to calculate Q0 and alfa for different forces
betax = 0;
while (betax >= 0 )
alfa=(F*L^2)/(2*E*I);
%%%%%%%%%%%%%%%%%%%%%%%%%%%%%%%%%%%%%%%%%%%%%%%%%%%%%%%%%%%%%%%%%%%%%%%%
%alfa integration
Qo = 1.57;
alfa_test = 100;
while (alfa_test < alfa - 10e-3) || (alfa_test > alfa + 10e-3) % adjust tolerances accordingly
Qo = Qo-10e-6;
fun = @(x) (1./((sin(Qo) - sin(x)).^(0.5)));
alfa_test = integral(fun,0,Qo-10e-6);% adjust tolerances accordingly
alfa_test = ((alfa_test)*.5).^(2);
end
alfa_array = [alfa_array; alfa];
alfa_test_array = [alfa_array; alfa_test];
%%%%%%%%%%%%%%%%%%%%%%%%%%%%%%%%%%%%%%%%%%%%%%%%%%%%%%%%%%%%%%%%%%%%%%%%
alta = (1/((alfa).^(0.5)))*(sin(Qo).^(0.5));
betax = 1 - alta;
betax_array = [betax_array; betax];
deltax_array = [deltax_array ; betax*L];
%%%%%%%%%%%%%%%%%%%%%%%%%%%%%%%%%%%%%%%%%%%%%%%%%%%%%%%%%%%%%%%%%%%%%%%%
%neta int
fun = @(x) (sin(x)./((sin(Qo) - sin(x)).^0.5));
neta_int = integral(fun,0,Qo);
neta = ((neta_int)./(2*((alfa).^0.5)));
neta_array = [neta_array; neta];
%%%%%%%%%%%%%%%%%%%%%%%%%%%%%%%%%%%%%%%%%%%%%%%%%%%%%%%%%%%%%%%%%%%%%%%%
%alfa_array = [alfa_array ; alfa];
deltay_array = [deltay_array ; neta * L];
F_array = [F_array ; F];
%%%%%%%%%%%%%%%%%%%%%%%%%%%%%%%%%%%%%%%%%%%%%%%%%%%%%%%%%%%%%%%%%%%%%%%%
F = F * 0.90; % Incremental Force step size
loop = loop +1
end

deltay_array

```

## Optimisation Program – MATLAB Code

```

% Piezo Resistive Calculation and basic optimization
% For: QC and TC MEMS Device
% Author: David Grech
% Date: 2nd March 2012
% Revision date: 19 September 2014
% Includes fine tuning features to find number of boxes, F_min and W
% for optimized l_pr, t_pr, V_bridge, n, w_min, t_c, beam separation,
% centre_piece
%
% Finding the minima of multiple functions using genetic algorithm.
% Objective 1 is F_min
% Objective 2 is Piezo Power

%%% Below solver settings for running directly from command window

% clear; clear; clear all; close all; clc;
% delete(gcf)
% Turn on multiprocessor support for multi-core machine.
% parpool

% FitnessFunction = @F_min_QC_Canti_complete_final_Thesis_copy;
% numberOfVariables = 12;

% A = []; b = [];
% Aeq = [];
% beq = [];

%lb = [x(1); x(2); x(3); x(4); x(5); x(6); x(7); x(8); x(9); x(10); x(11); x(12)];
%ub = [x(1); x(2); x(3); x(4); x(5); x(6); x(7); x(8); x(9); x(10); x(11); x(12)];

% x(1) = percent of l_c
% x(2) = t_pr
% x(3) = V_bridge
% x(4) = n
% x(5) = w_min
% x(6) = t_c
% x(7) = beam separation
% x(8) = centre_piece
% x(9) = k

```

```

% x(10) = 0 for Mono Si, 1 for Poly Si
% x(11) = 0 for QC, 1 for Cantilever
% x(12) = 0 for optimisation, 1 for dim. data

% options = gaoptimset('PlotFcns',@gaplotpareto);

% [x,Fval,exitFlag,Output] =gamultiobj(FitnessFunction,numberOfVariables,A,b,Aeq,beq,lb,ub,options);

% fprintf('The number of points on the Pareto front was: %d\n', size(x,1));
% fprintf('The average distance measure of the solutions on the Pareto front was: %g\n',
%Output.averagedistance);
% fprintf('The spread measure of the Pareto front was: %g\n', Output.spread);

function y = F_min_QC_Canti_complete_final_Thesis_copy(x) % function definition line

% Variables
t_pr = x(2);% Piezoresistor thickness in m
V_bridge = x(3);% Bridge Voltage
n = x(4);% Doping concentration 1e14 to 1e20 - variable - cm^-3
w_minimum = x(5);% Beam width in m
t_c = x(6);% Beam thickness in m
s = x(7);% Beam separation in m
SP = x(8);% Size of suspended platform in m
k_desired = x(9);% Desired k N/m
Silicon_type = x(10);% Material 0 = Si, 1 = Poly Si
QCTC = x(11);% 0 = QC, 1 = TC
Mode = x(12);% 0 = optimisation, 1 = dim. data

% Environment variables
T = 300;% Temperature (K) - room temperature
f = 1;% frequency (Hz)
f_min = 1;% minimum frequency (Hz) - adjust accordingly
f_max = 10;% maximum frequency (Hz) - adjust accordingly

% Universal Constants
q = 1.60217646e-19;% electron charge(C) - constant
k_b = 1.38065e-23;% Boltzmann's Constant (m2 kg s-2 K-) - constant

% Amplifier variables
C_j = 3.2e-9;% Input Noise for AD8421 amplifier at gain 100 (V/(Hz)^0.5) - amp dependant

```

C\_h = 6e-9;% For AD8421 amplifier at gain 100 (V/(Hz)^0.5) - amp dependant

% Design related parameters

E\_beam = 169e9;% Youngs Modulus in the <110> direction on a 100 wafer for beam material

E\_piezo = 169e9;% Youngs Modulus in the <110> direction on a 100 wafer for piezo material

if Silicon\_type == 1% if piezo is poly

E\_piezo = 139e9;% Youngs Modulus poly

end

h\_def = 15.e-6;% Actuation displacement - adjust accordingly

stress\_lin\_limit = 15.3e6;% Piezoresistor stress limit for linear output. 15.3MPa for 0.1% and 139 MPa for 1%

%%%

% QC structure calculations begins here %

if QCTC ==0

no\_beam = 4;% Number of beams in QC - 4 because box shape

accuracy = 0.1;% Accuracy of k

ro\_saftey = stress\_lin\_limit;% Maximum beam stress

%%% Initialisers %%%

l\_side\_matrix = [];% Matrix for l\_side

w\_max\_matrix = [];% Matrix for w\_max

k = 100;% Current calculated k total. Initially 100

def\_max= 0;% Maximum deflection

w\_min = w\_minimum;% Minimum width

l\_side = SP + 2\*s + 2\*w\_min;% 1st beam length for QC

Ptot = k\_desired \* h\_def;% Total Load

Psf = Ptot\*1;% Load including safety factor

P\_beam = Psf/no\_beam;% Total Load divided by the number of beams in N

no\_boxes = 0;% Number of boxes

%%%

% Calculation of the number of boxes loop begin here %

while k > k\_desired

```

ro_calc = (P_beam * (l_side)^3)/(4*w_min*t_c^2);% initial maximum stress calc

% primary width loop starts here

while ro_calc > ro_saftey

w_min = w_min + 0.001e-6;% increase w_min to reduce stress
l_side = l_side + 2*0.001e-6;% recalculate l_side based on new w_min

ro_calc = (P_beam * l_side ^ 3)/(4*w_min*t_c^2);% revised maximum stress calc

end

I = 1/12*(w_min*t_c^3);% Moment of inertia of the beam

def_min=(P_beam*l_side^3)/(192*E_beam*I); % max deflection for current beam
def_max=def_max+def_min; % current total structure deflection
k = (Psf/def_max); % current calculated k

no_boxes = no_boxes + 1; % Increment number of boxes

l_side_matrix = [l_side_matrix ; l_side];% Beam length matrix
w_max_matrix = [w_max_matrix ; w_min];% Beam width matrix

l_side = l_side + 2*s + 2*w_min;% New next box side length calculation

w_min = w_minimum;% Reinitialise w_max

end

%%%%%%%%%%%%%%%%%%%%%%%%%%%%%%%%%%%%%%%%%%%%%%%%%%%%%%%%%%%%%%%%%%%%%%%%
%k refinement loop – incremental%
i=1;
totdef=0;% Total deflection initialiser

while k < k_desired * (1-accuracy)

w_max_matrix = w_max_matrix + 0.01e-6;% increment beam width
l_side_matrix = l_side_matrix - 2*0.01e-6;% increment beam length

```

```

i=1;
totdef=0;

while i <= no_boxes

def=(P_beam*l_side_matrix(i)^3)/(192*E_beam*(1/12*(w_max_matrix(i)*t_c^3))); % Deflection calc
%for current beam
totdef = totdef + def;% Deflection addition of current beam to total

i=i+1;% increment counter
end

k = (Psf/totdef);% calculation of refined k
k_refined = k;

end
%%%%%%%%%%%%%%%%%%%%%%%%%%%%%%%%%%%%%%%%%%%%%%%%%%%%%%%%%%%%%%%%%%%%%%%%
% k refinement loop – decremented%
while k > k_desired * (1+accuracy)

w_max_matrix = w_max_matrix - 0.01e-6;% was 0.0001e-6 changed for speed
l_side_matrix = l_side_matrix + 2*0.01e-6;% was 0.0001e-6 changed for speed0.001e-6

i=1;
totdef=0;

while i <= no_boxes

def=(P_beam*l_side_matrix(i)^3)/(192*E_beam*(1/12*(w_max_matrix(i)*t_c^3))); % Deflection calc
%for current beam
totdef = totdef + def; Deflection addition of current beam to total

i=i+1;% increment counter

end

k = (Psf/totdef);% calculation of refined k

end

```

```

l_c = l_side_matrix(no_boxes);% outermost beam length initializer
w_c = w_max_matrix(no_boxes);% outermost beam width initializer

l_pr = x(1)*l_c;% Piezoresistor length in m

end
%%% QC structure calculations ends here %%%
%%%%%%%%%%%%%%%%%%%%%%%%%%%%%%%%%%%%%%%%%%%%%%%%%%%%%%%%%%%%%%%%%%%%%%%%
% TC structure calculations begins here %
if QCTC == 1
Ptot = k_desired * h_def; % Total Load
Psf = Ptot*1;% Load including safety factor
P_beam = Psf/1;% Total Load divided by the number of beams in N 1 for cantilever
no_boxes = 0;% Number of boxes

l_c = ((E_beam*w_minimum*(t_c)^3)/(4*k_desired))^(1/3);
l_pr = x(1)*l_c;

end
%%% TC structure calculations ends here %%%
%%%%%%%%%%%%%%%%%%%%%%%%%%%%%%%%%%%%%%%%%%%%%%%%%%%%%%%%%%%%%%%%%%%%%%%%
% Electrical calculations begin here %

% Piezoresistive Constants/Variables
if QCTC == 0
    w_pr = w_c;% width of piezoresistor width of beam
end
if QCTC == 1
    w_pr = w_minimum/2;% width of piezoresistor 1/2 width of cantilever
end
% Process Parameters
N = n*100*100*100*l_pr* w_pr * t_pr;% Total number of carriers in the resistor - assuming uniformly
%doped poly and ignoring gb
alfa = 1e-5;% Experimentally measured value that is dependent on the crystal lattice quality. For Epitaxy
%use 1e-5 [Doll, 2009], 1.8e-3 for poly
if Silicon_type == 1
alfa = 1.8e-3;
end
Pi_o = 72e-11;% piezo resistive coefficient for p-type boron doped piezoresistor
if Silicon_type == 1

```

```

Pi_o = 72e-11 * 0.4;% piezo resistive coefficient for p-type boron doped %piezoresistor %% X 0.4
%correction for poly [Bao, 2005]
end
uo = 44.9;% Using formula taken from "Modeling of carrier %Mobility Against Carrier Concentration in
%Arsenic, Phosphorus, and Boron Doped %Silicon
u1 = 29;% [Guido Masetti 1983]
u_max = 470.5;
C_r = 2.23e17;
C_s = 6.10e20;
alfa2 = 0.719;
beta = 2;
p_c = 9.23e16;
u = (uo*exp(-p_c/n) +((u_max)/(1+(n/C_r)^alfa2)) - ((u1)/(1+(C_s/n)^beta)))/100/100 ; % concentration
%dependent majority carrier mobility - (Guido Masetti 1983) - see tables %versus n units in paper
%cm^2/Vs so converted to m^2/Vs

% Resistance
if QCTC == 0
w_t = w_c;% width Al tracks
end
if QCTC == 1
w_t = w_minimum/2;% width Al tracks
end
t_t = 500e-9;% thickness of Al tracks
rho_t = 2.7e-8;% resistivity Al tracks
rho_pr = 1/(q*u*n*100*100*100);% for mono silicon
if Silicon_type == 1
rho_pr = (1e23)*(n^(-1.282))/100;% for poly silicon using graphs PJ French 2002 %units ohm * m
end

l_t = 100e-6;% Length Al tracks
a = 0.2014;% Constant (Harley/Kenny 2000 - 1/f noise %considerations) for concentrations above 10^17
%cm-3
b = 1.53e22;% Constant (Harley/Kenny 2000 - 1/f noise considerations) for %concentrations above 10^17
%cm-3

P = log10((b/n)^a);
Pi_1 = P * Pi_o;

if Silicon_type == 1

```

```

Pi_l = Pi_o;
end

R_t = rho_t*l_t/(w_t*t_t);% Resistance - Al tracks
R_pr = rho_pr*2*l_pr/(w_pr*t_pr); % Resistance - pr

Power = (V_bridge^2/4)/(R_pr);% Pair of piezoresistor Power Dissipated

Gamma = R_pr/(R_pr+R_t);% ratio of piezoresistance to total %resistance
if QCTC == 0 % if QC use this

stress_piezo_c = 3*P_beam*(l_c/4-(2*w_c + l_pr/2))/(w_c*(t_c+t_pr/2)^2); % stress at %2 x w + 1/2
%l_pr away from centre

end
if QCTC == 1% if TC use this
stress_piezo_c = 6*P_beam*(l_c-0.5*l_pr)/(w_minimum*((t_c+t_pr/2)^2));
end
if Silicon_type == 1% if Poly use this
%%%% Mono Si to Poly Si correction - the strain in the polysilicon is the
%%%% same as that in the adjacent region of the mono silicon.
stress_piezo_c = E_piezo * stress_piezo_c/E_beam; % [Bao, 2005]
end

B = P*(1 - t_pr/t_c);
if Silicon_type == 1
B = 1;% assume uniformly doped piezoresistor
end

if QCTC == 0%If QC use this
S_f = stress_piezo_c * V_bridge * B * Gamma * Pi_l / (P_beam*4); % sensitivity
end
if QCTC == 1% If TC use this
S_f = (1/4)*stress_piezo_c * V_bridge * B * Gamma * Pi_l / P_beam;% sensitivity
end

Vj_squared = 4* k_b * T * R_pr *(f_max - f_min);% Johnson Noise
Vj = Vj_squared^0.5;
Vh_squared = ((alfa * ((V_bridge/2)^2 * log(f_max/f_min))/(2*N)))^4;% Hooge Noise %*4 for 4 pairs
%of uncorrelated resistors

```

```

Vh = Vh_squared^0.5;
Va_squared = (C_j^2)*(f_max-f_min) + C_h^2*log(f_max/f_min);% Amp Noise
V_noise = sqrt(Vj_squared + Vh_squared + Va_squared);% Total Resultant Noise
F_min = V_noise/S_f;% F_min
if Mode == 1
if QCTC == 0
k
l_side_matrix
w_max_matrix
no_boxes
end
if QCTC == 1
l_c
end

Power
S_f
Vj
Vh
V_noise
R_pr
F_min
end

y(1) = F_min;
y(2) = Power;
y(3) = no_boxes;
end

```



## Appendix 2

### Fabrication Recipes

#### Wafer clean Recipe

Process	Time (minutes)
FNA	10
DI water rinse	n/a
RCA-1: NH <sub>4</sub> OH + H <sub>2</sub> O <sub>2</sub> + H <sub>2</sub> O (1:1:5)	10
BHF 20:1	1
RCA-2: HCl + H <sub>2</sub> O <sub>2</sub> + H <sub>2</sub> O (1:1:6)	10

#### PECVD Recipes

Equipment: OPT Plasmalab System 100 PECVD

Deposited material	SiO <sub>2</sub>	Si <sub>3</sub> N <sub>4</sub>
Deposition rate	63.6 nm/min	11.4 nm/min
Table heater	350°C	350°C
Pressure	1000 mT	650 mT
RF power	20 W	20 W
Gas/Flow	SiH <sub>4</sub> /4.2 sccm	SiH <sub>4</sub> /12.5 sccm
Gas/Flow	N <sub>2</sub> /80 sccm	N <sub>2</sub> /500 sccm
Gas/Flow	N <sub>2</sub> O/350 sccm	NH <sub>3</sub> /20 sccm

#### RIE Recipes

Equipment: OPT Plasmalab 80 plus

Etch material	SiO <sub>2</sub>	Si <sub>3</sub> N <sub>4</sub>
Etch rate	40-190 nm/min	25-50 nm/s
Table temperature	20°C	20°C
Pressure	30 mT	55 mT
RF power	200 W	150 W
Gas/Flow	Ar/38 sccm	O <sub>2</sub> /5 sccm
Gas/Flow	CHF <sub>3</sub> /12 sccm	CHF <sub>3</sub> /50 sccm

## ICP Recipe

Equipment: OPT Plasmalab System 100

Etch material	Si
Etch rate	~ 5 $\mu\text{m}/\text{min}$
Table temperature	10°C
Pressure	20 mT
RF power	100 W
ICP power	1500 W
Gas/Flow	SF <sub>6</sub> /200 sccm
Gas/Flow	Ar/50 sccm

## Photoresist spray recipes

AZ9260 (MicroChemicals)	AZ2070 (MicroChemicals)
MEK: 71%	MEK: 68%
AZ EBR: 25.5%	AZ EBR: 24.5%
AZ9260: 3.5%	AZ2070: 7.5%

## HWCVD polysilicon anneal temperature profile

Equipment: HiTech benchtop oxidation furnace

Process	Time (minutes)
Ar. pre-purge	30
Ramp 20°C to 430°C*	180
Constant 430°C (Hydrogen release phase) *	180
Ramp 430°C to 1000°C*	240
Constant 1000°C (Polysilicon anneal phase) *	30
Ramp 1000°C to 20°C*	540

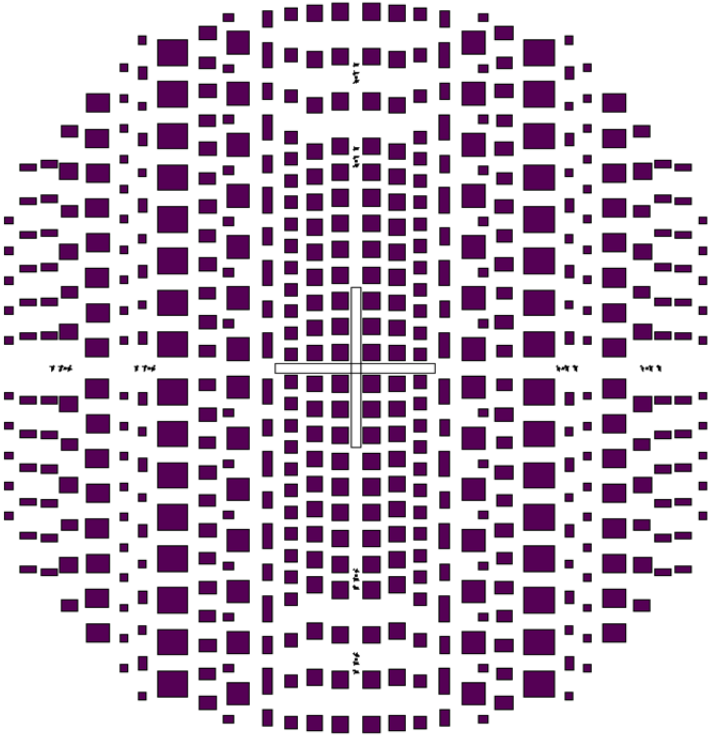
\*In an Ar. atmosphere

**Photoresist spray setting for 3 µm thick resist Recipe**

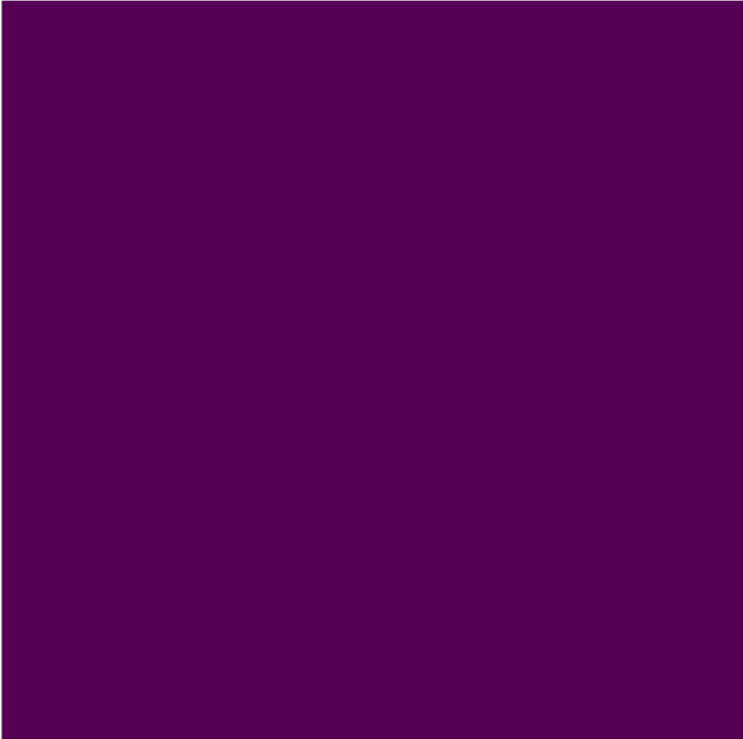
Equipment: EVG 150 - robotic resist processing station

<b>Syringe Spray Vortex</b>	yes
<b>Dispense rate</b>	35 µL/s
<b>Indices</b>	100, 300, 600, 1100, 1700, 1100, 600, 300, 100
<b>Suckback pressure</b>	35 µL
<b>Suckback rate</b>	10 µL/s
<b>Nozzle pressure</b>	100 mBar
<b>Ultrasonic power</b>	3500 mw
<b>Post dispense delay</b>	200 ms
<b>Height</b>	1000000
<b>Spline smoothing</b>	Yes
<b>Dispense arm up</b>	No
<b>Passes</b>	6

# Photolithography Masks

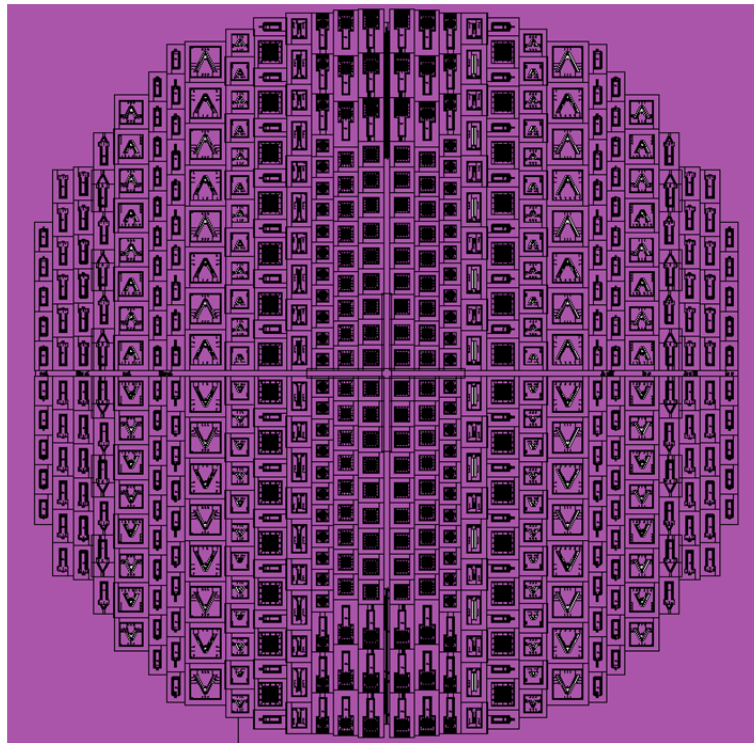


(a)

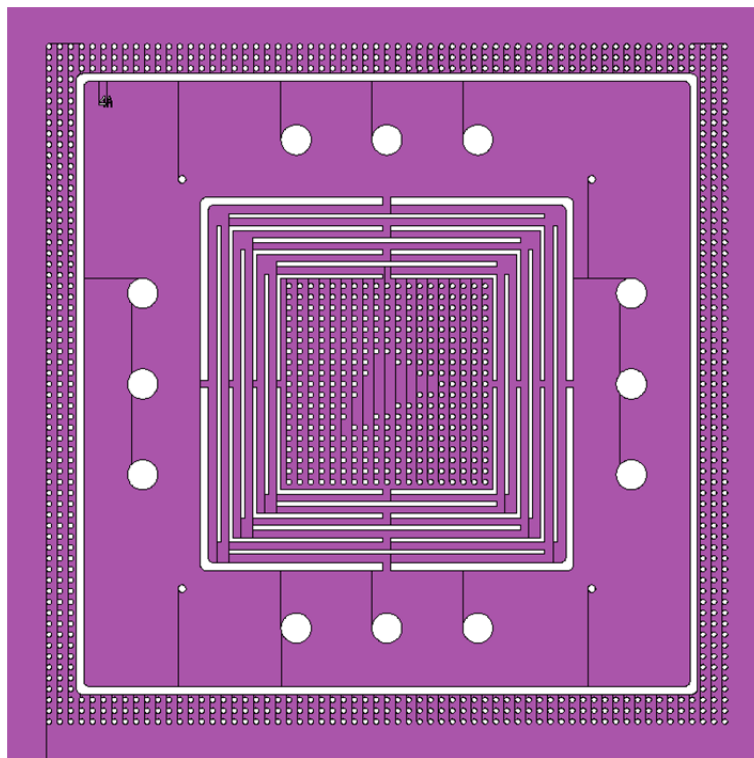


(b)

Figure A2-1: Photolithography Mask 1 for back side release (a) all devices, and (b) a single device.

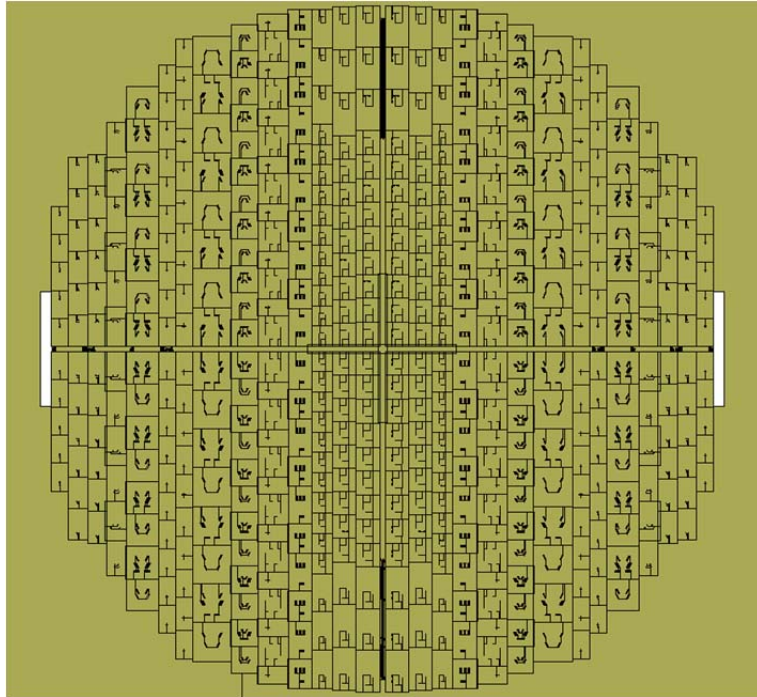


(a)

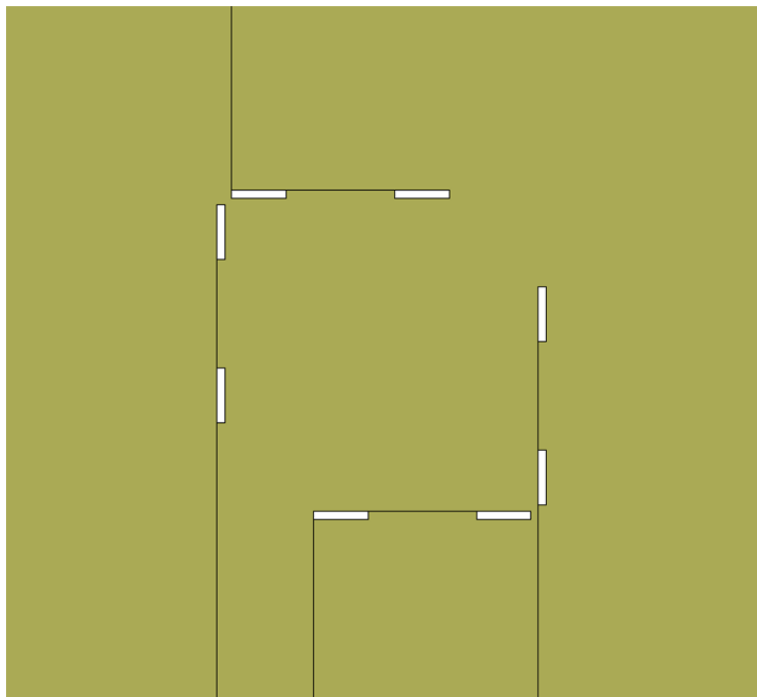


(b)

Figure A2-2: Photolithography Mask 2 for front side device structure (a) all devices, and (b) a single device.



(a)



(b)

Figure A2-3: Photolithography Mask 3 for front side piezoresistors (a) all devices, and (b) a single device.

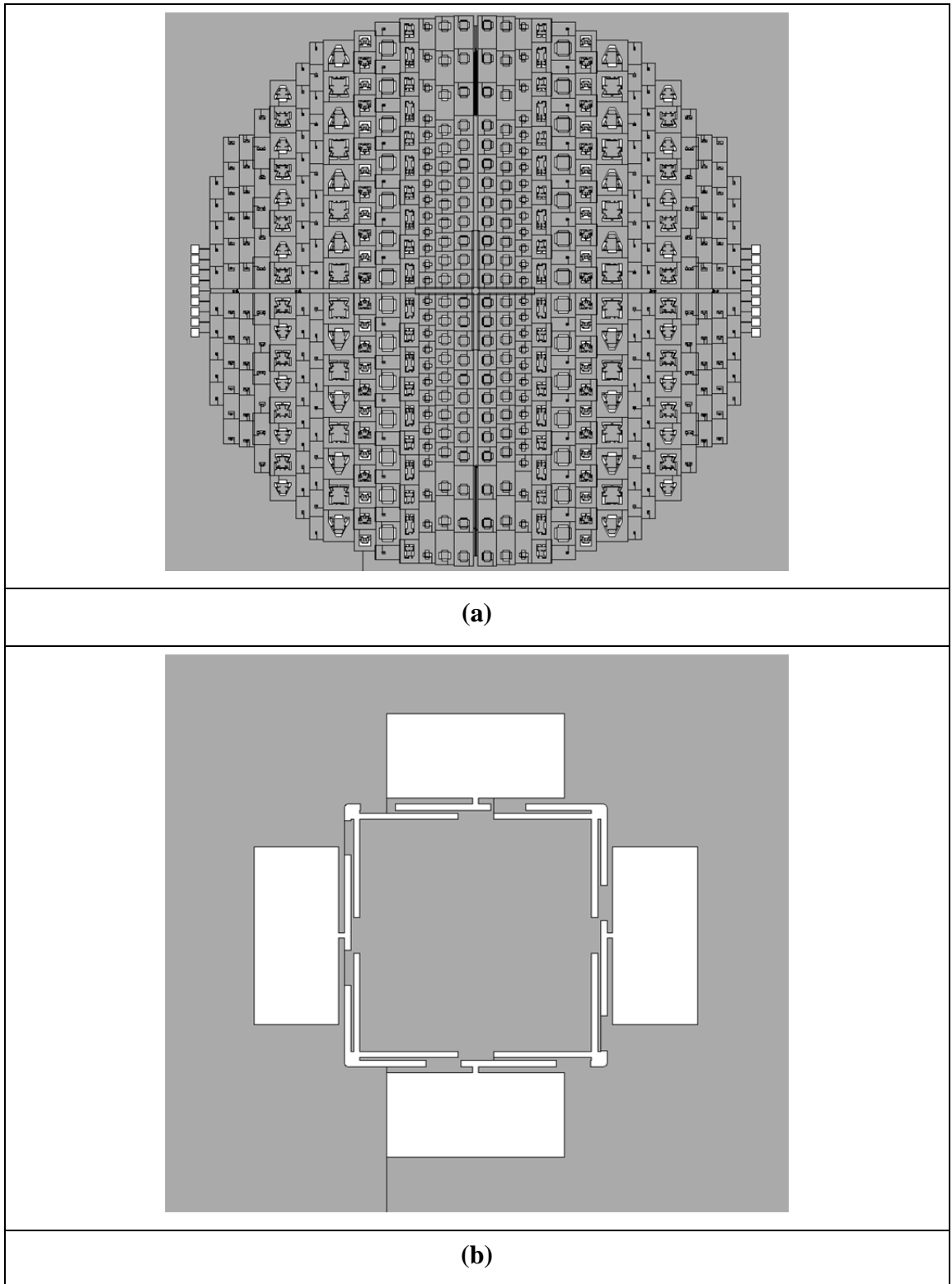


Figure A2-4 Photolithography Mask 4 for front side terminals (a) all devices, and (b) a single device.

## Images of Additional Fabricated Suspended Structures

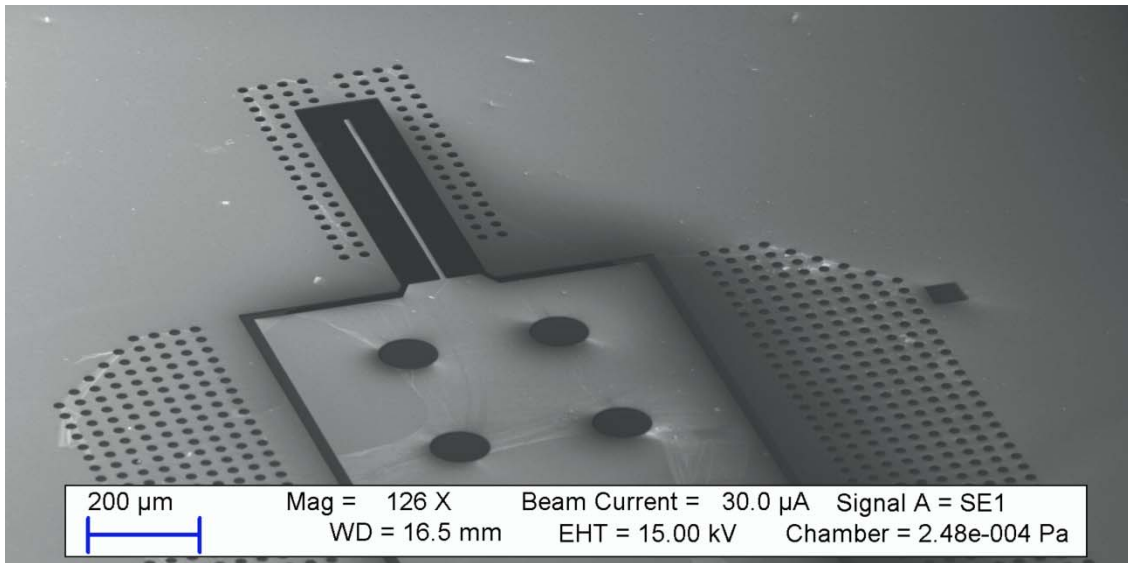


Figure A2-5: SEM image of a microfabricated cantilever

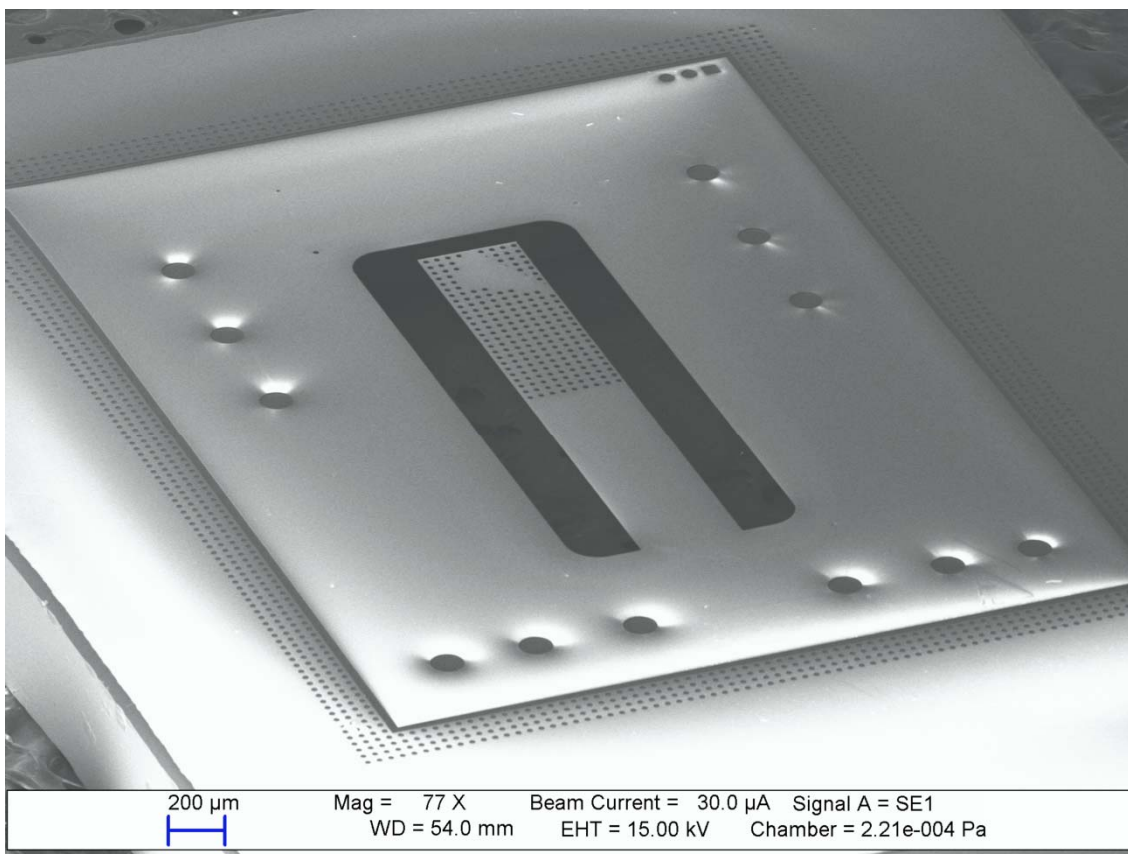


Figure A2-6: SEM image of a microfabricated wide cantilever

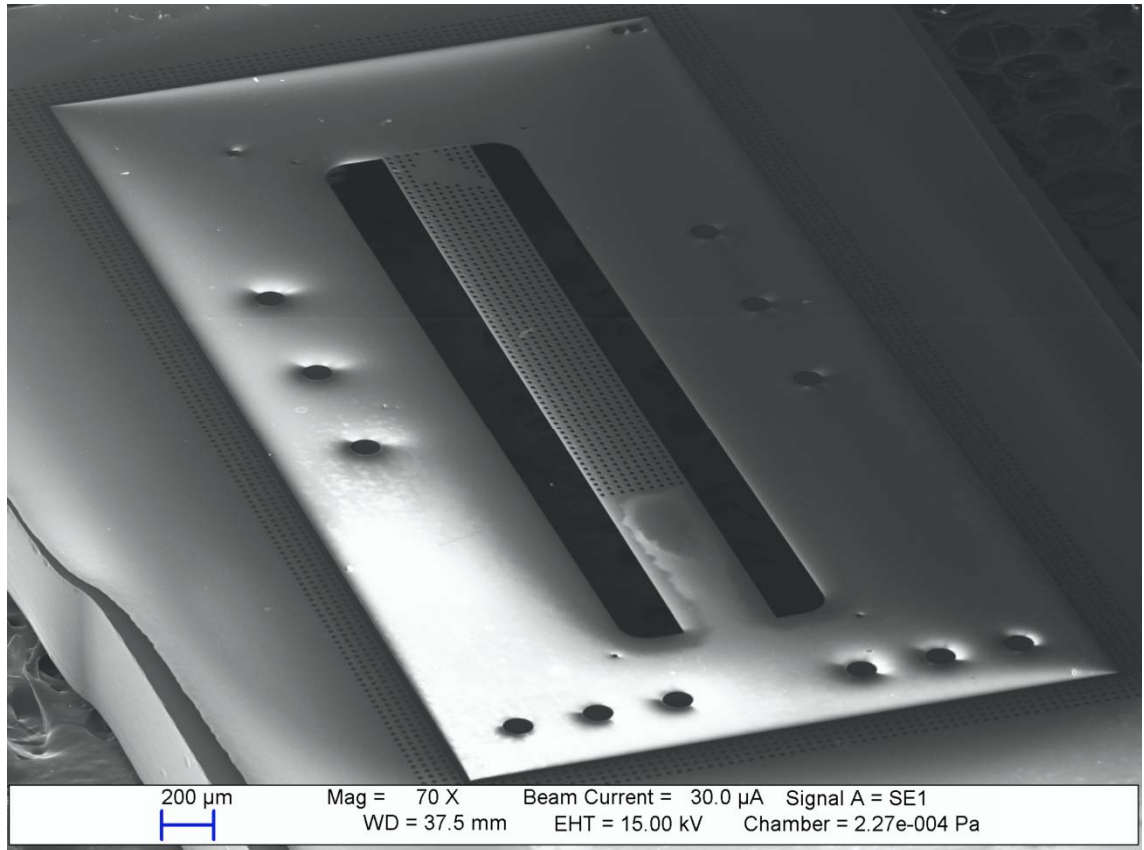


Figure A2-7: SEM image of a microfabricated wide cantilever (2)

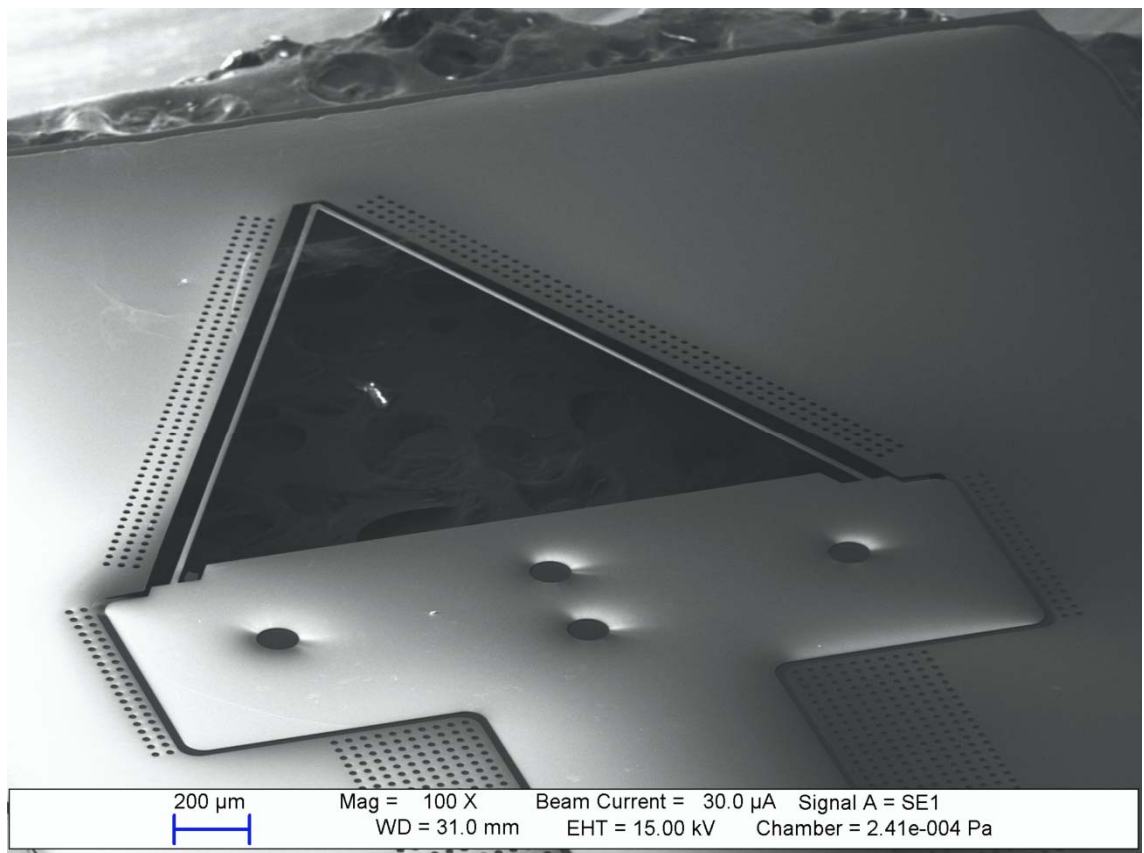
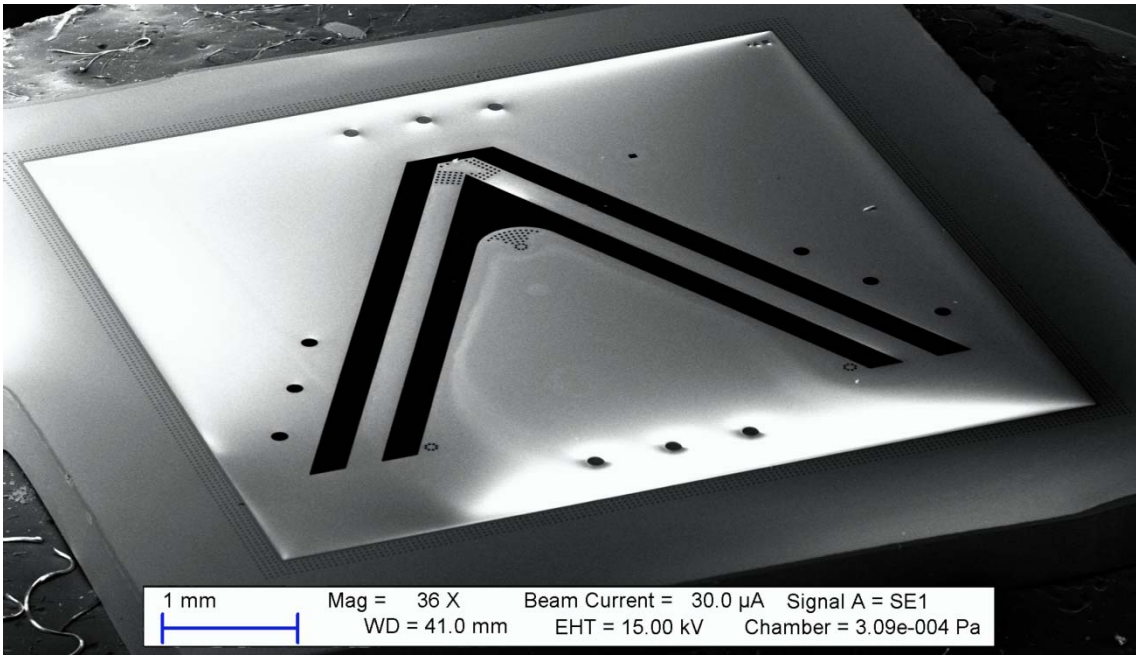
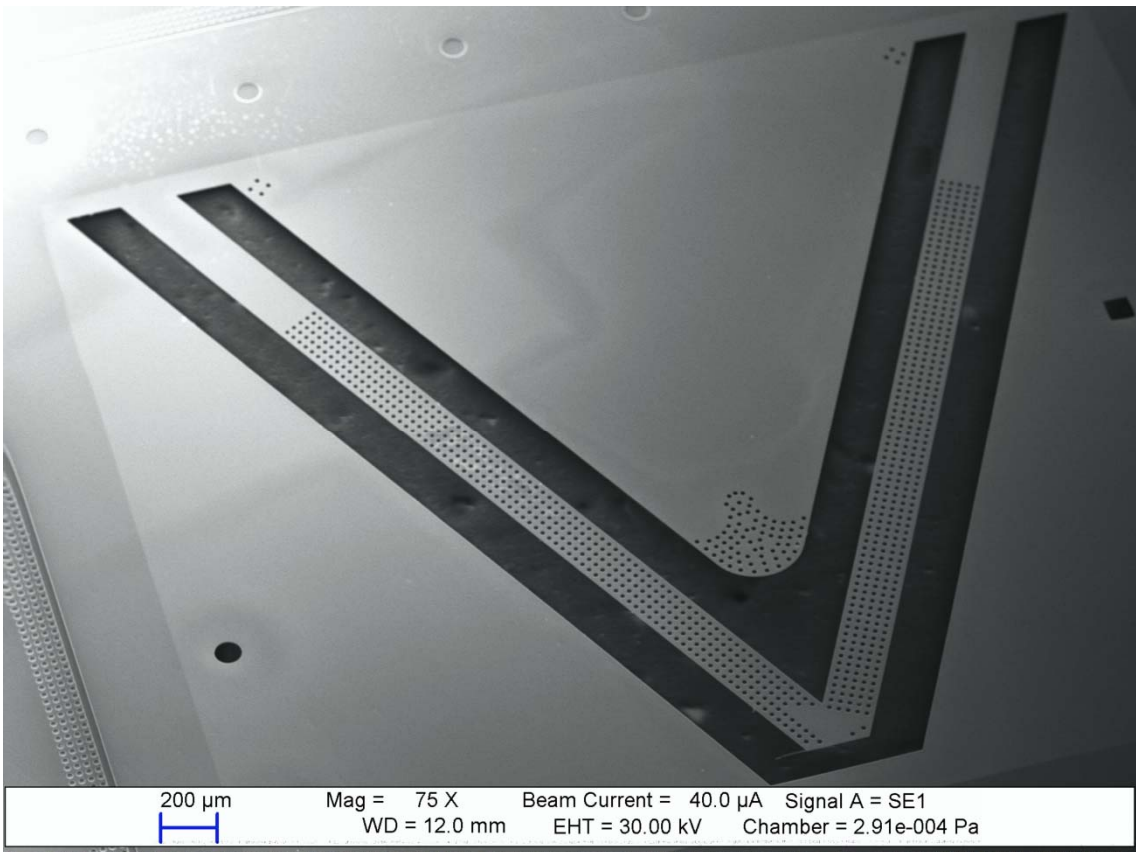


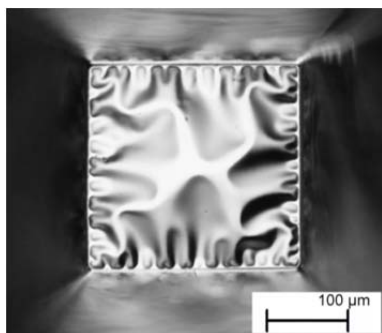
Figure A2-8: SEM image of a microfabricated thin triangular cantilever



**Figure A2-9: SEM image of a microfabricated wide triangular cantilever**



**Figure A2-10: SEM image of a microfabricated wide triangular cantilever (2)**



(a)



(b)

**Figure A2-11: SEM image of (a) 250 μm X 250 μm freestanding 280 nm thick NCG membrane and (b) 800 nm thick SiO<sub>2</sub> beams coated with 200 nm NCG fabricated by S. Fishlock et al. using the process outlined in this thesis.**



## Appendix 3

### Modified Cantilever on Cantilever Derivation

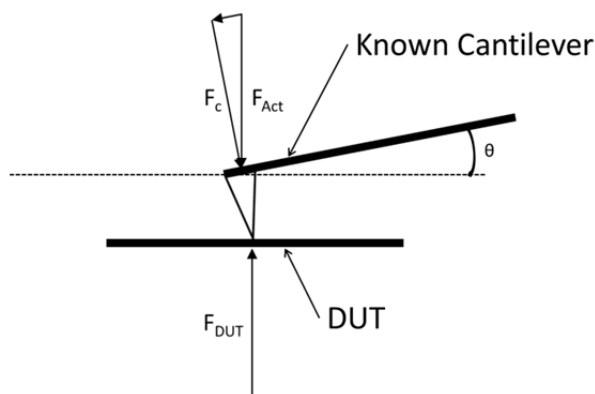


Figure A3-1: Cantilever on DUT – force vectors

The spring constant,  $k_{DUT}$ , of the known DUT is:

$$k_{DUT} = F_{DUT} / \delta_{DUT} \quad \text{Eq. A3-1}$$

where  $F_{DUT}$ , and  $\delta_{DUT}$  are the force and displacement of the DUT. The spring constant,  $k_c$ , of the known cantilever is:

$$k_c = F_c / \delta_c \quad \text{Eq. A3-2}$$

where  $F_c$ , and  $\delta_c$  are the force and displacement of the cantilever. The forces between the DUT and the cantilever are balanced, thus:

$$F_{DUT} = F_{Act} = F_c / \cos \theta \quad \text{Eq. A3-3}$$

where  $F_{Act}$  and  $\theta$  are the vertical component of the cantilever force transferred to the DUT and the angle of the cantilever to the horizon.

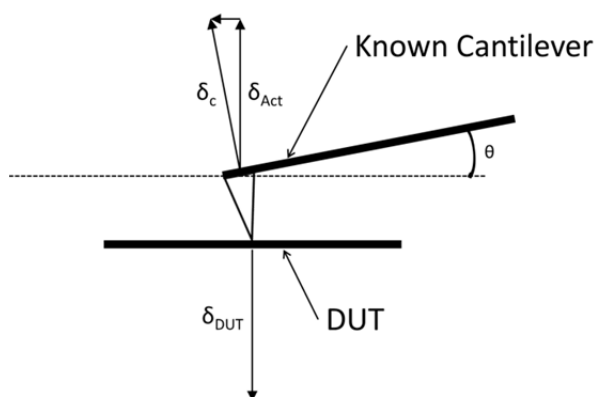


Figure A3-2: Cantilever on DUT – displacement vectors

The actual displacement,  $\delta_{Act}$ , in the vertical direction relative to the deflection of the cantilever is:

$$\delta_{Act} = \delta_c \cos\theta \quad \text{Eq. A3-4}$$

and the total actuation displacement,  $\delta_{tot}$ , is equal to:

$$\delta_{tot} = \delta_{DUT} + \delta_{Act} \quad \text{Eq. A3-5}$$

The slope,  $S_c$ , (Figure 5-2) is equal to:

$$S_c = \frac{\delta_{Act}}{\delta_{tot}} = \frac{\delta_{Act}}{\delta_{DUT} + \delta_{Act}} \quad \text{Eq. A3-6}$$

Substituting Eq. A4-2 into Eq. A4-4 gives:

$$\delta_{DUT} = \frac{\delta_c \cos\theta (1 - S_c)}{S_c} \quad \text{Eq. A3-7}$$

Substituting Eq. A4-2 and Eq. A4-7 into Eq. A4-1 gives:

$$k_{DUT} = k_c / (1/S_c - 1) \cos^2\theta \quad \text{Eq. 5-1}$$